UNIVERSITY OF CALIFORNIA
RIVERSIDE

Photodissociation Dynamics of Free Radicals Using High-n Rydberg Atom Time-of-Flight Technique

A Dissertation submitted in partial satisfaction
of the requirements for the degree of

Doctor of Philosophy

in

Chemistry

by

Yu Song

March 2011

Dissertation Committee:

Dr. Jingsong Zhang, Chairperson
Dr. Paul Ziemann
Dr. Yadong Yin

The Dissertation of Yu Song is approved:

Committee Chairperson

University of California, Riverside

Acknowledgements

First of all, I want to thank my advisor, Jingsong Zhang, for his great help during my past five years in UCR. He has taught me a lot in the spectroscopic field which I had never touched before. His knowledge in this field as well as in some other fields always impressed me. He is a very nice advisor who can give you help when you need him which I think is very precious for the graduate students. I also want to thank Jingsong's wife, Amber, for her great Sichuan food I have ever tasted and for her care in my daily life.

Secondly, I want to thank all my friends I met in Riverside. I cannot imagine living here alone without them. I want to thank my roommate Hongxia. Although she is at north California, I still miss the five years we stayed together and the help she gave me. Especially thank Wenjie Tang and Hongli Tao, my friends and roommates during my undergraduate study. They gave me valuable suggestion when I was upset. I also want to thank my group members.

Finally I want to thank all the staffs working in the chemistry department, graduate division and international education center.

Although my parents are in China now, they never stop missing me at the other side of the Pacific Ocean. Sometimes I blamed them on pushing me away from my hometown.

But I know they always love me no matter what. This dissertation is dedicated to them. I wish them happy and healthy all the time.

ABSTRACT OF THE DISSERTATION

Photodissociation Dynamics of Free Radicals
Using High-n Rydberg Atom Time-of-Flight Technique

by

Yu Song

Doctor of Philosophy, Graduate Program in Chemistry
University of California, Riverside, March 2011
Dr. Jingsong Zhang, Chairperson

The photodissociation dynamics of several important free radicals were studied using High-n Rydberg H-atom time-of-flight (HRTOF) technique, including the SD and CH_3S radicals which belong to the sulfur system, and C_3H_3, C_7H_7 and C_3H_5 radicals which are related to the formation of polycyclic aromatic hydrocarbons (PAHs).

The first chapter discusses the photodissociation dynamics as well as its experimental methodology. The experimental setup of the HRTOF technique is explained in detail.

The second chapter investigates the UV photodissociation dynamics of the SD radical in vibrationally ground and excited states in the photolysis wavelength region of 220 to 244 nm. The anisotropy parameter is ~ –1 while the spin-orbit branching fractions

of the $S(^3P_J)$ products are essentially constant. The dissociation mechanism and the bond dissociation energy are also obtained.

The third chapter investigates the near-UV photodissociation of the thiomethoxy (CH_3S) radical at 344-362 nm. Two vibronic levels of the thiomethoxy radical dissociate to $H + H_2CS$, while the others in the vicinity dissociate to $CH_3 + S(^3P_J)$. H-atom angular distribution is isotropic. The dissociation mechanism is consistent with internal conversion mechanism.

The fourth chapter investigates the UV photodissociation dynamics of the propargyl (C_3H_3) radical at 230-250 nm. The photofragment yield spectra of the $H + C_3H_2$ product channel are in good agreement with previous UV absorption spectrum. The $H + C_3H_2$ product translational energy distributions are obtained as well as the dissociation mechanism. The H-atom product angular distribution is isotropic.

Chapter 5 investigates the UV photodissociation dynamics of the benzyl (C_7H_7) radical at 228-270 nm. The H-atom photofragment yield spectra are in a good agreement with the previous UV absorption spectra. The $H + C_7H_6$ product translational energy distributions indicate the production of fulvenallene + H. The H/D product ratios from isotope labeling studies suggest that the H/D atoms are scrambled in the photodissociation of benzyl.

Chapter 6 investigates the UV photodissociation dynamics of the allyl (C_3H_5) radical at 216-238 nm. H-atom photofragment yield spectra suggest another dissociation channel $CH_3 + C_2H_2$ in this region. The C_3H_4 + H product translational energy release indicate the production of allene + H or propyne + H. The product angular distribution and dissociation mechanism are also obtained.

Chapter 7 discusses the future work on several radicals: phenyl (C_6H_5) radical, 1-propenyl ($CHCHCH_3$) and 2-propenyl (CH_2CCH_3) radicals.

Table of Contents

Lists of Figures

Lists of Tables

CHAPTER 1

Introduction

1.1 Photodissociation Dynamics

Photodissociation means a chemical compound (either molecule or radical) fragments following absorption of one or more photons. Once the photon energy is larger than the dissociation threshold of the chemical compound, the compound will fall apart and the excess energy will distribute among different degrees of freedom. Photodissociation dynamics aims to investigate this procedure in order to illustrate dissociation pathways and transition states, probe potential energy surfaces of excited electronic states and their couplings. In this dissertation, the main target is to study the photodissociation dynamics of free radicals. Free radicals are very reactive because they have unpaired electrons with open shell configuration. As a result, they are difficult to be detected. However, free radicals play a significant role in many aspects of chemistry and physics. In combustion, free radicals are the main intermediates in the chain reactions. Correctly predicting the radicals and their concentrations during the combustion is crucial to determine the final products. For example, each year combustion engines produce lots

of soot that contains polycyclic aromatic hydrocarbons (PAHs) into the environment which are carcinogenic to human. But the formation of soot in combustion is complicated and is constituted by many elementary radical-related reactions. Therefore studying the photodissociation dynamics of possible PAHs precursor radicals is important and could provide a fundamental understanding of the radicals, such as their excited electronic states and dissociation products. In the photodissociation process of some hydrocarbon radicals, the electronically excited radicals could undergo internal conversion to the highly vibrationally excited ground electronic state. These radicals possess an internal excitation energy equivalent to a vibrational temperature around several thousand Kelvin. Therefore the photodissociation dynamics of these radicals is important to predict the energetics and dissociation products of the radicals in combustion. In atmospheric chemistry, the dynamics of radicals are also important since the sunlight gives enough photon energy to dissociate molecules in the air and generates many kinds of radicals which will further react or dissociate. For example, the high temperature in automobile engines converts the nitrogen and oxygen gases to nitric oxide which is further converted into nitrogen dioxide in the atmosphere. Nitrogen dioxide is a brown gas and plays an important role in the smog formation. When the concentration of nitrogen dioxide is high, the sunlight in the troposphere photodissociates the nitrogen dioxide and finally forms the ozone, which is a constituent of the smog and causes respiratory illness. Another famous

example is the depletion of the ozone layer in the stratosphere. The unreactive chlorofluorocarbons (CFCs) released from the refrigerants and propellants are photodissociated by the UV radiation from the sunlight in the stratosphere, and eventually form the chlorine monoxide (ClO) radical which reacts with ozone in a series of chain reactions. This process in the upper atmosphere is believed to be the main mechanism for the depletion of the ozone layer. Another importance of free radicals shows up in interstellar chemistry. A number of spectroscopic studies have proved the existence of radicals in the interstellar space. Studying radical spectroscopy will help to identify the composition of interstellar clouds and their abundance.

1.2 Types of Photodissociation

1.2.1 Direct Photodissociation

Direct photodissociation is illustrated in Figure 1.1 (a). When a molecule or radical AB is excited by a photon energy hν to an upper electronic state, it hits a repulsive state which is not bound and doesn't have an equilibrium configuration. In such case, the excited compound AB* will directly dissociate along the potential energy curve. The time scale for this procedure is very short, making the energy distribution non-statistical. Most

Types of Photodissociation

$$AB + h\upsilon \rightarrow (AB)^* \rightarrow A + B$$

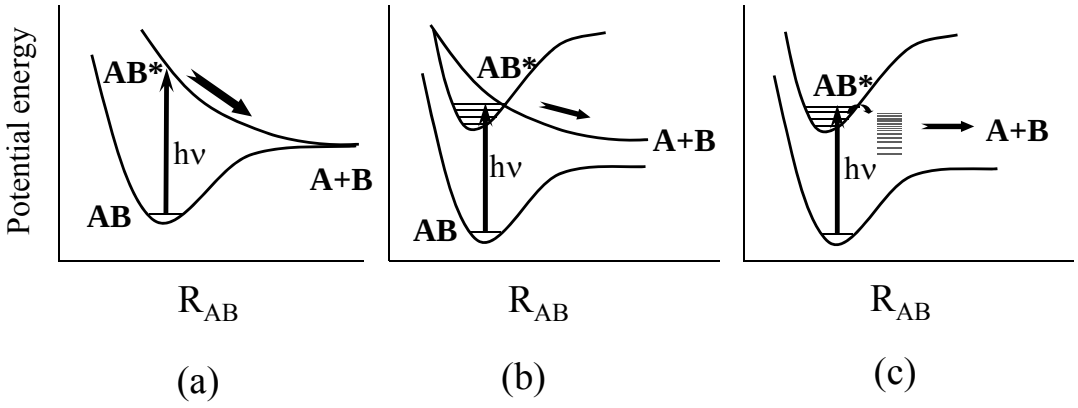

Figure 1.1 Three different types of photodissociation: (a) direct photodissociation; (b) indirect photodissociation: predissociation by coupling between a bound electronic state with a repulsive electronic state; (c) indirect photodissociation: internal conversion (IC) from a bound electronic state to the lower electronic state (vibrationally-rotationally excited), products are internally excited. AB* represents the excited AB compound.

of the excess energy will partition into the translational degree of freedom, instead of the internal degrees of freedom.

1.2.2 Indirect Photodissociation

Figure 1.1 (b) and (c) shows two types of indirect photodissociation. Indirect photodissociation happens when a molecule or radical AB is excited to a bound excited electronic state. If the lifetime of the excited AB* is long enough (~ns), fluorescence will take place. That is, the AB* relaxes to the ground state through a radiative decay. In competition with fluorescence is the non-radiative decay. One circumstance is that the excited bound electronic state couples with another repulsive state, as shown in Figure 1.1 (b). The AB* will finally decay through the repulsive state. The dissociation rate depends on the extent of coupling between the two electronic states. The other type of indirect photodissociation is internal conversion (IC). When AB is excited to a bound electronic state, the coupling between the excited electronic state and the lower electronic state makes the AB* undergo internal conversion to highly vibrationally-rotationally excited levels on lower electronic state, as shown in Figure 1.1 (c). Since these levels lie above the dissociation threshold of the lower electronic state or ground electronic state, AB* will decay through lower electronic state. This dissociation process is basically longer than the direct dissociation. The excited AB* have time to distribute its excess

energy to each degree of freedom, which tends to make the energy distribution statistical (each degree of freedom will obtain the same amount of energy). Therefore, the photofragments are internally excited with less translation energy than the direct dissociation.

1.3 Experimental Methodology to Study Photodissociation Dynamics

Photodissociation of free radicals has been studied extensively during these decades thanks to the development of laser and molecular beam techniques. The experimental methods to study photodissociation dynamics can be categorized into two parts according to the information gathered in the experiment: time-resolved measurements and energy-resolved measurements.

Time-resolved experiments aim to investigate the time evolution of a chemical reaction. In these measurements, the dissociation rate of the chemical compound and the lifetime of the transition state can be obtained. For a photodissociation process, the lifetime of the excited state is usually shorter than 1 ns. Therefore an ultrafast laser is suitable to measure the lifetime and dissociation rate of reaction. The times scales related to fast and ultrafast motions in photodissociation are listed in Table 1.1. The recent progress in this field is the femtochemistry first developed by Zewail et al. A review

article of femtochemistry by Zewail[1] was published in 1996 and he received the Nobel Prize in chemistry for his studies of the transition states of chemical reactions using femtosecond spectroscopy in 1999. However, according to the uncertainty principle, the energy resolution will be lost due to the short time (~fs) of the laser pulse.

Another branch in photodissociation chemistry is the energy-resolved experiments. Several experimental approaches are listed in Figure 1.2. The methods to record the product energy distribution can be separated into direct measurement and indirect measurement. Direct measurements include several powerful technologies: absorption spectroscopy, LIF (laser induced fluorescence) and MPI (multi-photon ionization). All of them are optical-based experiments. With the state-of-the-art laser technology, these experimental techniques have provided accurate results of probing the product quantum states. However, these methods are limited in the following aspects. The most important drawback is that both LIF and MPI require that the product must possess an optically accessible electronic excited state of which the lifetime is longer than dissociation period. Otherwise, the products would dissociate, leaves nothing for the detection. Meanwhile the transition probabilities of product between initial state and excited probe state are needed in order to calculate the initial relative product population and energy distribution. Finally, it is time-consuming to scan the probe laser along the entire product distribution region.

Time scales for fast and ultrafast motions

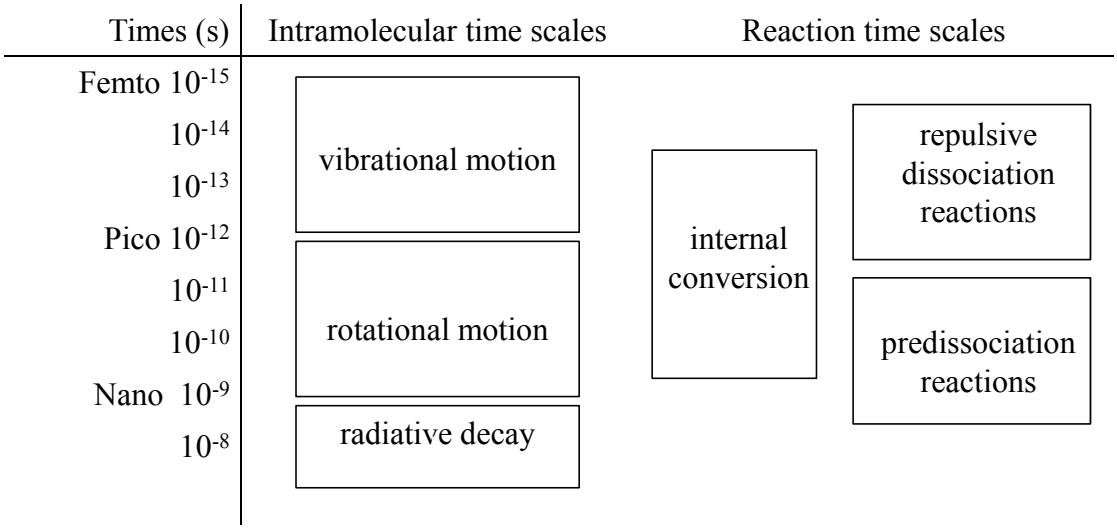

Table 1.1 Time scales of fast and ultrafast motions related to photodissociation. On the left are the times from femtosecond to nanosecond scale. In the middle are the intramolecular motions relevant to photodissociation. On the right are the three kinds of dissociation reactions mentioned in Figure 1.1.

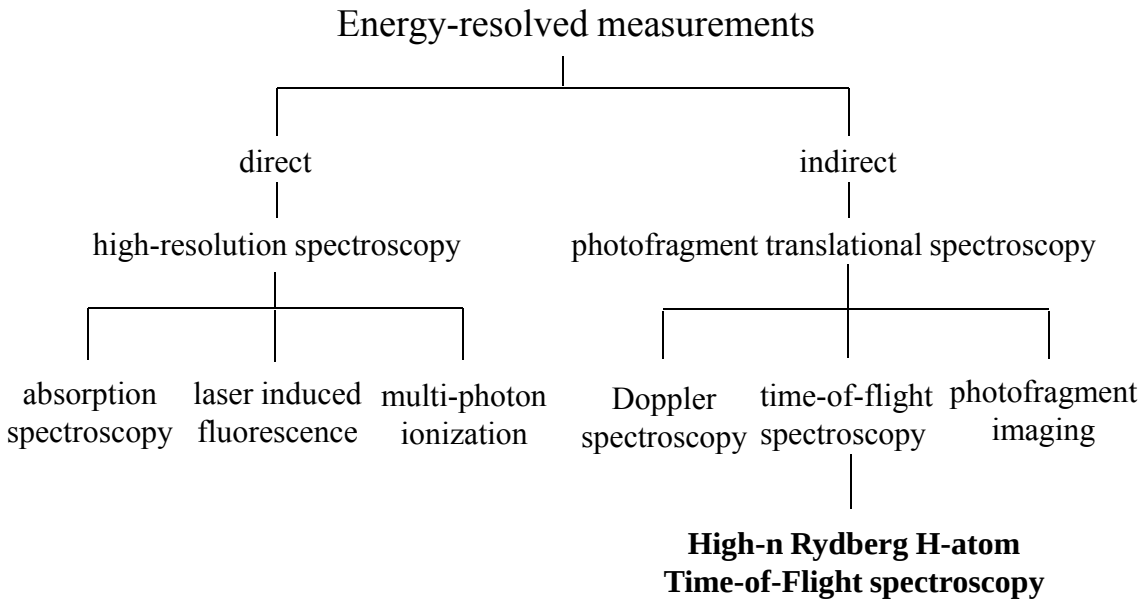

Figure 1.2 Overview of energy-resolved experimental approaches and position of High-n Rydberg H-atom Time-of-Flight (HRTOF) spectroscopy.

As a result, photofragment translational spectroscopy gives an alternate way to study photodissociation dynamics by deriving indirectly the product state distribution from the product translational energy distribution. Meanwhile one can also get the information of product angular distribution. This field includes methodologies such as Doppler spectroscopy, photofragment imaging, time-of-flight (TOF) spectroscopy, etc. Among them, high-n H-atom Rydberg Time-of-Flight technique (HRTOF) pioneered by Welge and co-workers[2] gives great resolution and sensitivity. This dissertation will mainly discuss the application of HRTOF technique on several important radicals.

1.4 High-n Rydberg H-atom Time-of-Flight spectroscopy

1.4.1 High-n Rydberg Hydrogen Atom

The high-n Rydberg hydrogen atom is an electronically excited hydrogen atom with a very large principle quantum number (n~50-90). The energy and radius of H atom can be described using the following equations:

$$E_n = -\frac{13.6}{n^2}\text{eV} \qquad n = 1,2,3,... \tag{1}$$

$$r_n = a_0 n^2 \tag{2}$$

In the equations, n is the principle quantum number, a_0 is the Bohr radius which is equal to 0.529 Å. Thus the ionization potential for the ground H atom is 13.6 eV, which is

equivalent to photon energy at 92 nm. The external electric field strength required to ionize the electron from the nucleus is 5.14×10^{11} V/m which is hardly achievable. However, when the hydrogen atom is excited to a high Rydberg state, the radius of H atom will increase quadratically with quantum number n. If n=50, the radius r~1300 Å. If n=90, radius n~4285 Å. The increasing radius between the electron and nucleus reduce the Coulomb force and thus the binding energy. So it is possible for a moderate electric field to ionize the H atom. For example, if the H is excited to n=50, the electric field strength is ~8.2×10^4 V/m. If n=90, the electric field strength is ~7800 V/m. Both of them are easy to achieve in laboratory.

In the HRTOF experiment, because of the very high energy of the first excited state for the H atom, basically all the H products from the photodissociation are lying on the ground state. Since one photon is not easy to excite H directly to high Rydberg state, two-color resonant excitation is used to generate Rydberg H atoms. As shown in Figure 1.3, at first H atom is excited from ground state $1^2S_{1/2}$ to the excited state 2^2P via Lyman-α transition with VUV photon at 121.6 nm. Then a second UV photon at ~366 nm excites the H atom to a high-n Rydberg state. Note here that because of the selection rules, the one-photon transition from 1s $^2S_{1/2}$ to 2s $^2S_{1/2}$ is forbidden ($\Delta l \neq 0$). The lifetime of 2^2P state of H atom is ~10 ns, which is longer than the delay time between the two probe lasers (~2 ns). Since the spontaneous emission rate on the high Rydberg state is small, the

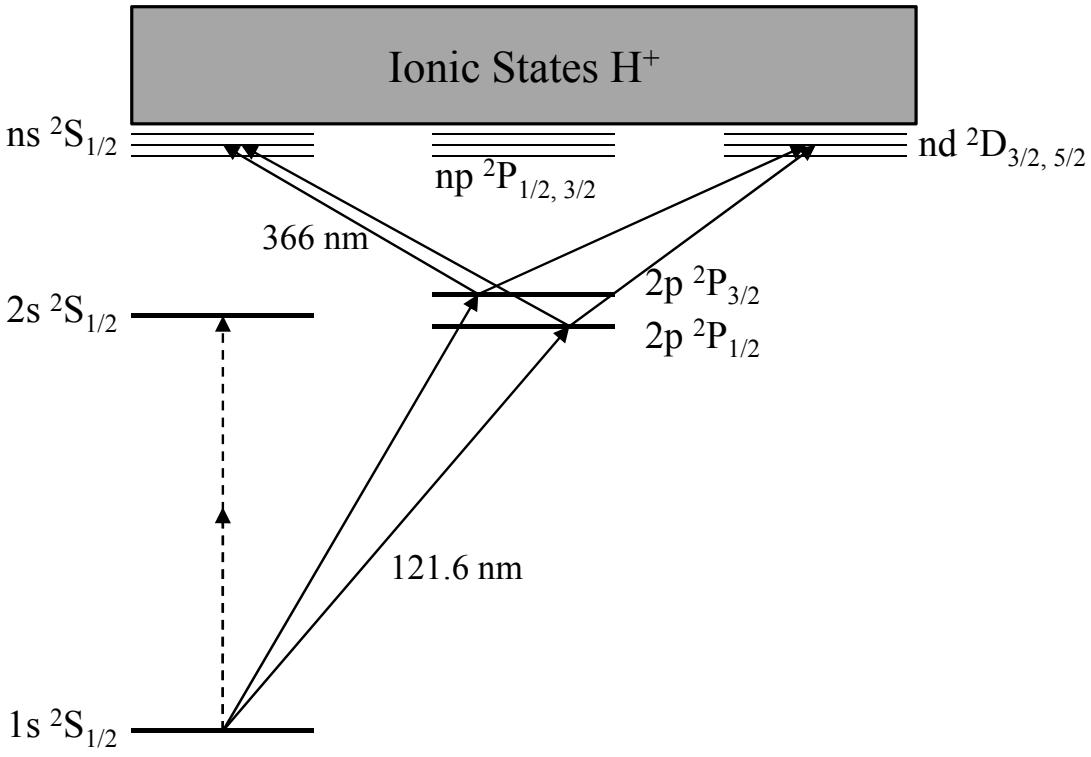

Figure 1.3 Energy diagram of H atom and scheme of two-color resonant excitation to form Rydberg H atoms.

lifetime of Rydberg H is longer than the time of flight of the H atom, as shown in Table 1.2. The long lifetime prevents the Rydberg H atom from decaying before they arrive at the detection region. After excitation to the Rydberg state, the neutral metastable H atom will drift toward the detector with their nascent velocity and will not be affected by space charge in the chamber. The detection of neutral H atoms instead of ionizing the H atoms also helps to avoid the explosion of ions in the interaction region. These advantages provide the HRTOF technique with high resolution and sensitivity, making this technique a powerful tool to study photodissociation dynamics of molecules and radicals.

1.4.2 High-n Rydberg H-atom Time-of-Flight (HRTOF) spectroscopy

Energy distribution

The product detection of HRTOF is limited to the H atom. However, HRTOF technique has some unique advantages in the photodissociation field because: (1) H dissociation channel is very common and energetic in many organic and inorganic species; (2) The detection of H product in HRTOF technique will give a very high resolution which will be discussed later. In this chapter, HR will be used to represent the radical before dissociation. The dissociation reaction can be written as:

$$\mathrm{HR}\,(v'', j'') + h\nu \rightarrow \mathrm{R}(v', j') + \mathrm{H} \qquad (3)$$

Table 1.2 calculated lifetimes of Rydberg H atoms*

l \ *n*	10	50	90
0	1.8 μs	0.18 ms	1 ms
n-1	6.2 μs	25 ms	390 ms

*see ref 3 for more details

If conservation of energy is considered, the following equation is derived:

$$E_{\text{int}}^{\text{HR}} + h\nu - \text{D}_0(\text{H - R}) = E_{\text{avail}} = E_{\text{int}}^{\text{R}} + E_{\text{trans}}^{\text{H}} + E_{\text{trans}}^{\text{R}} \quad (4)$$

In this equation, $E_{\text{int}}^{\text{HR}}$ is the internal energy of parent HR, D_0 (H-R) is the bond dissociation energy, E_{avail} is the available energy which is distributed among different degrees of freedom of the photofragments. The energy disposal will be different depending on the dissociation mechanism of each molecule. In the HRTOF technique, E_{avail} will be distributed among the internal energy of fragment R, translation energy of H atom and its counterpart R. An example of the photodissociation of HCO radical is shown in Figure 1.4.

Generally, $E_{\text{int}}^{\text{HR}}$ is small compared to the rest of the terms in the above equation. In the HRTOF experiment, supersonic expansion will be adopted to cool down the radical beam, which brings the rotational temperature down to 5-10 K and vibrational temperature down to 50-100 K. These temperatures correspond to an internal energy ~0.2 kcal/mol which is negligible compared to the dissociation energy (usually larger than 10 kcal/mol). Thus, E_{avail} can be calculated if the bond dissociation energy is known. In the TOF spectrum, the arrival time of the H atom from the dissociation point to the detector is recorded which can be connected to $E_{\text{trans}}^{\text{H}}$. According to the conservation of momentum, the total translational energy of H and R is:

$$E_{\text{trans}}^{\text{H}} + E_{\text{trans}}^{\text{R}} = (1 + \frac{m_{\text{H}}}{m_{\text{R}}}) E_{\text{trans}}^{\text{H}} \quad (5)$$

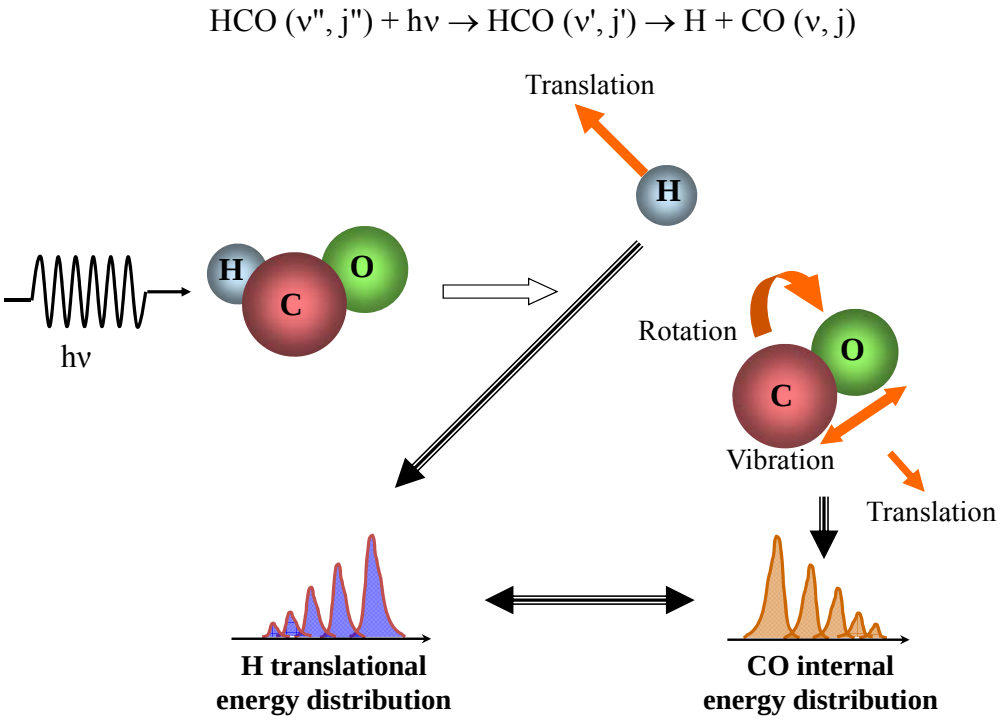

Figure 1.4 HCO radical is used as an example for the dissociation precursor. After absorbing a photon energy hν (larger than bond energy H-CO), HCO dissociates to H and CO. The excess energy after the dissociation will be partitioned among translational energies of H atom and CO, rotational and vibrational energies of CO. The translational energy of H can be measured from TOF spectrum. Since the translational energy of the counterpart CO is very small compared to H atom, the internal energy distribution can be calculated by using the energy conservation equation (4).

In this case, the internal energy distribution of R can be obtained which is helpful on deciding the dissociation pathway and mechanism, etc. However, one should notice that the $E_{\text{trans}}^{\text{H}}$ calculated from the arrival time of H atom is in the lab frame. In actual experimental setup, the flight path of H product is orthogonal to the molecular beam, as shown in Figure 1.5. The product center-of-mass (CM) translational energy expression is:

$$E_{\text{trans}}^{\text{H,R}} = \left(1+\frac{m_{\text{H}}}{m_{\text{R}}}\right)E_{\text{trans}}^{\text{H}} + \frac{m_{\text{H}}}{m_{\text{R}}}E_{\text{trans}}^{\text{HR}} = \frac{1}{2}m_{\text{H}}\left(1+\frac{m_{\text{H}}}{m_{\text{R}}}\right)\left(\frac{L}{t_{\text{H}}}\right)^2 + \frac{m_{\text{H}}}{m_{\text{R}}}E_{\text{trans}}^{\text{HR}} \qquad (6)$$

In this equation, $E_{\text{trans}}^{\text{H,R}}$ is the CM translational energy of the products. $E_{\text{trans}}^{\text{H}}$ and $E_{\text{trans}}^{\text{HR}}$ are the laboratory translation energies of the H product and parent HR, respectively. The second term $\frac{m_{\text{H}}}{m_{\text{R}}}E_{\text{trans}}^{\text{HR}}$ is due to the parent movement which is orthogonal to the flight path. However, it is very small compared to the first term. Normally it is neglected in the calculation. So the product translational energy and internal energy can be expressed as:

$$E_{\text{trans}}^{\text{H,R}} = \frac{1}{2}m_{\text{H}}\left(1+\frac{m_{\text{H}}}{m_{\text{R}}}\right)\left(\frac{L}{t_{\text{H}}}\right)^2 \qquad (7)$$

$$E_{\text{int}}^{\text{R}} = E_{\text{avail}} - E_{\text{trans}}^{\text{H,R}} = h\nu - \text{D}_0(\text{H - R}) - \frac{1}{2}m_{\text{H}}\left(1+\frac{m_{\text{H}}}{m_{\text{R}}}\right)\left(\frac{L}{t_{\text{H}}}\right)^2 \qquad (8)$$

The flight path length L is calibrated by the photodissociation of HBr whose dissociation energy and energy levels are well-known. The calibrated L value is 37.1 cm. The arrival time of the H atoms is recorded in the TOF spectrum. Therefore, the product energy distribution is resolved by using the above two equations.

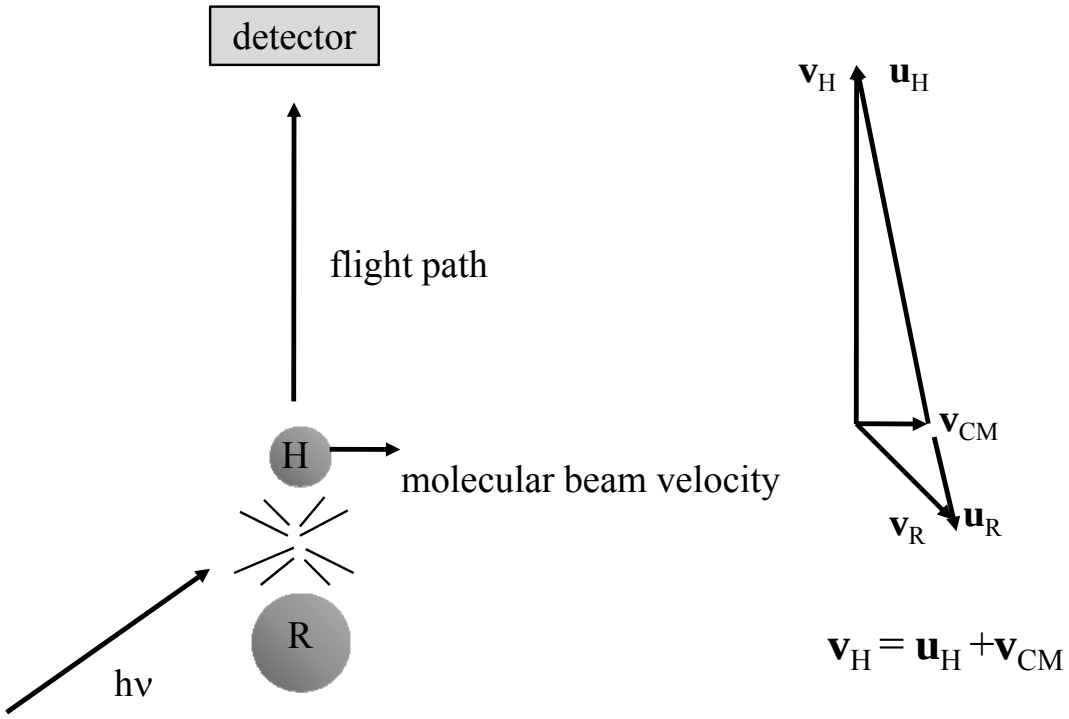

Figure 1.5 On the left is the schematic experimental setup showing the molecular beam and flight path directions. On the right is the simple Newton diagram showing the relationship between the center-of-mass frame and lab frame. The v_{CM} is the center-of-mass velocity. The v_H, v_R and u_H, u_R are the velocities in the lab frame and CM frame, respectively.

Then it is possible to describe the dissociation mechanism and the characteristics of excited electronic state.

By rearranging the above equation, the dissociation energy is expressed as:

$$D_0(H\text{-}R) = h\nu - E_{trans}^{H,R} - E_{int}^{R} \quad (9)$$

In the dissociation process, after photon breaks the H-R bond, the excess energy will be partitioned among $E_{trans}^{H,R}$ and E_{int}^{R}. In the distribution of E_{int}^{R}, one extreme is E_{int}^{R}=0 which means the internal energy of fragment R at this extreme is zero. This indicates that all the excess energy at this point belongs to the $E_{trans}^{H,R}$, corresponding to the largest $E_{trans}^{H,R}$. Thus by finding the largest translational energy of products, the upper limit of the bond dissociation energy is obtained:

$$D_0(H\text{-}R) \le h\nu - E_{trans}^{H,R}(MAX) \quad (10)$$

This is helpful on finding the dissociation pathway since different pathways have different dissociation energies. Meanwhile, if the bond dissociation energy is accessible, the maximum translational energy can be calculated. If there is multi-photon absorption occurs during dissociation, the maximum translational energy must become larger and thus one can judge if or not there is a multi-photon process.

Angular distribution

Energy distribution could provide valuable information of the photodissociation, such as the dissociation pathway and its mechanism, the characteristics of the excited electronic state. At the same time, angular distribution could also be measured and used to exam dissociation process from another angle.

Angular distribution, by its name, explores how the products recoil after the dissociation. Before dissociation, the parent HR molecules are randomly oriented. Then a linear polarized laser is used in HRTOF experiment to dissociate them. The polarized light will preferentially excite the parent molecules whose transition dipole moment $\vec{\mu}$ is parallel to the electric field $\vec{E}$ of the polarized light according to the absorption probability:

$$P = \left|\vec{\mu} \cdot \vec{E}\right|^2 \tag{11}$$

Thus immediately after absorbing the photons, the transition dipoles of all the excited parent molecules have the same orientation with the electric field of laser. If the dissociation time is shorter than the molecule's rotational period, before molecule has a chance rotate, it will dissociate along the breaking bond. However, if the dissociation time is long enough for the parent molecule to rotate, the fragments could orient randomly in space. Therefore the lifetime of the excited parent could be obtained from the product angular distribution. The photofragment angular distribution is given[4] as:

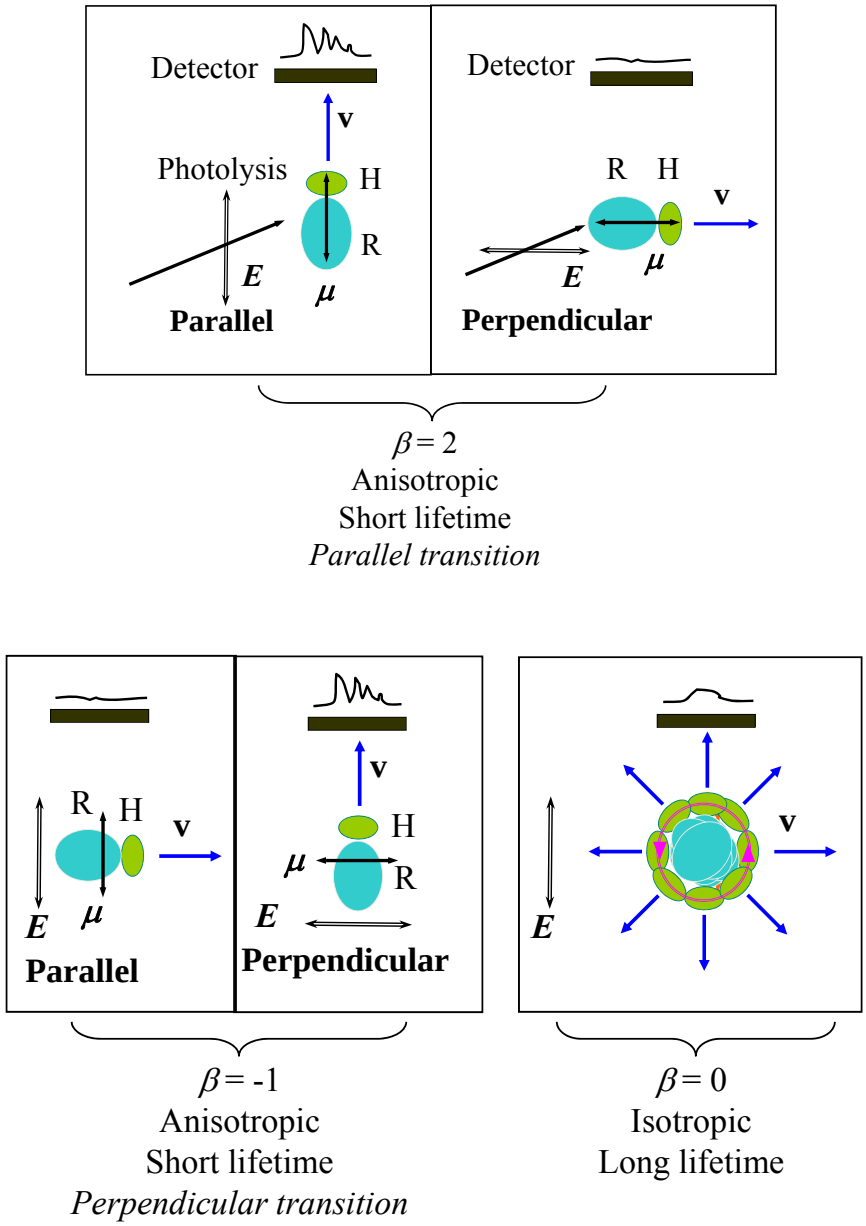

Figure 1.6 Angular distributions of the photoproducts following absorption of a linearly polarized light with electric vector ***E***. ***μ*** is the transition dipole moment and **v** is the recoil velocity vector. β is the anisotropy parameter. The top figure shows one anisotropic distribution with β=2, while the bottom left figure shows the other anisotropic distribution with β=-1. The bottom right figure shows an isotropic distribution with β=0.

$$I(\theta) = [1 + \beta P_2(\cos\theta)] / 4\pi \qquad (12)$$

where θ is the angle between the electric vector $\vec{E}$ and the recoil velocity $\vec{v}$. $P_2(\cos\theta) = (3\cos^2\theta - 1)/2$ is the second Legendre polynomial and $\beta = 2P_2(\cos\chi)$ is the anisotropy parameter with χ is the angle between transition dipole $\vec{\mu}$ and recoil velocity $\vec{v}$. The value of β lies between 2 and -1. When β=2, cosχ=1 and $\vec{\mu}$ is parallel to $\vec{v}$ (parallel transition). When β=-1, cosχ=0 and $\vec{\mu}$ is perpendicular to $\vec{v}$ (perpendicular transition). When β=0, $I(\theta)$=1/4π is independent of θ, corresponding to isotropic angular distribution, as shown in Figure 1.6. As discussed above, the lifetime of the excited electronic state can be estimated by looking at the value of anisotropy parameter. The isotropic angular distribution (β=0) indicates that the lifetime of excited state is at least longer than one rotational period of the parent molecule. Meanwhile the anisotropic angular distribution indicates the lifetime of the excited state is short. Sometimes, β is not constant for one TOF spectrum. This situation points out that different dissociation pathways are involved during the photodissociation process. The β value can be calculated using the following equation:

$$\beta = \frac{I(\theta = 90^\circ)/I(\theta = 0^\circ) - 1}{1 + 0.5 * [I(\theta = 90^\circ)/I(\theta = 0^\circ)]} \qquad (13)$$

$I(\theta = 90^\circ)$ and $I(\theta = 0^\circ)$ are the angular distributions when the electric vector $\vec{E}$ is perpendicular and parallel to the recoil velocity $\vec{v}$ (or the flight path), respectively.

1.5 High-n Rydberg H atom TOF experimental setup

The schematic HRTOF experimental setup is shown in Figure 1.7. The parent molecule is carried to the reaction chamber by the buffer gas Ar or He at ~5% concentration with a total pressure 115-120 kPa. A pulsed valve is used to generate a pulsed molecular beam which is then dissociated to the radical of interest by a laser radiation at 193 nm which crosses the pulsed molecular beam. Then the radical beam is collimated by a 1-mm diameter skimmer 2.8 cm away from the nozzle and is forced into the chamber. This procedure is called supersonic expansion because the beam is expanded from a high pressure (~1 atm) through a small orifice into a vacuum (~10^{-7} torr) at a speed larger than the speed of sound. In this procedure, the radicals undergo many collisions with the buffer gas and are cooled down both vibrationally (50-100 K) and rotationally (5 K). This will greatly simplify the spectrum since the initial state of radical is established. At 4.6 cm further downstream the skimmer, the radical beam crosses with a polarized laser radiation which photodissociates the radical to the photofragments. The laser wavelength is monitored by a wavemeter and the polarization is achieved by rotating a Fresnel-Rhomb achromatic $\lambda/2$ plate to obtain the product angular distribution. After the dissociation, one of the products H is probed by a two-color resonant excitation, as shown in Figure 1.3 or the embedded small figure in Figure 1.7. One laser at

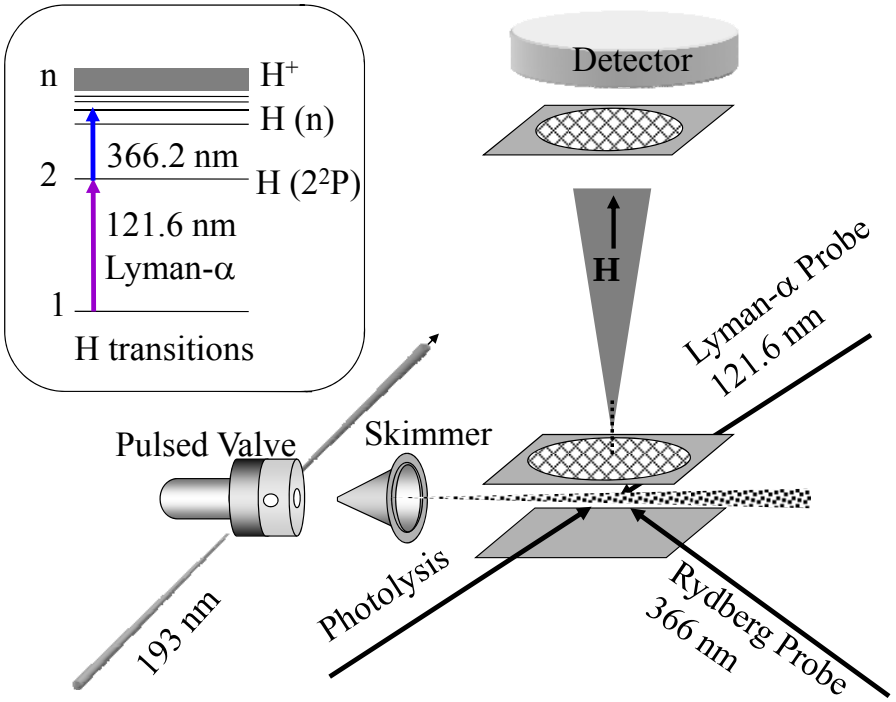

Figure 1.7 Schematic experimental setup for HRTOF technique. The embedded figure indicates the excitation of the H product to the high-n Rydberg state.

wavelength ~121.6 nm excites the H atom from ground state to 2^2P state, then another laser at ~366 nm excites H to a high-n Rydberg state (n=50-90). A small part of the Rydberg H atoms drift with the nascent velocities toward a microchannel plate detector (MCP). At about 1-2 mm in front of the detector, the H atoms are field ionized and then detected. The H atom TOF spectrum is recorded and typically accumulated with $1\text{-}2\times10^4$ laser firings.

The obvious advantage of the HRTOF technique compared to resonance-enhanced multi-photon ionization (REMPI) is that the background of H detection is largely reduced. Figure 1.8 displays the schematic voltage setup for the grids inside the main chamber. In the HRTOF setup, the radical beam goes through the center of repeller and first grid. The first and second grids are grounded while the repeller was applied with small negative voltage, as shown in Figure 1.8. Some cations are produced during the photodissociation process due to the 121 nm multi-photon ionization of H atoms and other compounds. This negative voltage attracts these background cations and thus prevents them flying to the detector. One of the MCP front grids near the field-ionization area is positively biased. It serves the same thing as the repeller grid and it is the last step to prevent the cations going into the detector. However, some negatively charged particles (such as electrons) are accelerated by the repeller grid and the MCP first grid. But they can never reach the detector due to the existence of -3k voltage in front of the detector. Another advantage of

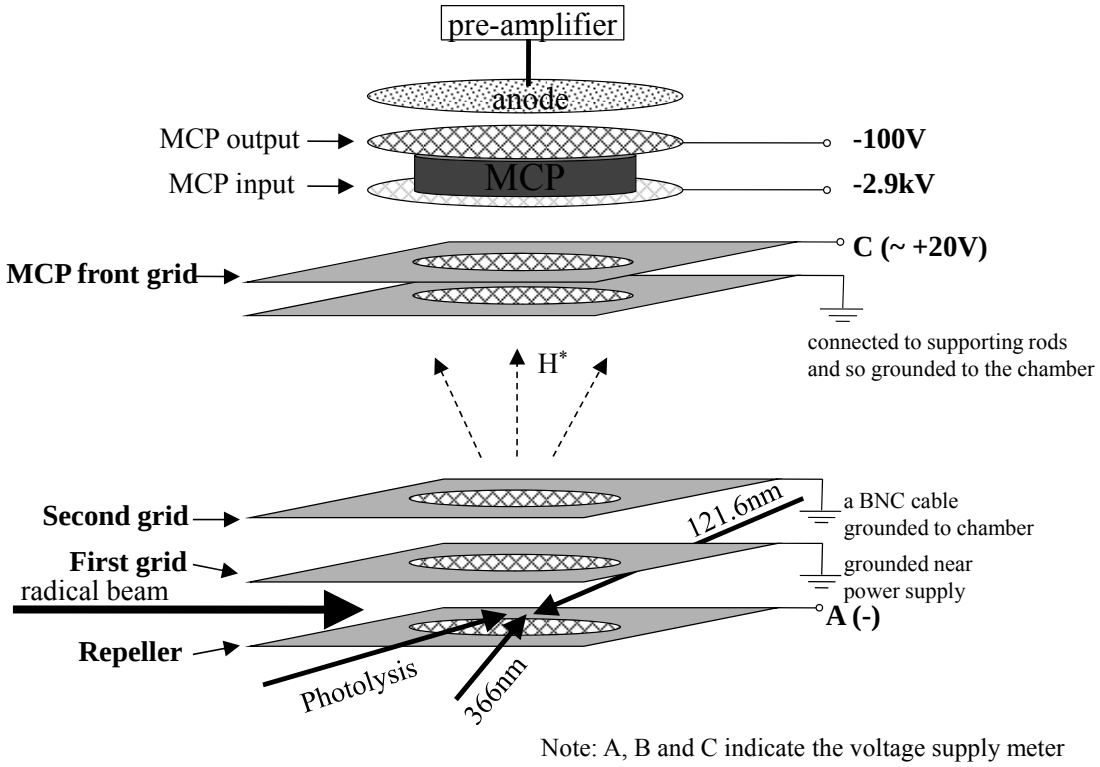

Figure 1.8 Schematic voltage setup for the Rydberg H detection in HRTOF technique.

HRTOF comes from the neutral Rydberg H atoms since they will not be affected by the space charge and stray field interferences in the chamber. This helps the Rydberg H atoms flying to the detector with the nascent velocity and thus helps increasing the resolution and sensitivity.

1.6 REMPI and TOFMS experimental setup

By changing the voltages of the grids in the main chamber, the same experimental setup can also be used to perform the REMPI and TOF mass spectroscopy (TOFMS), as shown in Figure 1.9. The alignments of all the laser beams are the same as HRTOF technique, but the wavelengths of some lasers need to be changed in order to excite the molecules to the resonant state or further ionize them, corresponding to the REMPI method. The voltages of the repeller and first girds are set to +765 V and +596 V, respectively, while The MCP front grid is grounded. The ions generated from the REMPI are accelerated by the repeller and first grids towards the MCP detector. The arrival time of each ion is proportional to the square root of the mass-to-charge ratio (m/z):

$$(t - t_0)^2 \times C = \frac{m}{z} \tag{14}$$

In equation (14), C is constant and t_0 is the absolute time zero when the ionization occurs. In the mass spectrum, some peaks are obvious to be identified. For example, H peak is

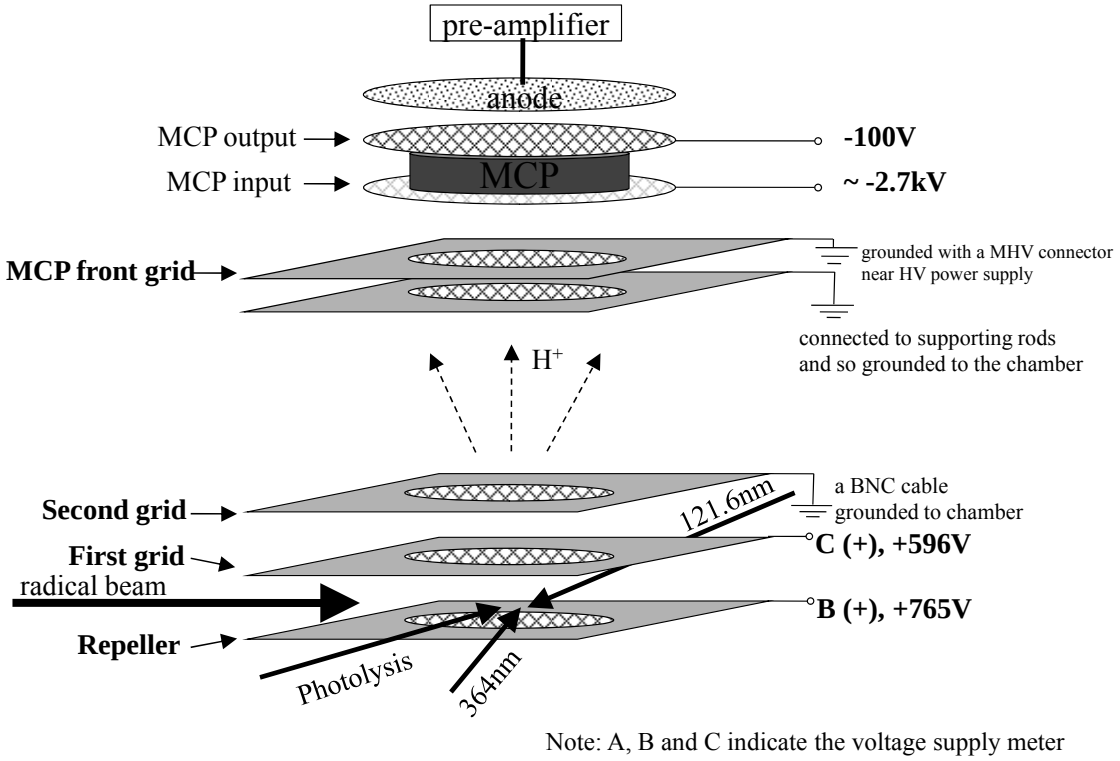

Figure 1.9 Schematic voltage setup for the H ions detection in REMPI and TOFMS techniques.

the strongest peak with a very small time-of-flight. In addition, the peak of the parent molecule usually has the second large intensity. In such case, the constant C and time zero t_0 can be solved from equation (14). Thus by converting the flight time to the m/z, all the peaks in the TOF mass spectrum can be identified.

The REMPI and TOFMS experimental setup is usually employed for the following purposes:

(1) H^+ action spectrum

In order to obtain the H^+ action spectrum, 193 nm radiation and photolysis laser are needed to generate the radical of interest and to photodissociate the radical to the H product and its counterpart, respectively. H atom can be ionized by two methods: 1+1' REMPI (121+364 nm) or 1+1 REMPI by 121-nm radiation only. The probe laser (Rydberg probe laser) is scanned to 364 nm which is shorter than the wavelength in HRTOF (~366nm). Under this condition, the H atoms are excited to the 2^2P state by the 121 nm radiation and then ionized by the 364 nm radiation (Figure 1.3). Since the 121 nm radiation is generated by the frequency-tripled 364.8 nm UV fundamental radiation, some 364.8 nm radiation remains in the 121 nm laser beam which can replace the Rydberg probe laser to ionize the H atoms. Therefore, sometimes the REMPI of H atoms is performed with only 121 nm radiation on. The H^+ signals on the MS spectrum is monitored by the oscilloscope and it is easy to be identified because the H peak is the

fasted one and is usually the strongest. The net H^+ signal coming from the photodissociation of the radical is obtained by removing the appropriate background MS spectrum (e.g. the precursor background with 193-nm radiation off) from the total MS spectrum with all the lasers on. By scanning the photolysis wavelength, the MS spectrum is recorded at each wavelength and saved by the oscilloscope. Thus H^+ action spectrum is obtained by integrating the H^+ signal as a function of the photolysis laser wavelength. Sometimes, there might be some interference from the impurities in the gas line and the reaction chamber which can bring some background signal to the H^+ peak. In this way the H^+ action spectrum may look a little different from the action spectrum obtained from integrating the HRTOF spectra.

(2) R^+ REMPI spectrum

The R^+ REMPI spectrum is used to investigate the spectroscopy of free radicals. The 193-nm radiation is turned on to produce the radical R and the photolysis laser is scanned to hit the resonance state of the radical and the second photon of the photolysis laser ionizes the radical to R^+ (in a 1+1 REMPI scheme). The probe laser radiations are blocked for this situation. For example, allyl radical (C_3H_5) can be ionized by 1+1 REMPI around 240 nm. If the photolysis laser around 240 nm is scanned to some excited vibronic state of the allyl radical, the signal of allyl peak in the TOF mass spectrum (m/z=41) would be enhanced greatly. The ion signal for allyl radical (m/z=41) is

monitored by an oscilloscope and integrated as a function of photolysis wavelength using a Boxcar averager (SR250). Boxcar averager consists of a gate generator and gated integrator which can select the signals on mass spectrum of specific area and integrate the signal of selected part, respectively. The averaged signal is sent to the computer data acquisition system to record the R^+ REMPI spectrum. Therefore, the spectroscopy of the radical at specific wavelength is studied.

(3) Single photon VUV TOFMS

This experimental scheme is achieved by ionizing the species in the molecular beam with 121-nm VUV radiation and characterizing the components in the molecular beam with TOFMS. The 193 nm radiation is turned on to produce the radical and 121 nm radiation to ionize the molecular beam. The photolysis laser radiation and the Rydberg probe laser radiation are blocked. The TOF mass spectrum is saved by the oscilloscope and the peaks can be characterized after the time is converted to the mass. Single photon VUV TOFMS is used to identify the species in the molecular beam and this technique is helpful to characterize the radicals in the beam.

This dissertation discusses the photodissociation dynamics of several important free radicals by applying the powerful HRTOF technique which is highly sensitive to resolve the energy distribution of the products. Meanwhile the angular distribution of the

products is obtained and thus the detail of the dissociation dynamics is explained. Chapter 2 and Chapter 3 of this dissertation will investigate the dissociation dynamics of SD and CH_3S radicals. These radicals belong to the sulfur system and they are important intermediates in atmospheric oxidation of naturally occurring sulfur compounds. Chapter 4, Chapter 5 and Chapter 6 will discuss the photodissociation dynamics of the C_3H_3, C_7H_7 and C_3H_5 radicals which belong to the aromatic system. These radicals are important in combustion chemistry because they are related to the formation of polycyclic aromatic hydrocarbons (PAHs) and the soot.

References

(1) Zewail, A. H. *Journal of Physical Chemistry* **1996**, *100*, 12701.

(2) Schnieder, L.; Meier, W.; Welge, K. H.; Ashfold, M. N. R.; Western, C. M. *Journal of Chemical Physics* **1990**, *92*, 7027.

(3) Schnieder, L.; Seekamprahn, K.; Liedeker, F.; Steuwe, H.; Welge, K. H. *Faraday Discussions* **1991**, *91*, 259.

(4) Zare, R. *Ph.D. Thesis*; Harvard University, 1964.

CHAPTER 2

Ultraviolet photodissociation of the SD radical in vibrationally ground and excited states

ABSTRACT

Ultraviolet (UV) photodissociation dynamics of the SD radical in vibrationally ground and excited states ($X^2\Pi_{3/2}$, v"=0-5) are investigated in the photolysis wavelength region of 220 to 244 nm using high-*n* Rydberg atom time-of-flight (HRTOF) technique. The UV photodissociation dynamics of SD ($X^2\Pi_{3/2}$) from v" = 0-5 are similar to each other and to that of SH studied previously. The anisotropy parameter of the D-atom product is ~ –1; the spin-orbit branching fractions of the $S(^3P_J)$ products are essentially constant, with an average $S(^3P_2):S(^3P_1):S(^3P_0)$ = 0.51:0.37:0.12. The UV photolysis of SD is a direct dissociation from the repulsive $^2\Sigma^-$ state following the perpendicular $^2\Sigma^-$-$X^2\Pi$ excitation. The $S(^3P_J)$ product fine-structure state distributions approach that in the sudden limit dissociation on the single repulsive $^2\Sigma^-$ curve, but it is also affected by nonadiabatic couplings among the repulsive $^4\Sigma^-$, $^2\Sigma^-$, and $^4\Pi$ states. A bond dissociation energy D_0(S-D) = 29660 ± 25 cm^{-1} is obtained.

2.1 Introduction

The spectroscopy and chemical kinetics of the SH radical have been the subject of many investigations, because of its importance in atmospheric chemistry of sulfur[1] and in fossil fuel combustion reactions of sulfur-containing species, as well as its astrochemical relevance.[2] The electronic states of the SH/SD radical have been examined by both theories[3-7] and experiments.[8-16] The potential energy curves (PECs) of the ground and electronically excited states of SD are shown in Figure 2.1. The ground state of SH/SD is $X^2\Pi_{3/2}$, with the upper spin-orbit component $^2\Pi_{1/2}$ higher by 376.7 cm^{-1}.[10] The $X^2\Pi_{3/2}$ ground state of SD correlates adiabatically with the $D(^2S) + S(^3P_J)$ products. The first electronically excited state $A^2\Sigma^+$ correlates asymptotically with $D(^2S) + S(^1D)$, and it could undergo predissociation via spin-orbit couplings with the three repulsive states, $^4\Sigma^-$, $^2\Sigma^-$, and $^4\Pi$, to the ground-state $D(^2S) + S(^3P_J)$ products. At higher energy, the repulsive $^2\Delta$ and $2^2\Pi$ states asymptotically correlate with $D(^2S) + S(^1D)$.

Photodissociation studies of the open-shell SD radical are limited, while those of the SH radical help understand the dissociation mechanism of SD that involves multiple coupled PECs. The UV photodissociation of SH was first observed in the H-atom TOF spectra of the secondary photolysis of H_2S at 193 nm by Continetti and co-workers;[17] both the $S(^3P)$ and $S(^1D)$ product channels were identified from perpendicular electronic

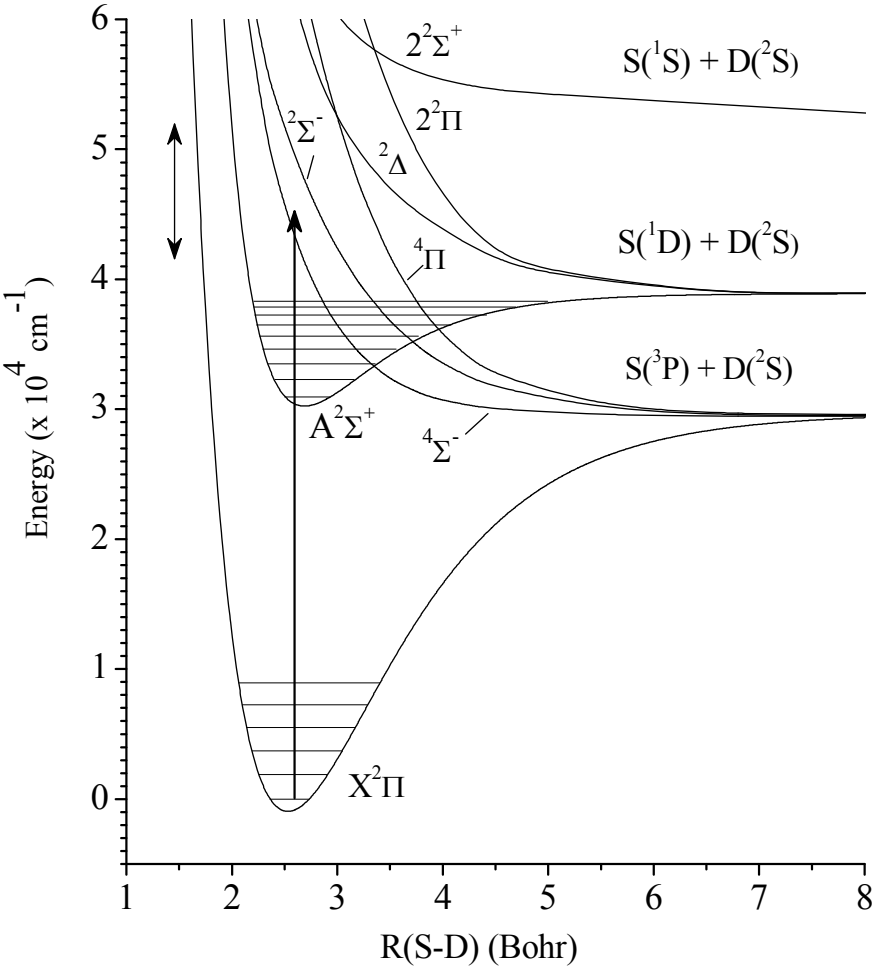

Figure 2.1 Potential energy curves for the $X^2\Pi$, $A^2\Sigma^+$, $^4\Sigma^-$, $^2\Sigma^-$, $^4\Pi$, $2^2\Pi$, $^2\Delta$, and $2^2\Sigma^+$ states of SD. The energetic information is adapted from refs. 5-7. The single arrow represents the 220-nm photon energy. The double arrow indicates the investigated energy region (photon energy + vibrational energy of SD) in this work.

transitions and were attributed to direct dissociation on the $^2\Sigma^-$ and $^2\Delta$ state, respectively. The 193-nm secondary photolysis of SH from H_2S was also examined using resonance-enhanced multiphoton ionization (REMPI) technique by Ng and co-workers.[18] The $S(^3P):S(^1D)$ products were observed with a branching ratio of 0.87:0.13, which were also attributed to the direct photodissociation of SH via the repulsive excited states $^2\Sigma^-$ and $^2\Delta$, and the $S(^3P_J)$ product fine-structure state distribution was measured to be $S(^3P_2):S(^3P_1):S(^3P_0)$ = 0.68±0.03:0.24±0.03:0.08±0.03. The UV photodissociation of D_2S/H_2S and secondary photolysis of SD/SH near 220 nm were investigated by Ashfold and co-workers.[19,20] At the photolysis wavelength 218.2 nm, the $S(^3P_J)$ product fine-structure state distribution was measured by REMPI to be $S(^3P_2):S(^3P_1):S(^3P_0)$ = 0.6:0.3:0.1, and further modeling the kinetic energy distribution of the H/D atom product from secondary photolysis of SH/SD indicated that the SH/SD photodissociation is involved in a perpendicular transition (such as $^2\Sigma^-$-$X^2\Pi$). The first study of photodissociation dynamics of jet-cooled SH was carried out by Zhou et al.[21] The UV photodissociation dynamics of the SH radical ($X^2\Pi_{3/2}$, v"=0-2) in the wavelength region of 216-232 nm was examined using high-*n* Rydberg atom time-of-flight (HRTOF) technique.[21] The anisotropy parameter of the H-atom product was measured to be ~-1, and the spin-orbit branching fractions of the $S(^3P_J)$ products were close to $S(^3P_2):S(^3P_1):S(^3P_0)$ = 0.51:0.36:0.13. The UV photolysis of SH was shown to be a

direct dissociation via the perpendicular transition $^2\Sigma^- \leftarrow X^2\Pi_{3/2}$. The S($^3P_J$) product fine-structure state distribution is close to that expected in the sudden limit dissociation on the single repulsive $^2\Sigma^-$ state, and it is also influenced by nonadiabatic couplings among the repulsive $^4\Sigma^-$, $^2\Sigma^-$, and $^4\Pi$ states.[21] Recently, the H/D(^{2}S) + S(^{1}D) product channels from UV photodissociation of vibrationally excited SH ($X^2\Pi$, v"=2-7) and SD ($X^2\Pi$, v"=3-7) were characterized at 288 and 291 nm by Janssen et al. by detection of S(^{1}D) using velocity map imaging technique.[22] Both the experimental results and the theoretical photodissociation cross sections from *ab initio* calculations suggested that vibrationally excited SH and SD in $X^2\Pi$ (v"≤7) could be excited to the repulsive wall of the $A^2\Sigma^+$ state with favorable Franck-Condon (FC) factors at 288 and 291 nm, which then leads to the S(^{1}D) products.[22] The observed alignment of S(^{1}D) was consistent with the sudden recoil limit of the $A^2\Sigma^+$ state. Vacuum ultraviolet (VUV) photodissociation of SH was studied at 121.6 nm by Chen et al.[23] The ground-state S(^3P_J) and excited-state S(^{1}D) and S(^{1}S) products were observed with a branching fraction of 0.07:0.82:0.11. The main production of S(^{1}D) was consistent with a direct dissociation from the repulsive $2^2\Pi$ state. The S(^3P_J) product fine-structure state distribution from the VUV photodissociation was significantly different from that in the UV region.[21,23]

The photodissociation of SH to the S(^3P_J) and S(^{1}D) products has been studied theoretically by Lee and co-workers.[24,25] Transition dipole moments from the ground

$X^2\Pi$ state to the $A^2\Sigma^+$, $^2\Sigma^-$, $^2\Delta$ and $2^2\Pi$ excited states were calculated using the effective valence shell Hamiltonian method.[24,25] Two frame transformation matrices were constructed, one to describe the correlation between the $S(^3P_J)$ atomic limit and $X^2\Pi$, $^4\Sigma^-$, $^2\Sigma^-$, and $^4\Pi$ states and another between the $S(^1D)$ limit and $A^2\Sigma^+$, $^2\Delta$, and $2^2\Pi$ states. Quantum interference effects in the dissociation and asymptotic interactions were predicted. At energies between the thresholds to the $H(^2S) + S(^3P_J)$ and $H(^2S) + S(^1D)$ limits, resonances in the absorption spectrum of the $A^2\Sigma^+$ state were largely Lorentzian, and the $A^2\Sigma^+$ state predissociated via the repulsive $^4\Sigma^-$, $^2\Sigma^-$, and $^4\Pi$ states with nearly constant $S(^3P_J)$ product branching ratios. At energies above the threshold to the $S(^1D)$ limit, direct dissociation of SH via the repulsive states dominated; quantum interferences among the dissociative pathways ($A^2\Sigma^+$, $^2\Sigma^-$, $^2\Delta$, and $2^2\Pi$) were predicted to give asymmetric resonances of multichannel character. At higher energies in the wavelength region of 196-209 nm, the interference among the direct dissociation pathways (e.g., between $^2\Sigma^-$ and the repulsive part of $A^2\Sigma^+$ accessed at the high photon energy) caused oscillatory variations in total cross sections for dissociation to $S(^3P_J)$, $S(^3P_J)$ product spin-orbit branching ratios [with the population $S(^3P_1) > S(^3P_2) > S(^3P_0)$], and $S(^3P_J)$ product angular distributions.[24,25]

This current work extends our previous study of the direct photodissociation of SH via the $^2\Sigma^-$ state,[21] and investigates photodissociation dynamics of jet-cooled SD ($X^2\Pi_{3/2}$,

v"=0-5) in the photolysis wavelength region of 220-244 nm, corresponding to 41670-52040 cm^{-1} total energy (relative to $X^2\Pi_{3/2}$, v"=0). The $S(^3P_J)$ product fine-structure state distributions and the D-atom product angular distributions are measured. The direct photodissociation dynamics of SD via the repulsive excited states and the nonadiabatic processes in SD are probed. In particular, the SD system is used to examine mass effect of the departing fragment on the nonadiabatic dissociation dynamics. The vibrationally excited SD ($X^2\Pi_{3/2}$, v"=1-5) radicals are utilized to probe the effect of vibrational excitation in the UV photodissociation of SD. With the additional vibrational energy, higher energy region of SD is accessed and photodissociation in the high-energy (sudden) limit can be examined. Furthermore, at the higher energy (with the total excitation energy equivalent to the photolysis wavelength from 240-192 nm for SD), the possible interference among the direct dissociation pathways and the oscillatory variations in the $S(^3P_J)$ spin-orbit branching ratios and angular distributions, which have been predicted theoretically for SH in the region of 196-209 nm,[24,25] are examined. An accurate bond dissociation energy D_0(S-D) is also determined.

2.2 Experimental

The HRTOF technique and experimental setup have been described before.[15,21,26,27] A pulsed SD radical beam was generated by photolyzing a ~ 5% mixture of D_2S (≥ 99.5%, Aldrich) seeded in Ar (at a total pressure of 120 kPa) with the 193-nm radiation of an ArF excimer laser that was focused in front of the pulse nozzle. The SD radicals produced from the photolysis were entrained in the seeded beam and subsequently cooled by supersonic expansion. The radical beam was collimated at 2.8 cm downstream by a 1-mm diameter skimmer into a high-vacuum chamber; at 4.6 cm further downstream of the skimmer, the SD radical beam was crossed with a slightly focused UV photolysis laser radiation (220-244 nm, 0.5-2 mJ/pulse, linewidth ≤ 0.3 cm^{-1}). The absolute photolysis laser wavelength was monitored by a wavemeter (Burleigh WA-4500). The polarization of the photolysis radiation could be rotated by a Fresnel-Rhomb achromatic λ/2 plate for product angular distribution measurements. The D atoms produced from the SD photodissociation were tagged by two-color resonant excitation (121.53 nm + 366.36 nm), from 1^2S to 2^2P via the D-atom Lyman-α transition (at 82280 cm^{-1}) and then further to a high-*n* Rydberg state. A small fraction of the radiatively metastable Rydberg D atoms drifted with their nascent velocities toward a microchannel plate detector, and were field-ionized in front of the detector and detected. The nominal flight length was 37.1

cm, which was calibrated by HBr photodissociation [with the spin-orbit splitting of Br($^2P_{3/2}$) and Br ($^2P_{1/2}$)][28] at the corresponding photolysis wavelengths for SD. The ion signals were amplified by a fast pre-amplifier, and the D-atom TOF spectra were recorded and averaged using a multichannel scaler. The D-atom TOF spectra were typically accumulated with ~10^4 laser shots.

2.3 Results

The TOF spectra of D-atom products in the UV photodissociation of SD were recorded in several photolysis wavelengths from 220 nm to 244 nm, with the photolysis laser polarization parallel and perpendicular to the flight path, respectively. Example TOF spectra at 230 nm with the 193-nm radiation (for SD production) on and off are shown in Figure 2.2. The strong signals in the region of 32.5-38 μs are from photodissociation of the D_2S precursor, $D_2S \rightarrow SD + D$, by the UV photolysis radiation at 230 nm, similar to a previous study at 218.2 nm[19] and to our previous study of the photodissociation of SH radical.[21] The D_2S signals with the 193-nm radiation on are slightly weaker than those with the 193-nm radiation off, showing depletion of the D_2S precursor molecules by the 193-nm photolysis radiation for the SD radical production. The signals in the region of 27.5 to 31.5 μs with the 193-nm radiation on are due to

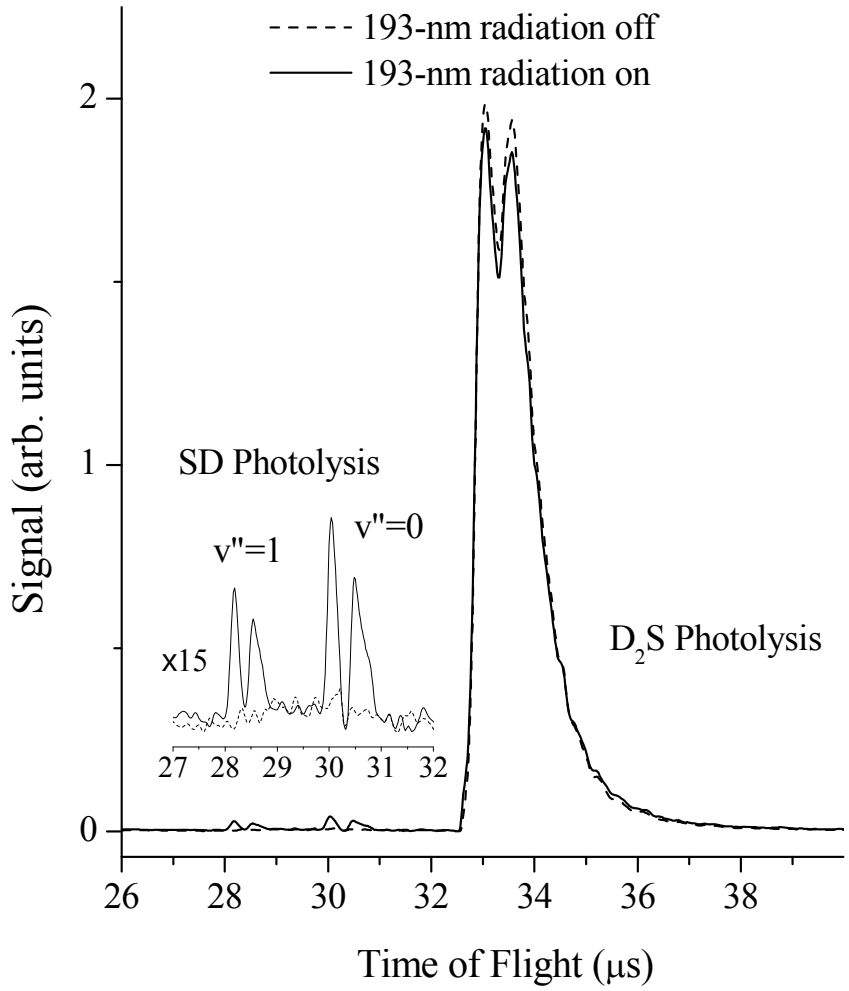

Figure 2.2 D-atom TOF spectra of 230-nm photodissociation of SD and D_2S, with the 193-nm photolysis laser (for SD radical production) on and off. The polarization vector of the 230-nm photodissociation radiation is perpendicular ($\theta = 90^o$) to the TOF axis. The spectrum in short dashed line is with the 193-nm radiation off, and the spectrum in solid line is with the 193-nm radiation on. The two groups of sharp peaks in the region of 27.5 to 31.5 μs are from the 230-nm photodissociation of jet-cooled SD radicals in $X^2\Pi_{3/2}$ v"=0 and 1 states.

photolysis of the SD radicals at 230 nm. With the 193 nm-radiation on, two groups of peaks with a similar structure and intensity appear between 27.5 and 31.5 μs; these are from the 230-nm photodissociation of jet-cooled SD radical (in $X^2\Pi_{3/2}$ v"=0 and 1 and with cold rotational temperature). Due to the large difference in the S-D bond dissociation energies of SD and D_2S, the D-atom signals from SD and D_2S are well separated. Similar to the previous study of the UV photodissociation of SH radical,[21] the main background in the current experiment is from the UV photolysis of D_2S ($D_2S \rightarrow$ SD + D) and the secondary photolysis of hot SD radicals by the UV photolysis radiation. The net D-atom signals from the UV photolysis of jet-cooled SD in the beam can be obtained by removing the background with the 193-nm photolysis laser off from the signals with the 193-nm laser on. As discussed later, analysis of the product translational energy release confirms that the peaks near 28.5 μs are from photodissociation of SD in the v"=1 vibrational state and those near 30.5 μs are from SD in v"=0.

The net D-atom TOF spectra of the jet-cooled SD photodissociation are transformed to total center-of-mass (CM) translational energy distributions, $P(E_T)$'s.[21,27] The CM translational energy of products, E_T, is converted from the D-atom flight time t_D using the following equation:

$$E_T = \left(1 + \frac{m_D}{m_S}\right) E_D + \frac{m_D}{m_S} E_{SD} = \frac{1}{2} m_D \left(1 + \frac{m_D}{m_S}\right) \left(\frac{L}{t_D}\right)^2 + \frac{m_D}{m_S} E_{SD} \qquad (1)$$

where E_D and E_{SD} are the laboratory translational energies of the D-atom photofragment and the SD radical, respectively, and L is the flight length. The second term $\left(\frac{m_D}{m_S}E_{SD}\right)$ is due to the SD radical motion in the molecular beam that is orthogonal to the TOF path, and it is very small compared with the first term (products' CM translation). In this experiment, the correction due to $\left(\frac{m_D}{m_S}E_{SD}\right)$ is ~28 cm^{-1}, based on an estimated beam velocity of 560 m/s for the D_2S/Ar gas mixture at room temperature before supersonic expansion.

Figure 2.3 shows the angle-dependent $P(E_T)$ distributions with the linear polarization of the 230-nm photolysis radiation perpendicular and parallel to the TOF path, respectively. These $P(E_T)$ distributions indicate a large anisotropy in the D-atom product angular distribution. The photofragment angular distribution can be described by[29]

$$I(\theta) = (1/4\pi)[1 + \beta P_2(\cos\theta)] \qquad (2)$$

where β is the anisotropy parameter ($-1 \le \beta \le 2$), θ is the angle between the electric vector of the polarized laser radiation and the recoiling velocity vector of the D-atom product (the direction of detection or the TOF axis), and $P_2(\cos\theta)$ is the second Legendre polynomial. Using equation (2) and the two angle-dependent $P(E_T)$ distributions at the perpendicular ($\theta = 90^o$) and parallel ($\theta = 0^o$) polarizations, anisotropy parameters for the

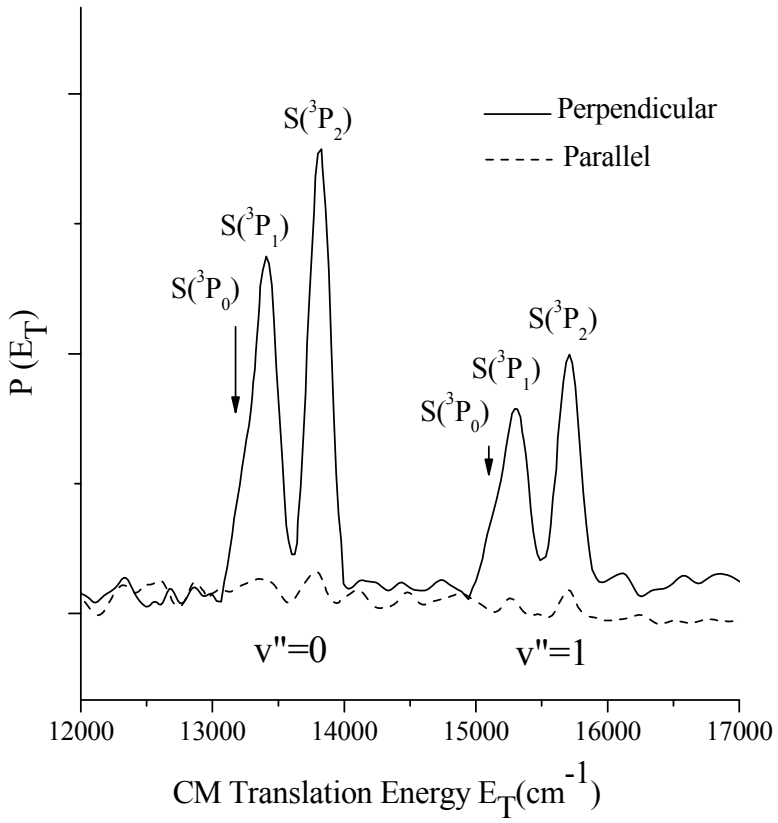

Figure 2.3 Center-of-mass D(^{2}S) + S(^{3}P$_J$) product translational energy distribution, $P(E_T)$, from 230-nm photodissociation of SD, with polarization vector of the photolysis radiation perpendicular ($\theta = 90^o$) and parallel ($\theta = 0^o$) to the TOF axis. The spin-orbit S(^{3}P$_{J=2,1,0}$) sublevels of the products are labeled.

summed D-atom signals of all the three S(^3P_J) peaks are derived for the SD photodissociation at 230 nm; for v"=0, β = -0.92 ± 0.1 and v"=1, β = -0.91 ± 0.1. The angular distributions from the photodissociation of SD in $X^2\Pi_{3/2}$, v"=0-5 at several photolysis wavelengths from 220 to 244 nm are measured, and the derived β parameters for the summed D-atom signals are listed in Table 2.1. The anisotropy parameters of SD photolysis from the initial $X^2\Pi_{3/2}$ v"=0-3 states are also plotted in Figure 2.4. The β parameters of the summed D-atom signals from SD ($X^2\Pi_{3/2}$ v"=0-5) in this UV wavelength region are essentially the same within experimental error and approach the limit of β = -1 for a pure perpendicular transition. In addition, the β parameters for the spin-orbit product channel D + S($^2P_2$) are nearly the same as those of the summed D signals. However, it is difficult to extract individual β parameters for the S($^2P_1$) and S($^2P_0$) channels due to the small magnitudes of these peaks and thus the uncertainties in the deconvolution processes (discussed in the following). Since the linearly polarized light preferentially excites the SD radicals with their electronic transition dipole moment parallel to the electric vector of the polarized laser radiation, the negative $\beta \approx$ -1 indicates that the transition dipole moment is predominantly perpendicular to the recoiling velocity vector of the D-atom fragment from the S-D dissociation, i.e., the S-D bond direction. As the ground-state is $^2\Pi_{3/2}$, the observed perpendicular transition shows that the excited state is $^2\Sigma^-$, as in the UV photodissociation of SH.[21]

Table 2.1 $S(^3P_J)$ spin-orbit branching fractions and anisotropy parameter β of photodissociation of SD ($X^2\Pi_{3/2}$, v"=0-5) at the UV wavelength range of 220-244 nm. The errors in the spin-orbit branching fractions (when available) are 95% confidence limit based on multiple measurement statistics. The error limit for the β values is ± 0.1. The total excitation energy is the sum of photon energy and vibrational energy of SD ($X^2\Pi_{3/2}$, v").

Total excitation energy (cm^{-1})	Photolysis λ (nm)	Spin-orbit branching fractions			β
		$^3P_2$	$^3P_1$	$^3P_0$	
Photodissociation of SD ($X^2\Pi_{3/2}$) in v"=0					
45454.5	220	0.51±0.02	0.36±0.04	0.13±0.04	-0.93
45045.0	222	0.50	0.38	0.12	-0.90
44642.9	224	0.51	0.37	0.12	
44247.8	226	0.50	0.37	0.13	-0.95
43859.6	228	0.51	0.37	0.12	
43478.3	230	0.51±0.02	0.37±0.03	0.12±0.03	-0.92
43103.4	232	0.49	0.39	0.12	
42735.0	234	0.50	0.38	0.12	
42372.9	236	0.50±0.04	0.38±0.05	0.12±0.05	-0.92
41666.7	240	0.51±0.05	0.38±0.07	0.11±0.08	-1.00
Photodissociation of SD ($X^2\Pi_{3/2}$) in v"=1					
46127.4	226	0.51	0.37	0.12	-0.93
45739.2	228	0.51	0.37	0.12	
45357.9	230	0.50±0.02	0.37±0.03	0.13±0.03	-0.91
44983.0	232	0.50	0.38	0.12	
44614.6	234	0.50	0.38	0.12	
44252.5	236	0.49±0.03	0.38±0.05	0.13±0.05	-0.93
43546.3	240	0.50	0.38	0.12	-0.90
42863.2	244	0.51±0.02	0.37±0.03	0.12±0.03	-1.00

Table 2.1 Continued

Total excitation Energy (cm^{-1})	Photolysis λ (nm)	Spin-orbit branching fractions			β
		$^3P_2$	$^3P_1$	$^3P_0$	
Photodissociation of SD ($X^2\Pi_{3/2}$) in v"=2					
46085.9	236	0.51±0.04	0.37±0.05	0.12±0.04	-0.91
45379.7	240	0.51	0.37	0.12	-0.93
44696.6	244	0.50±0.02	0.37±0.03	0.13±0.03	-1.00
Photodissociation of SD ($X^2\Pi_{3/2}$) in v"=3					
48608.4	232	0.50	0.38	0.12	
48240.0	234	0.51	0.37	0.12	
47877.9	236	0.51±0.03	0.38±0.04	0.11±0.04	-0.95
47171.7	240	0.51	0.37	0.12	-0.90
46488.6	244	0.51	0.37	0.12	-1.00
Photodissociation of SD ($X^2\Pi_{3/2}$) in v"=4					
50348.4	232	0.51	0.37	0.12	
49980.0	234	0.51	0.37	0.12	
49617.9	236	0.51±0.03	0.37±0.05	0.12±0.06	-0.94
Photodissociation of SD ($X^2\Pi_{3/2}$) in v"=5					
52037.5	232	0.50	0.37	0.13	
51669.1	234	0.51	0.37	0.12	
51307.0	236	0.50±0.04	0.38±0.05	0.12±0.05	-0.92

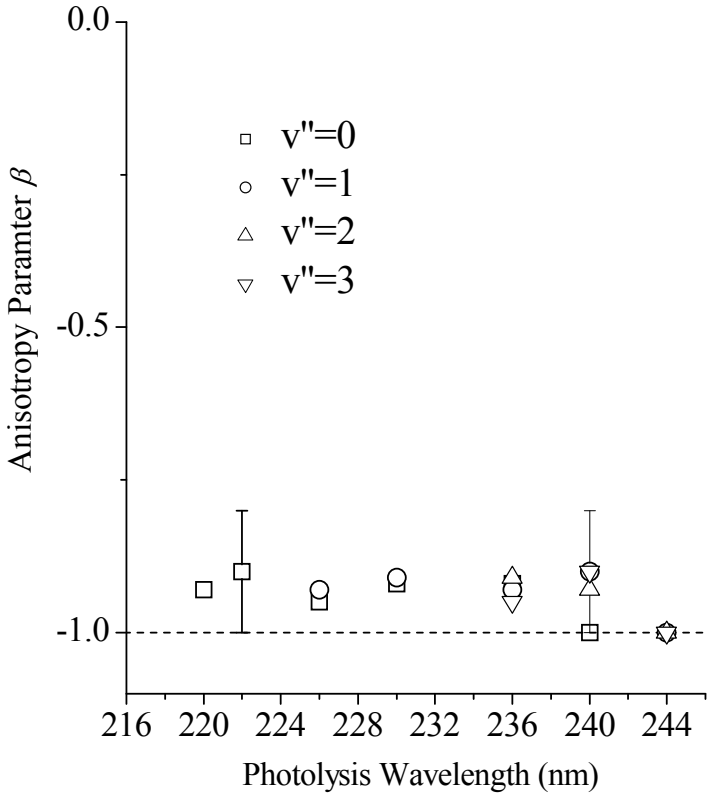

Figure 2.4 Anisotropy parameter β versus photolysis wavelengths. The measurements for SD ($X^2\Pi_{3/2}$) photodissociation from the vibrational states v"=0-3 are plotted. The error bars at 222 and 240 nm represent 95% confidence limit; error limits for other wavelengths are assumed to be the same. The dashed line is the β = -1 limit of a prompt dissociation from a perpendicular transition.

Detailed analysis of the CM translational energy distributions, $P(E_T)$'s, is shown in the examples in Figure 2.5. Figure 2.5 (a) is for 230-nm photolysis of SD. Two groups of peaks with a similar structure appear in this translational energy region. The intensities of these sharp product peaks are linearly dependent on the photolysis laser power. The product translational energies of the peaks near 13500 cm^{-1} are consistent with the SD bond dissociation energy for the vibrational ground state of SD ($X^2\Pi_{3/2}$) (see more discussion in the following). The energy interval of the two groups of peaks in Figure 2.5 (a) is 1880 cm^{-1}, the same as the energy level difference between the $X^2\Pi_{3/2}$ v"=0 and 1 states of SD.[10,11] All these confirm that the peaks around 13500 cm^{-1} correspond to photolysis of SD in the $X^2\Pi_{3/2}$ v"=0 state, and those around 15500 cm^{-1} are from the v"=1 state. Separations among the three peaks in v"=0 or 1 (see more about the deconvolution in the following) agree well with the spin-orbit splittings of the fine-structure levels of $S(^3P_J)$, which also supports that the product channels are $D(^2S)$ + $S(^3P_{J=2,1,0})$. The spectrum in Figure 2.5 (b) is from photolysis of SD ($X^2\Pi_{3/2}$, v"=1 and 2) at 244 nm. As listed in Table 2.1, the $D(^2S)$ + $S(^3P_{J=2,1,0})$ product channels from the photodissociation of SD($X^2\Pi_{3/2}$) in v"=0-5 are observed in the wavelength region from 220 to 244 nm. At each photolysis wavelength, the possible D-atom product peaks of vibrationally excited SD ($X^2\Pi_{3/2}$, v"≥1) are shifted, from the corresponding product peaks of the ground-state SD ($X^2\Pi_{3/2}$, v"=0), to higher E_T energy by the SD ($X^2\Pi_{3/2}$) vibrational

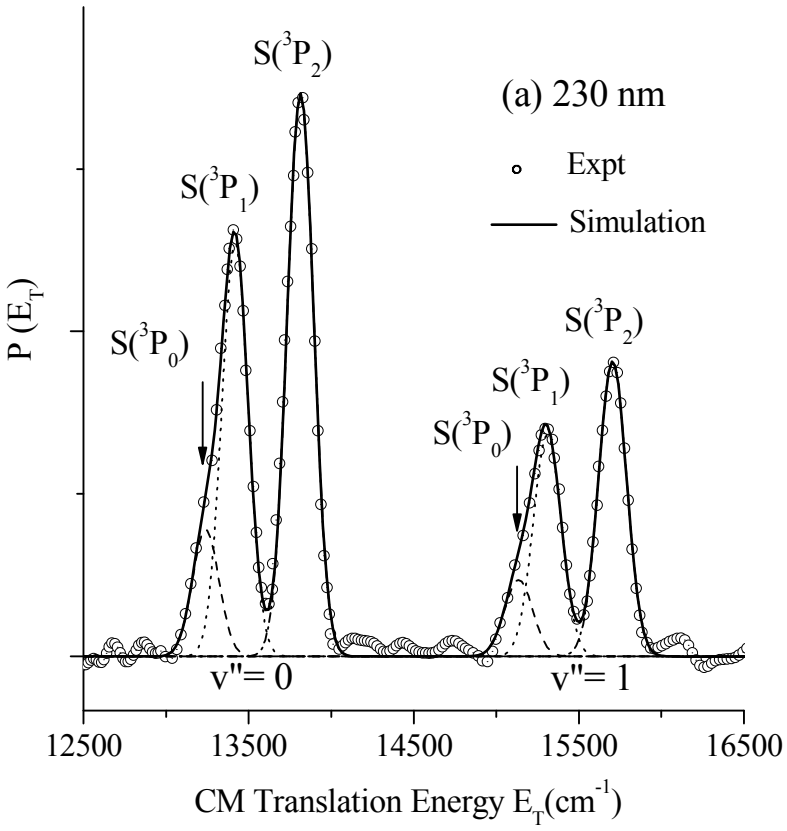

Figure 2.5 (a) Examples of CM product translational energy distributions, $P(E_T)$'s, of UV photodissociation of SD, with polarization of the photolysis radiation perpendicular (θ = 90^o) to the TOF axis. The spin-orbit S($^3P_{J=2,1,0}$) sublevels of the products are deconvoluted by fitting with slightly asymmetric Gaussian peaks and are shown in the figures. (a) Photodissociation of SD ($^2\Pi_{3/2}$, v"=0, 1) at 230 nm.

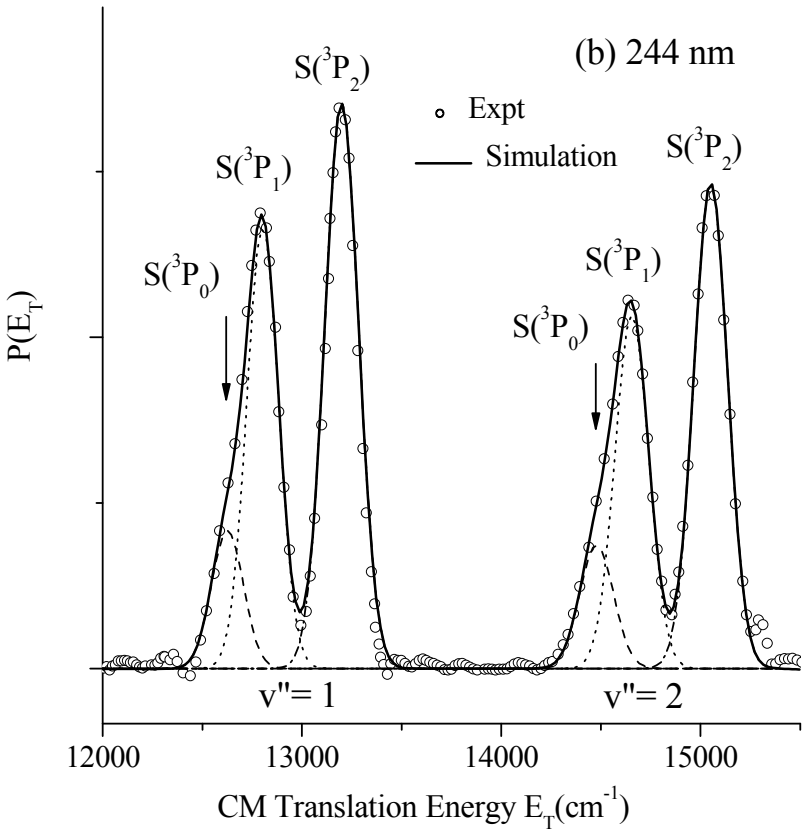

Figure 2.5 (b) Examples of CM product translational energy distributions, $P(E_T)$'s, of UV photodissociation of SD, with polarization of the photolysis radiation perpendicular (θ = 90^o) to the TOF axis. The spin-orbit S($^3P_{J=2,1,0}$) sublevels of the products are deconvoluted by fitting with slightly asymmetric Gaussian peaks and are shown in the figures. (b) photodissociation of SD ($^2\Pi_{3/2}$, v"=1, 2) at 244 nm.

energy spacing 1879.6 cm^{-1} for v"=1, 3713.0 cm^{-1} for v"=2, 5505.0 cm^{-1} for v"=3, 7245.0 cm^{-1} for v"=4, and 8934.1cm^{-1} for v"=5, respectively.[10,11] It is known that the 193-nm photolysis of D_2S produces vibrationally excited SD radicals, with a nascent population, v"= 0:1:2:3:4:5 = 0.560:0.127:0.057:0.072:0.045:0.053.[30] Apparently these vibrationally excited SD (v"≥1) radicals, although cooled rotationally (~30 K), are not completely relaxed in the molecular beam due to the difficulty of quenching high-frequency vibrational mode of diatomic species. Indeed, this is used for the studies of vibrationally excited SD radicals in this work. The relative intensities and variability of the photolysis signals of SD from the different vibrational states v" depend on the SD vibrational population in the beam (somewhat relaxed from the nascent population from 193-nm photolysis of D_2S), as well as the UV absorption cross sections of SD ($X^2\Pi_{3/2}$, v"=0-5) (i.e., the FC factors, etc.). In principle, the relative absorption cross sections of SD ($X^2\Pi_{3/2}$, v"=0-5) could be derived from the observed relative intensities. However, given the large uncertainty of the SD vibrational population in the beam, our attempt could not produce reliable results. The observed product peak positions in the $P(E_T)$'s are from the lower spin-orbit component of the ground electronic state $X^2\Pi_{3/2}$, instead of the upper component $X^2\Pi_{1/2}$ (376.7 cm^{-1} above $^2\Pi_{3/2}$). Although both SD ($^2\Pi_{3/2}$) and SD ($^2\Pi_{1/2}$) are produced in the 193-nm photolysis of D_2S (assumed with a nascent product ratio of $^2\Pi_{3/2}$:$^2\Pi_{1/2}$ ≈ 1.6:1 from H_2S),[31] the contribution from UV

photodissociation of SD ($^2\Pi_{1/2}$), which is expected to be 376.7 cm^{-1} higher in E_T than the peaks from $X^2\Pi_{3/2}$, is not detectable, indicating significant relaxation and small population of SD ($^2\Pi_{1/2}$) after supersonic cooling in the SD/Ar beam. The electronically excited S(^{1}D) + D(^{2}S) product channel, which correlates with the optically bright electronic states $^2\Delta$, $2^2\Pi$, and $A^2\Sigma^+$ (the repulsive wall), is energetically allowed from the UV photodissociation of the vibrationally excited SD ($X^2\Pi_{3/2}$) in the wavelength region of 220-244 nm (Figure 2.1). However, no evidence of the S(^{1}D) + D(^{2}S) channel is observed in this wavelength region, likely due to the poor FC factors between the ground-state $X^2\Pi$ (v"=0-5) and the excited states $^2\Delta$, $2^2\Pi$, and $A^2\Sigma^+$ in the investigated energy region.[22]

The S(^3P_J) product spin-orbit branching fractions are derived from the $P(E_T)$ distributions shown in Figure 2.5. Although these $P(E_T)$'s are obtained at perpendicular polarization ($\theta = 90^o$), our measurements show that the three S(^3P_J) spin-orbit product peaks likely have the same angular distribution and β parameter, and thus these $P(E_T)$'s are proportional to the angle-integrated partial cross sections of photodissociation and can be used to calculate the product branching fractions. This approach is also supported by the "magic angle" spectra that are synthesized from the spectra at perpendicular and parallel polarizations. In order to extract the S(^3P_J) product spin-orbit branching fractions, the groups of peaks for each vibrational state in the $P(E_T)$'s in Figure 2.5 are

modeled and deconvoluted with three peaks. The S(^3P_J) peaks in the $P(E_T)$'s are slightly asymmetric due to instrumentation function, and therefore a slightly asymmetric double Gaussian lineshape is used. The lineshape is first established by fitting the well-resolved S($^3P_2$) peak, and then the S($^3P_1$) and S($^3P_0$) peaks are deconvoluted by fitting with the same lineshape and with their relative positions fixed at the spin-orbit energy splittings of S(^3P_J) [S($^3P_1$) and S($^3P_0$) lie 396.1 and 573.6 cm^{-1} above the ground-state S($^3P_2$), respectively].[28] The deconvolution is robust, as only the heights of the peak S($^3P_1$) and S($^3P_0$) are adjusted. Examples of the fitted $P(E_T)$'s are shown in Figure 2.5. For the photodissociation of SD ($X^2\Pi_{3/2}$, v"=0 and 1) at 230 nm, spin-orbit branching fractions of the three fine-structure product channels D(^2S) + S($^3P_{J=2,1,0}$) are determined to be S($^3P_2$):S($^3P_1$):S($^3P_0$) = 0.51±0.02: 0.37±0.03: 0.12±0.03 for v"=0, and 0.50±0.02: 0.37±0.03: 0.13±0.03 for v"=1, where the experimental errors represent 95% confidence limit based on multiple measurement statistics. Note that the branching fraction of S($^3P_0$) has a larger relative error due to the small size of this peak. The S(^3P_J) spin-orbit branching fractions from the photolysis of SD ($X^2\Pi_{3/2}$, v"=0-5) at several UV wavelengths from 220 to 244 nm are obtained similarly, and are listed in Table 2.1 and plotted as a function of the total excitation energy (SD $X^2\Pi_{3/2}$ vibrational energy plus photon energy) in Figure 2.6. As shown in Figure 2.6 and Table 2.1, in the investigated energy region (41670-52040 cm^{-1}), the S(^3P_J) spin-orbit branching fractions from the UV

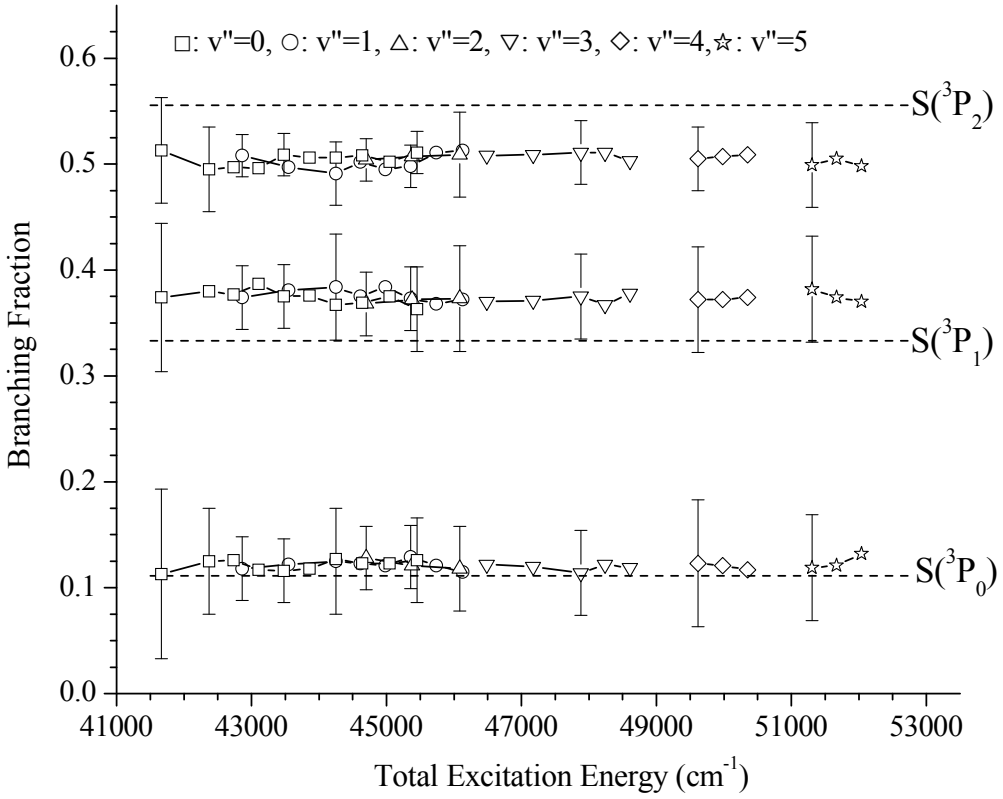

Figure 2.6 Spin-orbit branching fractions of the $S(^3P_J)$ products versus the total excitation energy, the photon energy plus the vibrational energy of SD ($^2\Pi_{3/2}$, v"). The error bars (when available) represent 95% confidence limit based on multiple measurement statistics; their sizes depend on the number of repeated measurements and statistical fluctuation. The $^2\Sigma^-$ sudden limit branching fraction ratios of the three product channels $S(^3P_{J=2,1,0})$ are 0.556:0.333:0.111 and are shown by the straight lines.

photolysis of SD ($X^2\Pi_{3/2}$, v"=0-5) are essentially constant within the experimental error, and the average spin-orbit branching fractions of the three product channels D(^{2}S) + S($^3P_{J=2,1,0}$) are S($^3P_2$):S($^3P_1$):S($^3P_0$) = 0.51:0.37:0.12.

The bond dissociation energy (BDE) of SD, D_0(S-D), is defined as the energy difference between the lowest level of SD, ($X^2\Pi_{3/2}$, v"=0, J"=3/2), and the lowest-energy product channel, D(^{2}S) + S($^3P_2$). D_0(S-D) can be obtained from the $P(E_T)$ distributions by conservation of energy:

$$E_{hv} + E_{vib}(\mathrm{SD}) + E_{rot}(\mathrm{SD}) = E_T + E_{\mathrm{int}}(\mathrm{S}) + D_0^0(\mathrm{S-D}) \qquad (3)$$

where E_{hv} is the UV photon energy, E_{vib}(SD), E_{rot}(SD) and E_{int}(S) are the vibrational energy and rotational energy of the parent SD radical, and the product S(^3P_J) atom spin-orbit energy, respectively. From the positions of the S(^3P_J) peaks in the $P(E_T)$ distributions, the products' CM translational energy E_T's (corresponding to the known initial vibrational energy levels v" of SD $X^2\Pi_{3/2}$) and internal energy E_{int}(S)'s are determined with precision. The rotational temperature of the SD radical in the supersonic beam is expected to about 30 K, which means that only a few rotational energy levels (such as J"=1.5 and 2.5) are significantly populated and E_{rot}(SD) is a minor quantity compared to the CM translational energy. The D_0(S-D) value can then be extracted using equation (3) for a collection of S(^3P_J) peaks at several photon energies. The derived BDE values are in excellent agreement with each other; an average value is

obtained, D_0(S-D) = 29660 ± 25 cm^{-1}. The uncertainty includes a statistical error based on multiple measurements and uncertainties in estimation of the beam velocity and initial rotational energy of SD. As in the case of UV photodissociation of SH,[21] the BDE D_0(S-D) can be evaluated with the BDE D_0(DS-D) of D_2S using the formula D_0(S-D) = D_0(DS-D) - ΔE_{kin}, where D_0(DS-D) = 32030 ± 50 cm^{-1} by Ashfold and co-workers (using photofragment translational spectroscopy),[19] and ΔE_{kin} is the difference between the energy onset for $D_2S + h\nu \rightarrow D + SD$ ($^2\Pi_{3/2}$, v"=0, J"=3/2) and the peak position of S($^3P_2$) from SD photodissociation in the $P(E_T)$ at the same UV photolysis wavelength. The energy onset for D_2S is determined by modeling the multiple rotational peak positions of the SD ($^2\Pi_{3/2,1/2}$, v"=0) product from D_2S. The D_0(S-D) value based on these measurements at several UV photolysis wavelengths is 29665 ± 50 cm^{-1}. This indirect approach requires no correction of molecular beam velocity, but it has uncertainties from the reported D_0(DS-D) and from determining the dissociation onsets of D_2S. Based on the accurate BDE D_0(S-H) = 29245±25 cm^{-1} previously measured by our group,[21] through subtracting the difference of the zero point energy of the ground state $X^2\Pi_{3/2}$ of SD and SH, D_0(S-D) could be inferred to be 29650 ± 25 cm^{-1}. Our D_0(S-D) values determined from above three approaches agree well within the experimental error. Our D_0(S-D) value is also in agreement within the error limit with the value of 29700 ± 100 cm^{-1} by Ashfold and co-workers.[19]

2.4 Discussion

As in the case of SH,[21] in the FC region the spin-orbit splittings among the electronically excited states of SD are far smaller than the energy separations among them, and spin-allowed electronic transitions in SD are expected to be dominant. In the UV region above the $D(^2S) + S(^1D)$ threshold, while the $^4\Sigma^-$ and $^4\Pi$ states are spin-forbidden from the doublet ground state $X^2\Pi$, the repulsive states $^2\Sigma^-$, $^2\Delta$, and $2^2\Pi$, as well as the repulsive part of the $A^2\Sigma^+$ state, are optically allowed. In this experiment, the SD radicals in $X^2\Pi_{3/2}$ v"=0-5 are excited by the UV photolysis radiation in the range from 220 to 240 nm, covering the total energy of 41670-52040 cm^{-1} (including both photon energy and SD vibrational energy). As shown by the PECs of SD in Figure 2.1, the excited repulsive state $^2\Sigma^-$ could be readily accessed from $X^2\Pi_{3/2}$ v"=0-5 by excitation with the UV photons in the region of 220–244 nm, with good FC factors and absorption cross sections. The other excited states $^2\Delta$, $2^2\Pi$, and $A^2\Sigma^+$, however, do not have significant photoexcitation cross sections in the UV region of 220–244 nm for SD $X^2\Pi_{3/2}$ v"=0-5.[22] As shown in the recent calculations,[22] the absorption cross sections of the $A^2\Sigma^+$–$X^2\Pi$ transition, which are significant only for the vibrationally excited SD ($X^2\Pi$) with v" ≥ 2, peak in the near-UV region of 280-340 nm and are negligible in the region of 220–244 nm. The same study indicated that the $^2\Delta$–$X^2\Pi$ transition is dominant in the

VUV region near 160 nm, and the contributions from the vibrationally excited SD ($X^2\Pi$, v" ≥ 2), although increasing, are also very small in the 220-244 nm region.[22] The $2^2\Pi$ state becomes important only at higher energy in VUV.[22,23] Therefore, $^2\Sigma^-$-$X^2\Pi$ is expected to be the dominant optically allowed transition for the SD ($X^2\Pi_{3/2}$, v"=0-5) radicals in the UV region of 220–244 nm.

The angular distributions of the D-atom products are anisotropic, and the experimental β parameters for the S(^3P_J) + D(^2S) product channel stay at the same value of ~ -1 (within experimental error limit) in this energy region for SD ($X^2\Pi_{3/2}$, v"=0-5) (Table 2.1). These observations are consistent with that in this energy region the perpendicular electronic transition $^2\Sigma^-$-$X^2\Pi$ is the dominant transition and SD photodissociation is initiated on the single repulsive $^2\Sigma^-$ PEC in the FC region, similar to the SH case.[21] The large anisotropy of the D-atom products also indicates that SD dissociates promptly at a time scale shorter than its rotational period, in agreement with the direct dissociation mechanism on the repulsive $^2\Sigma^-$ state.

Although calculated for SH, it is still helpful to compare the theoretical predictions by Lee and co-workers[24,25] with our experimental angular distributions and β parameters of SD. The calculated β parameters of the S(^3P_J) products from SH photodissociation in the photon energy region of 196-209 nm have oscillatory variations as a function of excitation energy. The predicted β parameters for the three spin-orbit S(^3P_J) products

are all negative, varying in the range of –0.4 to –1.0. The oscillatory behavior in the β parameters is attributed to the interference between two direct dissociation pathways, the repulsive $^2\Sigma^-$ and the repulsive part of $A^2\Sigma^+$, which could be optically excited simultaneously in the high-energy region above the threshold of the $H(^2S) + S(^1D)$ channel. However, in order to produce the oscillating patterns, it is necessary for contributions from the two indistinguishable dissociation pathways to be comparable, and when one is dominant, the photodissociation will then be reduced to that via a single pathway. In our previous study on the photodissociation of SH ($X^2\Pi_{3/2}$, v"=0-2) in the range of 216 to 232 nm, the experimental β parameters of the three $S(^3P_J)$ product channels were nearly constant (close to -1), and there were no oscillatory variations in these β parameters.[21] The results for SD in this work, with more measurements for the various v" levels in a larger energy region (Table 2.1), are essentially the same as for SH. Our experimental results for both SH and SD disagree with the theoretical predictions by Lee et al. in both the magnitude of the β parameters and the photolysis wavelength dependence. The comparison indicates that there is little or no interference in the two direct dissociation pathways of $^2\Sigma^-$ and $A^2\Sigma^+$ in the UV photolysis energy region of this study, and the theory overestimated the contribution from the repulsive part of $A^2\Sigma^+$. Indeed, the recent theoretical calculations by Janssen et al. showed that the $A^2\Sigma^+$–$X^2\Pi$ transition from the vibrationally excited SD ($X^2\Pi_{3/2}$, v" $\geq$ 2) peaks in the near-UV region

around 310 nm and the $^2\Delta$–$X^2\Pi$ transition in the VUV region near 160 nm, and there is very little absorption from the vibrationally excited SD ($X^2\Pi_{3/2}$, v" ≥ 2) to either $A^2\Sigma^+$ or $^2\Delta$ in the 220-244 nm region.[22] In this UV energy region the FC overlap between $X^2\Pi$ and the repulsive part of $A^2\Sigma^+$ is unfavorable compared to that between $X^2\Pi$ and $^2\Sigma^-$. This conclusion supports that in the 220-244 nm region the perpendicular $^2\Sigma^-$-$X^2\Pi$ transition is dominant and the SD photodissociation is initiated on the single repulsive $^2\Sigma^-$ state. This is also consistent with the nearly constant S(^3P_J) fine-structure state distributions in this study (discussed below).

In the photodissociation of diatomic species such as hydrogen halides and OH and SH, atomic product fine-structure state distributions provide detailed information about the dissociation mechanisms and nonadiabatic interactions among the dissociative PECs.[21,26,32-36] In the open-shell SD radical, the nonadiabatic interactions also influence the dissociation dynamics and product fine-structure state distribution.[24,25] In the FC region, SD is excited from $X^2\Pi$ to the single repulsive $^2\Sigma^-$ state; at large internuclear distances where the energy separations among the repulsive states $^4\Sigma^-$, $^2\Sigma^-$, and $^4\Pi$ are comparable to the spin-orbit interactions of these states, the dissociative $^2\Sigma^-$ state could couple with $^4\Sigma^-$ and $^4\Pi$ via the spin-orbit interactions. In the asymptotic region, the asymptotic spin-orbit interactions (i.e., frame transformation) also affect the S(^3P_J) product spin-orbit branching fractions. In our experiment, the fine-structure state

distribution of $S(^3P_J)$ from the photodissociation of SD ($X^2\Pi_{3/2}$, v"=0-5) in the total energy region of 41670-52040 cm^{-1} are measured (Figure 2.6 and Table 2.1). The observed fine-structure state distributions of $S(^3P_J)$ from SD ($X^2\Pi_{3/2}$, v"=0-5) are nearly constant in this region, with an average branching ratios of $S(^3P_2):S(^3P_1):S(^3P_0)$ = 0.51:0.37:0.12. While the theoretical spin-orbit branching fractions of $S(^3P_J)$ from the SH photolysis in the region of 196 to 209 nm exhibit oscillatory patterns as a function of excitation energy,[24] our experimental $S(^3P_J)$ spin-orbit branching ratios for SD show no observable oscillatory variations (within the experimental error) from 41670-52040 cm^{-1}, which again indicates that the $^2\Sigma^-$-$X^2\Pi$ transition is dominant and the interference between the two direct dissociation pathways ($^2\Sigma^-$ and $A^2\Sigma^+$) is not important in this energy region. The nearly constant $S(^3P_J)$ spin-orbit branching ratios for all the vibrational states also suggest that the SD ($X^2\Pi_{3/2}$) radicals in v"=0-5 are excited to the same repulsive state $^2\Sigma^-$ and follow the same dissociation dynamics. Furthermore, the fact that no $S(^1D)$ products are observed in this study implies that little or no SD ($X^2\Pi_{3/2}$, v"=0-5) is excited in the 220-244 nm region to either the $A^2\Sigma^+$ or $^2\Delta$ state that correlate to the $S(^1D)$ + D product channel. This is in agreement with the calculated photoabsorption cross sections by Janssen et al.,[22] and also supports that $^2\Sigma^-$-$X^2\Pi$ is the dominant transition the 220-244 nm region.

Two pictures are commonly used to illustrate the correlations between photofragments and molecular electronic states and the dissociation mechanisms of repulsive curves of diatomics. In the adiabatic picture, the electronic Hamiltonian (including spin-orbit coupling) is diagonalized to give Born-Oppenheimer PECs, an these PESs can then be coupled by nuclear kinetic energy operator.[32,33,35] In the adiabatic correlation scheme,[21] the ground and three repulsive electronic excited states of SD are correlated with the atomic product states $S(^3P_J) + D(^2S)$ on the adiabatic curves by the Ω quantum number (projection of the total electronic angular momentum along the internuclear axis and conserved between the molecular and atomic states). The $^2\Sigma^-$ state correlates adiabatically with the $S(^3P_1) + D(^2S)$ products.[21] In the adiabatic limit when the D atom departs very slowly, the initially excited $^2\Sigma^-$ state dissociates following the adiabatic correlation to the asymptotical $S(^3P_1) + D(^2S)$ products, which would be the only product channel. However, our experimental $S(^3P_J)$ distributions are clearly different from the adiabatic limit, and thus nonadiabatic transitions are important in the direct dissociation of the SD $^2\Sigma^-$ state. Specifically, the $^2\Sigma^-$ adiabat (with $\Omega = ½$) could couple with the $\Omega = ½$ components of the $^4\Sigma^-$ and $^4\Pi$ states at large internuclear distance, and the dissociation flux is then redistributed from $^2\Sigma^-$ to $^4\Sigma^-$ and $^4\Pi$.

In the diabatic representation, the electronic Hamiltonian (without spin-orbit coupling) and the nuclear kinetic energy operator is diagonalized and approximately

diagonalized, respectively.[32,33,35] The PECs in this representation are diabatic curves and they could recouple at the large internuclear distance by spin-orbit interactions. In the limit of high excitation energy when the atomic fragments depart rapidly (for high excess energy and light mass of D atom), there is insufficient time for the electronic and spin angular momentum to recouple at the large internuclear distance. The dissociation is then viewed to be essentially on the single diabatic curve that is initially excited in the FC region, and the dissociation mechanism is in the high-energy recoil limit (the sudden limit or diabatic limit). In this single-state sudden limit, the dissociation mechanism becomes independent of the details of the intrashell nonadiabatic interactions; the fine-structure state distribution of the products is determined by frame transformation (the asymptotic spin-orbit interaction, i.e., projection of the molecular wave function of the initial diabatic state onto the atomic basis states of the products), independent of the excitation energy. In the investigated energy region of SD, since the kinetic energy of the $S(^3P_J)$ + $D(^2S)$ products in the direct dissociation on the repulsive $^2\Sigma^-$ curve is far larger than the spin-orbit couplings among the repulsive $^4\Sigma^-$, $^2\Sigma^-$, and $^4\Pi$ states, the direct dissociation of $^2\Sigma^-$ to $S(^3P_J)$ + $D(^2S)$ could be considered to approach the sudden limit on the single diabatic $^2\Sigma^-$ curve. In the single-state sudden limit for $^2\Sigma^-$, the spin-orbit branching fractions are $S(^3P_2):S(^3P_1):S(^3P_0)$ = 0.556:0.333:0.111.[21,24] Our experimental

values from SD ($X^2\Pi_{3/2}$, v"=0-5) are close to this sudden limit distribution of the $^2\Sigma^-$ state.

It is interesting to compare the photodissociation of SH and SD and examine the effects of product mass and excitation energy. The spin-orbit branching fractions of $S(^3P_J)$ from SH ($X^2\Pi_{3/2}$, v"=0-2) are essentially constant (within the experimental error) at the total excitation energy from 43100-49300 cm^{-1}, with an average $S(^3P_2):S(^3P_1):S(^3P_0)$ = 0.51:0.36:0.13.[21] Those of SD ($X^2\Pi_{3/2}$, v"=0-5) from the total excitation energy 41670 to 52040 cm^{-1} are also nearly constant, with the average $S(^3P_2):S(^3P_1):S(^3P_0)$ = 0.51:0.37:0.12. Essentially, the spin-orbit branching fractions of $S(^3P_J)$ from both SH and SD are the same and are constant in the UV energy region. For the same excess energy, D atom in SD departs with 1.4 times smaller velocity than H atom in SH, and thus longer time for spin-orbit interactions at the large internuclear distance in SD. In the energy region of these two studies, the D atom from SD at the lowest excitation energy 41670 cm^{-1} departs with the smallest velocity, while the H atom from SH at the high energy 49300 cm^{-1} with the largest velocity; and yet the $S(^3P_J)$ spin-orbit branching fractions in both cases, as well as others in between, are essentially the same and constant within the experimental error. This indicates that the mass effect is minimal in the investigated energy region. It is plausible that the high-energy limit has been reached, as the $S(^3P_J)$ spin-orbit branching fractions are independent with the H/D atom product

mass and the available excess energy. Alternatively, the nearly constant $S(^3P_J)$ spin-orbit branching fractions may simply be due to the relatively limited range of energy, which is varied only by a factor of <1.25 in these two studies. The $S(^3P_J)$ spin-orbit branching fractions from both SH and SD are close to but are slightly different from those of the $^2\Sigma^-$ state at the single-state sudden limit. The $S(^3P_2)$ populations are slightly below the sudden limit and those of $S(^3P_1)$ are above (Figure 2.6). This comparison implies that the sudden-limit dissociation on the single $^2\Sigma^-$ state could not completely account for the UV photodissociation mechanism of SH and SD. The dissociation involves the other repulsive states $^4\Sigma^-$ and $^4\Pi$ along the dissociation pathways, i.e., the intrashell spin-orbit couplings between the $^2\Sigma^-$ and $^4\Sigma^-$ and $^4\Pi$ diabatic states (via their Ω = ½ components) are not negligible at the large internuclear distance; and the comparison and the difference indicate an observable amount of redistribution of photodissociation flux from $^2\Sigma^-$ to $^4\Sigma^-$ and $^4\Pi$. Further theoretical studies on the photodissociation of SH and SD would provide more insights into the detailed mechanisms.

In summary, the $S(^3P_J)$ product fine-structure state distributions and the anisotropy β parameters of the D-atom product from the photodissociation of vibrationally ground and excited SD ($X^2\Pi_{3/2}$, v"=0-5) in the wavelength region of 220–244 nm are obtained. These provide a sensitive probe for the direct photodissociation dynamics of the SD ($X^2\Pi_{3/2}$) radicals in the vibrational states v"=0-5 in the UV region. The $S(^3P_J)$ product

fine-structure state distributions are essentially the same for v"=0-5 in the wavelength region from 220-244 nm and show no oscillatory variations. The average spin-orbit branching fractions of $S(^3P_J)$ are $S(^3P_2):S(^3P_1):S(^3P_0) = 0.51:0.37:0.12$, approaching those in the sudden limit dissociation on the single repulsive $^2\Sigma^-$ state. The anisotropy parameters of the D-atom products stay essentially the same (close to -1) and have no oscillatory variations. Our results indicate that the UV photolysis of SD is a direct dissociation and is initiated on the single repulsive $^2\Sigma^-$ PEC in the FC region following the perpendicular transition $^2\Sigma^- \text{-} X^2\Pi$. Although the $S(^3P_J)$ product fine-structure state distributions are close to that in the sudden limit dissociation of $^2\Sigma^-$, they also show an observable amount of difference that is attributed to the redistribution of photodissociation flux from $^2\Sigma^-$ to $^4\Sigma^-$ and $^4\Pi$. The bond dissociation energy $D_0(\text{S-D}) = 29660 \pm 25\ \text{cm}^{-1}$ is obtained.

References

1. R. P. Wayne, *Chemistry of Atmospheres*, 3rd ed. (Oxford University Press, Oxford, 2000).

2. I. Yamamura, K. Kawaguchi, and S. T. Ridgway, *Astrophys. J.* **528**, L33 (2000).

3. P. J. Bruna and G. Hirsch, *Mol. Phys.* **61**, 1359 (1987).

4. J. Senekowitsch, H. J. Werner, P. Rosmus, E. A. Reinsch, and S. V. O'Neil, *J. Chem. Phys.* **83**, 4661 (1985).

5. J. K. Park and H. Sun, *Chem. Phys. Lett.* **194**, 485 (1992).

6. M. R. Manaa, *Int. J. Quant. Chem. Quant. Chem. Symp.* **29**, 577 (1995).

7. S. M. Resende and F. R. Ornellas, *J. Chem. Phys.* **115**, 2178 (2001).

8. S. H. Ashworth and J. M. Brown, *J. Mol. Spectrosc.* **153**, 41 (1992).

9. E. Klisch, T. Klaus, S. P. Belov, A. Dolgner, R. Schieder, G. Winnewisser, and E. Herbst, *Astrophys. J.* **473**, 1118 (1996).

10. D. A. Ramsay, *J. Chem. Phys.* **20**, 1920 (1952).

11. J. W. C. Johns and D. A. Ramsay, *Can. J. Phys.* **39**, 210 (1961).

12. W. Ubachs, J. J. ter Meulen, and A. Dymanus, *Chem. Phys. Lett.* **101**, 1 (1983).

13. R. R. Friedl, W. H. Brune, and J. G. Anderson, *J. Chem. Phys.* **79**, 4227 (1983).

14. J. J. Tiee, M. J. Ferris, and F. B. Wampler, *J. Chem. Phys.* **79**, 130 (1983).

15. L. Schnieder, W. Meier, K. H. Welge, M. N. R. Ashfold, and C. M. Western, *J. Chem. Phys.* **92**, 7027 (1990).

16. M. D. Wheeler, A. J. Orr-Ewing, and M. N. R. Ashfold, *J. Chem. Phys.* **107**, 7591 (1997).

17. R. E. Continetti, B. A. Balko, and Y. T. Lee, *Chem. Phys. Lett.* **182**, 400 (1991).

18. C. W. Hsu, C. L. Liao, Z. X. Ma, P. J. H. Tjossem, and C. Y. Ng, *Chem. Phys. Lett.* **199**, 78 (1992).

19. G. P. Morley, I. R. Lambert, D. H. Mordaunt, S. H. S. Wilson, M. N. R. Ashfold, R. N. Dixon, and C. M. Western, *J. Chem. Soc. Faraday. Trans.* **89**, 3865 (1993).

20. S. H. S. Wilson, J. D. Howe, and M. N. R. Ashfold, *Mol. Phys.* **88**, 841 (1996).

21. W. Zhou, Y. Yuan, S. Chen, and J. Zhang, *J. Chem. Phys.* **123**, 054330/1 (2005).

22. L. M. C. Janssen, M. P. J. van der Loo, G. C. Groenenboom, S.-M. Wu, D. C. Radenovic, A. J. A. van Roij, I. A. Garcia, and D. H. Parker, *J. Chem. Phys.* **126**, 094304/1 (2007).

23. S. Chen, W. Zhou, and J. Zhang, *Chem. Phys. Lett.* **418**, 328 (2006).

24. S. Lee, H. Sun, B. Kim, and K. F. Freed, *J. Chem. Phys.* **114**, 5537 (2001).

25. S. Lee, H. Sun, B. Kim, and K. F. Freed, *J. Chem. Phys.* **116**, 10656 (2002).

26. W. Zhou, Y. Yuan, and J. Zhang, *J. Chem. Phys.* **119**, 9989 (2003).

27. K. S. Xu, G. Amaral, and J. S. Zhang, *J. Chem. Phys.* **111**, 6271 (1999).

28. Y. Ralchenko, F.-C. Jou, D. E. Kelleher, A. E. Kramida, A. Musgrove, J. Reader, W. L. Wiese, and K. Olsen, *NIST Atomic Spectra Database (version 3.0)*, [Online]. Available: http://physics.nist.gov/asd3 ed. (National Institute of Standards and Technology, Gaithersburg, MD., 2007).

29. R. N. Zare, *Photochem.* **4**, 1 (1972).

30. X. Xie, L. Schnieder, H. Wallmeier, R. Boettner, K. H. Welge, and M. N. R. Ashfold, *J. Chem. Phys.* **92**, 1608 (1990).

31. B. R. Weiner, H. B. Levene, J. J. Valentini, and A. P. Baronavski, *J. Chem. Phys.* **90**, 1403 (1989).

32. G. G. Balint-Kurti, R. N. Dixon, and C. C. Marston, *J. Chem. Soc. Faraday. Trans.* **86**, 1741 (1990).

33. M. H. Alexander, B. Pouilly, and T. Duhoo, *J. Chem. Phys.* **99**, 1752 (1993).

34. G. Peoux, M. Monnerville, T. Duhoo, and B. Pouilly, *J. Chem. Phys.* **107**, 70 (1997).

35. P. M. Regan, S. R. Langford, A. J. Orr-Ewing, and M. N. R. Ashfold, *J. Chem. Phys.* **110**, 281 (1999).

36. S. R. Langford, Paul M. Regan, Andrew J. Orr-Ewing, and M. N. R. Ashfold, *Chem. Phys.* **231**, 245 (1998).

CHAPTER 3

H-atom product channel and mode specificity

in the near-UV photodissociation of thiomethoxy radical via the $\tilde{A}^2A_1$ state

ABSTRACT

Photodissociation of jet-cooled thiomethoxy radical (CH_3S) via the $\tilde{A}^2A_1 \leftarrow \tilde{X}^2E_{3/2}$ transition is studied in the region of 344-362 nm. The H-atom product channel is directly observed by H-atom photofragment yield spectrum and photofragment translational spectroscopy. Two vibronic levels of $\tilde{A}^2A_1$, 2^13^1 and 2^13^2, dissociate to H + H_2CS, while the others in the vicinity (2^13^3 and 3^n, n=3-6) dissociate to CH_3 + $S(^3P_J)$ (based on a previous study by Neumark and co-workers). The H + H_2CS product translational energy release is not repulsive and peaks at ~9 kcal/mole; the H-atom angular distribution is isotropic. The dissociation mechanism is consistent with internal conversion of the excited $\tilde{A}^2A_1$ to the ground-state $\tilde{X}^2E$ followed by unimolecular dissociation of $\tilde{X}^2E$.

3.1 Introduction

Thiomethoxy radical (CH_3S) is an important intermediate in atmospheric oxidation of naturally occurring sulfur compounds such as dimethyl sulfide (CH_3SCH_3) and dimethyl disulfide (CH_3SSCH_3).[1-4] The spectroscopy of the thiomethoxy radical has been studied extensively; this includes electronic absorption[5,6] and emission spectra,[7] microwave spectroscopy,[8] photoelectron and photodetachment spectroscopy,[9-11] laser-induced fluorescence (LIF),[12-15] fluorescence depletion spectroscopy (FDS),[16] four-wave mixing spectroscopy,[17,18] and photofragment yield (PFY) spectroscopy.[19] These studies have provided information on the geometric and spectral parameters of both the ground state $\tilde{X}^2E$ and the first electronic excited state $\tilde{A}^2A_1$.

In particular, the $\tilde{A}^2A_1$ state and the $\tilde{A}^2A_1 \leftarrow \tilde{X}^2E$ transition in the near ultraviolet (UV) region have been well characterized by the fluorescence,[12-16] four-wave mixing,[17,18] and PFY spectroscopy.[19] The $\tilde{A}^2A_1 \leftarrow \tilde{X}^2E$ spectra have predominant vibrational progressions in symmetric C-S stretch (ν_3) mode, 3^n, and its combination modes with CH_3 umbrella (ν_2), $2^1 3^n$, along with other combination states involving symmetric CH_3 stretching (ν_1) and asymmetric CH_3 stretching (ν_4) such as $1^1 3^n$ and $3^n 4^1$.[12-19] The rotationally resolved spectrum showed that the C-S bond is lengthened and the HCS bond angle decreases in the $\tilde{A}^2A_1$ state,[14] in agreement with the

predominant C-S stretching progression in the $\tilde{A}^2A_1 \leftarrow \tilde{X}^2E$ band. Above an excitation energy of 27321 cm^{-1} (the 3^2 level, 795 cm^{-1} above the $\tilde{A}$ state origin, 26526 cm^{-1}), radiative lifetimes of the $\tilde{A}$ state vibronic levels decrease significantly, and no emission is observed above 28016 cm^{-1} (the $2^1 3^1$ level, 1490 cm^{-1} relative to the $\tilde{A}$ origin). This is attributed to the predissociation of the $\tilde{A}$ state and limits the LIF measurements to lower vibrational levels of the $\tilde{A}$ state. Instead, the higher $\tilde{A}$ state vibronic levels, mainly the higher 3^n and $2^1 3^n$ states, as well as the $1^1 3^n$, $3^n 4^1$, and $2^1 3^n 4^1$ (or $1^1 2^1 3^n$) combination states, up to ~5200 cm^{-1} above the $\tilde{A}$ state origin, were observed by the fluorescence depletion spectroscopy,[16] four-wave mixing spectroscopy,[17,18] and PFY spectroscopy.[19]

Several *ab initio* calculations have been carried out to characterize the ground and excited electronic states of the CH_3S radical.[20-24] Figure 3.1 shows the potential energy diagram of CH_3S along the C-S and the C-H dissociation coordinate, based on the theoretical calculations of Hsu et al.[22] and Cui et al.[23] The $\tilde{X}^2E$ ground state correlates asymptotically with the $CH_3(\tilde{X}^2A_2'') + S(^3P_J)$ products and the $H + H_2CS(\tilde{X}^1A_1)$ products. The first electronic excited state $\tilde{A}^2A_1$ correlates asymptotically to the $CH_3(\tilde{X}^2A_2'') + S(^1D)$ channel and is crossed by three repulsive states, $^4A_2$, ^4E, and $\tilde{B}^2A_2$. These three repulsive states induce predissociation in the $\tilde{A}^2A_1$ state and correlate to the ground-state products $CH_3(\tilde{X}^2A_2'') + S(^3P_J)$. Photodissociation of the methoxy radical

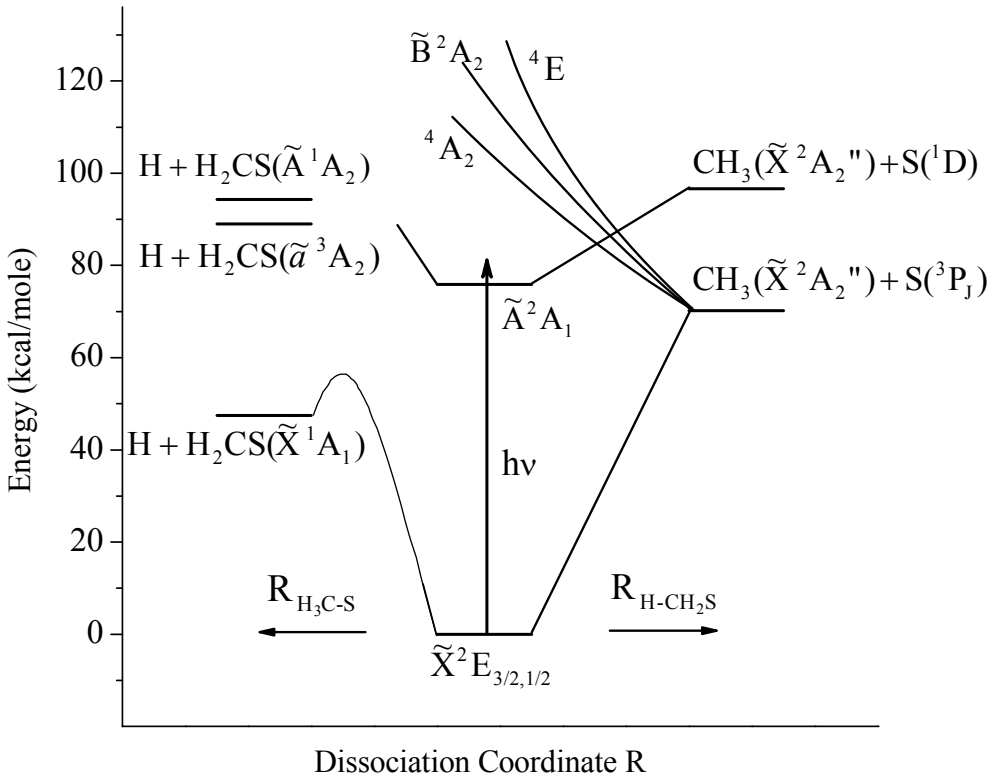

Figure 3.1 Schematics of the potential energy of the CH_3S system. The dissociation pathway leading to the CH_3 + S products is shown along the C-S dissociation coordinate (in C_{3v}). The H + H_2CS dissociation channel is shown along the C-H dissociation coordinate. The energetics are based on the theoretical calculations (from Ref. 22 and 23) and the experimental values (from Ref. 16 and 19).

family CX_3Y (X = H, F; Y = O, S) from the $\tilde{A}^2A_1$ state has been examined using *ab initio* MO calculations by Cui et al.,[23] and three dissociation channels, CX_3 + Y, CX_2 + YX, and CX_2Y + X, have been considered. The thermodynamically possible dissociation pathways of CH_3S in the $\tilde{A}^2A_1 \leftarrow \tilde{X}^2E$ excitation are [19]

$$CH_3S(\tilde{X}^2E) + h\nu \rightarrow CH_3(\tilde{X}^2A_2") + S(^3P_J) \quad \Delta H_{rxn,0} = 70.22 \pm 0.35 \text{ kcal/mole}$$

$$\rightarrow H_2CS(\tilde{X}^1A_1) + H \qquad \Delta H_{rxn,0} = 47.5 \pm 1.8 \text{ kcal/mole}$$

The photodissociation dynamics of the first excited state $\tilde{A}^2A_1$ of CH_3S have been studied experimentally by Neumark and co-workers using photofragment translational spectroscopy.[19] Only one major channel, $CH_3(\tilde{X}^2A_2") + S(^3P_J)$, was observed.[19] The PFY spectra for the $\tilde{A}^2A_1 \leftarrow \tilde{X}^2E$ transition revealed vibrationally resolved progressions of the C-S stretch and the associated combination bands.[19] The C-S stretch ν_3 progression was assigned to extend from 3^2 to 3^{15} (for $\tilde{A}^2A_1 \leftarrow \tilde{X}^2E_{3/2}$) and the ν_2 and ν_3 combination bands were assigned from 2^13^3 to 2^13^{12}, while interestingly the 2^13^1 and 2^13^2 bands were not observed in this experiment.[19] Later on, the higher states 3^n (n≥8) and 2^13^n (n≥5) in the progressions were reassigned to the 1^13^n, 3^n4^1, and $2^13^n4^1$ combination states in the four-wave mixing spectroscopy studies.[17,18]

The radiative and nonradiative decays of the $\tilde{A}^2A_1$ state have also been investigated using LIF and FDS by Miller and co-workers[16] and four-wave mixing spectroscopy by Lee and co-workers.[17,18] With the increase of energy, the lifetimes of

the 3^n and $2^1 3^n$ bands decrease and the homogeneous linewidths increase significantly, indicating mode specificity in the nonradiative processes and the ν_3 mode being the promoting mode for dissociation [to the $CH_3 + S(^3P)$ products from the 3^n ($n \geq 2$) and $2^1 3^n$ ($n \geq 3$) states].[16-19] The lower 3^2 and $2^1 3^1$ bands were observed by LIF with short lifetimes of 250 ns and 60 ns,[15,16] while the $2^1 3^2$ band was not observed in LIF but only in the FDS and four-wave mixing spectroscopy,[16,17] and thus is completely dark, with a lifetime in the range of 10 ps to 10 ns.[16] All these three vibronic states are strongly predissociative, and based on comparison of the natural lifetimes of these levels with that of the $\tilde{A}^2A_1$ state origin, more than 80%, 94%, and 99% of the CH_3S radicals excited into the 3^2, $2^1 3^1$, and $2^1 3^2$ levels, respectively, undergo nonradiative decays.[16] However, the two states $2^1 3^1$ and $2^1 3^2$ do not dissociate into the $CH_3 + S(^3P_J)$ products, as the $2^1 3^1$ and $2^1 3^2$ bands were not observed in the $CH_3 + S(^3P_J)$ PFY spectrum by Neumark and co-workers;[19] and the 3^2 peak was also very weak in the $CH_3 + S(^3P_J)$ PFY spectrum [19] It was then suggested by Miller and co-workers that in the near-UV excitation region of less than three quanta of ν_3, there might be another dissociation channel (likely the H + H_2CS product channel following internal conversion of the $\tilde{A}^2A_1$ state to the ground state $\tilde{X}^2E$),[16] although this H-atom product channel was not directly identified at that time. At higher UV energy, the H-atom product was observed from the 213-220 nm photodissociation of CH_3S in the secondary photolysis of CH_3SH.[25] In this case, CH_3S

was excited to the repulsive $\widetilde{B}^2A_2$ state via the $\widetilde{B}^2A_2 \leftarrow \widetilde{X}^2E$ transition, and H_2CS associated with the main H-atom elimination channel was believed to be produced in the electronically excited $\widetilde{A}^1A_2$ state.[25]

Recently, our group reported a direct observation and preliminary study of the H + H_2CS product channel in the photodissociation of CH_3S from the $\widetilde{A}^2A_1$ $2^1 3^2$ level at 352.145 nm.[26] In the current study, the dynamics of the H-atom photofragmentation channel of the CH_3S radical is examined in a larger wavelength range of 344-362 nm, which covers the $2^1 3^n$ (n = 0-3) and 3^n (n = 3-6) vibronic bands, and with improved background treatments. The H-atom product is detected by 1 + 1 resonance-enhanced multiphoton ionization (REMPI) (VUV at Lyman-α + UV at 364 nm), and the H-atom PFY spectrum is obtained as the action spectrum by scanning the near-UV photolysis radiation. The H-atom photofragment translational spectroscopy is obtained by the high-n Rydberg atom time-of-flight (HRTOF) technique. Two vibronic levels of CH_3S $\widetilde{A}^2A_1$, $2^1 3^1$ and $2^1 3^2$, are shown to dissociate to the H + H_2CS products, and the H-atom photodissociation dynamics is examined.

3.2 Experimental

The HRTOF technique and experimental setup have been described before.[27-30] A pulsed CH_3S radical beam was produced by photolysis of CH_3SSCH_3 (≥ 99.0%, Aldrich) seeded in He (~ 2% at a total pressure of 120 kPa) with the 193-nm radiation of an ArF excimer laser that was slightly focused in front of the pulse nozzle. The CH_3S radicals generated from the photolysis were entrained in the molecular beam and subsequently cooled by supersonic expansion. The radical beam was collimated at 2.8 cm downstream by a 1-mm diameter skimmer into a high-vacuum chamber; at 4.6 cm further downstream of the skimmer, the CH_3S radical beam was crossed with a slightly focused near-UV photolysis laser radiation (344-362 nm, 4-7 mJ/pulse, linewidth ≤ 0.3 cm^{-1}). The absolute photolysis laser wavelength was monitored by a wavemeter (Burleigh WA-4500). The polarization of the photolysis radiation was rotated by a Fresnel-Rhomb achromatic λ/2 plate for product angular distribution measurements. The H atom products from the CH_3S photodissociation were tagged by two-color resonant excitation (121.53 nm + 366.36 nm), i.e., from 1^2S to 2^2P via the H-atom Lyman-α transition and then to a high-*n* Rydberg state. A small fraction of the radiatively metastable Rydberg H atoms drifted with their nascent velocities toward a microchannel plate (MCP) detector, and were field-ionized in front of the detector and

detected. The nominal flight length was 37.1 cm. The ion signals were amplified by a fast pre-amplifier, and the H-atom TOF spectra were recorded and averaged by using a multichannel scaler (EG&G Turbo MCS). The H-atom TOF spectra were typically accumulated with 4×10^5 laser shots.

The H-atom PFY spectrum (action spectrum) was obtained by collecting the H-atom product REMPI signals as a function of photolysis wavelength. The REMPI experiment was conducted in the same HRTOF instrument, and the photolysis and REMPI ionization lasers were the same as in the HRTOF experiment. Upon photodissociation by the near-UV laser radiation in the range of 344-362 nm, the product H atoms were detected by 1 + 1 REMPI, with one Lyman-α photon resonantly exciting the H atom from 1^2S to 2^2P and a UV photon at ~364 nm ionizing the H atom. The photolysis and REMPI probe laser delay time was fixed at 20 ns. The H^+ ions were extracted and accelerated in a linear TOF mass spectrometer, and were detected by the MCP detector. The mass-resolved ion current signal (at m/z = 1, H^+) was preamplified and input into a Boxcar averager (SRS 250). The scanning rate of the photolysis laser was 0.005 or 0.01 nm/step; typically 100 laser shots were averaged at each wavelength step, and the averaged signal was input to the computer data acquisition system. Three types of REMPI spectra were obtained: (1) the 193-nm radiation on (for CH_3S radical production) and the near-UV photolysis on (for CH_3S radical photodissociation), (2) the 193-nm

radiation on and the near-UV photolysis off, and (3) the 193-nm radiation off and photolysis on. Only in (1), the vibronic transitions of CH_3S such as $2^1 3^1$ and $2^1 3^2$ were observed in the REMPI experiment. The PFY spectrum reported in the following section is the net H-atom REMPI signals with the flat backgrounds from (2) and (3) removed. No attempt was made to normalize the PFY spectrum with the photolysis laser power, which was maintained to be about constant in the small scanning ranges.

3.3 Results and discussion

The H-atom PFY spectrum in the region of 27,500-28,900 cm^{-1} is shown in Figure 3.2. The PFY spectrum shows the net H^+ signal from photodissociation of CH_3S, which is obtained from the spectrum with both the 193-nm radiation on and near-UV photolysis on minus the backgrounds with the 193-nm radiation on and photolysis off and with the 193-nm radiation off and photolysis on. Two peaks, the $2^1 3^1$ and $2^1 3^2$ bands in the $\tilde{A}^2 A_1 \leftarrow \tilde{X}^2 E_{3/2}$ transition, are observed at 28020 and 28397 cm^{-1}, and their positions are in excellent agreement (within 4 and 1 cm^{-1}, respectively) with those reported in the previous FDS and four-wave mixing spectroscopy studies.[16,17] This H-atom PFY spectrum provides direct evidence for the H + H_2CS dissociation channel in the near-UV photodissociation of the $2^1 3^1$ and $2^1 3^2$ levels of CH_3S $\tilde{A}^2 A_1$. The other two peaks of the

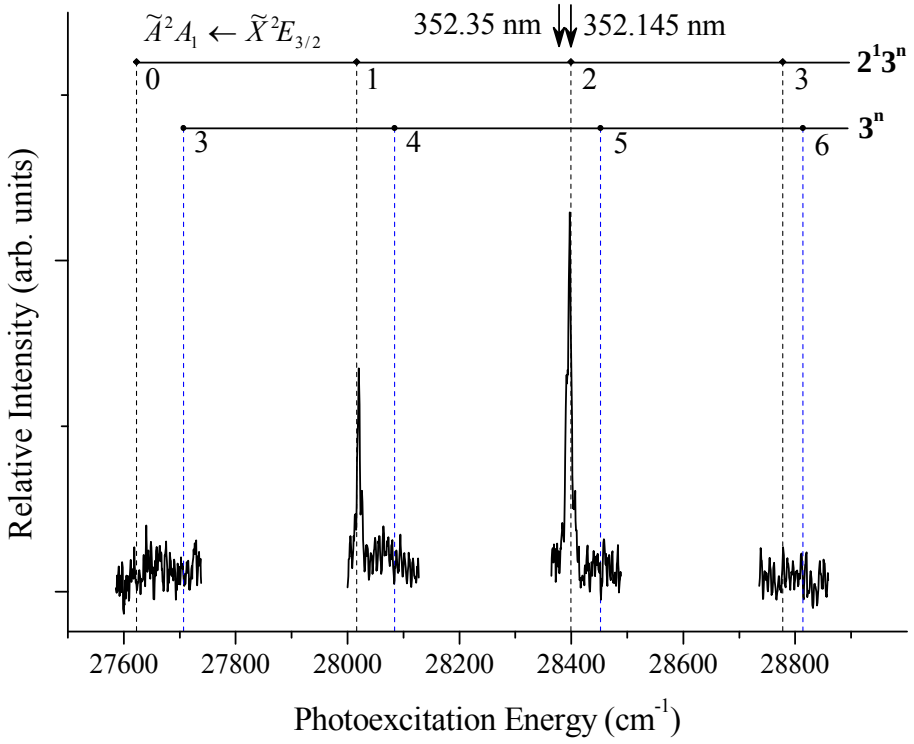

Figure 3.2 H-atom photofragment yield spectrum as a function of photolysis excitation energy (27,500-28,900 cm^{-1}) in the vicinity of the 2^13^1 and 2^13^2 levels of $\tilde{A}^2A_1$. The H atoms are detected by the 1 + 1 REMPI (VUV 121.6 nm + UV 364 nm). The arrows indicate the photolysis energies where the HRTOF spectra are taken.

$2^1 3^n$ series in the vicinity, $2^1 3^0$ and $2^1 3^3$, do not produce the H atom product; while the $2^1 3^3$ level dissociates to the $CH_3 + S(^3P_J)$ products,[19] the 2^1 state appears to mainly decay by fluorescence. [16] Based on the LIF and four-wave mixing spectra,[16,17] the 3^n (n=3-6) peaks in the vicinity are expected to have higher intensity compared to the $2^1 3^1$ and $2^1 3^2$ peaks. However, these 3^n peaks are not observed in the H-atom PFY spectrum in Figure 3.2, while they were identified in the PFY spectrum of the $CH_3 + S(^3P_J)$ products by Neumark and co-workers.[19] The H-atom dissociation channel clearly depends on the $\tilde{A}^2A_1$ vibronic state modes, indicating mode specificity in this dissociation channel, and this H-atom production channel appears in a narrow window of energy and vibronic modes. The H-atom product channel appears only at less than three quanta of ν_3 in the $\tilde{A}^2A_1$ state, and at higher ν_3 levels, which approach the crossing seams between the $\tilde{A}^2A_1$ state and the three repulsive states, the $CH_3 + S(^3P_J)$ predissociation channel competes strongly and becomes predominant. Interestingly, although the $2^1 3^1$ and 3^4 levels and the $2^1 3^2$ and 3^5 levels have nearly the same energy, respectively (Figure 3.2), 3^4 and 3^5 only dissociate to $CH_3 + S(^3P_J)$ [19] and $2^1 3^1$ and $2^1 3^2$ exclusively to $H + H_2CS$ (following the internal conversion of the $\tilde{A}^2A_1$ state to the ground state $\tilde{X}^2E$). This indicates that the one quanta energy in the CH_3 umbrella ν_2 mode does not efficiently couple to the C-S predissociation and the one or two quanta energy in the C-S stretching mode in the $2^1 3^1$ and $2^1 3^2$ states are not sufficient for the $CH_3 + S(^3P_J)$ predissociation

channel to be competitive, and thus the internal conversion of the $\tilde{A}^2A_1$ state to the ground state $\tilde{X}^2E$ and the subsequent H-atom product channel become predominant. And at the lower energy of 2^1, both nonradiative decay pathways (CH_3 + S and H + H_2CS) are slower, and the fluorescence decay becomes the main channel. The linewidth of the 2^13^1 and 2^13^2 levels in the H-atom PFY spectrum are ~10 cm^{-1}, much wider than expected from the excited lifetime of 2^13^1 (60 ns) and 2^13^2 (10 ps-10 ns); this is likely caused by laser power broadening. The observed vibronic bands in the H-atom PFY spectrum in Figure 3.2 belong to the $\tilde{A}^2A_1 \leftarrow \tilde{X}^2E_{3/2}$ transition; no signals were identified for the $\tilde{A}^2A_1 \leftarrow \tilde{X}^2E_{1/2}$ transition.

The TOF spectra of the H-atom product in the photodissociation of the CH_3S radical are recorded near the 2^13^2 band at 352.145 nm (Figure 3.3). For identification and subtraction of the background, four types of TOF spectra have been taken: (1) full spectrum, with both the 193-nm radiation on (for CH_3S radical production) and the near-UV photolysis radiation on, plus the Rydberg atom tagging probe laser radiations (121.6 nm + 366.3 nm); (2) radical background spectrum, with the 193-nm radiation on but the near-UV photolysis radiation off, plus the probe laser radiations on (this checks the background due to 121.6-nm photolysis of the CH_3S radical and/or byproducts); (3) precursor background spectrum, with the 193-nm radiation off but the near-UV

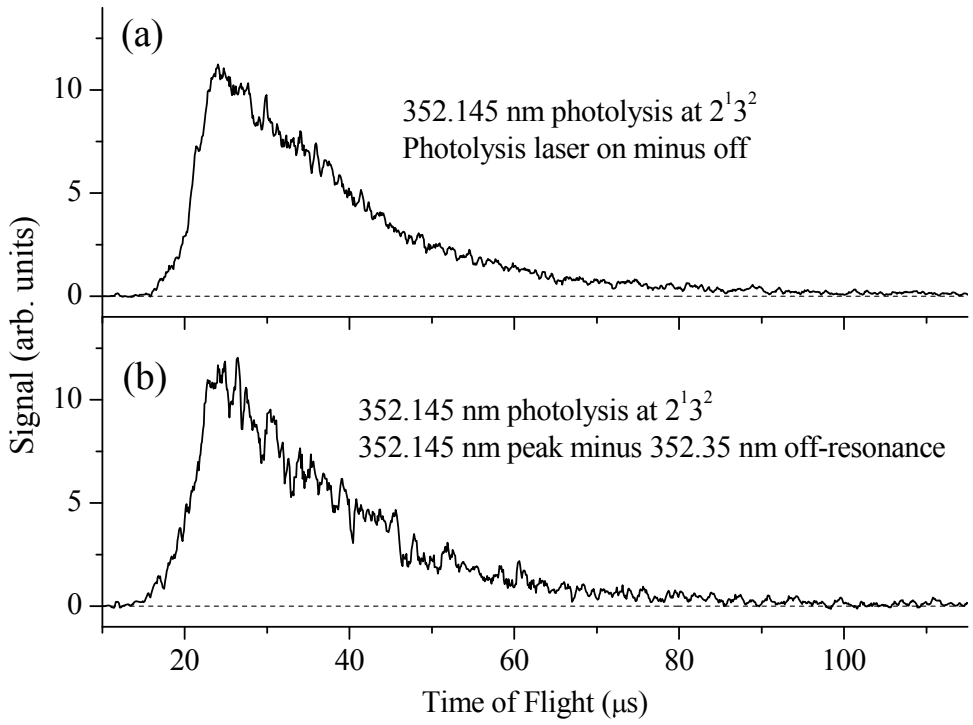

Figure 3.3 H-atom TOF spectrum of the CH_3S photodissociation via the $2^1 3^2$ level of $\tilde{A}^2 A_1$ at 352.145 nm. (a) The spectrum is the net signals with the 193-nm photolysis laser (for CH_3S radical production) on and 352.145-nm photolysis laser (for CH_3S radical photolysis) on minus off. (b) The spectrum is the difference signals of 352.145-nm photolysis laser (at the $2^1 3^2$ peak) minus 352.35 nm (off-resonance background); this approach removes the interference background in the TOF spectrum and ensures that the signals are from the on-resonance $2^1 3^2$ absorption peak of CH_3S. The polarization vector of the 352.145-nm photodissociation radiation is perpendicular ($\theta = 90^o$) to the TOF axis. The H-atom product angular distribution is isotropic with respect to θ (see Figure 3.5).

photolysis radiation on, plus the probe laser radiations; and (4) precursor background spectrum, with both the 193-nm radiation and near-UV photolysis off, but only the probe laser radiations on. It is found that the radical background spectrum (2) is the main background, and the precursor background spectra (3) and (4) are small and can be neglected or cancelled out in the background treatment. Thus the net spectrum is obtained by removing the background in spectrum (2) (with the 193-nm radiation on but the near-UV photolysis off) from the full spectrum (1) (with both the 193-nm radiation and near-UV photolysis on) (Figure 3.3 (a)). This net spectrum represents the H-atom product signals from photodissociation of the CH_3S radical by the near-UV photolysis radiation and removes the contribution from the 121.6 nm Lyman-α probe radiation. In order to verify this net spectrum, another approach is taken. The full spectra are obtained at the $2^1 3^2$ peak of 352.145 nm and off resonance at 352.35 nm. The difference spectrum (on resonance minus off resonance, Figure 3.3 (b)) presents the net signals due to the $2^1 3^2$ peak and effectively removes all the background contributions. This spectrum is essentially the same as the net spectrum in Figure 3.3 (a) obtained by background subtraction, thus supporting the background treatment procedures.

The net H-atom TOF spectrum of the jet-cooled CH_3S photodissociation at 352.145 nm is transformed by direct conversion to product center-of-mass (CM) translational energy distribution $P(E_T)$[28,31] and is shown in Figure 3.4. At the photolysis energy

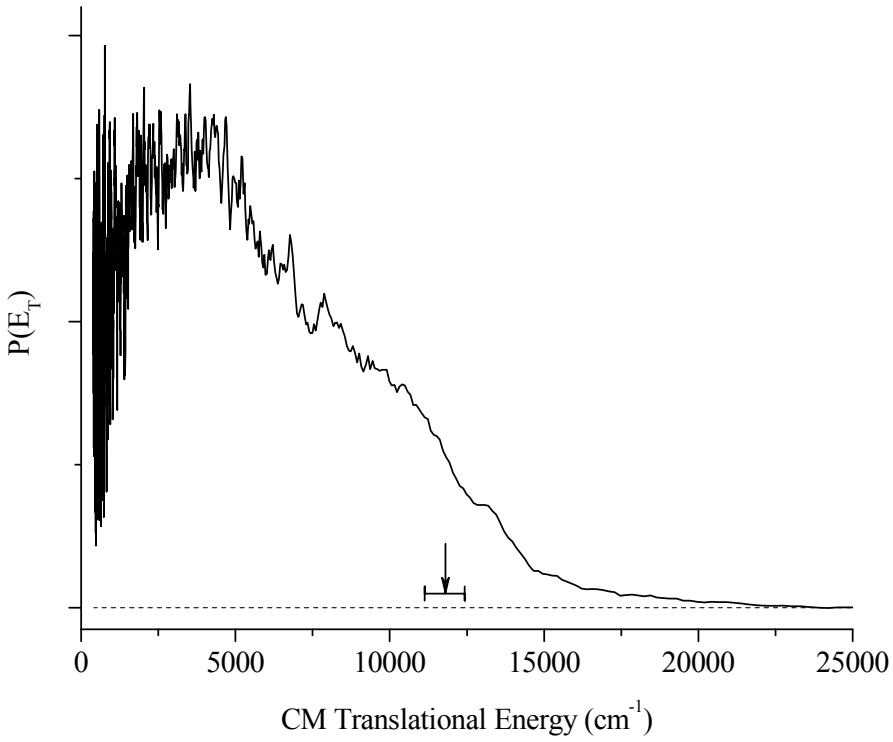

Figure 3.4 Center-of-mass H + H_2CS product translational energy distribution, $P(E_T)$, from 352.145 nm photodissociation of the $2^1 3^2$ state of $CH_3S(\tilde{A}^2A_1)$. The $P(E_T)$ distribution is converted from the TOF spectrum in Figure 3.3 (a). The maximum translational energy of the products from one-photon photodissociation of CH_3S at 352.145 nm is indicated by the range and arrow.

of 352.145 nm, the maximum CM translational energy of the H + $H_2CS(\tilde{X}^1A_1)$ products is 33.7 ± 1.8 kcal/mole, and is indicated by the range and arrow in Figure 3.4. The translational energy release is not repulsive, peaking at ~9 kcal/mole. The translational energy distribution $P(E_T)$ is broad, indicating internally excited $H_2CS(\tilde{X}^1A_1)$ product (note that the electronically excited H_2CS is energetically not possible here, Figure 3.1). The $P(E_T)$ distribution of the H + H_2CS channel is very different from that of the $CH_3(\tilde{X}^2A_2'') + S(^3P_J)$ product channel.[19] For the $CH_3(\tilde{X}^2A_2'') + S(^3P_J)$ product channel, the translational energy release is highly repulsive and the $P(E_T)$ peaks near the maximum available energy,[19] consistent with rapid dissociation on the repulsive $^4A_2$, ^4E, and $\tilde{B}^2A_2$ surfaces after surface crossing and predissociation of the $\tilde{A}^2A_1$ state. The smaller translational energy release in the H + H_2CS products, however, implies that the H + H_2CS channel occurs via a different dissociation mechanism. The $P(E_T)$ of the H + H_2CS channel is consistent with a mechanism in which the electronically excited $\tilde{A}^2A_1$ state undergoes internal conversion to the highly vibrationally excited ground-state $CH_3S(\tilde{X}^2E)$, followed by unimolecular dissociation of the hot CH_3S radical. It is unlikely for the excited $\tilde{A}^2A_1$ state to dissociate directly to the H + H_2CS products. The theoretical study by Cui et al. shows that the $\tilde{A}^2A_1$ state leads to the H atom and excited state $H_2CS(\tilde{a}^3A')$,[23] and this high energy channel is closed in the near-UV photodissociation of CH_3S.

The fastest part in the $P(E_T)$ of the H + H_2CS channel is beyond the energy limit of one-photon dissociation by the near-UV photolysis radiation (Figure 3.4). Several possibilities have been examined. The fastest component is unlikely to come from the 121.6-nm photodissociation of the CH_3S radical or CH_3SSCH_3 precursor, as this contribution is effectively removed or minimized in the background treatments (Figure 3.3 (a) and 3.3 (b)). CH_3 is another product in the photodissociation of CH_3S, and its photolysis by the 121.6-nm probe laser could generate some fast H-atom signals; however, a separate experiment indicates no H-atom signals from the 121.6-nm photolysis of CH_3 (produced from 193-nm photodissociation of acetone). The fast component is not from the hot $CH_3S(\tilde{X}^2E)$ radical, as the photoexcitation is on the $2^1 3^2$ resonance from the vibrationally cold $CH_3S(\tilde{X}^2E)$. It is plausible that the fastest part is due to multiphoton dissociation by the photolysis laser; however, the majority of the H-atom signals are shown to depend linearly on the near-UV photolysis laser power and are from the one-photon photodissociation of CH_3S by the near-UV photolysis radiation. Another source for the fastest H atoms is 121.6-nm photodissociation of the H_2CS product generated in the near-UV dissociation of CH_3S; this contribution cannot be completely removed in the background treatments or on-off resonance subtraction. The upper limit of the average product translational energy in the one-photon

photodissociation of the CH_3S $\tilde{A}^2A_1$ $2^1 3^2$ level at 352.145 nm is estimated to be ~15.5 kcal/mole, with $\langle f_T \rangle \leq 0.46$.

The angular distribution of the H-atom product from the CH_3S photodissociation is examined with the photolysis laser polarization parallel and perpendicular to the flight path, respectively. The 352.145-nm TOF spectra with the parallel and perpendicular polarization are identical, showing an isotropic H-atom product angular distribution (Figure 3.5). The photofragment angular distribution is described by[32] $I(\theta) = (1/4\pi)[1 + \beta P_2(\cos\theta)]$, where β is the anisotropy parameter ($-1 \leq \beta \leq 2$), θ is the angle between the electric vector of the polarized laser radiation **E** and the recoiling velocity vector of the H-atom product (the direction of detection or the TOF axis), and $P_2(\cos\theta)$ is the second Legendre polynomial. The anisotropy parameter β for the H-atom product channel in the photodissociation of CH_3S via the $2^1 3^2$ band is $\beta \approx 0$ (Figure 3.5). The isotropic angular distribution indicates that the H-atom elimination in CH_3S via the $2^1 3^2$ band occurs on a time scale longer than the rotational period (~ ps) of the CH_3S parent. This dissociation time scale, as well as the small kinetic energy release and the shape of the products' $P(E_T)$ distribution, supports the mechanism of internal conversion of the $\tilde{A}^2A_1$ state to the ground state $\tilde{X}^2E$ and subsequent unimolecular dissociation of the ground state $CH_3S(\tilde{X}^2E)$ to $H + H_2CS$.

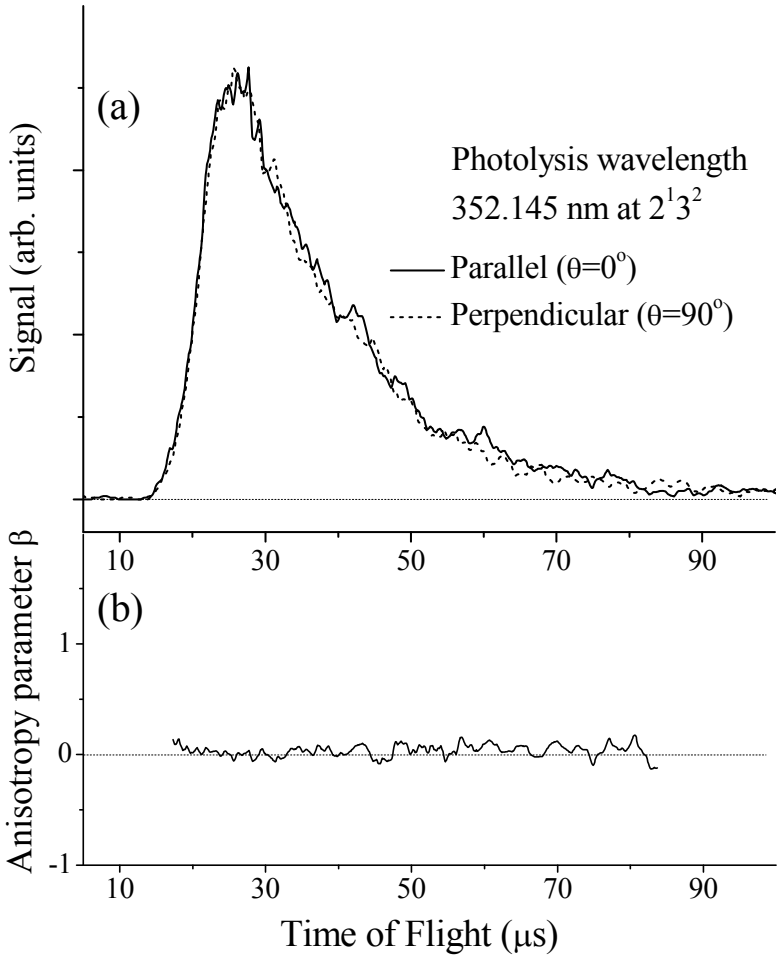

Figure 3.5 H-atom product angular distribution. (a) H-atom TOF spectra with the 352.145 nm photodissociation radiation parallel ($\theta = 0^o$) and perpendicular ($\theta = 90^o$) to the TOF axis. (b) Anisotropic parameter β.

Miller and co-workers first suggested in their fluorescence depletion study that the lower vibronic levels 3^2, $2^1 3^1$, and $2^1 3^2$ of the CH_3S $\tilde{A}^2A_1$ state may dissociate predominantly via the H + H_2CS product channel.[16] Their conclusion was based on two observations: (1) the 3^2, $2^1 3^1$, and $2^1 3^2$ vibronic levels decay via fast nonradiative processes, as the 3^2 and $2^1 3^1$ bands have short lifetimes in the LIF spectra, and the $2^1 3^2$ band is missing in the LIF spectrum and is observed only in the fluorescence depletion and four-wave mixing spectra;[16,17] and (2) the $2^1 3^1$ and $2^1 3^2$ vibronic levels do not dissociate to the CH_3 + $S(^3P_J)$ products, as the $2^1 3^1$ and $2^1 3^2$ bands were not observed in the CH_3 + $S(^3P_J)$ PFY spectrum by Neumark and co-workers, while the 3^2 band was rather weak.[19] These observations indicate that other nonradiative decay processes (other than the CH_3 + $S(^3P_J)$ channel) should be responsible for the fast decay of the 3^2, $2^1 3^1$, and $2^1 3^2$ levels of the $\tilde{A}^2A_1$ state, and the internal conversion of the $\tilde{A}^2A_1$ state followed by the H + H_2CS product channel is the likely decay pathway for these three states. Our current study shows that the $2^1 3^1$ and $2^1 3^2$ vibronic levels of the $\tilde{A}^2A_1$ state indeed dissociate exclusively to the H + H_2CS products, and this work characterizes the translational energy release and angular distribution of this H-atom channel.

The basic idea of the near-UV photodissociation of CH_3S via the $\tilde{A}^2A_1$ state can be described as follows (Figure 3.1). Upon excitation to the $\tilde{A}^2A_1$ state, two nonradiative decay processes, in addition to the radiative decay of the $\tilde{A}^2A_1$ state, are

involved. At energy above two quanta of ν_3 ($2^1 3^n$ and 3^n, n≥3), the $\tilde{A}^2A_1$ state couples efficiently with and predissociates via the three repulsive states $^4A_2$, ^4E, and $\tilde{B}^2A_2$, leading to the CH_3 + $S(^3P_J)$ products with a repulsive energy release, as observed by Neumark and co-workers.[19] As such, the $2^1 3^3$ and 3^n (n=3-6) states examined in this study do not dissociate to H + H_2CS (Figure 3.2), but instead to CH_3 + $S(^3P_J)$.[19]. The predissociation process is mode selective; the C-S stretching ν_3 of the $\tilde{A}^2A_1$ state is shown to be the promoting mode for the CH_3 + S predissociation,[16-19] while the umbrella mode ν_2 is not as efficient. In the region of two or less quanta of ν_3 excitation (such as 3^2 and those with some energy in the umbrella quanta, $2^1 3^1$ and $2^1 3^2$), the effective energy along the C-S coordinate is lowered to be closer to the minimum of the $\tilde{A}^2A_1$ state potential energy surface and is thus further away from the crossing seams with the three repulsive states (Figure 3.1); therefore, the CH_3+ S predissociation via the three repulsive states is less efficient, and the second nonradiative decay process, internal conversion of the $\tilde{A}^2A_1$ state to the ground state $\tilde{X}^2E$ and subsequent unimolecular dissociation to H + H_2CS, could become significant.[16] This second nonradiative decay channel occurs in a narrow window of energy and vibronic modes. In this window, the effective energy in the C-S stretching mode is below the crossing seams between the $\tilde{A}^2A_1$ and the three repulsive states, and thus the internal conversion of the $\tilde{A}^2A_1$ state and the subsequent H + H_2CS pathway are competitive with the predissociation of the $\tilde{A}^2A_1$ state to CH_3 +

$S(^3P_J)$, while this window is also above the minimum of the $\tilde{A}^2A_1$ state and in a region where the $\tilde{A}^2A_1$ state couples efficiently with the ground state $\tilde{X}^2E$ to compete with the radiative decay process (where the ground vibrational level of the $\tilde{A}^2A_1$ state has a lifetime of ~1000 ns). The nature of the internal conversion mechanism is not clear yet, but in the region of the 2^13^1 and 2^13^2 levels of the $\tilde{A}^2A_1$ state, the coupling between the excited state $\tilde{A}^2A_1$ and the ground state $\tilde{X}^2E$ should be stronger than the predissociation of the $\tilde{A}^2A_1$ state and its spin-orbit couplings with the three repulsive states $^4A_2$, ^4E, and $\tilde{B}^2A_2$, and also the internal conversion is fast enough to compete with the fluorescence decay. Indeed, at the even lower level 2^13^0, no H-atom product is observed in this work (Figure 3.2) and this peak is also missing in the $CH_3 + S(^3P_J)$ PFY spectrum by Neumark and co-workers,[19] consistent with the increasing importance of the fluorescence decay at the lowest vibronic levels of the $\tilde{A}^2A_1$ state. Further theoretical study will help reveal more insights of the nonradiative decay of the $\tilde{A}^2A_1$ state via internal conversion.

There are two steps in the H-atom product channel: the internal conversion of the $\tilde{A}^2A_1$ state to the ground state $\tilde{X}^2E$, followed by unimolecular decomposition of the vibrationally hot CH_3S radical in the $\tilde{X}^2E$ ground state to the $H + H_2CS(\tilde{X}^1A_1)$ products. The initial competition of the nonradiative decay pathways is between internal conversion of the $\tilde{A}^2A_1$ state to the ground state and predissociation of the $\tilde{A}^2A_1$ state

via the repulsive states, and this competition determines the nonradiative decay mechanisms. The unimolecular dissociation after internal conversion of the $\tilde{A}^2A_1$ $2^1 3^1$ and $2^1 3^2$ states is not in direct competition with the predissociation of the $\tilde{A}^2A_1$ $2^1 3^3$ and 3^n (n=3-6) states, but rather it is the subsequent step that follows the internal conversion. The observed $P(E_T)$ distribution with the modest translational energy release is consistent with the unimolecular dissociation process from the ground-state hot radical, and the isotropic H-atom product angular distribution also supports this mechanism.[33,34] The $P(E_T)$ distribution peaks at ~9 kcal/mole, indicating an exit channel barrier of the similar magnitude.[33,34] Note that in the similar system CH_3O, a 4 kcal/mole exit channel barrier for the H+ H_2CO product channel has been suggested.[35]

3.4 Conclusions

Photodissociation dynamics of the jet-cooled CH_3S radical via the $\tilde{A}^2A_1 \leftarrow \tilde{X}^2E$ transition is studied in the region of 344-362 nm. The H + $H_2CS(\tilde{X}^1A_1)$ product channel in the photodissociation of CH_3S $\tilde{A}^2A_1$ is observed directly by the H-atom PFY spectrum and photofragment translational spectroscopy. This H-atom product channel appears in a narrow window of energy and selective modes: the two vibronic levels of $\tilde{A}^2A_1$, $2^1 3^1$ and $2^1 3^2$, dissociate to the H + H_2CS products, while the others in the vicinity

($2^1 3^3$ and 3^n, n=3-6) to CH_3 + S(^3P_J). The H + $H_2CS(\tilde{X}^1A_1)$ product translational energy release is not repulsive and peaks at ~9 kcal/mole. The H-atom product angular distribution is isotropic. The H-atom photodissociation mechanism is consistent with internal conversion of the excited $\tilde{A}^2A_1$ state to the $\tilde{X}^2E$ ground state and subsequent unimolecular dissociation on the ground state $\tilde{X}^2E$ to the H + $H_2CS(\tilde{X}^1A_1)$ products.

References

(1) Charlson, R. J.; Lovelock, J. E.; Andreae, M. O.; Warren, S. G. *Nature* **1987**, *326*, 655.

(2) Bates, T. S.; Lamb, B. K.; Guenther, A.; Dignon, J.; Stoiber, R. E. *Journal of Atmospheric Chemistry* **1992**, *14*, 315.

(3) Ravishankara, A. R.; Rudich, Y.; Talukdar, R.; Barone, S. B. *Philosophical Transactions of the Royal Society of London Series B-Biological Sciences* **1997**, *352*, 171.

(4) Tyndall, G. S.; Ravishankara, A. R. *International Journal of Chemical Kinetics* **1991**, *23*, 483.

(5) Callear, A. B.; Connor, J.; Dickson, D. R. *Nature* **1969**, *221*, 1238.

(6) Callear, A. B.; Dickson, D. R. *Transactions of the Faraday Society* **1970**, *66*, 1987.

(7) Ohbayashi, K.; Akimoto, H.; Tanaka, I. *Chemical Physics Letters* **1977**, *52*, 47.

(8) Endo, Y.; Saito, S.; Hirota, E. *Journal of Chemical Physics* **1986**, *85*, 1770.

(9) Engelking, P. C.; Ellison, G. B.; Lineberger, W. C. *Journal of Chemical Physics* **1978**, *69*, 1826.

(10) Janousek, B. K.; Brauman, J. I. *Journal of Chemical Physics* **1980**, *72*, 694.

(11) Moran, S.; Ellison, G. B. *Journal of Physical Chemistry* **1988**, *92*, 1794.

(12) Suzuki, M.; Inoue, G.; Akimoto, H. *Journal of Chemical Physics* **1984**, *81*, 5405.

(13) Black, G.; Jusinski, L. E. *Journal of the Chemical Society-Faraday Transactions Ii* **1986**, *82*, 2143.

(14) Hsu, Y. C.; Liu, X. M.; Miller, T. A. *Journal of Chemical Physics* **1989**, *90*, 6852.

(15) Chiang, S. Y.; Lee, Y. P. *Journal of Chemical Physics* **1991**, *95*, 66.

(16) Pushkarsky, M. B.; Applegate, B. E.; Miller, T. A. *Journal of Chemical Physics* **2000**, *113*, 9649.

(17) Liu, C. P.; Matsuda, Y.; Lee, Y. P. *Journal of Chemical Physics* **2003**, *119*, 12335.

(18) Liu, C. P.; Reid, S. A.; Lee, Y. P. *Journal of Chemical Physics* **2005**, *122*, 124313.

(19) Bise, R. T.; Choi, H.; Pedersen, H. B.; Mordaunt, D. H.; Neumark, D. M. *Journal of Chemical Physics* **1999**, *110*, 805.

(20) Fournier, R.; Depristo, A. E. *Journal of Chemical Physics* **1992**, *96*, 1183.

(21) Curtiss, L. A.; Nobes, R. H.; Pople, J. A.; Radom, L. *Journal of Chemical Physics* **1992**, *97*, 6766.

(22) Hsu, C. W.; Liao, C. L.; Ma, Z. X.; Tjossem, P. J. H.; Ng, C. Y. *Journal of Chemical Physics* **1992**, *97*, 6283.

(23) Cui, Q.; Morokuma, K. *Chemical Physics Letters* **1996**, *263*, 54.

(24) Marenich, A. V.; Boggs, J. E. *Journal of Chemical Theory and Computation* **2005**, *1*, 1162.

(25) Wilson, S. H. S.; Ashfold, M. N. R.; Dixon, R. N. *Journal of Chemical Physics* **1994**, *101*, 7538.

(26) Zheng, X. F.; Song, Y.; Wu, J. Z.; Zhang, J. S. *Chin. J. Chem. Phys.* **2007**, *20*, 377.

(27) Schnieder, L.; Meier, W.; Welge, K. H.; Ashfold, M. N. R.; Western, C. M. *Journal of Chemical Physics* **1990**, *92*, 7027.

(28) Xu, K. S.; Amaral, G.; Zhang, J. S. *Journal of Chemical Physics* **1999**, *111*, 6271.

(29) Amaral, G.; Xu, K. S.; Zhang, J. S. *Journal of Chemical Physics* **2001**, *114*, 5164.

(30) Zhou, W. D.; Yuan, Y.; Chen, S. P.; Zhang, J. S. *Journal of Chemical Physics* **2005**, *123*.

(31) Zhang, J. S.; Dulligan, M.; Wittig, C. *Journal of Physical Chemistry* **1995**, *99*, 7446.

(32) Zare, R. N. *Mol. Photochem.* **1972**, *4*, 1.

(33) Osborn, D. L.; Choi, H.; Mordaunt, D. H.; Bise, R. T.; Neumark, D. M.; Rohlfing, C. M. *Journal of Chemical Physics* **1997**, *106*, 3049.

(34) Mordaunt, D. H.; Osborn, D. L.; Neumark, D. M. *Journal of Chemical Physics* **1998**, *108*, 2448.

(35) Geers, A.; Kappert, J.; Temps, F.; Wiebrecht, J. W. *Journal of Chemical Physics* **1993**, *99*, 2271.

CHAPTER 4

Ultraviolet photodissociation dynamics of the propargyl radical

ABSTRACT

Ultraviolet (UV) photodissociation dynamics of jet-cooled propargyl (C_3H_3) radical is studied in the photolysis wavelength region of 230 to 250 nm using high-n Rydberg atom time-of-flight (HRTOF) and resonance enhanced multiphoton ionization (REMPI) techniques. In this wavelength region, the photofragment yield (PFY) spectra of the H + C_3H_2 product channel are obtained using propargyl chloride, allene, and propyne as precursors of the C_3H_3 radicals, and they have a broad peak centered near 240 nm and are in good agreement with the previous UV absorption spectrum of C_3H_3 by Fahr et al. The H + C_3H_2 product translational energy distributions, $P(E_T)$'s, are obtained from all the three precursors and are essentially the same. The $P(E_T)$ distributions peak at ~5 kcal/mole, and the fraction of average translational energy in the total excess energy, $\langle f_T \rangle$, is ~ 0.3. The H-atom product angular distribution is isotropic, with the anisotropy parameter $\beta \approx 0$. The dissociation mechanism is consistent with internal conversion of the electronically excited propargyl followed by unimolecular decomposition on the ground state. Our study supports the previously observed UV absorption spectrum of propargyl near 240 nm by Fahr et al. and is in general agreement with the results in the

UV photodissociation of propargyl by Chen group and Neumark group, but disagrees with the recent theoretical calculations by Eisfeld.

4.1 Introduction

Propargyl radical ($HCCCH_2$) is a prototypical conjugated hydrocarbon radical, and it is also an important intermediate in hydrocarbon combustion, particularly in its recombination reaction to form the first aromatic ring and in the subsequent production of polycyclic aromatic hydrocarbons (PAH) and soot.[1-4] Consequently, the electronic states and spectroscopy of the C_3H_3 radical have been studied extensively by both theories and experiments.

The propargyl radical was first identified by Farmer and Lossing in a mass spectrometric study that determined its ionization potential.[5] The first electronic absorption spectrum of the C_3H_3 radical was recorded by Ramsay and Thistlethwaite in the photolysis of propargyl bromide, propargyl chloride, methyl acetylene, allene, and other compounds.[6] A series of diffuse bands were found between 290 to 345 nm, and the diffuseness of the bands was attributed to predissociation in the excited state and gave an upper limit of 86.0 kcal/mole for the bond dissociation energy (BDE) of the propargyl radical. This near ultraviolet (UV) absorption spectrum was later confirmed in the region between 280 and 370 nm by matrix isolation spectroscopy[7,8] and cavity ringdown spectroscopy[9] using various precursors. This near-UV absorption band was assigned to the dipole-allowed $2^2B_1 \leftarrow \tilde{X}\ ^2B_1$ transition.[8,10]

The second absorption band of the propargyl radical was first reported in the UV range of 230-300 nm by Fahr et al.[11] The UV absorption spectra of the propargyl radicals produced from the C_3H_3Cl and C_3H_3Br precursors by both photolysis and abstraction reaction were nearly identical. The UV absorption band had a broad peak with a maximum at 242 nm and was much stronger than the first absorption band in the near-UV region. The UV band was assigned to the dipole-allowed $3^2B_1 \leftarrow \tilde{X}^2B_1$ transition.[10,11] This UV absorption spectrum was confirmed by H-atom product action spectrum in the UV photodissociation of the propargyl radical by Deyerl et al.[12] However, this strong UV absorption band of propargyl was questioned, as it was not observed in a later study using halogen-free precursors,[13] and thus was attributed to chlorine and bromine adducts of propargyl halides (such as $C_3H_3Cl_2$).[9,14] Fahr and Laufer then rechecked the UV absorption spectra between 220-350 nm of transient species generated from 193-nm photolysis of allene, propyne and 2-butyne.[15] A strong band around 240 nm and a weaker band in the 330 nm region were identified, similar to their early results using the C_3H_3Cl and C_3H_3Br precursors.[11] This recent study indicated that the strong UV absorption feature peaking at 242 nm may not be due to the halogenated adducts and the spectrum using the allene precursor was most likely from the propargyl radical.[15]

The electronic states of the propargyl radical have also been examined by theoretical studies.[10,11,16-19] The propargyl radical, $HCCCH_2$, was shown to be the lowest energy structure of C_3H_3, and the molecular geometry and electronic structure of the $\tilde{X}^2B_1$ ground state of propargyl were examined.[16,17] The lowest two doublet excited states were identified by Honjou et al. to be 1^2B_2 and 2^2B_1 in C_{2v} symmetry, and they relax to lower energy states $1^2A''$ and $2^2A'$ in C_s symmetry, respectively.[16,19] The transition from the $\tilde{X}^2B_1$ ground state to the lowest excited state 1^2B_2 is dipole forbidden, while the near-UV absorption band in the region of 280 to 370 nm was assigned to the dipole-allowed $2^2B_1 \leftarrow\tilde{X}^2B_1$ transition.[10] The next higher excited states are 2^2B_2 and 3^2B_1.[10,11,16,17] Fahr et al. assigned the strong absorption feature peaking at 242 nm to the dipole-allowed $3^2B_1 \leftarrow\tilde{X}^2B_1$ transition based on their calculated vertical excitation energy.[11] However, Eisfeld recently calculated the four electronically excited states 1^2B_2, 2^2B_1, 2^2B_2, and 3^2B_1 and the absorption spectrum of C_3H_3 in the region from 180-400 nm.[10,17] While the dipole-allowed $2^2B_1 \leftarrow\tilde{X}^2B_1$ band agreed well with the near-UV absorption spectrum, the dipole-allowed $3^2B_1 \leftarrow\tilde{X}^2B_1$ transition was predicted to be a much weaker band with the vertical energy near 220 nm and the dipole-forbidden $2^2B_2 \leftarrow X^2B_1$ transition was also very weak and peaked near 260 nm.[10,17] It was then concluded that the strong UV absorption observed near 242 nm by Fahr et al.,[11] as well as

the H-atom product signals and the H-atom action spectrum observed by Deyerl et al.,[12] was not due to the propargyl radical but some other transient species.[10]

Photodissociation of the propargyl radical has been investigated by both theory and experiments.[12,20-23] The potential energy diagram of the ground electronic state[18-20] and the dissociation pathways for the H atom and H_2 elimination channels of C_3H_3 are shown in Figure 4.1. There are three H atom loss channels to different C_3H_2 isomers that are close in energy and one H_2 loss channel,

$$H_2CCCH(\tilde{X}^2B_1) + h\nu \rightarrow c\text{-}C_3H_2(^1A_1) + H, \qquad \Delta H_{rxn,0} = 82.4 \text{ kcal/mole}$$

$$\rightarrow HCCCH(^3B) + H, \qquad \Delta H_{rxn,0} = 94.9 \text{ kcal/mole}$$

$$\rightarrow H_2CCC(^1A_1) + H, \qquad \Delta H_{rxn,0} = 95.9 \text{ kcal/mole}$$

$$\rightarrow HCCC(^2A') + H_2, \qquad \Delta H_{rxn,0} = 84.0 \text{ kcal/mole}$$

The energetics are based on the recent high-level theoretical calculations by Nguyen et al.,[19,20] which are in reasonable agreements with the thermochemistry data.[19,20,24] The UV photodissociation of propargyl was first studied in the secondary photolysis of hot propargyl radical produced in 193 nm photodissociation of allene.[21] Both the C_3H_2 + H and C_3H + H_2 product channels were identified, with a branching ratio of 0.94 to 0.04. The photofragment translational energy distribution $P(E_T)$ showed that the product translational energy release of the C_3H_2 + H channel was modest, peaking at ~12.5 kcal/mole and with the fraction of average kinetic energy in the total excess energy, $\langle f_T \rangle$,

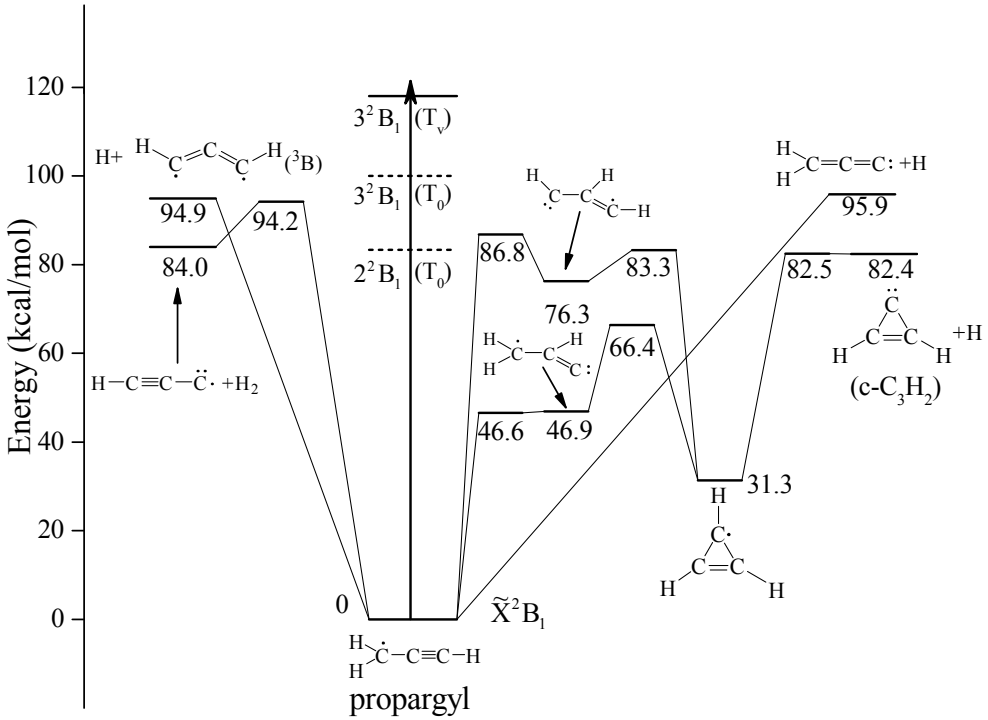

Figure 4.1 Potential energy diagram of the C_3H_3 system. The three H-atom dissociation pathways and the H_2 elimiantion pathway are shown in the figure. The energetics and pathways are based on the theoretical calculations in Ref. 19. The energies of the C_3H_3 excited states are based on Refs. 8,10,11,16,17. The adiabatic energy T_0 of 2^2B_1 is from Wyss et al.,[8] and T_0 and vertical energy T_v of 1^2B_1 are estimated from the absorption spectrum by Fahr et al.[11]

being ~0.31. The UV photodissociation dynamics of jet-cooled propargyl radical produced from flash pyrolysis of propargyl bromide was examined in the region of 240 to 265 nm by Chen group.[12] The H atom product from the C_3H_2 + H channel was ionized by 1+1' (Lyman-α + 365 nm radiation) resonance enhanced multiphoton ionization (REMPI) and then detected by a time-of-flight mass spectrometer (TOFMS). The H-atom Doppler profile was measured to provide the $P(E_T)$ distribution that peaked at ~ 2.5 kcal/mole and with $\langle E_T \rangle$ ~ 6.2 kcal/mole and $\langle f_T \rangle$ ~ 0.22. The shape of the $P(E_T)$ distribution is close to that in a prior distribution,[12] and indicated a mechanism in which the electronically excited propargyl decayed via internal conversion to the ground state then followed by unimolecular decomposition. A statistical analysis of the energetics suggested that the dominant channel in the photodissociation of propargyl radical at 242 nm was the formation of cyclopropenylidene, *c*-C_3H_2 + H. Using partially deuterated propargyl radical, H_2CCCD, nearly complete isotopic scrambling was observed, and the dissociation mechanism was shown to proceed via an initial 1,2 H-shift followed by cyclization.

Nguyen et al. investigated theoretically the photodissociation of propargy radical at photon energies of 193 and 242 nm, assuming that the electronically excited propargyl radical underwent internal conversion to the ground electronic state followed by unimolecular decomposition.[19,20] RRKM rate constant calculations for the various

dissociation channels were carried out on the potential energy surface obtained with high-level theory.[19,20] The calculated product branching ratios for the C_3H_2 + H and C_3H + H_2 channels at 193 nm were in good agreement with the experimental measurements in the secondary photolysis of C_3H_3.[21] The product branching ratios at 242 nm were calculated to be 90.2% for HCCCH(^{3}B) + H, 5.1% for *c*-C_3H_2($^1A_1$) + H, 1.6% for H_2CCC($^1A_1$) + H, 3.0% for HCCC(^{2}A') + H_2, and 0.1% for CH($^2\Pi$) + C_2H_2. The HCCCH(^{3}B) + H were predicted to be the major products while the *c*-C_3H_2 + H channel, although energetically most favorable H loss channel, was calculated to be minor. These results were in disagreement with those from the experimental study by Chen group,[12] where *c*-C_3H_2 + H was shown to be the major product.

Most recently, Neumark group investigated the photodissociation of jet-cooled propargyl radical and its perdeuterated isotopologue using photofragment translational spectroscopy.[23] The propargyl radicals were produced from 193 nm photolysis of allene, and photodissociated at 248 nm. Both the H loss and H_2 loss dissociation channels were characterized by observations of the counterparts C_3H_2 and C_3H, respectively. The branching ratio for H loss/H_2 loss was 97.6/2.4 ± 1.2, in agreement with the value of 96.9/3.0 from the RRKM calculations by Nguyen et al.[20] The average translational energy, $\langle E_T \rangle$, for the H loss and H_2 loss channels were 5.7 and 15.3 kcal/mole, respectively. The $P(E_T)$ distribution for the H atom loss was similar to that by the Chen

group and the prior distribution[12] and peaked at 1.8 kcal/mole. The $P(E_T)$ distributions of the photofragments indicated that internal conversion to the ground electronic state occurred following the excitation to the excited electronic state, and that the ground-state propargyl dissociated to H + C_3H_2 via a loose transition state without an exit channel barrier while to H_2 + C_3H via a tight transition state with an exit barrier.[23] The decomposition of hot ground state propargyl was also studied in the secondary dissociation of propargyl radical produced in 157 nm photodissociation of propargyl chloride.[22] Both the H loss and H_2 loss were observed via the secondary fragments of propargyl. Based on the difference between the translational energy distributions of the Cl atom and the propargyl radical fragments, a propargyl dissociation energy (or barrier) of 71.5 (+5/-10) kcal/mole was suggested,[22] which is more than 10 kcal/mole lower than the theoretical and thermochemistry values.[19]

This current work investigates the UV photodissociation dynamics of jet-cooled propargyl radical in the photolysis wavelength region of 230-250 nm using three different precursors, propargyl chloride, allene, and propyne. This study aims to probe the photodissociation dynamics of C_3H_3 via the 3^2B_1 excited state, confirm the origin of the previously observed broad absorption peak of propargyl near 240 nm and the H-atom photodissociation,[11,12] and search for the possible absorption bands of propargyl that were predicted by the theory.[10] Propargyl chloride, allene, and propyne provide both halogen

and halogen-free precursors of propargyl, and moreover they have less absorption at 230-250 nm (thus less interference to the propargyl radical photodissociation) than the propargyl bromide precursor.[11,12] The H-atom photofragment yield (PFY) spectra of propargyl radicals produced from the three precursors are measured using the REMPI technique, and are compared with the UV absorption spectrum of C_3H_3 near 240 nm in order to confirm this broad absorption of propargyl. The product translational energy and angular distributions for the H + C_3H_2 channel are obtained by detecting the H-atom products with the high-*n* Rydberg atom time-of-flight (HRTOF) technique. Our approach is complementary to the previous studies by Chen group and Neumark group;[12,23] the HRTOF technique has a higher resolution than the H-atom Doppler profile, and HRTOF also has less interference for the low kinetic energy products compared to the H-atom Doppler profile and the TOF spectra of the heavy fragment C_3H_2 (which recoiled little from the parent C_3H_3 beam). By directly providing reliable $P(E_T)$ and angular distributions using the three different precursors, the photodissociation signals and dynamics of the propargyl radical are further established. In order to compare with the recent theory,[10] REMPI detection of C_3H_3, in addition to the H-atom PFY spectra, is also attempted in the region of 220-280 nm.

4.2 Experimental

The HRTOF technique and experimental setup have been described previously.[25-27] A pulsed C_3H_3 radical beam was generated by photolyzing propargyl chloride (purity ≥ 98%), allene (purity ≥ 99.7%), or propyne (purity ≥ 99.7%) precursors seeded in Ar or He (at ~ 4% concentration and a total pressure of 120 kPa),[9,11,15] with the 193-nm radiation of an ArF excimer laser that was focused in front of the pulse nozzle. The C_3H_3 radicals produced from the photolysis were entrained in the seeded beam and subsequently cooled by supersonic expansion. The radical beam was collimated at 2.8 cm downstream by a 1-mm diameter skimmer into a high-vacuum chamber; at 4.6 cm further downstream of the skimmer, the C_3H_3 radical beam was crossed with a slightly focused UV photolysis laser radiation (at 230-250 nm, 1.5-3 mJ/pulse, linewidth ~ 0.3 cm^{-1}). The absolute photolysis laser wavelength was monitored by a wavemeter (Burleigh WA-4500). The polarization of the photolysis radiation was rotated by a Fresnel-Rhomb achromatic $\lambda/2$ plate for product angular distribution measurements. The H atoms produced from the C_3H_3 photodissociation were tagged by two-color resonant excitation (121.53 nm + 366.36 nm), i.e., from 1^2S to 2^2P via the H-atom Lyman-α transition and then further to a high-*n* Rydberg state. A small fraction of the radiatively metastable Rydberg H atoms drifted with their nascent velocities toward a microchannel plate (MCP) detector that is

positioned perpendicular to the molecular beam, and were field-ionized in front of the detector and detected. The nominal flight length was 37.1 cm,[27] which was calibrated by 230-250 nm photodissociation of HBr [with the spin-orbit splitting of Br($^2P_{3/2}$) and Br ($^2P_{1/2}$)]. The ion signals were amplified by a fast pre-amplifier, and the H-atom TOF spectra were recorded and averaged by using a multichannel scaler. The H-atom TOF spectra were accumulated with ~10^5 laser firings. Typically four types of HRTOF spectra were taken (including the full spectrum and three background spectra), and the net HRTOF spectra from the UV photolysis of the C_3H_3 radical were obtained after proper background subtraction (see the Results section for more details).

The H-atom photofragment yield (PFY) spectra (i.e., action spectra) were measured using two methods. The first method involved integrating the net HRTOF spectra (after the background removal) as a function of photolysis wavelength. The second method was based on collecting the H-atom product REMPI signals as a function of photolysis wavelength. The H-atom REMPI experiment was conducted in the same HRTOF instrument, and the photolysis and REMPI ionization lasers were the same as in the HRTOF experiment. Upon photodissociation by the UV laser radiation in the range of 230-250 nm, the product H atoms were detected by 1 + 1' REMPI, with one Lyman-α photon resonantly exciting the H atom from 1^2S to 2^2P and a UV photon at ~364 nm ionizing the H atom. The photolysis and REMPI probe laser delay time was fixed at 15

ns. The H^+ ions were extracted and accelerated in the linear TOF mass spectrometer, and were detected by the MCP detector. The mass-resolved ion current signal (at m/z = 1, H^+) was amplified by a preamplifier, recorded in a digital storage oscilloscope, and transferred to the computer. At each UV wavelength, typically 512 laser shots were averaged. Two types of REMPI signal were recorded, (i) with the 193-nm radiation on (for the propargyl radical production), the UV photolysis radiation on, and the REMPI probe lasers on; and (ii) background with the 193-nm radiation off, but the UV photolysis radiation and the REMPI probe lasers on. The PFY spectra were the net H-atom REMPI signals with the background (ii) removed. The photolysis laser power was normalized for the H-atom PFY spectra.

REMPI spectra of the propargyl radical were also searched by using a (1 + 1) scheme. The UV laser radiation in the region of 220-280 nm was focused with a f.l. ~ 20 cm lens onto the propargyl radicals beam, and the m/z =39 peak was directly monitored using TOFMS.

4.3 Results

The TOF spectra of the H-atom product in the UV photodissociation of C_3H_3 were recorded in the photolysis wavelength region of 230-248 nm, with the photolysis laser

polarization parallel and perpendicular to the flight path, respectively. In order to identify the origins of the H-atom signals and to establish procedures for background subtraction, four types of TOF spectra were taken: (1) full spectrum, with both the 193-nm radiation on (for C_3H_3 radical production) and the UV photolysis radiation on (for C_3H_3 radical photodissociation), plus the Rydberg atom tagging probe laser radiations (121.6 nm + 366.3 nm); (2) precursor background spectrum, with the 193-nm radiation off but the UV photolysis radiation on, plus the probe laser radiations; (3) radical production background spectrum, with the 193-nm radiation on but the UV photolysis radiation off, plus the probe laser radiations; and (4) probe laser background spectrum, with both the 193-nm radiation off and the UV photolysis radiation off, but only the probe radiations on. The background spectra (3) and (4) were observed to be essentially identical, with only a small and broad background in the flight time range of interest, and were thus negligible. The precursor background spectrum (2) represents the main background, i.e., contributions from photolysis of the C_3H_3Cl, allene, and propyne precursors by the UV photolysis radiation. The net HRTOF spectra from the UV photolysis of the C_3H_3 radical are obtained by removing the main background (2) from the full spectrum (1). The net H-atom product TOF spectra at 240-nm photolysis wavelength with 2 mJ/mm^2 UV radiation intensity are shown in Figure 4.2, where panel (a), (b), and (c) represent those using propargyl chloride, allene, and propyne as the C_3H_3

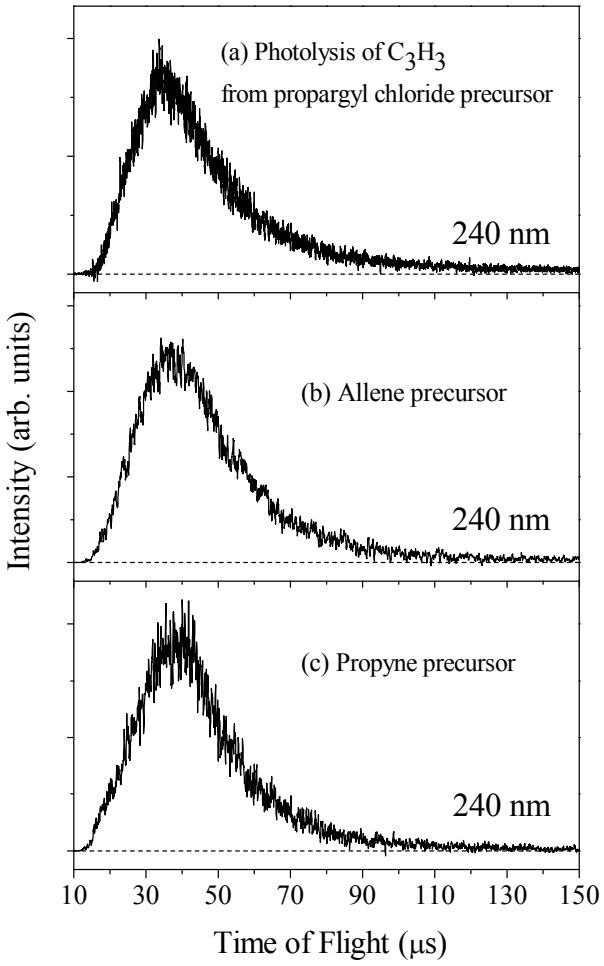

Figure 4.2 H-atom TOF spectra in the 240-nm photodissociation of jet-cooled C_3H_3, produced from 193-nm photolysis of (a) propargyl chloride, (b) allene, and (c) propyne. The spectra are shown as the net signals with the 193-nm photolysis laser (for radical production) on minus off. The polarization vector of the 240 photodissociation radiation is parallel ($\theta = 0^{o}$) to the TOF axis. The photolysis radiation power intensity is 2 mJ/mm^2.

radical precursor, respectively. These three TOF spectra using the C_3H_3Cl, allene, and propyne precursors are essentially the same, with a broad peak in the region of 15-120 μs and peaking around 35 μs. These common features support that the H-atom signals come from the same species, the propargyl radical. Several previous studies of the photodissociation of propargyl chloride at 193 nm reported the propargyl production, $C_3H_3Cl + h\nu \rightarrow C_3H_3 + Cl$, as the main channel.[2,11,28] The 193-nm photolysis of allene and propyne have also been studied before,[15,21,29-31] and the $H + C_3H_3$ product channel was shown to be the primary process in both allene and propyne photolysis. Indeed, 193-nm photolysis of propargyl chloride, allene, and propyne have been used previously for propargyl radical productions.[11,15]

To further confirm that the observed HRTOF spectra are originated from the photolysis of propargyl radicals, two types of action or PFY spectra, integral HRTOF intensity as a function of photolysis wavelength and H-atom PFY spectrum using H-atom (1+1') REMPI, were obtained. The resulting H-atom action spectra from 230-250 nm are scaled at 240 nm and plotted in Figure 4.3. The full diamonds and open diamonds represent the HRTOF action spectra using propargyl chloride and allene as the precursors, respectively. The full triangles are for the H-atom REMPI action spectrum using the propargyl chloride precursor. For comparison, the UV absorption spectrum previously reported by Fahr et al. is plotted as open circles and dashed line in Figure 4.3.[11] The

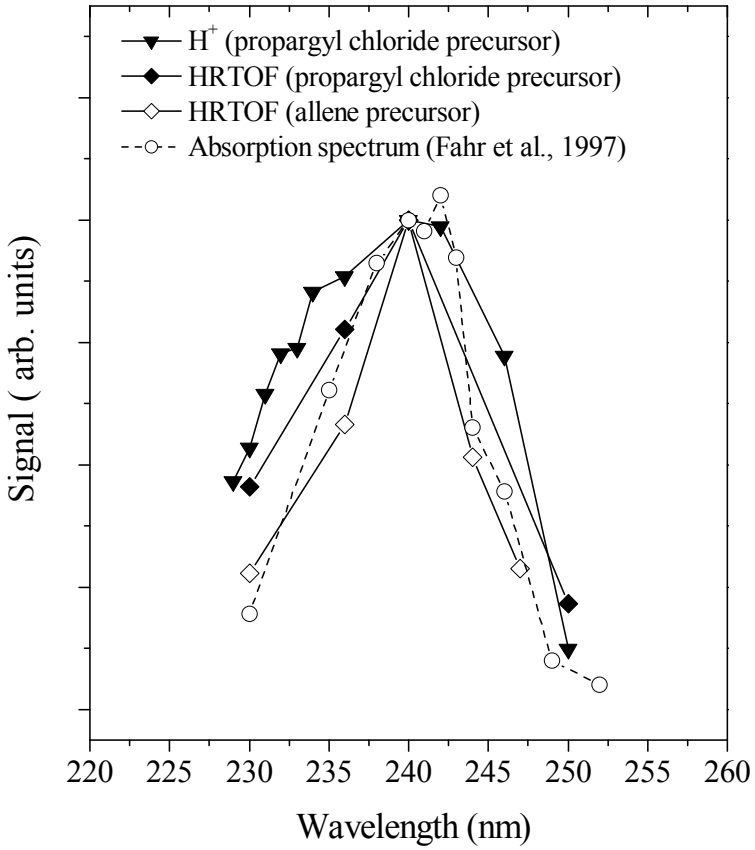

Figure 4.3 H-atom product yield (PFY) spectra as a function of photolysis excitation energy in the region of 229-250 nm. Diamonds represent the integrated HRTOF signals: ◆ for the C_3H_3Cl precursor and ◇ for the allene precursor. Triangles (▼) represent the H-atom (1 + 1') REMPI signals for the C_3H_3Cl precursor. Open circles and dashed line are the absorption spectrum taken from Ref. 11. The photolysis laser power is normalized for the PFY spectra. The PFY spectra and the absorption spectrum are scaled at 240 nm.

H-atom PFY spectra from HRTOF and REMPI agree well with each other, as well as with the UV absorption spectrum by Fahr et al. This comparison provides further confirmation that the H-atom signals originate from the photodissociation of propargyl radicals and that the strong UV absorption feature peaking at 240 nm is due to the propargyl radical. Attempts were also made to search for the REMPI spectra of propargyl by directly monitoring the m/z = 39 peak via the (1+1) scheme. As the ionization potential of propargyl is 8.68 eV,[32,33] two photons at $\lambda \leq 285$ nm are sufficient to ionize the propargyl radical. However, no C_3H_3 REMPI spectrum was found near 240 nm, likely due to the fast decay of the electronically excited propargyl (in a time scale of 50 ± 10 fs)[34] and the dissociation of the propargyl radical. In addition, both H-atom PFY spectra and m/z = 39 C_3H_3 REMPI spectra were searched for the theoretically predicted dipole-allowed $3^2B_1 \leftarrow \tilde{X}^2B_1$ transition near 220 nm and dipole-forbidden $2^2B_2 \leftarrow \tilde{X}^2B_1$ transition near 260 nm,[10,17] but no C_3H_3 absorption features were identified in these two regions, in disagreement with the theory.

The net H-atom TOF spectra of the jet-cooled C_3H_3 photodissociation are transformed to the total center-of-mass (CM) translational energy distributions, $P(E_T)$'s. The CM translational energy of products, E_T, is converted from the H-atom flight time t_H using the following equation:

$$E_T = \left(1 + \frac{m_H}{m_{C_3H_2}}\right) E_H + \frac{m_H}{m_{C_3H_2}} E_{C_3H_3} = \frac{1}{2} m_H \left(1 + \frac{m_H}{m_{C_3H_2}}\right) \left(\frac{L}{t_H}\right)^2 + \frac{m_H}{m_{C_3H_2}} E_{C_3H_3},$$

where E_H and $E_{C_3H_3}$ are the laboratory translational energies of the H-atom photofragment and the C_3H_3 radical, respectively, and L is the flight length. The second term $\left(\frac{m_H}{m_{C_3H_2}} E_{C_3H_3}\right)$ is due to the C_3H_3 radical motion in the molecular beam that is orthogonal to the TOF path, but it is negligible compared with the first term (products' CM translation). In this experiment, the correction due to $\left(\frac{m_H}{m_{C_3H_2}} E_{C_3H_3}\right)$ is ~ 0.04 kcal/mole, based on an estimated beam velocity of 560 m/s for the C_3H_3/Ar gas mixture. The resulted $P(E_T)$ distributions of the 240-nm photodissociation of C_3H_3 using (a) proparpyl chloride, (b) allene, and (c) propyne precursors are shown in Figure 4.4. These $P(E_T)$'s are relative probability distributions (scaled to the peak height). These CM translation energy distributions for the H + C_3H_2 products from the three different precursors of C_3H_3 agree well with each other. The $P(E_T)$ distributions have a broad feature that peaks at low energy around 5 kcal/mole and extends to large translational energy of ~55 kcal/mole. The bond dissociation energy (BDE) for the lowest energy H-atom loss channel, *c*-C_3H_2 + H, is calculated to be 82.4 kcal/mole in high-level theory,[19] while the heat of reaction for this dissociation channel is estimated to be 86.2 kcal/mole at 0 K and 85.6 kcal/mole at 298 K, respectively, based on thermochemistry

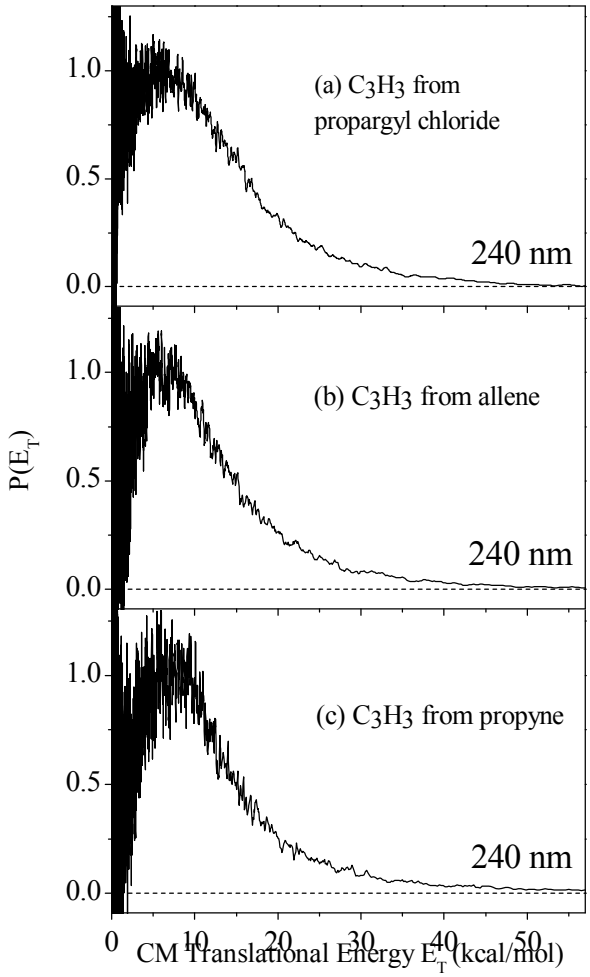

Figure 4.4 Center-of-mass product translational energy distributions, $P(E_T)$, of the H + C_3H_2 product channel from 240-nm photodissociation of C_3H_3. These distributions are converted from the H-atom TOF spectra shown in Figure 4.2. Figure (a), (b), and (c) correspond to the propargyl chloride, allene, and propyne precursor, respectively, for producing the C_3H_3 radicals.

and theoretical calculations.[19,20,24] Our preliminary study on the near-UV photolysis of C_3H_3 in the region of 278-357 nm and its H-atom PFY spectrum[35] indicate that the H-atom loss threshold is around 82.8 ± 0.3 kcal/mole, in good agreement with the 82.4 kcal/mole BDE. Based on this theoretical BDE value of 82.4 kcal/mole, the maximum translational energy release of the H loss channel in one-photon photodissociation of propargyl at 240 nm is 36.7 kcal/mole.

Figure 4.5 shows the translational energy distribution and the power dependence at 240 nm with the propargyl chloride precursor. The $P(E_T)$ distributions here are converted directly from the H-atom TOF spectra, without being normalized to the integrated area or peak height. The main peak at ~5 kcal/mole in the $P(E_T)$ distribution has a linear dependence on the photolysis laser power, in agreement with a one-photon photodissociation process, $C_3H_3 + h\nu \rightarrow H + C_3H_2$. However, in the high translational energy region (from ~37-55 kcal/mole), it increases nonlinearly with the increase of the photolysis power intensity (from 1 to 2 mJ/mm^2), which indicates that these fast H-atom signals, although relatively small, come from multiphoton photodissociation of C_3H_3. Indeed, the maximum translational energy release in the $P(E_T)$ distribution at the lower photolysis power intensity of 1 mJ/mm^2 is close to 36.7 kcal/mole, consistent with the expected upper limit in a one-photon process and the C-H bond dissociation energy of C_3H_3. While the $P(E_T)$ distributions presented here are obtained by direct conversion of

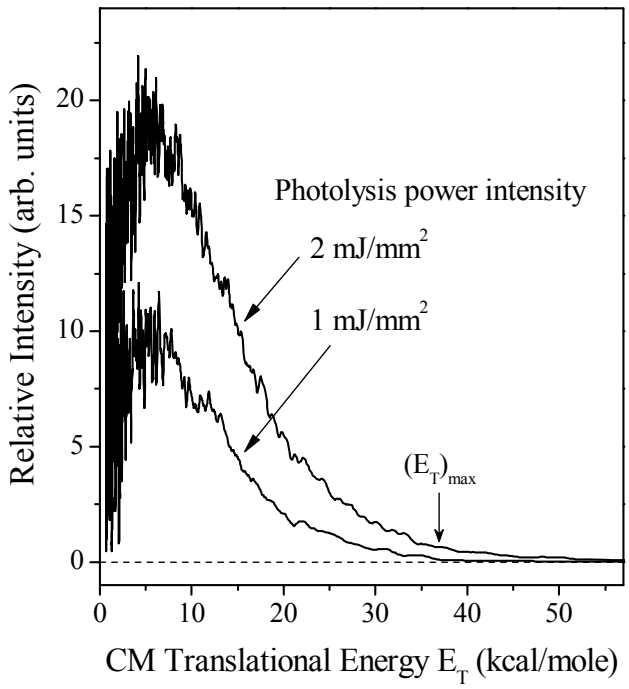

Figure 4.5 Photolysis laser power dependence at 2 mJ/mm^2 and 1 mJ/mm^2. The spectra are directly converted from the H-atom TOF and are normalized to the same number of laser shots. Propargyl chloride precursor was used. The vertical arrow indicates the maximum translational energy release for a one-photon photodissociation of C_3H_3 at 240 nm.

the TOF spectra, they can also be derived from modeling the TOF spectra in a forward-convolution procedure.[36,37] In this procedure, the H-atom TOF spectrum is calculated by using a trial CM translational energy distribution $P(E_T)$ convoluted with the instrument and molecular beam functions. The calculated TOF spectrum is iteratively optimized by comparison with the experimental spectrum and readjustment of the trial $P(E_T)$ distribution until an optimized $P(E_T)$ distribution is reached. The forward-convolution approach is particularly helpful when the TOF spectra are noisy, such as those at low photolysis power. Figure 4.6 shows the fitted TOF spectrum of the 240-nm photodissociation of C_3H_3 at low photolysis energy intensity 1mJ/mm^2 (from Figure 4.5) and the optimized $P(E_T)$ distribution.

The $P(E_T)$ distributions from the direct conversion are used to calculate the average translation energy releases, $\langle E_T \rangle$, up to the one-photon maximum E_T. For example, $\langle E_T \rangle$ at 240 nm is 11.1, 11.2, and 11.5 kcal/mole for the propargyl chloride, allene, and propyne precursor, respectively. The $\langle E_T \rangle$ values averaged from the three precursors are listed as a function of photolysis wavelength in Table 4.1. These $\langle E_T \rangle$ values are the upper limits due to the small contributions from the multiphoton processes. Alternatively, $\langle E_T \rangle$ can be calculated from the $P(E_T)$ distributions derived from the forward-convolution of TOF spectra at low photolysis power. For example, $\langle E_T \rangle$ at 240 nm is calculated to be 10.0 kcal/mole for the 1mJ/mm^2 photolysis power (Figure 4.5 and

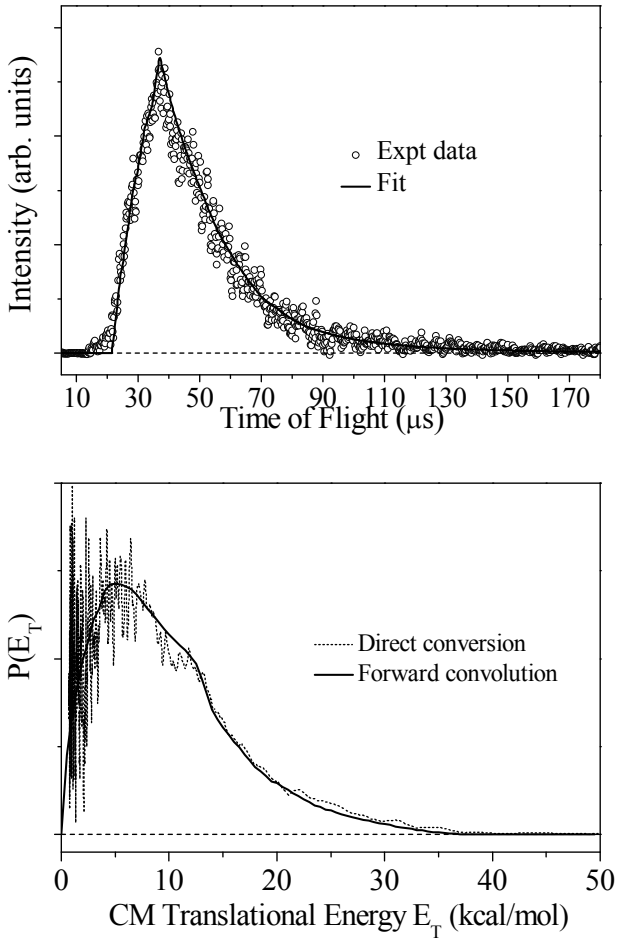

Figure 4.6 240-nm photodissociation of C_3H_3 (from propargyl chloride precursor) at low photolysis laser power 1 mJ/mm^2. (a) Forward-convolution fitting of the TOF spectrum. (b) CM translational energy distribution optimized in the forward-convolution procedure compared with that derived from direct conversion. See text for more details.

Table 4.1. Photolysis wavelength, translational energy release, and anisotropy parameter β in the UV photodissociation of the propargyl radical. The energy unit is kcal/mole.

Photolysis Wavelength (nm)	$(E_T)_{max}$[a]	$\langle E_T \rangle$[b]	$\langle f_T \rangle$[c]	β
230	41.8	13.8	0.33	0.0
236	38.7	12.5	0.32	0.0
240	36.6	11.3	0.31	0.0
244	34.7	10.4	0.30	0.0
248	32.8	9.5	0.29	0.0

[a] Maximum translational energy release, derived from the corresponding photon energy and the dissociation of propargyl to the H + *c*-C_3H_2 products, $D_0(H\text{-}C_3H_2)$ = 82.4 kcal/mole. The $D_0(H\text{-}C_3H_2)$ is in the range of 82.4-86.2 kcal/mole, estimated from both theories and thermochemistry data.[19,20,24]

[b] Average translational energy release calculated from the experimental $P(E_T)$ distributions and averaged over the three precursors (whenever available).

[c] Fraction of average translational energy release in the total available energy.

4.6), and this $\langle E_T \rangle$ value is at the lower limit. The $\langle E_T \rangle$'s in Table 4.1 could be over estimated by up to ~10%. As shown in Table 4.1, $\langle E_T \rangle$ increases with the increasing photolysis photon energy and excess energy, while the fraction of $\langle E_T \rangle$ in the total available energy, $\langle f_T \rangle$, increases only slightly between 0.29 and 0.33 and is close to a constant. The $P(E_T)$ peak position is at ~5 kcal/mole and does not change significantly with the photolysis wavelength. For all the wavelengths, the $P(E_T)$ peak position is smaller than the average translational energy release.

The H-atom product angular distributions in the UV photodissociation of propargyl are examined using linearly polarized laser radiation. Figure 4.7 (upper two panels) illustrates the H-atom TOF spectra from the C_3H_3 photodissociation by the polarized 240-nm photolysis radiation, with the polarization direction parallel and perpendicular to the TOF axis. The two TOF spectra are identical, indicating an isotropic H atom product angular distribution. The linearly polarized light preferentially excites those radicals with their electronic transition dipole moment parallel to the electric $\boldsymbol{E}$ of the polarized laser radiation. The photofragment angular distribution is given by $I(\theta) = (1/4\pi)[1 + \beta P_2(\cos\theta)]$, where β is the anisotropy parameter ($-1 \leq \beta \leq 2$), θ is the angle between the electric vector of the polarized laser radiation $\boldsymbol{E}$ and the recoiling velocity vector of the H-atom product (the direction of detection or the TOF axis), and $P_2(\cos\theta)$ is the second Legendre polynomial.[38] Using this equation and the H-atom TOF spectra at

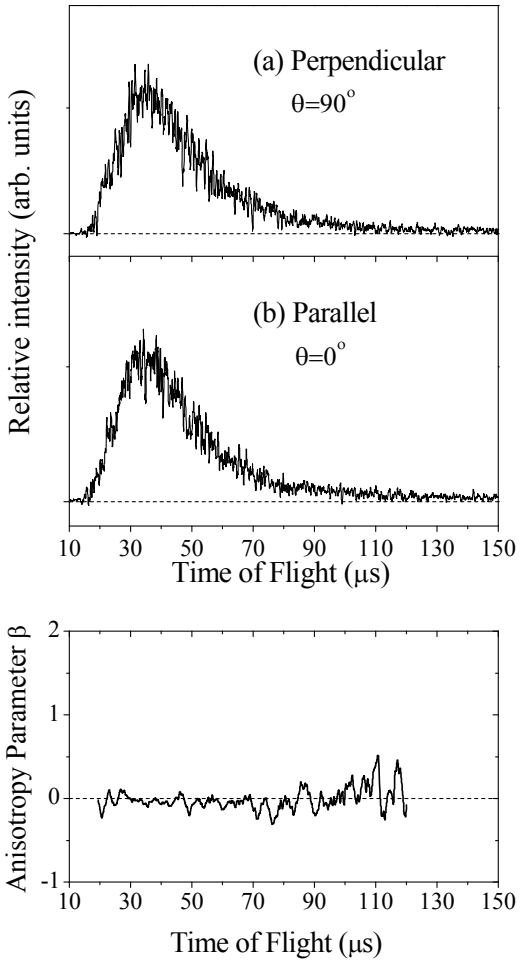

Figure 4.7 H-atom TOF spectra of 240-nm photodissociation of C_3H_3, with the polarization **E** vector of the photolysis radiation (a) perpendicular ($\theta = 90^{o}$) and (b) parallel ($\theta = 0^{o}$) to the TOF axis. The 240 nm radiation power intensity was 2 mJ/mm^2. The signals have been normalized to the same photolysis power and laser shots. Anisotropy parameter β is plotted as H-atom time of flight. The β parameter stays very close to the limit of an isotropic angular distribution.

240 nm, an anisotropy parameter $\beta \approx 0$ is derived for the H+ C_3H_2 product channel in the C_3H_3 photodissociation (Figure 4.7). For other photolysis wavelengths in this UV region, the β parameters of the summed H-atom signals in the H-atom TOF spectra are calculated and listed in Table 4.1; these β parameters are essentially the same within experimental error and are at the limit of $\beta = 0$ for isotropic angular distribution. The isotropic product angular distributions are consistent with a dissociation time scale of more than one rotational period of the C_3H_3 radical (> ps).[38]

The H-atom yield time profile in the UV photolysis of propargyl is also monitored as a function of the photolysis laser and probe laser delay time (Figure 4.8), which provides a measurement for the microcanonical rate of unimolecular dissociation of propargyl. In this time profile, the initial rise indicates the rate for H-atom production from the propargyl radical, while the decay of signal after the peak is simply due to flight out of the H atoms from the interaction region between the photolysis and probe laser pulses.[12] The H-atom signal monotonically decays after the initial rise within the 10 ns overlapping window of the photolysis and probe lasers (i.e., the time resolution of the 7 ns pump and probe pulses in this experiment). As a calibration system, UV photolysis of SH radical, which has a fast dissociation time of *sub*-pico sec in a direct repulsive dissociation,[27] was checked, and the delay time profile of its H-atom product was recorded. The H-atom time profile from propargyl is very similar to that of the SH

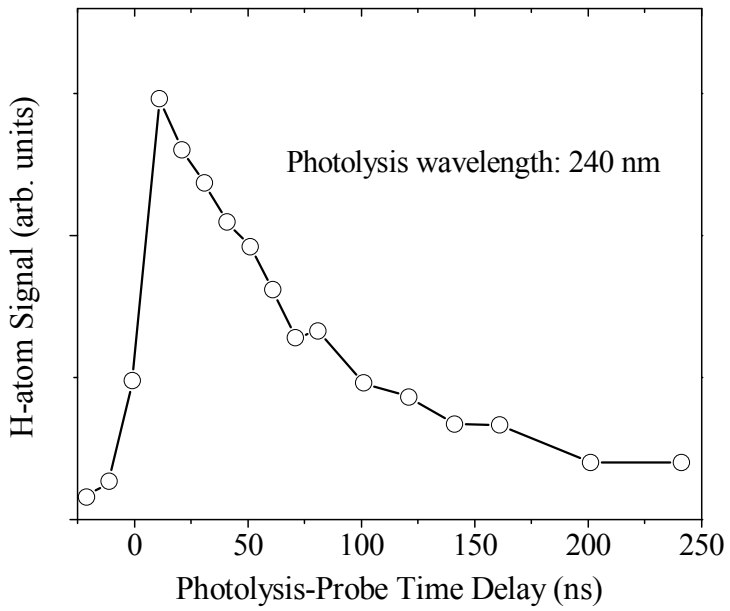

Figure 4.8 H-atom product signal as a function of photolysis and probe laser delay time. Propargyl chloride is the precursor. The photolysis wavelength is 240 nm. The signals are obtained by H-atom product REMPI spectra at the various photolysis-probe delay time.

radical. This indicates that the H-atom products from propargyl rise to the maximum within the 10 ns time resolution of this experiment, and the dissociation time scale of propargyl at 240 nm is < 10 ns or the dissociation rate is > 10^8/sec. The dissociation time of propargyl observed in this study is much shorter than the ~100 ns appearance time of H atoms (i.e., dissociation rate of 1.3 × 10^7/sec at 242 nm) by Chen and co-workers.[12]

4.4 Discussion

The main motivations for this study are to probe the UV photodissociation dynamics of C_3H_3, confirm the previously observed broad absorption peak and the H-atom photodissociation signals of C_3H_3 near 240 nm,[11,12] and examine the theoretical predications of the electronic excited states and UV absorption spectrum of C_3H_3 by Eisfeld.[10] The broad UV absorption band of propargyl at 242 nm was first reported by Fahr et al. using the C_3H_3Cl and C_3H_3Br precursors,[11] and it was then supported by the H-atom PFY spectrum in the UV photodissociation of propargyl using the C_3H_3Br precursor,[12] the more recent absorption study by Fahr et al. using the allene, propyne and 2-butyne precursors,[15] and the most recent 248-nm photodissociation study of C_3H_3 using the allene precursor.[23] This strong broad UV absorption band, however, was questioned

previously by absorption experiments,[9,13,14] which attributed it to the chlorine and bromine adducts of propargyl halides. Furthermore, this strong UV absorption band was not confirmed by the high-level multireference configuration interaction (MRCI) calculations by Eisfeld,[10,17] which showed that for propargyl radical in the region between 180 nm and 280 nm both the dipole-allowed $3^2B_1 \leftarrow \tilde{X}^2B_1$ transition and dipole-forbidden $2^2B_2 \leftarrow \tilde{X}^2B_1$ transition were weak bands with vibronic structures, peaking near 220 nm and 260 nm, respectively.[10] Instead, the strong broad absorption feature at 242 nm was suggested to be due to vinylidene carbene (H_2CCC) or chlorine adduct of propargyl chloride.[10] The conclusion from the theory[10] questioned the validity of the H-atom photodissociation signals in the study by Chen group.[10,12] Our current experiment, nevertheless, indicates that the propargyl radical is responsible for the observed strong broad absorption peak near 242 nm.[11] Our H-atom PFY spectra derived from both H-atom TOF spectra and REMPI mass spectra using the three different precursors, propargyl chloride, allene and propyne, are in very good agreement with the absorption spectrum by Fahr et al. (Figure 4.3) and with the H-atom action spectrum by Chen group,[12] supporting that they are originated from the propargyl absorption and photodissociation. The H-atom TOF spectra and $P(E_T)$ distributions in Figure 4.2 and 4.4 for the photodissociation of propargyl using the three different precursors are essentially the same, further supporting that they are from the propargyl radical.

Meanwhile, no H-atom PFY spectra or C_3H_3 REMPI spectra are identified for the theoretically predicted $3^2B_1 \leftarrow \tilde{X}^2B_1$ transition (peaking near 220 nm) and $2^2B_2 \leftarrow \tilde{X}^2B_1$ transition (peaking near 260 nm).[10,17] Therefore, this study supports the strong broad absorption spectrum of propargyl near 242 nm by Fahr et al.[11] and the H-atom photodissociation signals of C_3H_3 near 240 nm by Deyerl et al.,[11,12] and disagrees with the theoretical predications of the UV absorption spectrum and the 2^2B_2 and 3^2B_1 electronic excited states of C_3H_3 by Eisfeld.[10,17]

The CM product translational energy distributions of the H + C_3H_2 channel from the three different precursors have very similar shape and peak position. All of these distributions are not repulsive and peak at a low kinetic energy of ~5 kcal/mole. In general, these distributions are similar to those obtained by the previous C_3H_3 photodissociation studies, detection of C_3H_2 in the secondary photolysis of C_3H_3 at 193 nm by Jackson et al.,[21] H-atom Doppler profile in the photodissociation at 242 nm by Chen group,[12] and TOF measurements of C_3H_2 fragment in the photodissociation at 248 nm by Neumark group.[23] Our $P(E_T)$ distributions are consistent with a dissociation mechanism in which internal conversion of propargyl from the electronic excited state to the ground state, followed by unimolecular dissociation on the highly vibrationally excited ground state,[20] as suggested previously by Chen group[12] and Neumark group.[23]

The $P(E_T)$ distribution at 193 nm by Jackson et al. peaks at ~12.5 kcal/mole with $\langle f_T \rangle$ ~ 0.31 (using BDE of 82.4 kcal/mole for the lowest energy *c*-C_3H_2 + H channel), while our $P(E_T)$'s at 240 nm peak at ~5 kcal/mole with comparable $\langle f_T \rangle$ in the range of 0.29-0.33. The $P(E_T)$ distribution at 193 nm was obtained from the secondary photolysis of hot propargyl radical and thus is less reliable than those from the primary photodissociation of jet-cooled propargyl radicals. On the other hand, the $P(E_T)$ distribution at 242 nm from Chen group peaks at ~2.5 kcal/mole with $\langle f_T \rangle$ ~ 0.17 (assuming BDE of 82.4 kcal/mole), and the $P(E_T)$ at 248 nm from Neumark group peaks at 1.8 kcal/mole with $\langle f_T \rangle$ ~ 0.17 (using BDE of 82.4 kcal/mole). The last two $P(E_T)$ distributions, peaking near $E_T = 0$, are close to that predicted in a prior distribution,[12] and are consistent with the mechanism of H loss with no exit channel barrier.[12,23] Our $P(E_T)$ distributions peak at higher energy of ~5 kcal/mole with larger $\langle f_T \rangle$ ~ 0.3. While our $P(E_T)$'s are in general consistent with a statistical dissociation mechanism of C_3H_3 in its ground state, they have a larger E_T release than expected in the prior distribution, and it is not clear the cause for the small difference between our results and those by Chen (from Doppler profile of H atoms) and Neumark (from TOF spectra of C_3H_2 fragments). The H-atom REMPI Doppler profile has a much lower resolution than HRTOF, and it is difficult to extract reliable $P(E_T)$ information at the center of the Doppler profile, where components of all the H-atom signals in the direction of Doppler probe are added up, and the Doppler

profile could be contaminated by slow H atom background peaking at the center of profile. The TOF spectra of C_3H_2, due to the heavy mass of the C_3H_2 fragments and thus little recoils from the C_3H_3 parent beam, were measured at small angles from the beam, and could potentially be interfered in the low E_T part by the $C_3H_2^+$ ionization fragment from the C_3H_3 radical in the beam. In the HRTOF setup, the light H atoms are detected perpendicular to the C_3H_3 beam direction. The detection efficiency for the very slow H atoms decreases due to the reduced detector solid angle, and the slowest ones (E_T ~ 0.4 kcal/mole in the He beam and 0.04 kcal/mole in the Ar beam) eventually miss the detector. For an isotropic product distribution and for a pure geometrical correction, the detection efficiency can be corrected by dividing a factor of $\left[1-(v_P/v_H)^2\right]^{3/2}$, where v_P and v_H are the parent beam velocity and the H atom recoil velocity, respectively.[39] The correction for the Ar beam is rather small due to the smaller v_P ~ 560 m/s; for example, the correction for the detection efficiency is estimated to be 10% at E_T = 0.6 kcal/mole, 3% at 2 kcal/mole, and 1% at 5 kcal/mole. Most of the $P(E_T)$ distributions in this study were obtained using the Ar beam, and the observed ~5 kcal/mole peak in the $P(E_T)$'s is reliable and is not caused by a shift due to the detection efficiency. Furthermore, the $P(E_T)$'s from 240-nm photodissociation of allene in He and Ar carrier gas are compared in this study and are shown to nearly identical (within the noise, particularly at the low E_T), also supporting our $P(E_T)$ distributions. Therefore, it is concluded that the ~5 kcal/mole

peak and higher $\langle f_T \rangle$ observed in our experiments are not significantly affected by the detection efficiency of slow H atoms and are thus reliable.

The average translational energy release, $\langle E_T \rangle$, in the photodissociation of propargyl increases with the increasing photon energy and excess energy (Table 4.1), while $\langle f_T \rangle$ increases slightly from 0.29 to 0.33. The fact that $\langle f_T \rangle$ stays nearly constant when the excess energy increase from 33-42 kcal/mole is largely consistent with the statistical unimolecular dissociation. As the total excitation energy increases from 115 to 124 kcal/mole, the overall dissociation rate of propargyl in its unimolecular decomposition on the ground electronic state increases (from ~1.7×10^{10}/sec for the fastest dissociation channel, HCCCH(^{3}B) + H, at 240 nm, estimated by the RRKM calculations),[20] and thus the lifetime of the highly vibrationally C_3H_3 in its ground electronic state is shortened. The small increase of $\langle f_T \rangle$ could also indicate that energy randomization is less complete and the energy redistribution toward each degree of freedom of the H + C_3H_2 products becomes less statistical, when the lifetime of the vibrationally excited ground electronic state C_3H_3 after internal conversion becomes shorter.

The $P(E_T)$ distributions do not allow us to differentiate the three possible H + C_3H_2 product channels, *c*-C_3H_2($^1A_1$) + H, HCCCH(^{3}B) + H, and H_2CCC($^1A_1$) + H, as discussed in the previous study by Neumark group.[23] The propargyl BDE of 82.4 kcal/mole is for the lowest energy channel, *c*-C_3H_2 + H. As shown in Figures 4.4-4.6, the $P(E_T)$

distributions extend to the maximum possible E_T for the *c*-C_3H_2 + H channel in a one-photon dissociation process of propargyl, while the next higher energy channel (also the dominant channel predicted by the RRKM calculations),[20] HCCCH(^{3}B) + H, should appear at 12.5 kcal/mole lower than the maximum E_T. The $P(E_T)$ distributions clearly show the *c*-C_3H_2 + H dissociation channel, while the two other H-loss channels, HCCCH(^{3}B) + H and $H_2CCC(^1A_1)$ + H, could also contribute in the photodissociation process. As shown in the potential energy surface in Figure 4.1, both the HCCCH(^{3}B) + H and $H_2CCC(^1A_1)$ + H channels are simple C-H bond rapture via loose transition states with no exit channel barriers,[18,19] while the *c*-$C_3H_2(^1A_1)$ + H channel also proceeds via a barrierless H-atom loss from the *c*-C_3H_3 intermediate after isomerization of propargyl over a 66.4 kcal/mole barrier or a higher barrier of 86.8 kcal/mole.[19] The later pathway has an overall barrier of 4.4 kcal/mole relative to the *c*-$C_3H_2(^1A_1)$ + H dissociation products.[19] However, the ~5 kcal/mole peak and $\langle f_T \rangle$ in our $P(E_T)$ distributions that are higher than those in the studies by Chen group and Neumark group,[12,23] as well as that in the prior distribution,[12,23] could not be explained by this barrier, as the lower isomerization pathway via the lower barrier of 66.4 kcal/mole dominates the isomerization of propargyl to the *c*-C_3H_3 intermediate,[20] and furthermore the final step to the *c*-C_3H_2 + H dissociation via the *c*-C_3H_3 intermediate is through a loose transition state without exit channel barrier.

The angular distributions of the H-atom product from the UV photodissociation of propargyl are shown to be isotropic (Figure 4.7), with the anisotropy parameter $\beta \sim 0$ from 230-248 nm (Table 4.1). This isotropic angular distribution indicates that the UV photodissociation of propargyl occurs at a time scale longer than the rotational period of the C_3H_3 radical (> ps). This isotropic distribution and the dissociation time scale are also consistent with the dissociation mechanism which is internal conversion to the vibrationally hot ground electronic state, followed by the dissociation on the ground electronic state. In this time scale, isomerization of propargyl to the *c*-C_3H_3 intermediate could readily occur before its dissociation to H + *c*-C_3H_2.[20] In the H-atom yield time profile (Figure 4.8), our data indicate that at the UV photoexcitation energy of 119.0 kcal/mole (240 nm), the H-loss dissociation time of propargyl is < 10 ns, and the microcanonical rate of unimolecular dissociation is > 10^8/sec. This dissociation rate is much faster than that of 1.3×10^7/sec at 242 nm observed by Chen and co-workers.[12] The lower rate of ~10^6-10^7/sec (to the H + *c*-C_3H_2 products) could be modeled using the RRKM calculations, assuming that the vibrational frequencies of propargyl were scaled by a factor of 0.71 to account for the effects of anharmonicity and that the dissociation energy to H + *c*-C_3H_2 was 90 kcal/mole.[12] However, the RRKM rate calculations on a high-level potential energy surface by Nguyen et al., using their calculated vibrational frequencies of the propargyl system and BDE of 82.4 kcal/mole for *c*-C_3H_2 + H,

predicted an overall dissociation rate of ~1 × 10^9/sec to *c*-C_3H_2 + H;[20] and the rate to HCCCH(^{3}B) + H and $H_2CCC(^1A_1)$ + H were calculated to be 1.7 × 10^{10}/sec and ~3 × 10^8/sec, respectively. These rates are much higher than those given in the previous study by Chen and co-workers.[12] The range of the dissociation time scale of propargyl in our study, from a few ps to less than 10 ns, is more consistent with the RRKM rates calculated by Nguyen et al.[20]

4.5 Conclusion

The H-atom product channel in the UV photodissociation of jet-cooled propargyl is studied in the wavelength region of 230 to 250 nm using HRTOF and REMPI techniques. The PFY spectra of the H + C_3H_2 product channel obtained using the propargyl chloride, allene, and propyne precursors have a broad peak near 240 nm and are in good agreement with the UV absorption spectrum of C_3H_3. The H + C_3H_2 product translational energy distribution peaks at ~5 kcal/mole, with $\langle f_T \rangle \sim 0.3$. The H-atom product has an isotropic angular distribution. The dynamic information indicates that the UV photodissociation mechanism of propargyl is internal conversion of the electronically excited propargyl followed by unimolecular decomposition on the ground state. While our H-atom PFY spectra support the previously observed UV absorption spectrum near 240 nm by Fahr et

al. and our $P(E_T)$ distributions are in general agreement with those from the UV photodissociation of propargyl by Chen and co-workers and Neumark and co-workers, no H-atom action spectrum or C_3H_3 REMPI spectrum are observed for the predicted UV absorption bands in the recent theoretical calculations by Eisfeld.

References

(1) Kern, R. D.; Chen, H.; Kiefer, J. H.; Mudipalli, P. S. *Combustion and Flame* **1995**, *100*, 177.

(2) Morter, C. L.; Farhat, S. K.; Adamson, J. D.; Glass, G. P.; Curl, R. F. *Journal of Physical Chemistry* **1994**, *98*, 7029.

(3) Miller, J. A.; Klippenstein, S. J. *Journal of Physical Chemistry A* **2003**, *107*, 7783.

(4) Richter, H.; Howard, J. B. *Progress in Energy and Combustion Science* **2000**, *26*, 565.

(5) Farmer, J. B.; Lossing, F. P. *Canadian Journal of Chemistry* **1955**, *33*, 861.

(6) Ramsay, D. A.; Thistlethwaite, P. *Canadian Journal of Physics* **1966**, *44*, 1381.

(7) Jacox, M. E.; Milligan, D. E. *Chemical Physics* **1974**, *4*, 45.

(8) Wyss, M.; Riaplov, E.; Maier, J. P. *Journal of Chemical Physics* **2001**, *114*, 10355.

(9) Atkinson, D. B.; Hudgens, J. W. *Journal of Physical Chemistry A* **1999**, *103*, 4242.

(10) Eisfeld, W. *Journal of Physical Chemistry A* **2006**, *110*, 3903.

(11) Fahr, A.; Hassanzadeh, P.; Laszlo, B.; Huie, R. E. *Chemical Physics* **1997**, *215*, 59.

(12) Deyerl, H.-J.; Fischer, I.; Chen, P. *Journal of Chemical Physics* **1999**, *111*, 3441.

(13) Giri, B. R.; Hippler, H.; Olzmann, M.; Unterreiner, A. N. *Physical Chemistry Chemical Physics* **2003**, *5*, 4641.

(14) Atkinson, D. B.; Hudgens, J. W. *Journal of Physical Chemistry A* **1999**, *103*, 7978.

(15) Fahr, A.; Laufer, A. H. *Journal of Physical Chemistry A* **2005**, *109*, 2534.

(16)Honjou, H.; Yoshimine, M.; Pacansky, J. *Journal of Physical Chemistry* **1987**, *91*, 4455.

(17)Eisfeld, W. *Physical Chemistry Chemical Physics* **2005**, *7*, 3924.

(18)Vereecken, L.; Pierloot, K.; Peeters, J. *Journal of Chemical Physics* **1998**, *108*, 1068.

(19)Nguyen, T. L.; Mebel, A. M.; Kaiser, R. I. *Journal of Physical Chemistry A* **2001**, *105*, 3284.

(20)Nguyen, T. L.; Mebel, A. M.; Lin, S. H.; Kaiser, R. I. *Journal of Physical Chemistry A* **2001**, *105*, 11549.

(21)Jackson, W. M.; Anex, D. S.; Continetti, R. E.; Balko, B. A.; Lee, Y. T. *Journal of Chemical Physics* **1991**, *95*, 7327.

(22)McCunn, L. R.; FitzPatrick, B. L.; Krisch, M. J.; Butler, L. J.; Liang, C.-W.; Lin, J. J. *Journal of Chemical Physics* **2006**, *125*, 133306/1.

(23)Goncher, S. J.; Moore, D. T.; Sveum, N. E.; Neumark, D. M. *Journal of Chemical Physics* **2008**, *128*, 114303.

(24)Wheeler, S. E.; Robertson, K. A.; Allen, W. D.; Schaefer, H. F.; Bomble, Y. J.; Stanton, J. F. *Journal of Physical Chemistry A* **2007**, *111*, 3819.

(25)Xu, K. S.; Amaral, G.; Zhang, J. S. *Journal of Chemical Physics* **1999**, *111*, 6271.

(26)Amaral, G.; Xu, K. S.; Zhang, J. S. *Journal of Chemical Physics* **2001**, *114*, 5164.

(27)Zhou, W.; Yuan, Y.; Chen, S.; Zhang, J. *J. Chem. Phys.* **2005**, *123*, 054330/1.

(28)McCunn, L. R.; Bennett, D. I. G.; Butler, L. J.; Fan, H.; Aguirre, F.; Pratt, S. T. *Journal of Physical Chemistry A* **2006**, *110*, 843.

(29)Sun, W.; Yokoyama, K.; Robinson, J. C.; Suits, A. G.; Neumark, D. M. *Journal of Chemical Physics* **1999**, *110*, 4363.

(30)Ni, C.-K.; Huang, J. D.; Chen, Y. T.; Kung, A. H.; Jackson, W. M. *Journal of Chemical Physics* **1999**, *110*, 3320.

(31) Qadiri, R. H.; Feltham, E. J.; Hendrik Nahler, N.; Perez Garcia, R.; Ashfold, M. N. R. *Journal of Chemical Physics* **2003**, *119*, 12842.

(32) Lossing, F. P. *Canadian Journal of Chemistry-Revue Canadienne De Chimie* **1972**, *50*, 3973.

(33) Gilbert, T.; Pfab, R.; Fischer, I.; Chen, P. *Journal of Chemical Physics* **2000**, *112*, 2575.

(34) Zierhut, M.; Noller, B.; Schultz, T.; Fischer, I. *Journal of Chemical Physics* **2005**, *122*, 094302.

(35) Zheng, X. F.; Song, Y.; Wu, J.; Zhang, J. S. *unpublished*.

(36) Zhao, X. Ph.D. Thesis, University of California, Berkeley, 1988.

(37) Myers, J. D. Ph.D. Thesis, University of California, Berkeley, 1993.

(38) Zare, R. N. *Mol. Photochem.* **1972**, *4*, 1.

(39) Qadiri, R. H.; Feltham, E. J.; Cottrill, E. E. H.; Taniguchi, N.; Ashfold, M. N. R. *Journal of Chemical Physics* **2002**, *116*, 906.

CHAPTER 5

Ultraviolet photodissociation dynamics of the benzyl radical

ABSTRACT

Ultraviolet (UV) photodissociation dynamics of jet-cooled benzyl radical via the 4^2B_2 electronically excited state is studied in the photolysis wavelength region of 228 to 270 nm using high-*n* Rydberg atom time-of-flight (HRTOF) and resonance enhanced multiphoton ionization (REMPI) techniques. In this wavelength region, H-atom photofragment yield (PFY) spectra are obtained using ethylbenzene and benzyl chloride as the precursors of benzyl radical, and they have a broad peak centered around 254 nm and are in a good agreement with the previous UV absorption spectra of benzyl. The H + C_7H_6 product translational energy distributions, $P(E_T)$'s, are derived from the H-atom TOF spectra. The $P(E_T)$ distributions peak near 5.5 kcal/mol, and the fraction of average translational energy in the total excess energy, $\langle f_T \rangle$, is ~0.3. The $P(E_T)$'s indicate the production of fulvenallene + H, which was suggested by recent theoretical studies. The H-atom product angular distribution is isotropic, with the anisotropy parameter $\beta \approx 0$. The H/D product ratios from isotope labeling studies using $C_6H_5CD_2$ and $C_6D_5CH_2$ are reasonably close to the statistical H/D ratios, suggesting that the H/D atoms are scrambled in the photodissociation of benzyl. The dissociation mechanism is consistent

with internal conversion of the electronically excited benzyl followed by unimolecular decomposition of the hot benzyl radical on the ground state.

5.1 Introduction

Benzyl radical is a prototypical aromatic radical and plays important roles in the combustion of toluene and other aromatic compounds. It is the primary fragment of oxidation and pyrolysis of toluene and other aromatic hydrocarbons, and its further reactions and decomposition in combustion are important in the production of polycyclic aromatic hydrocarbons and soot formation. Consequently, the electronic spectroscopy,[1-15] thermal decomposition, and chemical reaction kinetics of the benzyl radical[16-29] have been studied extensively for the past several decades.

The ground electronic state of the benzyl radical is 1^2B_2 in a C_{2v} planar symmetry.[1] Its first electronic transition is 1^2A_2-1^2B_2,[2,3] which gives rise to weak bands in the visible region with the 0_0^0 band at 22002 cm^{-1}. The second electronic excited state 2^2B_2 was found to lie only 850 cm^{-1} above the first electronic excited state 1^2A_2, and the vibronic coupling between these two closely lying states causes complex vibronic structures in the visible region around 450 nm.[3-9] A diffuse structure in the 305 nm region was observed in the near ultraviolet (UV) absorption spectrum of benzyl,[10,11] and this transition was assigned to 2^2A_2-1^2B_2, with its 0_0^0 band at 32760 cm^{-1}. The next higher transition 3^2B_2-1^2B_2 was suggested by Cossart-Magos and Leach[4] and was expected to be weak and occur around 270 nm.[12] The strongest absorption of benzyl was identified in the UV

region at 253 nm and was assigned to the 4^2B_2-1^2B_2 transition.[11-15] At the shorter wavelength region, a new band was found at 230 nm by Bayrakceken et al.,[14] which was attributed to the first Rydberg state of the benzyl radical. A summary of the electronic states of benzyl is illustrated in Figure 5.1.

Thermal decomposition of the benzyl radical has been studied experimentally via various methods. The rate constant of benzyl decomposition has been measured several times in shock tube experiments by monitoring UV absorption of the benzyl radical[16-20] and using time-resolved H-atom atomic resonance absorption spectrometry (ARAS).[21,22] Baulch et al. evaluated the kinetic data up to 1992 and recommended $k = 5.1 \times 10^{13}$ exp(-36370/T) s^{-1} in the temperature range 1350-1900 K.[23] A more recent shock tube study by Oehlschlaeger et al. yielded $k = 8.20 \times 10^{14}$ exp(-40600/T) s^{-1} in the temperature range 1430-1730 K,[20] in good agreement with Baulch et al.'s value. The unimolecular decomposition pathways and primary products of benzyl, however, could not be determined unambiguously and have been subject to debates. In the study of toluene pyrolysis using Knudsen cell and mass spectrometry, Smith suggested that the benzyl radical decomposed to $C_5H_5 + C_2H_2$ and $C_4H_4 + C_3H_3$,[24] which was supported by a shock tube study with product gas analysis via flame ionization detection by Colket and Seery.[25] On the other hand, in two shock tube and H-atom ARAS studies, Braun-Unkhoff et al. and Rao and Skinner concluded that benzyl dissociates mainly to H atom and an

unknown C_7H_6 product.[21,22] Hippler, Troe, and co-workers analyzed a series of their shock tube studies based on UV absorption detection of benzyl and concluded that the H atom production was the primary channel in the benzyl unimolecular decomposition.[18] Oehlschlaeger et al. also suggested that the decomposition products of benzyl were C_7H_6 and H in their shock tube and kinetics study.[20] The unimolecular decay of the benzyl radical was also investigated in a molecular beam experiment using mass spectrometry.[26] Toluene and cycloheptatriene were photodissociated with two photons at 248 or 193 nm and highly vibrationally excited benzyl radicals were produced. The hot benzyl radicals subsequently decomposed to fragments with mass 90 amu, indicating the C_7H_6 + H product channel.

The unimolecular decomposition of the benzyl radical and its products have also been examined by quantum chemical methods,[19,27-29] and the H-atom production channels are summarized in Figure 5.1. Jones et al. investigated four possible benzyl (**1**) decomposition pathways and their potential energy surfaces.[19] By comparing the reaction energetics, two primary pathways were suggested, direct ring opening followed by fission into small fragments such as C_4H_3 and C_3H_4 and C_4H_4 and C_3H_3, and isomerization to 6-methylenebicyclo[3.1.0]hex-3-en-2-yl (MBH) bicyclic ring intermediate (**3**) and then to cyclopentadiene-vinyl radical (**10**) followed by H loss to 5-ethynyl-1,3-cyclopentadiene (at a barrier height of ~99 kcal/mol) and to a lesser extent formation of cyclopentadiene

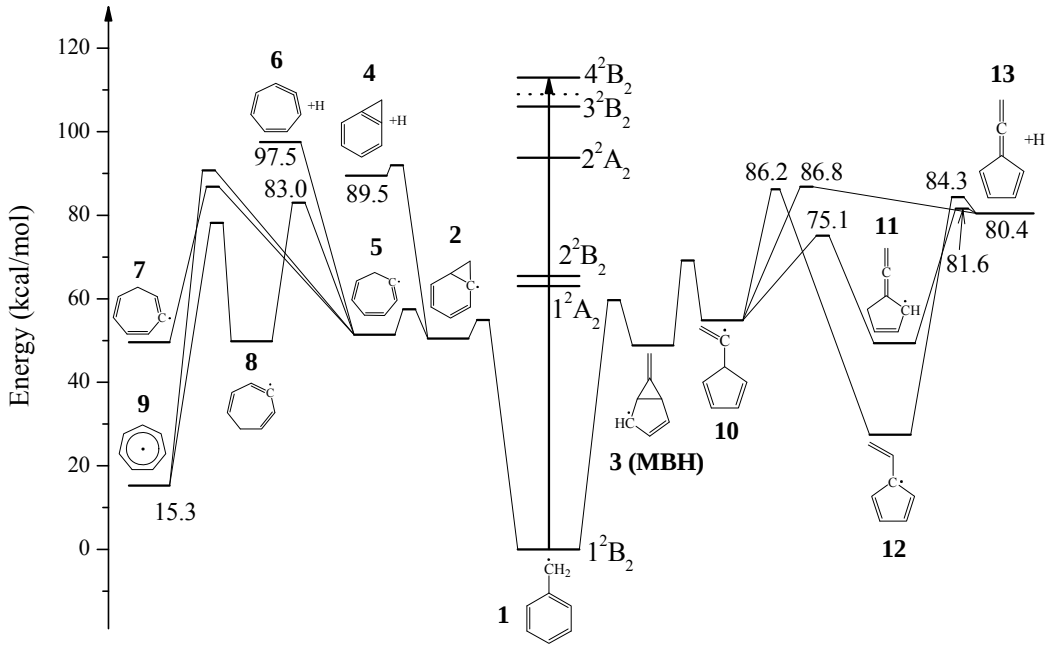

Figure 5.1 Potential energy diagram of the C_7H_7 system. Three possible H-atom dissociation channels are shown in the figure. The energetics and pathways are based on the theoretical calculations in Ref 27. The energies of the electronic excited states of the benzyl radical are based on Refs [3,4,7,10,12,14] and the T_0 levels are represented by the solid lines and the vertical energy T_v levels by dashed lines. The vertical arrow shows the photon energy at 254 nm. For the symmetry species in the C_{2v} point group, the *y* axis is chosen to be perpendicular to the plane of radical.

and acetylene (not shown in Figure 5.1). However, the calculated overall activation energy of the benzyl decomposition based on these two dominant pathways was 97 kcal/mol, significantly higher than those found in the shock tube experiments.[17,20,23] In a more recent theoretical study, Cavallotti et al. recalculated the potential energy surfaces, decomposition pathways, and rate constants of each elementary reaction in benzyl decomposition.[27] Considering the energy barriers and rate determining step, the main decomposition channel of benzyl was found to be fulvenallene (**13**) + H (Figure 5.1). The first step was isomerization of benzyl (**1**) to the MBH bicyclic intermediate (**3**) and then to the cyclopentadiene-vinyl radical (**10**), similar to Jones et al.'s study.[19] The cyclopentadiene-vinyl radical (**10**) could then dissociate into fulvenallene (**13**) + H in three pathways: (i) direct dissociation of **10** by losing the tertiary H atom on the cyclopentadiene ring over an energy barrier of 86.8 kcal/mol; (ii) isomerization of **10** to cyclopentadienyl-ethene radical (**12**) via 1,2 H shift of the tertiary H atom to the CCH_2 group, followed by the loss of this H atom, with an overall barrier of 86.2 kcal/mol; and (iii) isomerization of **10** to cyclopentadienyl-allene radical (**11**) via 1,2 H shift of the tertiary H atom to a vicinal CH group on the ring, followed by the loss of an H atom from this CH_2 group, with an overall barrier of 81.6 kcal/mol. The calculated dissociation energy of 80.4 kcal/mol and lowest energy barrier of 81.6 kcal/mol for the fulvenallene (**13**) + H channel were consistent with the activation energy of 80-83 kcal/mol from the

previous experimental studies.[17,20,23] The benzyl radical (**1**) could also isomerize to the bicyclic norcaradienyl (NCDE) radical (**2**), which could then dissociate to bicycle[4.1.0]hepta-1,3,5-triene (**4**) + H with a barrier of 92.0 kcal/mol or isomerize to a 7-member ring *ortho*-1,3,5-cyclohepta-triene radical (**5**, *o*CHTE). The *o*CHTE radical (**5**) could dissociate to cycloheptatriene (**6**) + H at 97.5 kcal/mol or isomerize to the *meta* and *para* isomers (**7**, *m*CHTE and **8**, *p*CHTE) and to the cycloheptatrienyl radical (**9**). However, the two H-loss channels (**4** and **6**) involving NCDE (**2**) require much higher energy than the fulvenallne (**13**) + H channel, and thus are less important. In another recent theoretical study, Silva et al.[28,29] identified essentially the same reaction schemes as those by Cavallotti et al.[27] and confirmed that the fulvenallene (**13**) + H channel was most energetically favorable and the main dissociation channel of benzyl. The activation energies and product energies in these two theoretical studies agreed with each other within ~4 kcal/mol.[27-29] The RRKM rate constants for decomposition of benzyl to fulvenallene (**13**) + H were calculated at different pressures and temperatures, with the atmospheric pressure decomposition rate constant in reasonable agreement with the experimental results.[17,20,23] The branching ratios of the three reaction pathways leading to the fulvenallene (**13**) + H product channel were investigated at different temperatures. It was shown that between 700 and 2500 K the primary pathways to fulvenallene (**13**) + H were (i) via direct dissociation of the cyclopentadiene-vinyl radical (**10**) and (iii) via

isomerization of **10** to cyclopentadienyl-allene radical (**11**), followed by dissociation of **11**. The three H-loss product channels of benzyl and the energetics are summarized in the following (Figure 5.1):

$C_6H_5CH_2(1^2B_2) + h\nu$

$\rightarrow C_7H_6$ (**13**, fulvenallene) + H, $\Delta H_{rxn,0}$ = 80.4[27](84.9[28]) kcal/mol (1)

$\rightarrow C_7H_6$ (**4**) + H, $\Delta H_{rxn,0}$ = 89.5 kcal/mol[27] (2)

$\rightarrow C_7H_6$ (**6**) + H, $\Delta H_{rxn,0}$ = 97.5 kcal/mol[27] (3)

The studies on the photochemistry of the benzyl radical are limited. Damm et al. investigated the collisional deactivation and unimolecular dissociation and photodissociation of the vibratiaonlly excited benzyl radicals.[13,30] The vibrationally excited benzyl radicals were produced in 193-nm photolysis of ethylbenzene, which after some delay time were excited again by 308-nm radiation via the 2^2A_2-1^2B_2 transition. These hot benzyl radicals decayed to the ground electronic state presumably via internal conversion, and a fraction of them decomposed. The dissociation of the vibrationally excited benzyl was monitored using the strong 253-nm absorption of benzyl and C_7H_6 + H were assumed to be the decomposition products.[30] In the molecular beam study of the photodissociation of toluene and cycloheptatriene at 248 and 193 nm, secondary dissociation of the highly vibrationally excited benzyl radical (primary product) was observed to produce the C_7H_6 + H fragments.[26] Time-of-flight (TOF) spectra of the C_7H_6

fragment were analyzed assuming 2-photon excitation of toluene and cycloheptatriene. Due to the complexity and poorly defined secondary dissociation, only the average kinetic energy release of C_7H_6 was modeled and shown to be ~ 7% of the total available energy to the C_7H_6 + H products, while the dynamical information for the benzyl dissociation was limited.[26] Decay of the 4^2B_2 excited state of benzyl at 255 nm was investigated by Zierhut et al. using femtosecond time-resolved photoionization.[31] The 4^2B_2 state decayed within 150 ± 30 fs, presumably via fast internal conversion to the electronic ground state of benzyl.[31]

The current work investigates the UV photodissociation dynamics of jet-cooled benzyl radical via the 4^2B_2 electronically excited state in the photolysis wavelength region of 228-270 nm. The H-atom photofragment yield (PFY) spectra of benzyl as a function of photolysis wavelength are obtained using the high-n Rydberg atom time-of-flight (HRTOF) and resonance enhanced multiphoton ionization (REMPI) techniques. These spectra are in good agreement with the previous UV absorption spectra of benzyl, directly confirming the H + C_7H_6 product channel. The H-atom product TOF spectra in the photodissociation of benzyl were recorded using the HRTOF technique, and transformed to product center-of-mass (CM) translational energy distributions, P(E_T)'s. The P(E_T) distributions indicate that the C_7H_6 (fulvenallene) + H product channel is one of the dissociation pathways for benzyl radical. The H-atom product angular distribution

was also obtained by linearly polarized UV photolysis laser radiation. Isotope labeling studies using $C_6H_5CD_2$ and $C_6D_5CH_2$ are carried out for more insights into the dissociation mechanisms of benzyl.

5.2 Experimental

The HRTOF technique and experimental setup have been described previously.[32-34] A pulsed benzyl (C_7H_7) radical beam was generated by photolyzing a ~2% mixture of ethylbenzene or benzyl chloride seeded in Ar (at a total pressure of 120 kPa) with the 193-nm radiation from an ArF excimer laser. The benzyl radical precursors are ethylbenzene [$C_6H_5CH_2CH_3$ (99.8%, Aldrich), $C_6H_5CD_2CD_3$ (99.5% chemical purity, 99.4 atom % D, CDN Isotopes), and $C_6D_5CH_2CH_3$ (99.3% chemical purity, 99.5 atom % D, CDN Isotopes)] and benzyl chloride [$C_6H_5CH_2Cl$ (99%, Fisher), $C_6H_5CD_2Cl$ (99.6% chemical purity, 99.5 atom % D, CDN Isotopes), and $C_6D_5CH_2Cl$ (99.6% chemical purity, 99.3 atom % D, CDN Isotopes)]. Both ethylbenzene and benzyl chloride have been used to produce benzyl radicals before.[11,30,35,36] The partially dueterated precursors are used for isotope labeled benzyl radicals. The radical beams were characterized using the 121.6 nm vacuum ultraviolet (VUV) photoionization TOF mass spectrometry (TOFMS), and productions of the various benzyl radicals were confirmed.

The 193-nm photolysis radiation for radical production was focused in front of the pulse nozzle. The benzyl radicals produced from the photolysis were entrained in the seeded beam and subsequently cooled by supersonic expansion. The radical beam was collimated at 2.8 cm downstream by a 1-mm diameter skimmer into a high-vacuum chamber. At 4.6 cm further downstream the skimmer, the benzyl radical beam was crossed with a slightly focused UV photolysis laser radiation (at 228-270 nm, 0.5-3.5 mJ/pulse, linewidth ~ 0.3 cm^{-1}). The absolute photolysis laser wavelength was monitored by a wavemeter (Burleigh WA-4500). The polarization of the photolysis radiation was rotated by a Fresnel-Rhomb achromatic $\lambda/2$ plate for product angular distribution measurements. The H/D atoms produced from the benzyl photodissociation were tagged by two-color resonant excitation (121.6 + 366.3 nm), i.e., from 1^2S to 2^2P via the H/D-atom Lyman-α transition and then further to a high-*n* Rydberg state. A small fraction of the radiatively metastable Rydberg H/D atoms drifted with their nascent velocities toward a microchannel plate (MCP) detector that is positioned perpendicular to the molecular beam, and were field-ionized in front of the detector and detected. The nominal flight length was 37.1 cm, which was calibrated by 230-250 nm photodissociation of HBr [with the spin-orbit splitting of Br($^2P_{3/2}$) and Br($^2P_{1/2}$)]. The ion signals were amplified by a fast preamplifier, and the H/D-atom TOF spectra were recorded and averaged by using a multichannel scaler. The H/D-atom TOF spectra were accumulated with ~10^5 laser

shots. Typically four types of HRTOF spectra were taken (including the full spectrum and three background spectra), and the net HRTOF spectra from the UV photolysis of the benzyl radical were obtained after proper background subtraction (see the Results section for more details).

The H-atom PFY spectra (action spectra) were measured using two methods. The first method involved integrating the net HRTOF spectra (after the background removal) as a function of photolysis wavelength. The second was based on collecting the H-atom REMPI signals as a function of photolysis wavelength. The H-atom REMPI experiment was conducted in the same HRTOF instrument. Upon photodissociation by the UV laser radiation in the range of 228-270 nm, the H atom products were detected by 1+1' REMPI, with one Lyman-α photon resonantly exciting the H atoms from 1^2S to 2^2P and a UV photon at ~364 nm ionizing the H atoms. The photolysis and REMPI probe laser delay time was fixed at 15 ns for the action spectra but varied for the pump-probe time profile measurements later. The H^+ ions were extracted and accelerated in the linear TOF mass spectrometer, and were detected by the MCP detector. The mass-resolved ion current signal (m/z=1 for H^+ and 2 for D^+) was amplified by a preamplifier, recorded in a digital storage oscilloscope, and transferred to the computer. At each UV wavelength, typically 512 laser shots were averaged. Two types of REMPI signal were recorded, (i) with the 193-nm radiation on (for the benzyl radical production), the UV photolysis radiation on,

and the REMPI probe lasers on; and (ii) background with the 193-nm radiation off, but the UV photolysis radiation and the REMPI probe lasers on. The PFY spectra were the net H-atom REMPI signals with the background (ii) removed. The photolysis laser power was normalized for the H-atom PFY spectra.

In order to study the site specific dissociation pathways and further illustrate the photodissociation mechanism, partially deuterated benzyl radicals, $C_6H_5CD_2$ (produced from the $C_6H_5CD_2CD_3$ and $C_6H_5CD_2Cl$ precursors) and $C_6D_5CH_2$ (from $C_6D_5CH_2CH_3$ and $C_6D_5CH_2Cl$), were used. The H and D atom product yields were measured using 1+ 1' REMPI of H and D atoms, respectively. The HRTOF spectra of the neutral H and D atom products were also obtained, and the integrated intensities were used for the H/D branching ratios as well. In both approaches, the proper backgrounds were taken and removed.

5.3 Results

VUV photoionization TOF mass spectra were taken to characterize the benzyl radical beams using both the ethylbezene and benzyl chloride precursors. Figure 5.2 is a net TOF mass spectrum of ethylbenzene in Ar with the 193-nm photolysis on minus 193-nm off. The benzyl radical at m/e 91 was shown as the major product from

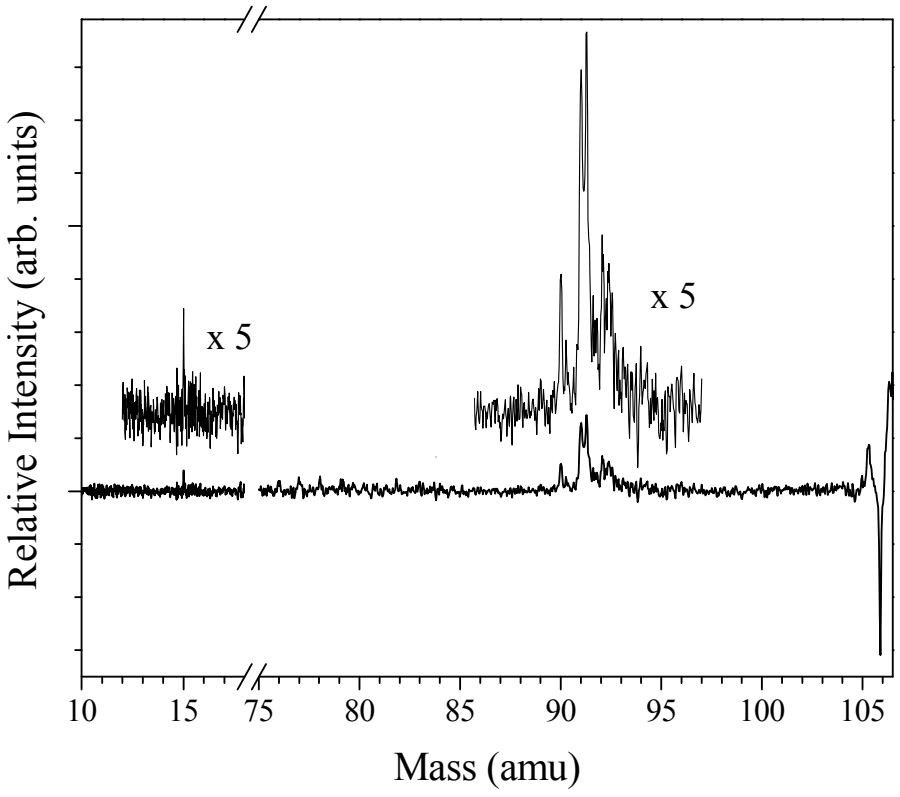

Figure 5.2 121.6 nm VUV photoionization mass spectrum of the benzyl radical beam using the ethylbenzene precursor in Ar carrier gas. This is the net mass spectrum of ethylbenzene with the 193 nm photolysis laser on minus off. The main product is benzyl radical at m/z = 91 amu, while the ethylbenzene parent peak at m/z =106 is depleted due to the 193 nm photolysis. Photoionization fragmentation is minimum due to the low photon energy at 121.6 nm and is removed in the net mass spectrum.

ethylbenzene photolysis at 193 nm, along with its cofragment CH_3 at m/z 15. The CH_3 radical co-product has an absorption maximum at 216 nm[37] and did not interference the photochemistry of benzyl near 254 nm. The mass spectra of benzyl radical beams using benzyl chloride also showed predominant production of the benzyl radicals.

The TOF spectra of the H-atom product from the photodissociation of C_7H_7 were measured in the photolysis wavelength region 228-270 nm, with the photolysis laser polarization parallel and perpendicular to the flight path, respectively. In order to identify the origins of the H-atom signals and to establish procedures for background subtraction, four types of TOF spectra were taken: (1) full spectrum, with both the 193-nm radiation on (for C_7H_7 radical production) and the UV photolysis radiation on, plus the Rydberg atom tagging probe-laser radiations (121.6 + 366.3 nm); (2) precursor background spectrum, with the 193-nm radiation off but the UV photolysis radiation on, plus the probe-laser radiations; (3) radical background spectrum, with both the 193-nm radiation on and probe radiations on, but the UV photolysis radiation off; and (4) probe-laser background spectrum, with both the 193-nm radiation off and the UV photolysis radiation off, but only the probe radiations on. The background spectra (3) and (4) were observed to be negligibly small. The precursor background spectrum (2) represents the main background, i.e., contributions from photolysis of ethylbenzene precursor by the UV photolysis radiation. The net H-atom TOF spectrum of the benzyl

photodissociation is obtained by removing the precursor background spectrum (2) from the full spectrum (1). Figure 5.3 shows the net H-atom TOF spectra at 254-nm photolysis wavelength with 0.5 mJ/pulse UV radiation intensity using ethylbenzene and benzyl chloride precursors. The TOF spectra of the benzyl radicals from both precursors are essentially the same, supporting that the signals are from the benzyl radicals. Photolysis laser power dependence was also studied. Figure 5.4 shows the H-atom TOF spectra of benzyl at 254 nm with two different photolysis energies, 0.5 and 2.5 mJ/pulse. Both TOF spectra are normalized to the same laser power and number of laser shots. The main peak at ~ 42 μs in the TOF spectra has a linear dependence on the photolysis laser power, while there is a small component of faster H atoms that depend nonlinearly with the laser power. These fast H-atom signals, although small compared with the slower signals with linear laser power dependence, are from multiphoton dissociation of benzyl. Consequently, low photolysis energy (0.5-1 mJ/pulse) was used in this study.

To further confirm that the observed HRTOF spectra were originated from the photolysis of benzyl radical, two types of PFY spectra from the integrated HRTOF intensities and H-atom (1+1') REMPI were recorded using both ethylbezene and benzyl chloride precursors. To correct for the variation and drift of the experimental conditions, H-atom signals from the 254 nm photolysis were used as a reference and were monitored

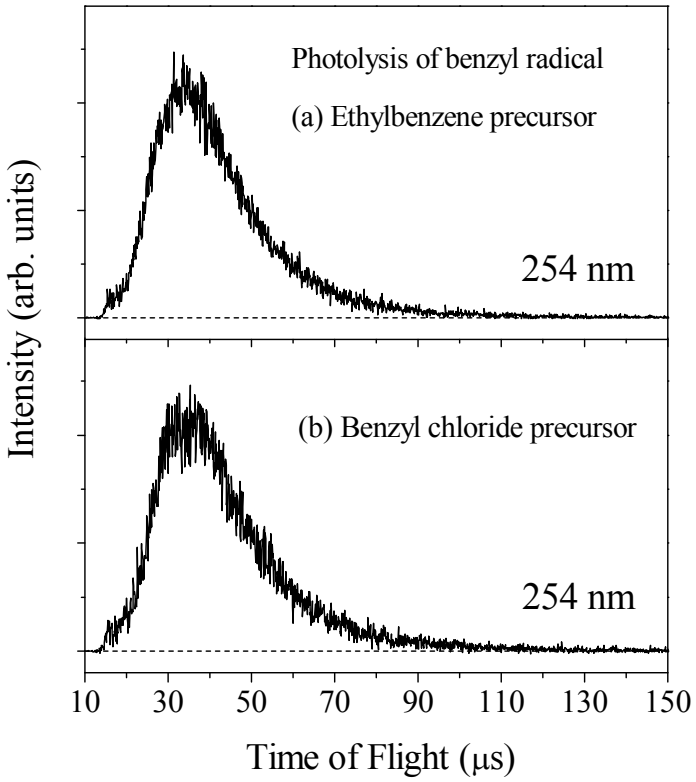

Figure 5.3 H-atom TOF spectra in the 254-nm photodissociation of jet-cooled benzyl radical, produced from 193-nm photolysis of (a) ethylbenzene precursor and (b) benzyl chloride precursor. These are the net TOF spectra with the 193-nm photolysis laser (for radical production) on minus off. The polarization vector of the 254 photodissociation radiation is parallel ($\theta = 0^{o}$) to the TOF axis. The photolysis radiation power intensity is 0.5 mJ/pulse.

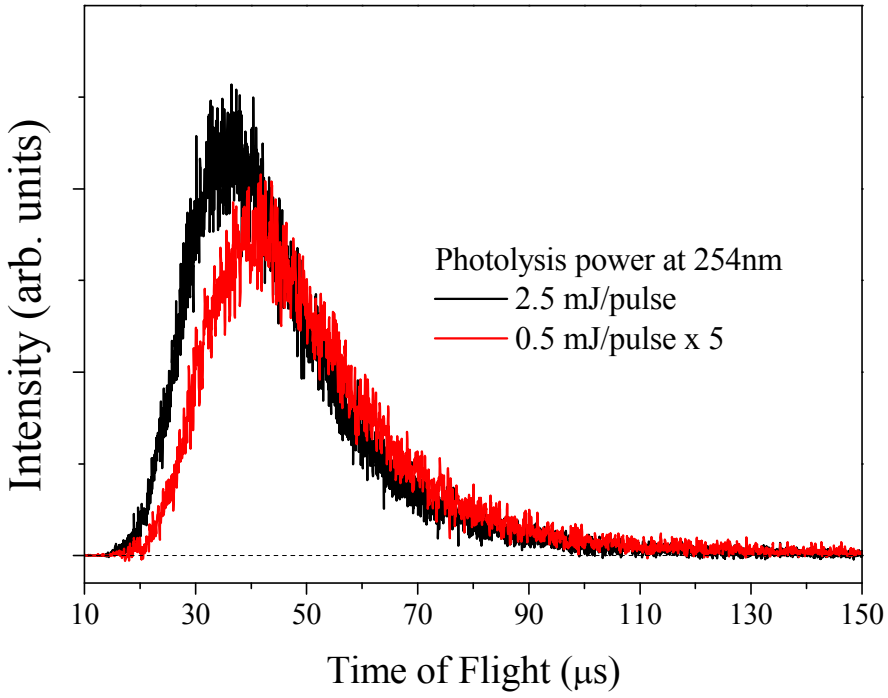

Figure 5.4 Photolysis laser power dependence: the H-atom product TOF spectra of the benzyl radical at 254 nm with photolysis energy 0.5 and 2.5 mJ/pulse. The TOF spectra are scaled to the same laser power and number of laser shots. The signals at flight time > 40 μs have a linear dependence on the photolysis laser power, while a portion of the faster H-atom signals have nonlinear dependence on the photolysis laser power.

after every 2 to 3 measurements at other wavelengths. The H-atom intensities at other photolysis wavelength were scaled to that of 254 nm and normalized to the photolysis laser power. The resulting H-atom action spectra in 228-270 nm are plotted in Figure 5.5. All of the PFY spectra peak near 254 nm. For comparison, the UV absorption spectra of the benzyl radical previously reported by Markert et al. and Ikeda et al. are shown in Figure 5.5.[11,15] The H-atom PFY spectra from HRTOF and REMPI using both precursors agree well with each other and with the two absorption spectra. These PFY spectra unambiguously confirm that the H-atom products originated from the photodissociation of the benzyl radical.

The net H-atom TOF spectra of the jet-cooled benzyl photodissociation are transformed to total product center-of-mass (CM) translational energy distributions, $P(E_T)$'s. The CM translational energy of the products, E_T, is converted from the H-atom flight time t_H using the following equation:

$$E_T = \left(1+\frac{m_H}{m_{C_7H_6}}\right)E_H + \frac{m_H}{m_{C_7H_6}}E_{C_7H_7} = \frac{1}{2}m_H\left(1+\frac{m_H}{m_{C_7H_6}}\right)\left(\frac{L}{t_H}\right)^2 + \frac{m_H}{m_{C_7H_6}}E_{C_7H_7} \quad (4)$$

where E_H and $E_{C_7H_7}$ are the laboratory translational energies of the H-atom photofragment and the parent C_7H_7 radical, respectively, and L is the flight length. The second term $\left(\frac{m_H}{m_{C_7H_6}}E_{C_7H_7}\right)$ is due to the parent C_7H_7 radical motion in the molecular beam that is orthogonal to the TOF path, but it is much smaller compared with the first

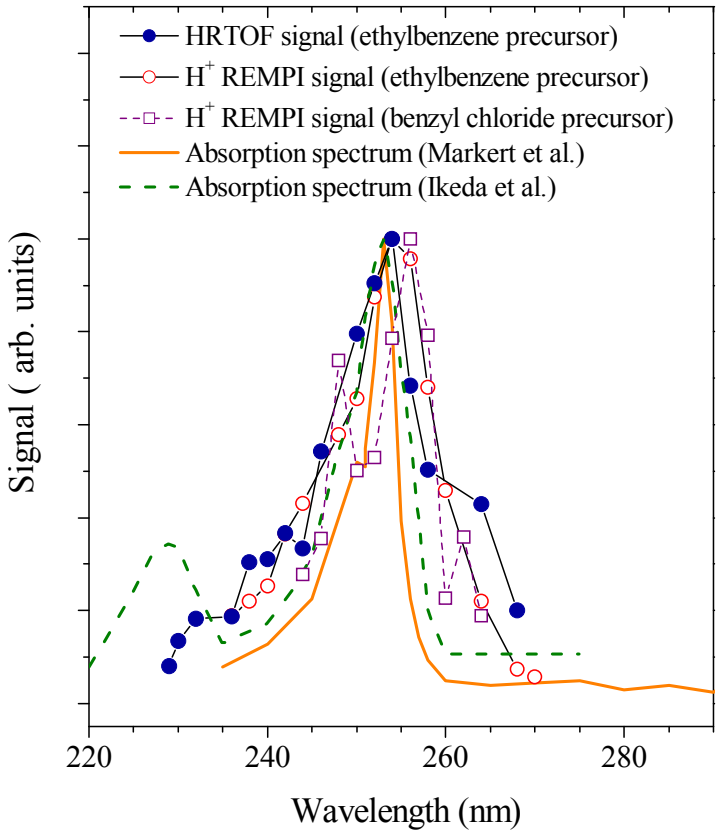

Figure 5.5 H-atom product yield (PFY) spectra as a function of photolysis excitation energy in the region of 228-270 nm. Full circles (●) represent the integrated HRTOF signals using the ethylbenzene precursor. Open circles (○) represent the H-atom (1 + 1') REMPI signals using ethylbenzene. Open squares (□) represent the H-atom REMPI signals for the benzyl chloride precursor. Solid and dashed lines are the absorption spectra taken from Refs [11,15]. The photolysis laser power is normalized for the PFY spectra. The PFY spectra and the absorption spectrum are referenced and scaled at 254 nm.

term (products' CM translation) and is neglected. The $P(E_T)$ distributions can be derived from the TOF spectra by direct conversion.[33] The resulted $P(E_T)$ distribution of the 254-nm photodissociation of C_7H_7 using ethylbenzene precursor is shown in Figure 5.6 (b). The $P(E_T)$ distribution can also be derived from modeling the TOF spectrum in a forward-convolution procedure.[38,39] In this procedure, the H-atom TOF spectrum is calculated by using a trial $P(E_T)$ distribution convoluted with the instrument and molecular beam functions. The calculated TOF spectrum is iteratively optimized by comparison with the experimental spectrum and readjustment of the trial $P(E_T)$ distribution until an optimized $P(E_T)$ distribution is reached. The forward-convolution approach is particularly helpful when the TOF spectrum is noisy, such as those at low photolysis power. Figure 5.6 (a) shows a forward-convolution fitting (in solid line) and the experimental H-atom TOF spectrum (in open circles (○)) from 254-nm photolysis with 0.5 mJ/pulse laser energy (from Figure 5.3a). The solid line in Figure 5.6 (b) shows the optimized $P(E_T)$ distribution used in the fitting, which is in good agreement with the $P(E_T)$ distribution from direct conversion. This $P(E_T)$ has a broad feature that peaks at low energy around 5.5 kcal/mol and extends to the maximum available energy of 32.2 kcal/mol at 254 nm photolysis energy [using a bond dissociation energy (BDE) = 80.4 kcal/mol for the C_7H_6 (**13**, fulvenallene) + H channel[27]]. The translational energy release of the H-atom elimination channel of benzyl is modest; the average product CM

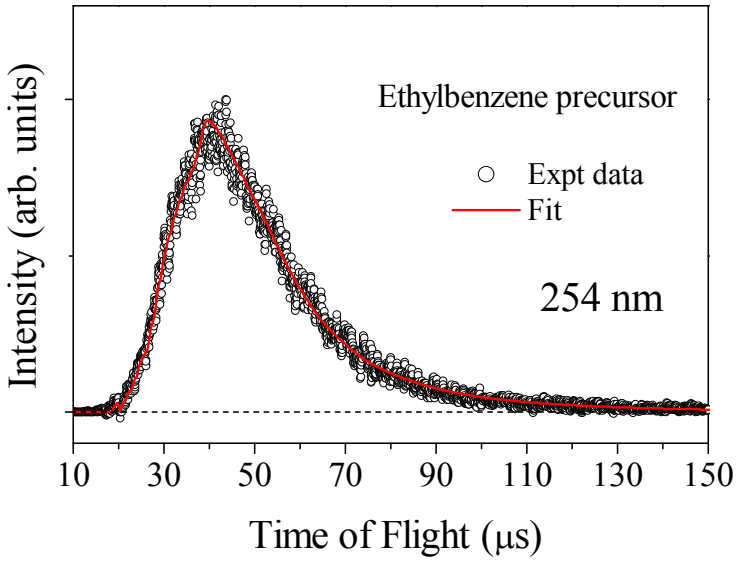

Figure 5.6 (a) Experimental H-atom TOF spectrum in the 254-nm photodissociation of benzyl radical (from Figure 5.3a) is represented in open circles (○). The solid line represents forward convolution fitting for the experimental TOF spectrum.

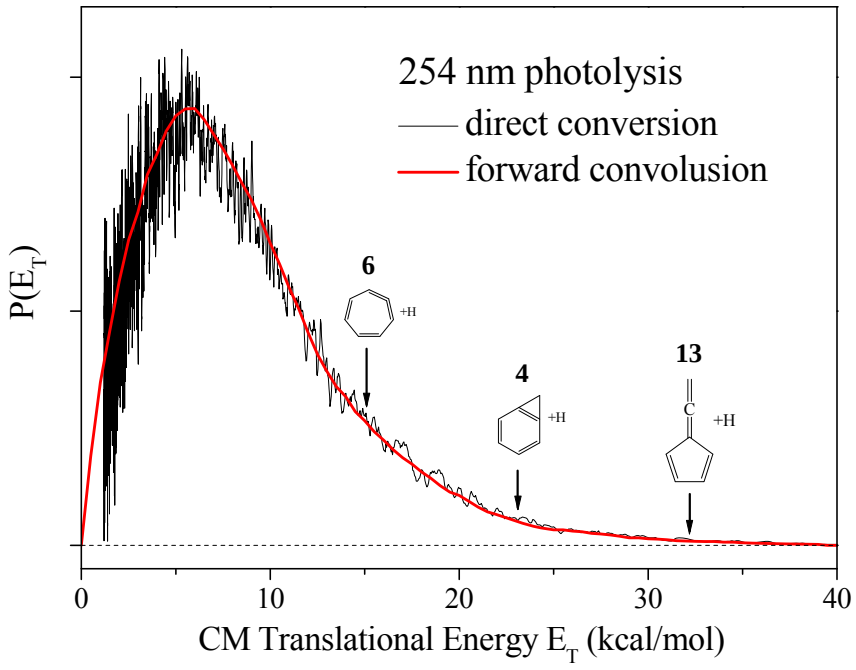

Figure 5.6 (b) Center-of-mass product translational energy distributions, $P(E_T)$, of the H + C_7H_6 product channel from 254-nm photodissociation of C_7H_7. The photolysis laser power was 0.5 mJ/pulse. The thin line is for the $P(E_T)$ from direct conversion of the H-atom TOF spectrum in Figure 5.3a. The red thick line is the $P(E_T)$ distribution from optimized forward-convolution procedure. See text for more details. The vertical arrows indicate the maximum translational energies of the three H-atom production channels.

translational energy $\langle E_T \rangle$ is 9.2 kcal/mol, and the fraction of $\langle E_T \rangle$ in the total available energy is $\langle f_T \rangle \approx 0.29$. The $P(E_T)$ distributions at other photolysis wavelengths from 230-270 nm are also obtained at photolysis laser energy 0.5–1.5 mJ/pulse, and they are very similar to that at 254 nm. The $\langle f_T \rangle$ value stays around 0.3, nearly a constant from 230-270 nm (Figure 5.7).

The H-atom product angular distributions in the UV photodissociation of benzyl were examined using linearly polarized laser radiation. Figure 5.8 illustrates the H-atom TOF spectra from the C_7H_7 photodissociation by polarized 254-nm photolysis radiation, with the polarization direction parallel and perpendicular to the TOF axis. The two TOF spectra are identical, indicating an isotropic H atom product angular distribution. The linearly polarized light preferentially excites those radicals with their electronic transition dipole moment parallel to the electric $\boldsymbol{E}$ of the polarized laser radiation. The photofragment angular distribution is given by $I(\theta) = (1/4\pi)[1 + \beta P_2(\cos\theta)]$, where β is the anisotropy parameter ($-1 \leq \beta \leq 2$), θ is the angle between the electric vector of the polarized laser radiation $\boldsymbol{E}$ and the recoiling velocity vector of the H-atom product (the direction of detection or the TOF axis), and $P_2(\cos\theta)$ is the second Legendre polynomial.[40] Using this equation and the H-atom TOF spectra at 254 nm, an anisotropy parameter $\beta \approx 0$ is derived for the H + C_7H_6 product channel in the C_7H_7 photodissociation (Figure 5.8).

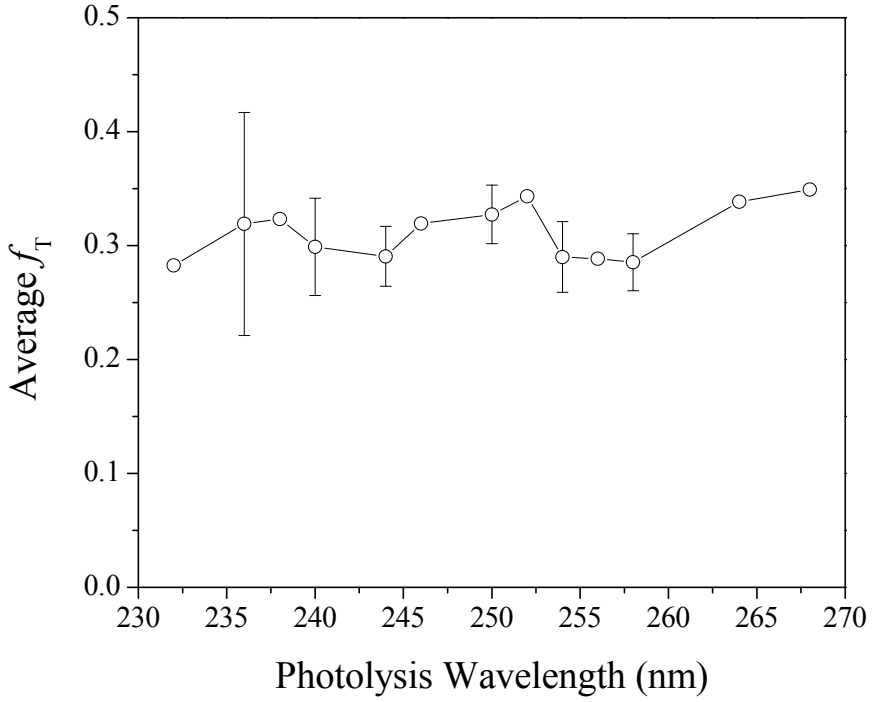

Figure 5.7 Photolysis wavelength and fraction of average translational energy release in the total available energy, $\langle f_T \rangle$, in the UV photodissociation of the benzyl radical. The average translational energies are calculated from the experimental $P(E_T)$ distributions. The total available energy at each photolysis wavelength is derived from the corresponding photon energy and the dissociation of benzyl radical to the H + fulvenallene products, $D_0(H\text{-}C_7H_6)$ = 80.4 kcal/mol.[27] The error bar represents 95% confident limit from repeated measurements.

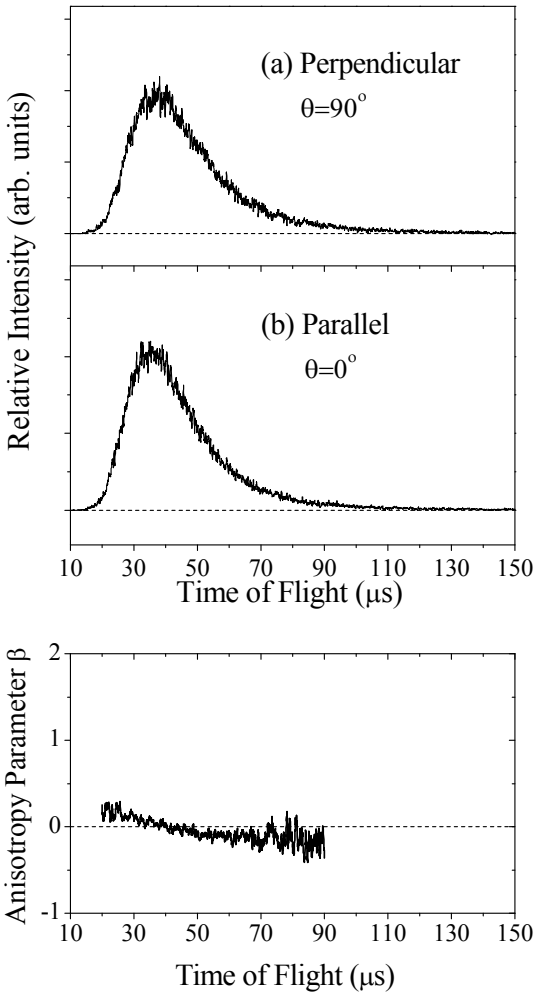

Figure 5.8 H-atom TOF spectra of 254-nm photodissociation of C_7H_7, with the polarization **E** vector of the photolysis radiation (a) perpendicular ($\theta = 90^{o}$) and (b) parallel ($\theta = 0^{o}$) to the TOF axis. The 254 nm radiation power intensity was 2 mJ/pulse. The signals have been normalized to the same photolysis power and laser shots. Anisotropy parameter β is plotted as a function of H-atom time of flight. The β parameter stays close to the limit of an isotropic angular distribution.

The H-atom yield time profile in the UV photolysis of benzyl was monitored as a function of the photolysis laser and probe laser delay time, which provides a measurement for the microcanonical rate of unimolecular dissociation of the benzyl radical. In this time profile, the initial rise indicates the rate for H-atom production from the benzyl radical, while the decay of signal after the peak is due to flight out of the H atoms from the interaction region between the photolysis and probe laser beams. Two approaches were used to obtain the delay time profile, one by integrating the HRTOF spectra and another by the H-atom (1+ 1') REMPI signal, as a function of the pump-probe delay time. The H-atom yield time profiles from integrating the HRTOF spectra are shown in Figure 5.9. In order to check any possible bias on the H-atom time profile due to the flight out of the H atoms and the multiphoton processes, different time windows in the HRTOF spectra (thus different velocities of the H atoms) are integrated (also see Figure 5.4). The time profile of the slow H atoms in 60-100 μs is least affected by the flight out bias and multiphoton processes; nevertheless, the time profiles in the 20-100 and 40-100 μs time windows have essentially the same rise time as the 60-100 μs profile but faster decays (due to faster flight out). The rise times in these time profiles are in the order of 10-20 ns, indicating that benzyl dissociation rate upon 254 nm excitation is ~5-10 x 10^7/s. Note that this fast rise time approaches the laser pulse time width of ~ 7-10 ns. The H-atom yield time profiles from H-atom 1+ 1' REMPI at low photolysis

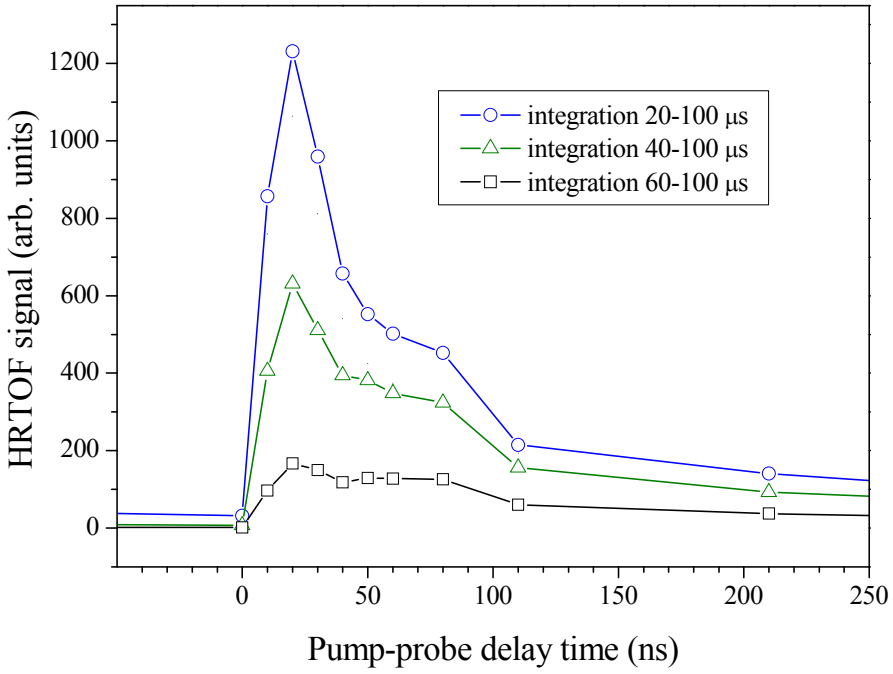

Figure 5.9 H-atom product signal as a function of photolysis and probe laser delay time. The photolysis wavelength is 254 nm and power is ~ 1.5 mJ/pulse. The signals are obtained by integrating the HRTOF spectra at the various photolysis-probe delay time. Different windows of integration 20-100, 40-100, and 60-100 μs, are used.

power (0.3 mJ/pulse) are similar and have the same rise time of 10-20 ns. The H- and D-atom time profiles of $C_6H_5CD_2$ using 1+1' REMPI also have the same rise time. The fast rise of both the H and D atom profiles also implies that the detection sensitivity was not significantly affected by the flight out, as the D atoms have 1.4 times smaller velocities than the H atoms. Furthermore, additional H-atom time profiles were taken with the 1+ 1' REMPI probe laser beams defocused to increase the probe volume, and the rise time stayed the same, also suggesting that the detection sensitivity was not significantly biased by the flight out. These are consistent with the fact that the flight out time (decay time) of the H atom signals is on the order of 100 ns, which should not significantly affect the 10-20 ns rise time of the H atom signals.

Isotope labeling experiments were carried out to probe the site specificity in H-atom elimination and the photodissociation mechanisms of benzyl. The partially deuterated benzyl radicals $C_6H_5CD_2$ and $C_6D_5CH_2$ were photodissociated by the 254-nm radiation at a low power (~0.5 mJ/pulse) in order to prevent multi-photon dissociation, and the H- and D- atom products were detected by 1+1' REMPI, with the experimental conditions for the H and D yield spectra maintained the same. Two types of H and D REMPI TOFMS spectra were recorded, (i) with the 193-nm radiation on (for the benzyl production), the UV photolysis radiation on, and the REMPI probe lasers on; and (ii) with the 193-nm radiation off, but the UV photolysis radiation and the REMPI probe lasers on.

The H and D yield spectra were the net REMPI signals with (i)-(ii). The experimental H/D ratios for the partially deuterated benzyl radicals from the benzyl chloride precursors were obtained by integrating the H^+ and D^+ mass peaks and were determined to be 2.7 for $C_6H_5CD_2$ and 1.2 for $C_6D_5CH_2$, respectively. However, it was found that benzyl chloride was sticky in the sample line; although the line was cleaned, a mixture of $C_6H_5CD_2Cl$ and $C_6D_5CH_2Cl$ with a minor amount of $C_6H_5CH_2Cl$ was found in the molecular beam. Consequently, the mass spectra of the partially deuterated benzyl radicals and their precursors were taken in order to correct for the H/D product ratios. The relative populations of the isotope labeled benzyl radicals and the depletions of the precursors were obtained from the mass peak areas. With the assumption that $C_6H_5CH_2$, $C_6H_5CD_2$, and $C_6D_5CH_2$ have the same UV absorption cross sections and that the summed yields of H and D from $C_6H_5CH_2$, $C_6H_5CD_2$, and $C_6D_5CH_2$ are the same, the H/D yield ratios are corrected to be 5.5 ± 1.2 for $C_6H_5CD_2$ and 0.55 ± 0.1 for $C_6D_5CH_2$, respectively (Table 5.1). The HRTOF spectra of the H and D atom products from $C_6H_5CD_2$ and $C_6D_5CH_2$ were also measured and compared with those of $C_6H_5CH_2$ and $C_6D_5CD_2$ in Figure 5.10. The H-atom TOF spectra of $C_6H_5CH_2$, $C_6H_5CD_2$, and $C_6D_5CH_2$ are very similar, and the same for the D-atom TOF spectra from $C_6D_5CD_2$ and $C_6D_5CH_2$.

Table 5.1 The corrected H and D product ratios from the partially deuterated benzyl radicals. The error limit represents 95% confident limit from repeated measurements. The expected H/D product ratios from simple models are listed for comparison. See the text for more details.

	H/D branching ratio			
Sample	experiment	statistical model	ring model	side-chain model
$C_6H_5CD_2$	5.5 ± 1.2	2.5	5/0	0/2
$C_6D_5CH_2$	0.55 ± 0.1	0.4	0/5	2/0

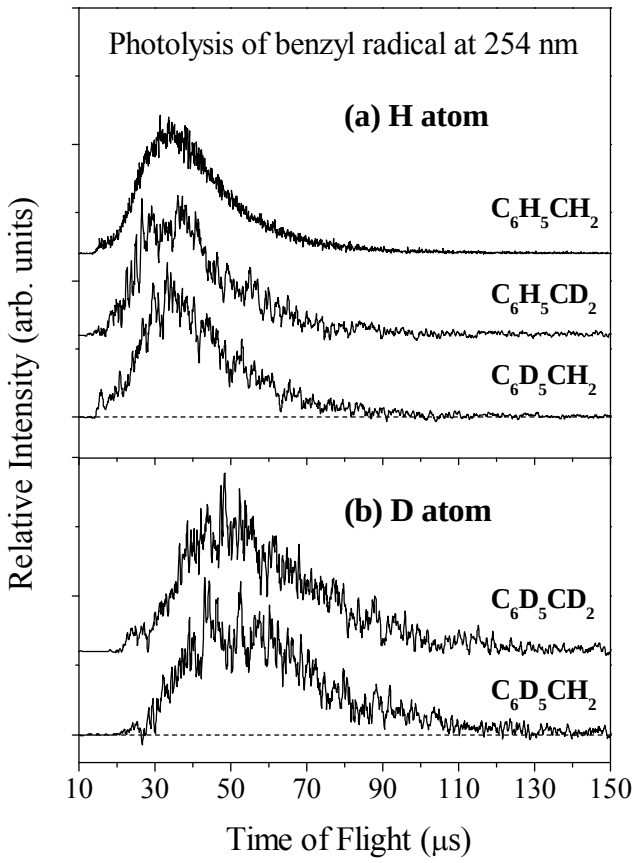

Figure 5.10 TOF spectra of (a) H atoms from $C_6H_5CH_2$, $C_6H_5CD_2$ and $C_6D_5CH_2$, and (b) $C_6D_5CD_2$ and $C_6D_5CH_2$. Note the similarity of the H-atom spectra from the differently labeled benzyl radicals and the similarity of the D-atom spectra. Ethylbenzene was used as the precursor.

5.4 Discussion

The UV photodissociation of the benzyl radical via its 4^2B_2 state in the range of 228-270 nm is studied for the first time. The H + C_7H_6 product channel is directly observed in the UV photodissociation of benzyl, which is in agreement with the early work on the secondary dissociation of hot benzyl radicals from 248 nm and 193 nm photolysis of toluene and cycloheptatriene,[26] as well as the kimetics studies.[18,21,22] This is also consistent with the recent theoretical calculations,[27-29] which suggested that H-atom elimination to fulvenallene (**13**) is the dominant channle of benzyl decomposition, although our current study cannot rule out other possible product channels, such as C_5H_5 + C_2H_2. The CM product translational energy distributions, $P(E_T)$'s, of the H + C_7H_6 channel are not repulsive and have a modest translational energy release. The fraction $\langle f_T \rangle$ stays around 0.3 throughout the photolysis wavelength range of 230-270 nm. The $P(E_T)$ distributions peak at a low energy of 5.5 kcal/mol and have a shape similar to a typical statistical distribution in unimolecular dissociation. All these features of the $P(E_T)$ distributions support the dissociation mechanism of unimolecular decomposition of the hot benzyl radical on the ground electronic state following internal conversion of the initially excited 4^2B_2 state. This conclusion is also consistent with the time-resolved study which observed a fast internal conversion of the 4^2B_2 state to the ground state

(within 150 fs).[31] In the study of secondary dissociation of hot benzyl radicals from the 248 nm and 193 nm photolysis of toluene and cycloheptatriene,[26] $\langle f_T \rangle$ of the H + C_7H_6 fragments was modeled to be ~ 0.07, significantly smaller than the value in this study. However, this early study was complicated by the poorly defined secondary dissociation, and the $P(E_T)$ distribution was not obtained.

The $P(E_T)$ distribution at 254 nm extends to the maximum allowed energy (E_T = 32.2 kcal/mol) for the fulvenallene (**13**) + H channel in a one-photon dissociation process of benzyl (Figure 5.6b).[27] The onsets of the other two H-elimination channels, bicycle[4.1.0]hepta-1,3,5-triene (**4**) + H and cycloheptatriene (**6**) + H, are E_T = 23.1 and 15.1 kcal/mol, respectively (Figure 5.6b). The population between the fulvenallene (**13**) + H and C_7H_6 (**4**) + H onsets clearly shows the production of fulvenallene, with a minimum fraction of 0.05. As it is established here that the H-atom signals are from the benzyl photodissociation and the $P(E_T)$ distribution is from one-photon dissociation (at a low energy of 0.5 mJ/pulse), the conclusion of the first direct observation of the fulvenallene (**13**) + H product channel is reliable. It is expected that the contribution of the fulvenallene (**13**) + H channel in the $P(E_T)$ distribution can extend to the smaller E_T with a larger contribution; in fact, the theoretical studies concluded that due to its low energy barriers the fulvenallene (**13**) + H channel is the dominant channel of benzyl dissociation.[27-29] The $P(E_T)$ peak at 5.5 kcal/mol suggests a small exit channel barrier in

the H-elimination channel. The theoretical studies indicated that there are three reaction pathways leading to fulvenallene (**13**) + H, and two are dominant at high temperatures: (i) direct dissociation of the cyclopentadiene-vinyl radical (**10**), with an exit channel barrier of 6.4 kcal/mol, and (iii) isomerization of **10** to cyclopentadienyl-allene radical (**11**), followed by dissociation of **11**, with an exit channel barrier of 1.2 kcal/mol (Figure 5.1).[27-29] The observed peak in the $P(E_T)$ distribution is consistent with these two pathways.

The angular distributions of the H-atom product from the UV photodissociation of benzyl radical are isotropic, which indicate that the UV photodissociation of benzyl occurs at a time scale longer than the rotational period of the C_7H_7 radical (> ps). This isotropic distribution and the dissociation time scale are also consistent with the dissociation mechanism which is internal conversion to the vibrationally hot ground electronic state, followed by the dissociation on the ground electronic state.

The pump-probe experiments in this study show that the dissociation rate of the benzyl radical at the 254 nm excitation wavelength is on the order of ~ 5-10 x 10^7/s. The unimolecular dissociation rate of the benzyl radical is also calculated using the RRKM theory from an online RRKM calculation program [Chemical Dynamics Software and Simulation System (http://cdssim.chem.ttu.edu)]. The structures, vibrational frequencies, and rotational constants for the transition states and product are from the

theoretical work of Cavallotti et al.[27] The loss of the H atom is assumed to be the rate determining step during the dissociation of benzyl radical. The decomposition rate constant of benzyl at 254 nm excitation is calculated to be ~10^5/s, much smaller than the experimental value measured here. Although it has been shown that the experimental thermal dissociation rate of the benzyl radical is about 10 times larger than the RRKM theoretical thermal dissociation rate in the temperature range of 1500-2000 K,[28,30] the observed dissociation rate in this study is still much larger than expected from the previous thermal dissociation study and the RRKM calculations. It is unlikely for this to be caused by two-photon dissociation of benzyl, as low laser power was used and only the slower H-atom signals (with linear photolysis laser power dependence) was integrated for the delay time profiles. The H-atom detection efficiency should not be significantly affected by the flight out time of H atoms, as indicated by a few experimental checks [the slower H-atom signals (40-100 μs) were integrated for the HRTOF time profile, D atoms slowed down the flight out, and defocused probe beams were used, etc.]. Barring any other experimental bias, the measured dissociation rate of benzyl might suggest that the internal energy of the benzyl radical is not completely randomized in the photoexcitation and unimolecular dissociation process. Indeed, if fewer than the 36 full vibrational modes of the benzyl radical are involved in the randomization of the internal energy and dissociation, the RRKM dissociation rate would increase. A faster rate of 10^7-10^8/s can

be reached if only 21-22 vibrational modes (both large and low frequency) are considered in the RRKM calculation. Further experimental and theoretical studies would help to resolve the discrepancy in the dissociation rate of the benzyl radical.

The isotope labeling experiments show that at 254 nm the H/D product yield ratios are 5.5 ± 1.2 for $C_6H_5CD_2$ and 0.55 ± 0.1 for $C_6D_5CH_2$, respectively. Table 5.1 also shows the H/D ratios based on three simple models, the statistical model which assumes total scrambling of the H and D in benzyl, the ring model with elimination of only H/D on the aromatic ring (the fulvenallene channel via **3** →**10**, **11**, **12**→ **13**), and the side-chain model where the H/D is eliminated from the CH_2 group [via **2** and **5**, to C_7H_6 (**4**) + H and C_7H_6 (**6**) + H, respectively, Figure 5.1]. The measured H/D ratios indicate that the H/D elimination from benzyl is not site specific and are reasonably close to the statistical H/D ratios, with a small preference for H elimination than D. Clearly, the ring model or side-chain model alone could not explain the experimental H/D ratios. If both the ring model and side-chain model are involved, the statistical H/D ratios could be observed. However, the products in the side-chain model, C_7H_6 (**4**) + H and C_7H_6 (**6**) + H, are much higher in energy than fulvenallene (**13**) + H in the ring model (Figure 5.1), and therefore are unlikely.[27-29] In order to explain the statistical H/D ratios or the observed H/D ratios using only the lower energy fulvenallene (**13**) + H channel, where the H/D is eliminated only from the ring (Figure 5.1), the H and D atoms in the partially

labeled benzyl have to scramble. One possible mechanism is for benzyl to isomerize via **1** ↔ **2** ↔ **5** ↔ **8**, where the last step is via 1,6 H/D shift and scrambles H/D. H/D could be further scrambled via **8** ↔ **9** (cycloheptatrienyl radical, Figure 5.1). These processes have an overall barrier of 83.0 kcal/mol, comparable to those of the fulvenallene (**13**) + H channel. If the hot benzyl radical with a total excitation energy of 112.6 kcal/mol (at 254 nm) samples and isomerizes to this region and then back to MBH (**3**), the H/D on the ring and the CH_2 group could be scrambled before dissociating to fulvenallene (**13**) + H, generating an H/D product ratio close to the statistical model. The similar H TOF spectra of $C_6H_5CH_2$, $C_6H_5CD_2$, and $C_6D_5CH_2$ and the similar D TOF spectra from $C_6D_5CD_2$ and $C_6D_5CH_2$ also support the mechanism in which the H atom elimination from benzyl is not site specific and the H and D atoms are scrambled before dissociation. As the H/D migration should be very fast, this mechanism is still consistent with the 5-10 x 10^7/s dissociation rate of benzyl.

5.5 Conclusion

The H-atom product channel in the UV photodissociation of jet-cooled benzyl is studied in the wavelength region of 228 to 270 nm using the HRTOF and REMPI techniques. In this wavelength region, the H-atom PFY spectra using both the

ethylbenzene and benzyl chloride precursors have a broad peak centered around 254 nm and are in good agreement with the previous UV absorption spectra of benzyl. The H + C_7H_6 product translational energy distributions, $P(E_T)$'s, are derived from the H-atom TOF spectra. The $P(E_T)$ distributions peak at ~5.5 kcal/mol, and the fraction of the average translational energy in the total excess energy, $\langle f_T \rangle$, is nearly a constant of ~0.3 in the wavelength region of 228 to 270 nm. The $P(E_T)$ distributions indicate the production of fulvenallene + H, in agreement with the recent theoretical studies. The H-atom product angular distribution is isotropic, with the anisotropy parameter $\beta \approx 0$. Isotope labeling studies show that the H/D product ratios from $C_6H_5CD_2$ and $C_6D_5CH_2$ are close to the statistical H/D ratios, indicating that the H/D atoms are scrambled in the photodissociation of benzyl. The dissociation mechanism is consistent with internal conversion of the electronically excited benzyl followed by unimolecular decomposition on the ground state.

References

(1) Carrington, A.; Smith, I. C. P. *Molecular Physics* **1965**, *9*, 137.

(2) Porter, G.; Ward, B. *Journal De Chimie Physique Et De Physico-Chimie Biologique* **1964**, *61*, 1517.

(3) Cossart-Magos, C.; Leach, S. *Journal of Chemical Physics* **1972**, *56*, 1534.

(4) Cossart-Magos, C.; Leach, S. *Journal of Chemical Physics* **1976**, *64*, 4006.

(5) Okamura, T.; Charlton, T. R.; Thrush, B. A. *Chemical Physics Letters* **1982**, *88*, 369.

(6) Orlandi, G.; Poggi, G.; Zerbetto, F. *Chemical Physics Letters* **1985**, *115*, 253.

(7) Negri, F.; Orlandi, G.; Zerbetto, F.; Zgierski, M. Z. *Journal of Chemical Physics* **1990**, *93*, 600.

(8) Fukushima, M.; Obi, K. *Journal of Chemical Physics* **1992**, *96*, 4224.

(9) Lin, T.; Tan, X.; Cerny, T. M.; Williamson, J. M.; Cullin, D. W.; Miller, T. A. *Chemical Physics* **1992**, *167*, 203.

(10) Ward, B. *Spectrochimica Acta Part a-Molecular Spectroscopy* **1968**, *A 24*, 813.

(11) Ikeda, N.; Nakashima, N.; Yoshihara, K. *Journal of Physical Chemistry* **1984**, *88*, 5803.

(12) Porter, G.; Savadatt, M. *Spectrochimica Acta* **1966**, *22*, 803.

(13) Damm, M.; Deckert, F.; Hippler, H. *Berichte Der Bunsen-Gesellschaft-Physical Chemistry Chemical Physics* **1997**, *101*, 1901.

(14) Bayrakceken, F.; Nicholas, J. E. *Journal of the Chemical Society B-Physical Organic* **1970**, 691.

(15) Markert, F.; Pagsberg, P. *Chemical Physics Letters* **1993**, *209*, 445.

(16) Astholz, D. C.; Troe, J. *Journal of the Chemical Society-Faraday Transactions Ii* **1982**, *78*, 1413.

(17) Mullermarkgraf, W.; Troe, J. *Journal of Physical Chemistry* **1988**, *92*, 4899.

(18) Hippler, H.; Reihs, C.; Troe, J. *Zeitschrift Fur Physikalische Chemie Neue Folge* **1990**, *167*, 1.

(19) Jones, J.; Bacskay, G. B.; Mackie, J. C. *Journal of Physical Chemistry A* **1997**, *101*, 7105.

(20) Oehlschlaeger, M. A.; Davidson, D. F.; Hanson, R. K. *Journal of Physical Chemistry A* **2006**, *110*, 6649.

(21) Braunukhoff, M.; Frank, P.; Just, T. *Berichte Der Bunsen-Gesellschaft-Physical Chemistry Chemical Physics* **1990**, *94*, 1417.

(22) Rao, V. S.; Skinner, G. B. *Proceedings of the Combustion Institute* **1986**, *21*, 809.

(23) Baulch, D. L.; Cobos, C. J.; Cox, R. A.; Esser, C.; Frank, P.; Just, T.; Kerr, J. A.; Pilling, M. J.; Troe, J.; Walker, R. W.; Warnatz, J. *Journal of Physical and Chemical Reference Data* **1992**, *21*, 411.

(24) Smith, R. D. *Journal of Physical Chemistry* **1979**, *83*, 1553.

(25) Colket, M. B.; Seery, D. J. *Proceedings of the Combustion Institute* **1994**, *25*, 883.

(26) Frochtenicht, R.; Hippler, H.; Troe, J.; Toennies, J. P. *Journal of Photochemistry and Photobiology a-Chemistry* **1994**, *80*, 33.

(27) Cavallotti, C.; Derudi, M.; Rota, R. *Proceedings of the Combustion Institute* **2009**, *32*, 115.

(28) da Silva, G.; Cole, J. A.; Bozzelli, J. W. *Journal of Physical Chemistry A* **2009**, *113*, 6111.

(29) da Silva, G.; Cole, J. A.; Bozzelli, J. W. *Journal of Physical Chemistry A* **2010**, *114*, 2275.

(30) Damm, M.; Deckert, F.; Hippler, H.; Rink, G. *Physical Chemistry Chemical Physics* **1999**, *1*, 81.

(31) Zierhut, M.; Noller, B.; Schultz, T.; Fischer, I. *Journal of Chemical Physics* **2005**, *122*.

(32) Amaral, G.; Xu, K. S.; Zhang, J. S. *Journal of Chemical Physics* **2001**, *114*, 5164.

(33) Xu, K. S.; Amaral, G.; Zhang, J. S. *Journal of Chemical Physics* **1999**, *111*, 6271.

(34) Zhou, W. D.; Yuan, Y.; Chen, S. P.; Zhang, J. S. *Journal of Chemical Physics* **2005**, *123*, 054330.

(35) Brand, U.; Hippler, H.; Lindemann, L.; Troe, J. *Journal of Physical Chemistry* **1990**, *94*, 6305.

(36) Tonokura, K.; Koshi, M. *Journal of Physical Chemistry A* **2003**, *107*, 4457.

(37) Wendt, H. R.; Hunziker, H. E. *Journal of Chemical Physics* **1984**, *81*, 717.

(38) Zhao, X. Ph.D. Thesis, University of California, Berkeley, 1988.

(39) Zhang, J. S.; Dulligan, M.; Wittig, C. *Journal of Physical Chemistry* **1995**, *99*, 7446.

(40) Zare, R. N. *Mol. Photochem.* **1972**, *4*, 1.

CHAPTER 6

Ultraviolet photodissociation dynamics of the allyl radical

ABSTRACT

Ultraviolet (UV) photodissociation dynamics of jet-cooled allyl radical via the $\widetilde{E}^2B_1(3p_x)$ electronically excited state is studied in the photolysis wavelength region of 216 to 238 nm using high-*n* Rydberg atom time-of-flight (HRTOF) and resonance enhanced multiphoton ionization (REMPI) techniques. In this wavelength region, H-atom photofragment yield (PFY) spectra are obtained using allyl chloride and 1,5-hexadiene as the precursors of allyl radical, and they have a broad peak centered around 228 nm while the previous UV absorption spectra of allyl radical peak at around 220 nm. This comparison suggests another dissociation channel in this region (possibly $CH_3 + C_2H_2$ channel) in addition to the $C_3H_4 + H$ channel. The $C_3H_4 + H$ product translational energy release is modest, with the $P(E_T)$ distributions peaking near 9 kcal/mol and the fraction of average translational energy in the total excess energy, $\langle f_T \rangle$, is ~0.2. The $P(E_T)$'s indicate the production of allene + H or propyne + H, which was suggested by previous experimental and theoretical studies. The H-atom product angular distribution is isotropic, with the anisotropy parameter $\beta \approx 0$. The H dissociation rate from pump-probe

study gives a lower limit 1×10^{8} s^{-1}. The dissociation mechanism is consistent with internal conversion of the electronically excited allyl followed by unimolecular decomposition of the hot allyl radical on the ground state.

6.1 Introduction

Allyl radical (C_3H_5) is a representative species in organic chemistry mainly due to its special structure. The three carbon atoms in allyl radical are sp^2 hybridized and lie in a plane. The three unpaired π electrons of the carbon atoms are resonance delocalized, making this radical very stable. Thus allyl radical is the smallest π conjugated system with odd number of π electrons. Meanwhile allyl radical plays an important role in combustion chemistry and interstellar chemistry[1]. In addition to the propargyl radical (C_3H_3), allyl radical was proposed to be one of the most important precursors for the formation of benzene and other cyclic compounds in the flames[2-4]. As a result, this radical has been studied extensively for decades.

The first electronic absorption spectrum of allyl radical was measured by Currie and Ramsay[5] in 1966 by flash photolysis of allyl bromide and other allyl precursors at 370-410 nm. The band origin at 408.3 nm was assigned to be the 0-0 transition from the ground electronic state 1^2A_2 to the first excited electronic state 1^2B_1. Later, this transition was confirmed by Tonokura et al.[6] using the cavity ring-down spectroscopy between 370 and 420 nm. In 1967, a new electronic spectrum of allyl radical was reported by Callear and Lee[7] at 210-250 nm by flash photolysis of eight allyl compounds and repeated later by van den Bergh et al.[8] and Jenkin et al.[9] This band was stronger than that at 408.3 nm

region and had diffuse structure with a maximum absorption around 220-222 nm. In 2003, another electronic absorption spectrum at the same region was taken by Bayrakceken et al.[10] and the extinction coefficients at several wavelengths were calculated based on the decay rate constants of the allyl radical. The three electronic absorption spectra were shown in Figure 6.6.

A series of 1+1 and 2+2 MPI studies[11-13] were carried out by Chen's group to locate the electronic states of allyl radical and its isotopic compounds. The B^2A_1, C^2B_1 and D^2B_2 band origins of allyl radical were assigned to be at 40056.5cm^{-1} (249.68 nm), 40305.5cm^{-1} (248.15 nm) and 41557.8 cm^{-1} (240.60 nm), respectively. Several vibronic states were observed as well. It is noteworthy that in these studies, the MPI signal decreased blow 238 nm, in contrast with the strong absorption spectrum of allyl radical around 220-222 nm, indicating that a fast nonradiative decay may exist at that region. Very recently, Chen's group reported their new results[14] on the revised assignments of several excited electronic states, including the previous observed vibronic states, using the REMPI technique. They generated the allyl radicals by two methods: pyrolysis of 1,5-hexadiene and photolysis of allyl iodide, followed by supersonic cooling in the beam. Since the pyrolytically produced allyl radicals were not cooled down as efficiently as those by the photolysis, more vibronic peaks showed up in the REMPI spectrum of the former condition as well as in the REMPI spectra previously observed.[11,12] These peaks

were attributed to the hot radicals on the vibrationally excited ground electronic state. Thus new assignments of the excited electronic states of allyl radical were given and the band origin for each state is listed as following: B^2A_1 (3s) at 40046 cm^{-1}, C^2B_2 ($3p_y$) at 41556 cm^{-1}, D^2A_1 ($3p_z$) at 42230 cm^{-1}. By combing with the electronic depletion spectroscopy, a defuse band starting from 43300 cm^{-1} up to 45000 cm^{-1} was detected and was assigned to the Rydberg electronic state E^2B_1 ($3p_x$). This band was in good agreement with the absorption spectrum at 220-222 nm. Since this band was not observed in the REMPI spectrum in the same frequency region, lifetime of this excited state was indicated to be very short. Some theoretical calculations[15-19] were performed at the same time to exam the upper excited electronic states. However, the assignments and energies of the excited electronic states were not quite consistent with the experimental work except for the first excited electronic state A^2B_1.

From 1997, UV photodissociation dynamics of the allyl radical was investigated by several groups around the photolysis wavelength 248 nm[20-25] while the unimolecular dissociation of the hot allyl radical was studied through the secondary decomposition of the allyl iodide with 193 nm radiation.[26,27] Fischer and Chen's work[20,21] detected the H product channel of allyl radical by using time- and frequency-resolved photoionization of H products at 248.15 nm and 245.85 nm (previously assigned as $C\,0_0^0$ and $C\,7_0^1$, now revised to be $B12_0^1$ and $B7_0^112_0^1$ electronic states[14]). The dominant dissociation channel

was identified to be a fast loss of H atom to generate allene as confirmed by the loss of central H atom from the isotopic labeled CH_2CDCH_2 and CD_2CHCD_2. The second H channel was a slower 1,2 shift isomerization of allyl radical to 2-propenyl, followed by H loss to form allene + H and propyne + H. This channel was proposed since the time delay study showed two different H decay rates (~10^8/s and 4×10^7/s). The branching ratio of these two channels was between 2:1 and 3:1. The third H channel is to generate the cyclopropene and H products (*c*-C_3H_4 + H). These three possible H loss reaction channels are summarized as following:

CH_2CHCH_2 (X^2A_2) + hν → CH_2CCH_2 + H, ΔH=57.1[21] (54.4[28]) kcal/mol

CH_2CHCH_2 (X^2A_2) + hν → $CHCCH_3$ + H, ΔH=56.1[21] (53.3[28]) kcal/mol

CH_2CHCH_2 (X^2A_2) + hν → *c*-C_3H_4 + H, ΔH=78.6[21] kcal/mol

CH_2CHCH_2 (X^2A_2) + hν → CH_3 + C_2H_2, ΔH=46.2[28] kcal/mol

The product energy distribution was statistical, and the dissociation mechanism of allyl radical around 248 nm was the hot radical dissociated at the ground electronic state following internal conversion from UV excited electronic state. At the same time, the lifetimes of vibronic states of allyl radical between 238 nm and 250 nm were measured using picoseconds time-resolved pump-probe photoelectron spectroscopy by Fischer's group[29,30]. The allyl radical was excited by a pump laser and then detected by probe laser using MPI in order to measure the disappearance time of allyl radical on the excited state.

The lifetimes were ranging from 9 ps to 20 ps, supporting the fast nonradiative decay of allyl radical in the previous study. Besides the dominant H channel, another dissociation channel of allyl radical, $CH_3 + C_2H_2$, was investigated by Stranges et al.[23,24] using photofragment translational spectroscopy at 248 nm and 351 nm. The branching ratio of H channel to $CH_3 + C_2H_2$ channel was 84:16 at 248 nm. The dissociation mechanisms for both channels at 248 nm were discussed. The H dissociation pathway may come from the internal conversion or the predissociation of a higher excited electronic state. The main dissociation products were allene and propyne, with minor *c*-C_3H_4 produced. The observation of the H atom is consistent with Chen's work.[21] The dissociation pathway of CH_3 elimination was proposed to be direct dissociation to the $CH_3 + C_2H_2$ or isomerization from allyl to 1-propenyl and 2-propenyl radical, followed by dissociation to the $CH_3 + C_2H_2$ products.

Figure 6.1 shows the potential energy diagram and electronic states for allyl radical. The energies of the various pathways and electronic states are based on previous theoretical and experimental studies.[5,14,21,28] Three H dissociation pathways and one methyl channel are presented in the figure. They are allene + H, propyne + H, *c*-C_3H_4 + H and $CH_3 + C_2H_2$. According to the energies of different transition states, the direct dissociation from allyl radical to allene + H channel has the lowest activation energy of

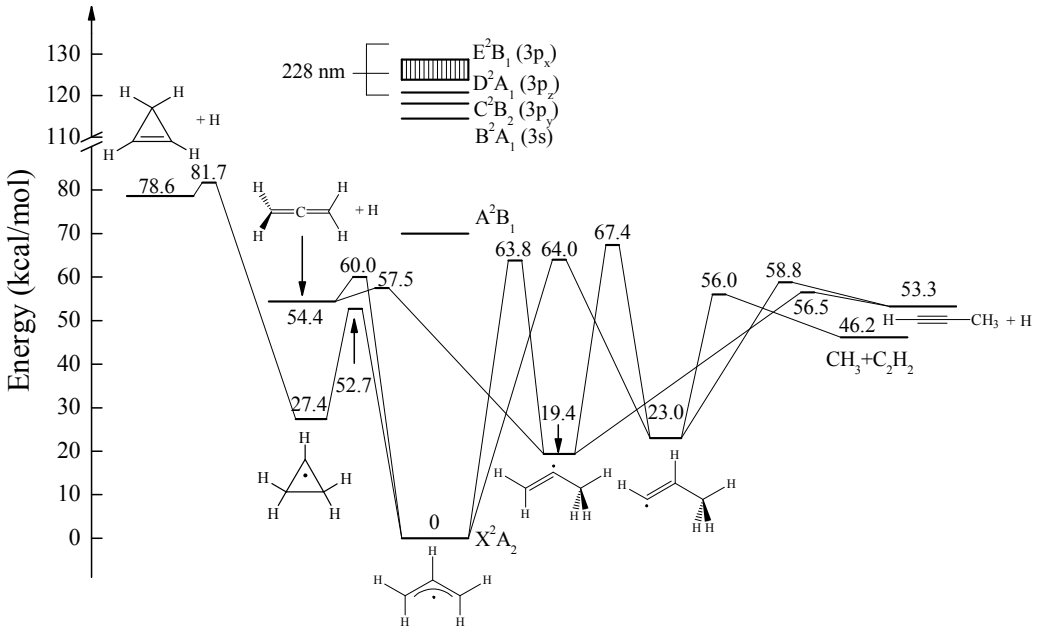

Figure 6.1 Potential energy diagram of the C_3H_5 system. Three possible H-atom dissociation channels and CH_3 elimination channel are shown in the figure. The energetics and pathways are based on the theoretical calculations in Refs 21 and 27. The energies of the electronic excited states of the allyl radical are based on Refs 5 and 14. The bracket next to the electronic states shows the photolysis wavelength region 216-238 nm in this study.

60.0 kcal/mol and thus is the most energetic favorable dissociation channel for allyl radical. Additional pathway to allene product is the isomerization from allyl to 2-propenyl radical which dissociates to allene product (with an overall activation energy of 63.8 kcal/mol). Although allene is the most energetic favorable pathway of the allyl radical, other dissociation channels cannot be neglected since the barriers of transition states are comparable to that of the allene + H channel. One example is propyne (CH_3CCH) + H. There are several pathways to form propyne. (1) Allyl radical isomerizes to 2-propenyl which dissociates to propyne and H, $CH_2CHCH_2 \rightarrow CH_2CCH_3 \rightarrow CH_3CCH + H$ (activation energy 63.8 kcal.mol). (2) Allyl isomerizes to 1-propenyl radical then dissociates to propyne and H, $CH_2CHCH_2 \rightarrow CHCHCH_3 \rightarrow CH_3CCH + H$ (activation energy 64.0 kcal/mol). (3) Allyl first isomerizes to 2-propenyl which further isomerizes to 1-propenyl and then dissociates to propyne and H, $CH_2CHCH_2 \rightarrow CH_2CCH_3 \rightarrow CHCHCH_3 \rightarrow CH_3CCH + H$ (activation barrier 67.4 kcal/mol). Another H dissociation channel forms the cyclo-C_3H_4 product. The thermal ring opening of the cyclopropyl radical into allyl radical has been discussed theoretically[31,32]. The activation energy of the cyclopropene + H channel (81.7 kcal/mol) is higher than the other two H dissociation channels and thus is considered as a minor dissociation pathway on the ground electronic state. Besides the H dissociation channel, the $CH_3 + C_2H_2$ product channel also contributes 16% in the total dissociation events around 248 nm[23]. The two

possible pathways to form methyl are: (1) Allyl isomerizes to 1-propenyl radical then dissociates to products, $CH_2CHCH_2 \rightarrow CHCHCH_3 \rightarrow CH_3 + C_2H_2$ (activation energy 64.0 kcal/mol). (2) Allyl first isomerizes to 2-propenyl which further isomerizes to 1-propenyl and then dissociates, $CH_2CHCH_2 \rightarrow CH_2CCH_3 \rightarrow CHCHCH_3 \rightarrow CH_3 + C_2H_2$ (activation barrier 67.4 kcal/mol). These two pathways are very similar to the last two propyne pathways mentioned above. The energies of the electronic states of the allyl radical are also labeled in Figure 6.1 which are based on the recent REMPI study[14], while the bracket next to the electronic states represents the photolysis wavelength region 216-238 nm in this study.

In the present study, the high-n Rydberg H atom time-of-flight (HRTOF) technique was employed to detect the H dissociation channel of the allyl radical in the photolysis wavelength region 216-238 nm, which covers the absorption maximum of 222 nm in UV region. As mentioned above, most of the previous photochemistry work focused on the dissociation of allyl radical around 248 nm[21] at electronic state B^2A_1 (3s), 351 nm[23] at the first excited electronic state A^2B_1, or secondary decomposition of allyl iodide with 193 nm radiation to generate hot allyl radical which confirmed the allene production[26,27]. There is no photodissociation work related to the short wavelength of 216-238 nm. However, the decreased REMPI signal and the large oscillator strength around 222 nm indicates a nonradiative decay and decomposition of the allyl radical, promotes us to

move to the shorter region. This is the first time that the H channel of allyl radical was observed and unimolecular dissociation dynamics was studied around this wavelength.

6.2 Experimental

The HRTOF technique and experimental setup have been described previously.[33-35] A pulsed allyl (C_3H_5) radical beam was generated by photolyzing a ~5% mixture of allyl chloride (98%, Aldrich) or 1,5-hexadiene (97%, Aldrich) seeded in Ar (at a total pressure of 115kPa), with the 193-nm radiation of an ArF excimer laser that was focused in front of the pulse nozzle. The allyl radicals produced from the photolysis were entrained in the seeded beam and subsequently cooled by supersonic expansion. The radical beam was collimated at 2.8 cm downstream by a 1-mm diameter skimmer into a high-vacuum chamber; at 4.6 cm further downstream the skimmer, the allyl radical beam was crossed with a slightly focused UV photolysis laser radiation (at 216-238 nm, 0.25-1.2 mJ/pulse, linewidth ~0.3 cm^{-1}). The absolute photolysis laser wavelength was monitored by a wavemeter (Burleigh WA-4500). The polarization of the photolysis radiation was rotated by a Fresnel-Rhomb achromatic $\lambda/2$ plate for product angular distribution measurements. The H atoms produced from the allyl photodissociation were tagged by two-color resonant excitation (121.6+366.3 nm), i.e., from 1^2S to 2^2P via the H-atom Lyman-α

transition and then further to a high-n Rydberg state. A small fraction of the radiatively metastable Rydberg H atoms drifted with their nascent velocities toward a microchannel plate (MCP) detector that is positioned perpendicular to the molecular beam, and were field-ionized in front of the detector and detected. The nominal flight length was 37.1cm, which was calibrated by 236 nm photodissociation of HBr [with the spin-orbit splitting of $Br(^2P_{3/2})$ and $Br(^2P_{1/2})$ and the difference between the various vibrational levels of the vibrationally hot and rotationally cold HBr in the beam]. The ion signals were amplified by a fast preamplifier, and the H-atom TOF spectra were recorded and averaged by using a multichannel scaler. The H-atom TOF spectra were accumulated with ~10^5 laser firings. Typically four types of HRTOF spectra were taken (including the full spectrum and three background spectra), and the net HRTOF spectra from the UV photolysis of allyl radical were obtained after proper background subtraction.

The H-atom photofragment yield (PFY) spectra (i.e., action spectra) were recorded using two methods. The first method involved integrating the net HRTOF spectra (after the background removal) as a function of photolysis wavelength. The second was based on collecting the H-atom REMPI signals as a function of photolysis wavelength. The H-atom REMPI experiment was conducted in the same HRTOF instrument. Upon photodissociation by the UV laser radiation in the range of 231-248 nm, the H atom products were detected by 1+1' REMPI, with one Lyman-α photon resonantly exciting

the H atoms from 1^2S to 2^2P and a UV photon at ~364 nm ionizing the H atoms. The photolysis and REMPI probe laser delay time was fixed at 10 ns for the action spectra but varied for the pump-probe time profile measurements later. The H^+ ions were extracted and accelerated in the linear TOF mass spectrometer, and were detected by the MCP detector. The mass-resolved ion current signal (m/z=1) was amplified by a preamplifier, recorded in a digital storage oscilloscope, and integrated by the Boxcar averager (SR250), then transferred to the computer. Two types of REMPI signal were recorded, (i) with the 193-nm radiation on (for the allyl radical production), the UV photolysis radiation on, and the REMPI probe lasers on; and (ii) background with the 193-nm radiation off, but the UV photolysis radiation and the REMPI probe lasers on. The PFY spectra were the net H-atom REMPI signals with the background (ii) removed. The photolysis laser power was normalized for the H-atom PFY spectra.

REMPI spectra of the allyl radical were also searched by using a (1+1) scheme. The UV laser radiation in the region of 237-248 nm was focused with a f.l. ≈ 100 cm lens onto the allyl radical beam, and the m/z=41 peak was monitored by an oscilloscope and integrated as a function of photolysis wavelength using a Boxcar averager (SR250). The averaged signal from the Boxcar averager was sent to the LAS data acquisition software to record the allyl REMPI spectrum.

6.3 Results

In order to confirm the allyl radical in the molecular beam, VUV photoionization TOF mass spectroscopy was performed for both precursors: allyl chloride and 1,5-hexadiene. Figure 6.2 is a net TOF mass spectrum of allyl chloride precursor with 193-nm radiation on minus 193-nm off. Two predominant peaks showed up in the whole mass spectrum: m/z=41 represents allyl radical and m/z=76 represents allyl chloride. The negative allyl chloride peak is due to the depletion of allyl chloride to make allyl radical. The TOF mass spectrum of 1,5-hexadiene was recorded and allyl peak was also observed in the spectrum.

The REMPI spectra of the allyl radical generated from allyl chloride in the region 237-248.5 nm are shown in Figure 6.3. Six peaks were observed at around 40300 cm^{-1}, 40630 cm^{-1}, 40670 cm^{-1}, 41550 cm^{-1}, 42130 cm^{-1} and 42500 cm^{-1}. The positions of the first five peaks are in good agreement with the previous REMPI spectra of the allyl radical[14] with these five peaks assigned to $B1 2_0^1$, $B9_0^1$, $B7_0^1 12_0^1$, $C\,0_0^0$ and $C\,9_0^1$, supporting the allyl production in the molecular beam. Meanwhile the H^+ REMPI signals from photodissociation of the allyl radical are shown in the same figure as a function of the photolysis wavelength. The recorded H^+ REMPI peaks appeared at different photolysis wavelengths (40630 cm^{-1}, 40670 cm^{-1}, 42130 cm^{-1} and 43270 cm^{-1}) comparing

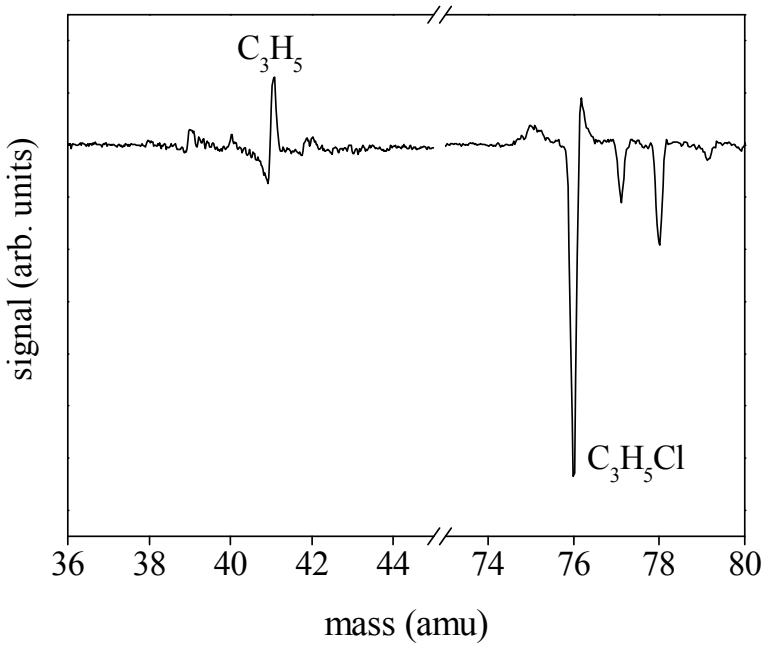

Figure 6.2 121.6 nm VUV photoionization mass spectrum of the allyl radical beam using the allyl chloride precursor in Ar carrier gas. This is the net mass spectrum of allyl chloride with the 193 nm photolysis laser on minus off. The main product is allyl radical at m/z = 41 amu, while the allyl chloride parent peak at m/z = 76 is depleted due to the 193 nm photolysis. Photoionization fragmentation is small due to the low photon energy at 121.6 nm and is removed in the net mass spectrum.

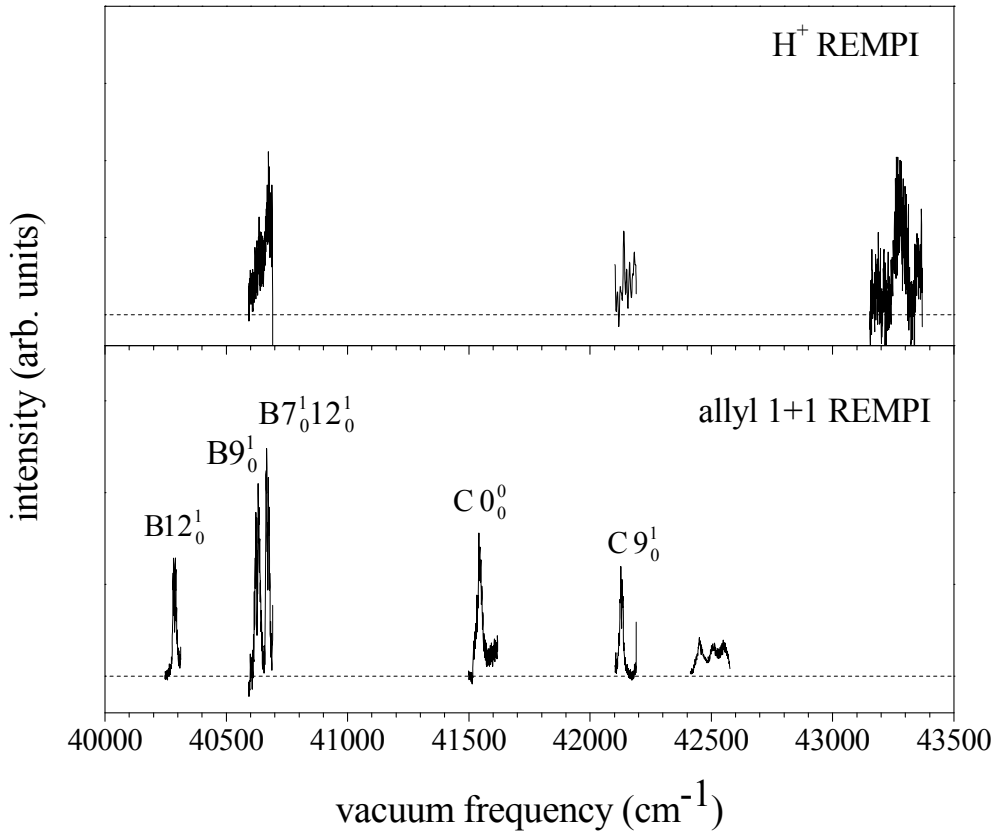

Figure 6.3 The bottom part is the REMPI spectra of the allyl radical generated from allyl chloride in the region 237-248.5 nm. The top part is the H^+ REMPI signal from photodissociation of the allyl radical as a function of the photolysis wavelength.

to the allyl REMPI peaks. Although the H^+ signals were not as intense as the allyl radical due to the lower sensitivity of H detection in the small range, the H signals still showed an increasing trend at the corresponding allyl REMPI resonances, confirming the H atoms were produced during the photodissociation of the allyl radical.

The H-atom TOF spectra from the photodissociation of allyl radical were measured in the photolysis wavelength region 216-238 nm, with the photolysis laser polarization parallel and perpendicular to the flight path, respectively. Four types of TOF spectra were recorded to identify the origins of the H-atom signals and to establish procedures for background subtraction,: (1) full spectrum, with both the 193-nm radiation on (for allyl radical production) and the UV photolysis radiation on, plus the Rydberg atom tagging probe-laser radiations (121.6+366.3 nm); (2) precursor background spectrum, with the 193-nm radiation off but the UV photolysis radiation on, plus the probe-laser radiations; (3) radical background spectrum caused by probe lasers, with both the 193-nm radiation on and probe radiations on, but the UV photolysis radiation off; and (4) probe-laser background spectrum, with both the 193-nm radiation off and the UV photolysis radiation off, but only the probe radiations on. The background spectra (3) and (4) were observed to be small in the time range of interest. The difference of these two spectra was possibly caused by the H signal produced from photodissociation of allyl radical by the probe lasers. These two background spectra were taken at each experimental day and were

removed from the full spectrum. The precursor background spectrum (2) represents the main background, i.e., contributions from photolysis of allyl chloride or 1,5-hexadiene precursor by the UV photolysis radiation. The net H-atom TOF spectrum of allyl photodissociation is obtained by removing the background spectrum (2) (3) (4) from the full spectrum (1). Figure 6.4a and 6.4b shows the net H-atom TOF spectra at two different photolysis wavelengths 228 nm and 222 nm (0.55-0.85 mJ/pulse) with two precursors allyl chloride and 1,5-hexadiene. The two TOF spectra from different precursors at the same wavelength were essentially identical, supporting the H signals are from the allyl photodissociation.

Figure 6.5a shows H-atom TOF spectra from 1,5-hexadiene precursor at 230 nm with three different photolysis powers: 1.15, 0.8 and 0.45 mJ/pulse. The shapes of the TOF spectra stayed the same, and intensities of the TOF spectra increased linearly with the laser power. No fast component was observed at these three TOF spectra, illustrating the single-photon dissociation process with the highest photolysis power 1.15 mJ/pulse. The accumulated H signals were plot as a function of photolysis power in Figure 6.5b, which shows a linear power dependence. Thus the photolysis power was maintained below 1.2 mJ/pulse at all times in the present study to prevent any multi-photon dissociation.

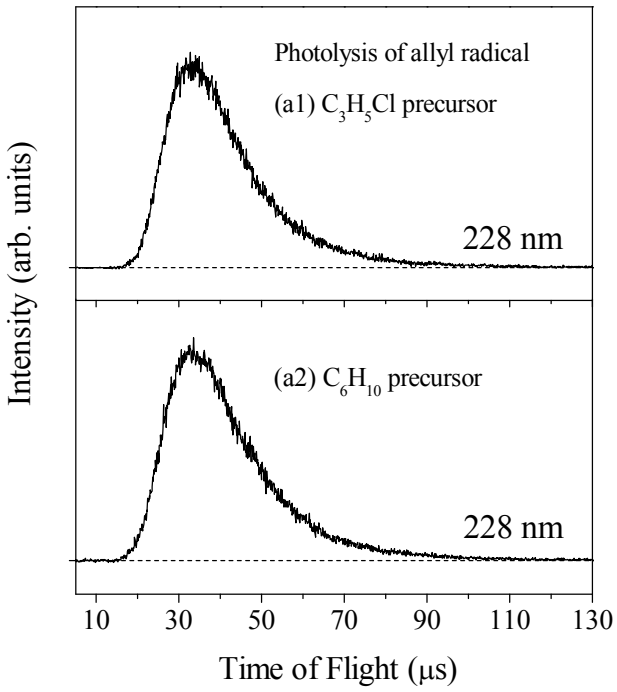

Figure 6.4a H-atom TOF spectra of jet-cooled allyl radical at photolysis wavelength 228 nm, produced from 193-nm photolysis of (1) allyl chloride precursor and (2) 1,5-hexadiene precursor. These are the net TOF spectra with the full spectrum minus three backgrounds. The polarization vector of the photolysis laser radiation is parallel (θ = 0°) to the TOF axis. The photolysis radiation power intensity is 0.55-0.85 mJ/pulse.

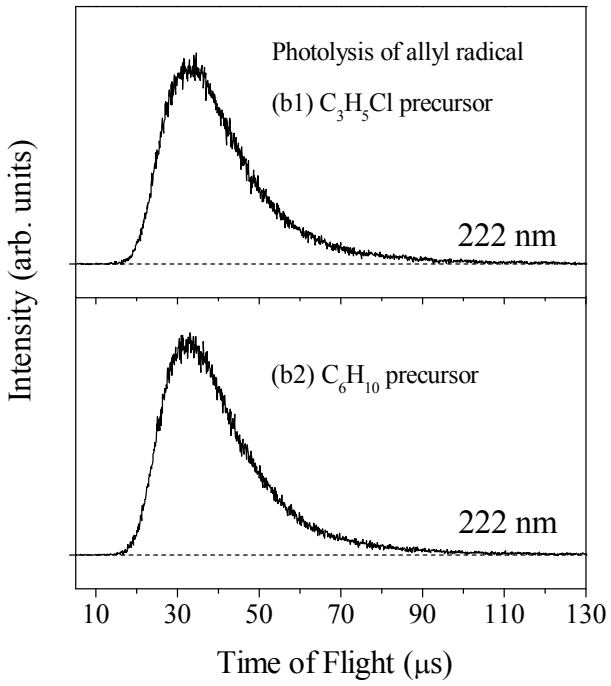

Figure 6.4b H-atom TOF spectra of jet-cooled allyl radical at photolysis wavelength 222 nm, produced from 193-nm photolysis of (1) allyl chloride precursor and (2) 1,5-hexadiene precursor. These are the net TOF spectra with the full spectrum minus three backgrounds. The polarization vector of the photolysis laser radiation is parallel (θ = 0°) to the TOF axis. The photolysis radiation power intensity is 0.55-0.85 mJ/pulse.

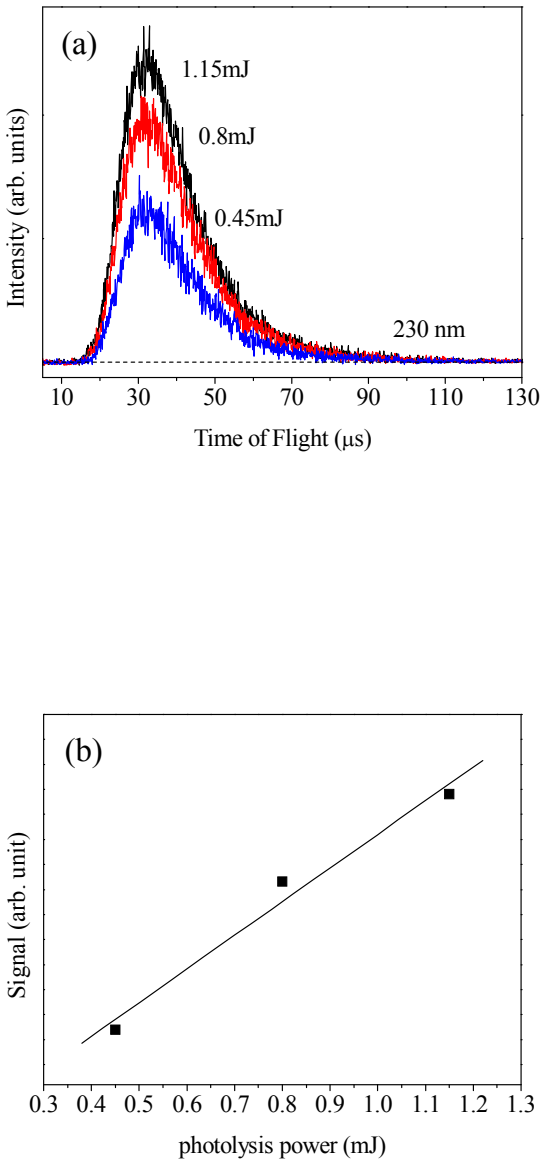

Figure 6.5 Photolysis laser power dependence: (a) the H-atom product TOF spectra of the allyl radical at 230 nm with photolysis energy 1.15, 0.8 and 0.45 mJ/pulse. (b) integration of the H signals in the TOF spectra as a function of the photolysis power which shows the H signals have a linear dependence on the photolysis laser power.

Figure 6.6 shows the PFY spectra of both precursors from integrating the HRTOF signal as a function of photolysis wavelength at 216-238 nm. To correct for the variation and drift of the experimental conditions, H-atom signals from the 222 and 230 nm photolysis were used as a reference and were monitored after every 3 measurements at other wavelengths. The H-atom intensities at other photolysis wavelength were scaled to that of 228 nm and normalized to the photolysis laser power. The two PFY spectra agree well with each other, with maximum signal at 228 nm. Figure 6.6 also shows three previous UV absorption spectra by van den Bergh et al., Jenkin et al. and Bayrakceken et al.[8-10] Both absorption spectra from van den Bergh et al. and Jenkin et al. are strong and diffuse, peaking at ~222 nm. In order to compare these three absorption spectra with the PFY spectra from present study, the absorption cross sections for each absorption spectrum were divided by 1.8×10^{-17} to give a comparable intensity as PFY spectra in the present study.

The net H-atom TOF spectrum of the jet-cooled allyl radical could be transformed to total center-of-mass (CM) translational energy distributions, $P(E_T)$'s. The CM translational energy of products, E_T, is converted from the H-atom flight time t_H using the following equation:

$$E_T = \left(1+\frac{m_H}{m_{C_3H_4}}\right)E_H + \frac{m_H}{m_{C_3H_4}}E_{C_3H_5} = \frac{1}{2}m_H\left(1+\frac{m_H}{m_{C_3H_4}}\right)\left(\frac{L}{t_H}\right)^2 + \frac{m_H}{m_{C_3H_4}}E_{C_3H_5} \quad (1)$$

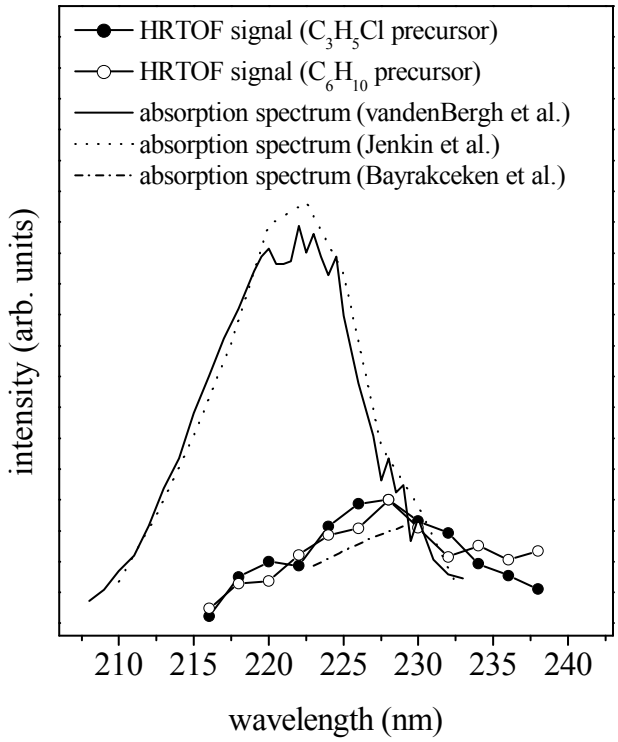

Figure 6.6 H-atom product yield (PFY) spectra as a function of photolysis excitation energy in the region of 216-238 nm. Full circles (●) represent the integrated HRTOF signals using the allyl chloride precursor. Open circles (○) represent the integrated HRTOF signals using the 1,5-hexadiene precursor. Solid, dotted and dash-dotted lines are the absorption spectra taken from Refs 8, 9, 10. The photolysis laser power is normalized for the PFY spectra. The PFY spectra are scaled at 228 nm and the cross sections of the absorption spectra are divided by 1.8×10^{-17}.

where E_H and $E_{C_3H_5}$ are the laboratory translational energies of the H-atom photofragment and the parent C_3H_5 radical, respectively, and L is the flight length. The second term $\left(\frac{m_H}{m_{C_3H_4}} E_{C_3H_5}\right)$ is due to the parent C_3H_5 radical motion in the molecular beam that is orthogonal to the TOF path, but it is small compared with the first term (products' CM translation) and neglected. By using equation (1), the CM $P(E_T)$ distribution can be obtained directly from the H-atom TOF spectrum. The resulted $P(E_T)$ distributions at 228 nm and 222 nm using both allyl chloride and 1,5-hexadiene precursors are shown in Figure 6.7a and 6.7b. All $P(E_T)$ distributions have a broad feature and peak at ~9 kcal/mol and extend to ~60 kcal/mol, indicating the highly internally excited C_3H_4 product. The translational energy release from Figure 6.7 is modest, with an average product translational energy $\langle E_T \rangle$ 13.5 kcal/mol at 228 nm and $\langle E_T \rangle$ 13.7 kcal/mol at 222 nm. The fraction of translational energy in the total available energy $\langle f_T \rangle$ is around 0.19 and 0.18 at 228 and 222 nm, respectively. The $\langle E_T \rangle$ distributions and $\langle f_T \rangle$ values were also recorded at different photolysis wavelengths from 216 nm to 245.75 nm with photolysis energy 0.15-0.9 mJ/pulse, as shown in Figure 6.8a and 6.8b. The average translational energy $\langle E_T \rangle$ in this region is nearly constant, with a slightly decreasing trend following the increasing wavelength. The $\langle f_T \rangle$ increased gradually from 216 nm to 245.75 nm, with the values ranging from 0.18 to 0.22.

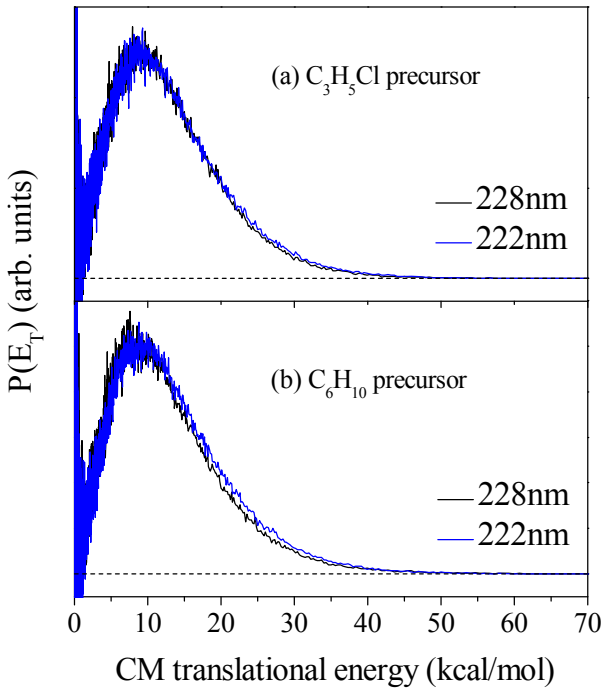

Figure 6.7 Center-of-mass product translational energy distributions, $P(E_T)$, of the H + C_3H_4 product channel from 228 nm and 222 nm photodissociation of C_3H_5 with (a) allyl chloride (b) 1,5-hexadiene as precursor. The $P(E_T)$ distributions are directly converted from the H-atom TOF spectra in Figure 6.4a and 6.4b. The photolysis laser power was 0.55-0.85 mJ/pulse.

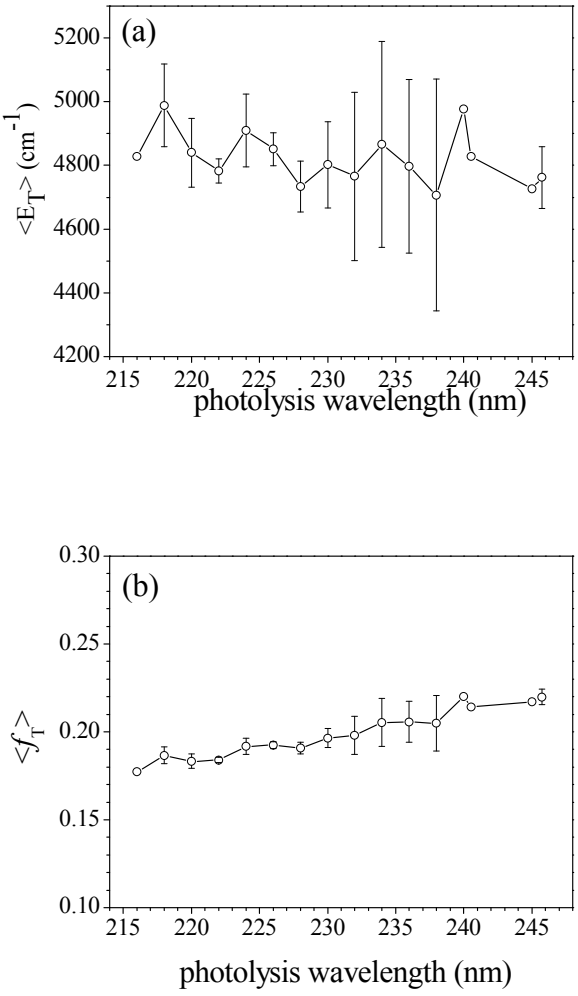

Figure 6.8 (a) average translational energy $\langle E_T \rangle$ and (b) fraction of average translational energy release in the total available energy, $\langle f_T \rangle$, in the UV photodissociation of the allyl radical as a function of photolysis wavelength 216-238 nm. The average translational energies are calculated from the experimental $P(E_T)$ distributions. The total available energy at each photolysis wavelength is derived from the corresponding photon energy and the dissociation of allyl radical to the H + allene products, $D_0(H\text{-}C_3H_4)$ = 54.4 kcal/mol.[28] The error bar represents 95% confident limit from repeated measurements.

Figure 6.9 shows the H product angular distributions at 228 nm with polarization of photolysis laser perpendicular and parallel to the TOF pathway (upper panel). The two H-atom TOF spectra at both polarizations are identical, indicating an isotropic product angular distribution in the dissociation process. The lower panel in Figure 6.9 is the anisotropy parameter β at different flight times. Since the linearly polarized light preferentially excites the radicals whose electronic transition dipole moment parallel to the electric vector $\boldsymbol{E}$ of the polarized laser radiation, the product angular distribution is important to determine the vector correlations during dissociation. The photofragment angular distribution is given[36] by $I(\theta) = (1/4\pi)[1 + \beta P_2(\cos\theta)]$, where β is the anisotropy parameter ($-1 \leq \beta \leq 2$), θ is the angle between the electric vector of the polarized laser radiation $\boldsymbol{E}$ and the recoiling velocity vector of the H-atom product (the direction of detection or the TOF axis), and $P_2(\cos\theta)$ is the second Legendre polynomial. Based on this equation and the H-atom TOF spectra at both polarizations, an anisotropy parameter $\beta \approx 0$ is derived.

The H-atom TOF spectra at 228 nm with both precursors were recorded at different delay times between photolysis pump laser and probe lasers. The integral of H signals at each delay time was plotted as a function of the pump-probe delay time, as shown in Figure 6.10 with allyl chloride as the allyl radical precursor. The purpose of this measurement is to obtain the microcanonical rate for the dissociation of allyl radical. The

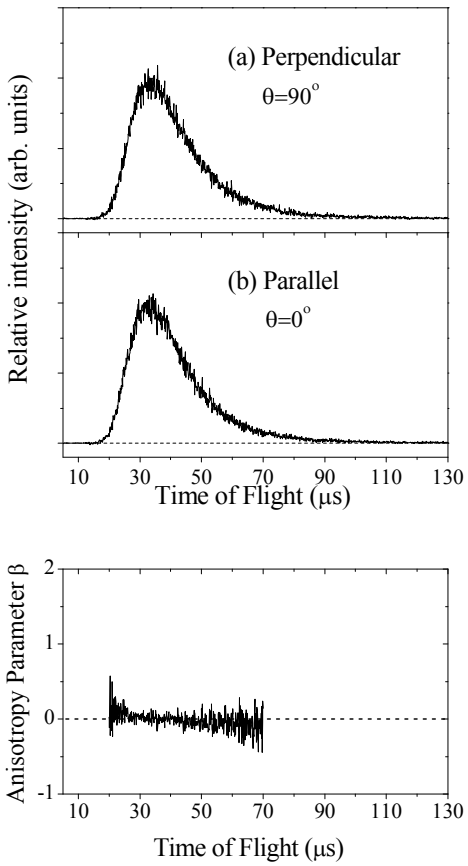

Figure 6.9 H-atom TOF spectra of 228-nm photodissociation of C_3H_5, with the polarization **E** vector of the photolysis radiation (a) perpendicular (θ = 90°) and (b) parallel (θ = 0°) to the TOF axis. The 228 nm radiation power intensity was 0.55-0.65 mJ/pulse. The signals have been normalized to the same photolysis power and laser shots. Anisotropy parameter β is plotted as a function of H-atom time of flight. The β parameter stays close to the limit of an isotropic angular distribution.

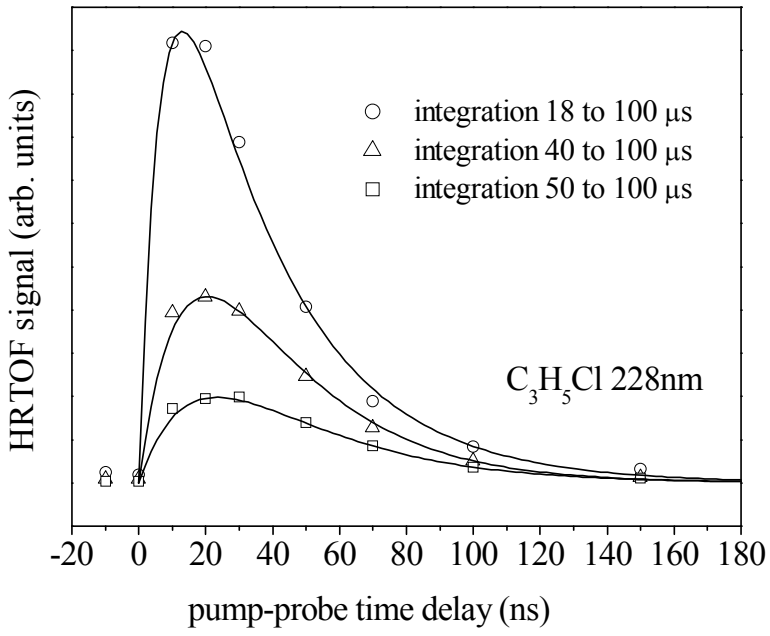

Figure 6.10 H-atom product signal as a function of photolysis and probe laser delay time. The photolysis wavelength is 228 nm and power is 0.5-0.55 mJ/pulse. The signals are obtained by integrating the HRTOF spectra with allyl chloride precursor at the various photolysis-probe delay time. Different windows of integration 18-100, 40-100, and 50-100 μs, are used. The solid line represents an exponential fit which gives the unimolecular decay rate.

initial rise in Figure 6.10 represents the H production rate from the photodissociation of allyl radical, while the following decay is due to the flight out of the H atoms from the interaction region between photolysis laser and probe lasers. Different integral areas on the TOF spectra were selected to check the bias of the flying-out H atoms and the possibility of multi-photon process, as shown by different symbols in Figure 6.10. The time profile of the slow H atoms should have the least effect by the flight out bias. However, the three time profiles give the same initial rise time 10-20 ns, indicating similar dissociation rates of allyl dissociation. The slower decay of 50-100 μs compared to 18-100 and 40-100 μs is due to the smaller speed of the H atoms which will fly out the detection region slower. The time profile with another precursor was also recorded which gave the similar dissociation rates as allyl chloride. The average dissociation rate for the allyl radical at 228 nm from both precursors is $\sim 1\times10^{8}$/s (note that this rate is the lower limit since this number approaches the laser pulse time width ~10ns).

6.4 Discussion

The UV photodissociation of the allyl radical via its E^2B_1 ($3p_x$) state in the range of 216-238 nm is studied for the first time. The H + C_3H_4 product channel is directly observed in the UV photodissociation of the allyl radical, supporting the nonradiative

decay of the allyl radical at wavelength shorter than 238 nm in the previous REMPI studies.[11-13]

The two PFY spectra from two different allyl precursors were performed at 216-238 nm and they were in good agreement with each other, with the maximum signal at 228 nm (Figure 6.6), supporting that the H signal comes from the dissociation of allyl radical. The previous MPI study of allyl radical indicated that a fast nonradiative decay was dominant in this region. However, the two H-atom PFY spectra do not match the previously reported absorption spectra. The variation is possibly due to the participation of another dissociation channel centered at ~222 nm. Based on Stranges et al.[23], there were two dissociation pathways for the allyl radical at 248 nm: H dissociation channel and CH_3 elimination channel with a branching ratio 84:16. In 2010, the same group[25] also reported that the CH_3 elimination from the allyl radical resulted in two dissociation channels, which were CH_3 + HCCH and CH_3 + CCH_2 (vinylidene). Since the H dissociation channel is one of the above dissociation channels, and the CH_3 elimination channel becomes more important with the decreasing photolysis wavelength, the missing part on Figure 6.6 might be due to the CH_3 + C_2H_2 channel (the pathway for CH_3 + C_2H_2 is illustrated in Figure 6.1). Further experimental and theoretical work is required to confirm this assumption.

The CM product translational energy distributions of the C_3H_4 + H channel are not repulsive and have a modest translational energy release. The $P(E_T)$ distributions at the photolysis wavelength 228 nm and 222 nm (Figure 6.7, corresponding to the E^2B_1 ($3p_x$) Rydberg state assigned by Chen's group[14]) peak around 9 kcal/mol with the average product translational energy $\langle E_T \rangle$ 13.5 kcal/mol at 228 nm and 13.7 kcal/mol at 222 nm. The fraction of the product translational energy in the total available energy $\langle f_T \rangle$ is 0.19 and 0.18 at 228 and 222 nm, respectively. The trend in the region 216 nm to 245.75 nm is shown in Figure 6.8. The H-atom TOF spectra were also recorded at longer photolysis wavelengths and directly transformed to the product CM translational energy distributions $P(E_T)$ using equation (1), as shown in Figure 6.11. The two longer photolysis wavelengths are 240.555 nm ($C\,0_0^0$) and 245.75 nm ($B7_0^1 12_0^1$), which belong to the two different excited electronic states B^2A_1 and C^2B_2. Since the H signals at these two longer photolysis wavelengths were not as strong as those at the shorter wavelength (e.g. 228 nm and 222 nm), the $P(E_T)$ distributions in Figure 6.11 are noisier than those in Figure 6.7. The $P(E_T)$ distributions at 240.555 nm and 245.75 nm peak around 8 kcal/mol with the average product translational energy $\langle E_T \rangle$ 13.8 kcal/mol at 240.555 nm and 13.6 kcal/mol at 245.75 nm. The fraction of the product translational energy in the total available energy $\langle f_T \rangle$ is 0.21 at 240.555 nm and 0.22 at 245.75 nm. Two photodissociation studies at the similar photolysis wavelength region have performed previously using

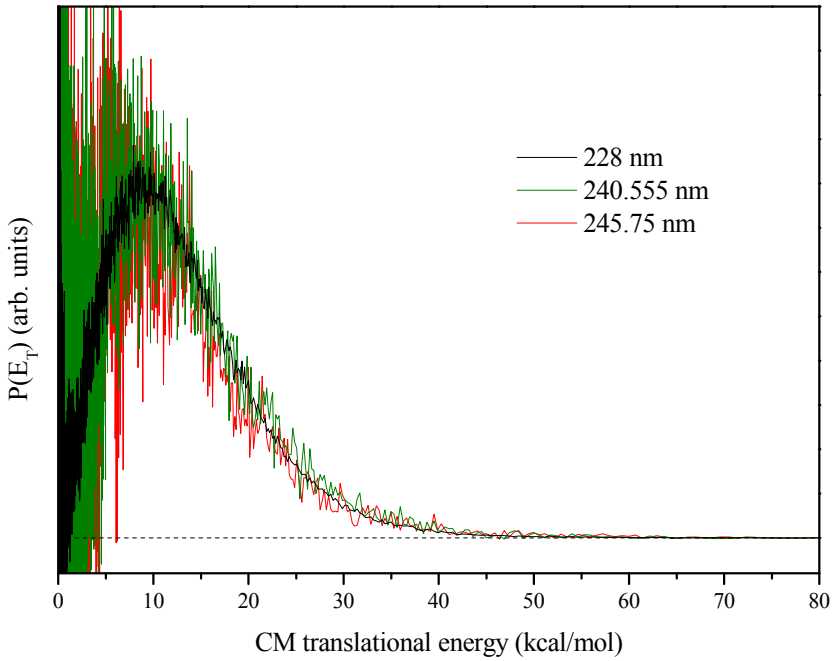

Figure 6.11 Center-of-mass product translational energy distributions, $P(E_T)$, of the H + C_3H_4 product channel at photolysis wavelength 228 nm, 240.555 nm and 245.75 nm. The $P(E_T)$ distributions are directly converted from the H-atom TOF spectra.

photoionization of hydrogen product with Lyman-α radiation and photofragment translational spectroscopy with dissociation products ionized by an electron bombardment ionizer. In their studies, Chen's group[21] reported $\langle E_T \rangle$ as 14 ± 1 kcal/mol at around 246 nm and 248 nm ($C\,0_0^0$ and $C\,7_0^1$) while Stranges et al.[23] reported $\langle E_T \rangle$ as 13.2 kcal/mol at 248 nm (C^2B_2). These results are consistent with the $\langle E_T \rangle$ values at the similar wavelength region 240.555 nm ($C\,0_0^0$) and 245.75 nm ($B7_0^1 12_0^1$) in this study and further confirms the H signals in this study originates from the photodissociation of allyl radical. When comparing the $P(E_T)$ distributions in Figure 6.11, it was found that the $P(E_T)$ distributions at different photolysis wavelengths, 240.555 nm, 245.75 nm and 228 nm, are essentially identical, suggesting the similar dissociation mechanism for the allyl radical at all the three B, C and E electronic excited states. Based on the translational energy distribution and polarization dependence, Stranges et al.[23] proposed two possible dissociation mechanisms for the allyl radical at 248 nm. The first mechanism is the internal conversion for the allyl radical from the excited electronic state to the ground electronic state followed by the dissociation of the allyl radical on the ground electronic state. The second mechanism is the internal conversion into the higher excited electronic A state followed by the electrocyclic transformation into the cyclopropyl radical which goes through the isomerization to form allyl radical on the ground electronic state. Therefore, a similar dissociation mechanism could be proposed around 228 nm at E^2B_1

($3p_x$) state, which is internal conversion of the allyl radical from excited electronic state into the lower or ground electronic state followed by the dissociation on the ground electronic state.

As shown in Figure 6.1, there are several possible dissociation pathways for the allyl radical at the ground electronic state X^2A_2, with four different photofragment products which are CH_3 + C_2H_2, CH_2CCH_2 (allene) + H, CH_3CCH (propyne) + H and *c*-C_3H_4 (cyclopropene) + H. The $P(E_T)$ distributions at 228 nm and 222 nm photolysis wavelengths extend to the maximum available energy $E_T \approx 60$ kcal/mol (Figure 6.7). Using the bond dissociation energies[28] of three H dissociation channels, the maximum available energies for each dissociation channel can be calculated at 228 nm: 71 kcal/mol for allene channel, 72 kcal/mol for propyne channel and 47 kcal/mol for *c*-C_3H_4 channel. The $P(E_T)$ distributions in Figure 6.7 beyond the *c*-C_3H_4 + H onset (47 kcal/mol) suggest that the productions of both allene and propyne are possible since the enthalpies of formation for both products are very similar. The dissociation pathways for allene product channel in Figure 6.1 are: (1) allyl radical dissociates directly to allene + H products with an activation barrier 60.0 kcal/mol; (2) allyl radical isomerizes to the 2-propenyl radical with an activation barrier 63.8 kcal/mol, followed by the dissociation of 2-propenyl into allene + H with a barrier 57.5 kcal/mol. The dissociation pathways for propyne product channel are: (1) allyl radical isomerizes to the 2-propenyl radical with a barrier 63.8

kcal/mol, followed by the dissociation of 2-propenyl into propyen + H with a barrier 56.5 kcal/mol; (2) allyl radical isomerizes to the 2-propenyl radical with a barrier 63.8 kcal/mol, followed by the isomerization of 2-propenyl radical to 1-propenyl radical with a barrier 67.4 kcal/mol which further dissociates to propyne + H via the barrier 58.8 kcal/mol; (3) allyl radical isomerizes to the 1-propenyl radical with a barrier 64.0 kcal/mol, followed by the dissociation of 1-propenyl into propyen + H with a barrier 58.8 kcal/mol. Since the lowest activation barrier for one of the allene pathways (60.0 kcal/mol) is smaller than that for propyne (63.8 kcal/mol), the dominate dissociation channel allene + H is assumed at this photolysis wavelength region. This is consistent with the previous experimental result and RRKM calculations[21,23] which studied the branching ratios for different dissociation channels of allyl radical on the ground state. These results showed that the probabilities to generate the allene and propyne products were almost the same at photolysis wavelength 248 nm, with minor contribution from cyclopropene channel.

In 1997 and 1998, Chen's group[29,30] measured the decay time of allyl radical from 250 nm to 238 nm, corresponding to three different electronic states B^2A_1, C^2B_2 and D^2A_1, The lifetime of the allyl radical on these electronic states monotonically decreased with the deceasing wavelengths, with values ranging from 20 ps to 9 ps. Later, Chen's group studied the photodissociation of the allyl radical at 248 nm[21] which showed the

unimolecular dissociation rates of allene channel (experimental result: > 10^8 s^{-1}, RRKM calculation: 4.2×10^8 s^{-1}) and propyne channel (experimental result: 4×10^7 s^{-1}, RRKM calculation: 1.9×10^8 s^{-1}). At the same time, Stranges et al.[23] calculated the RRKM microcanonical rate constants for different dissociation channels (4.4×10^{10} s^{-1} for allene channel and 13.0×10^{10} s^{-1} for propyne channel) and estimated the lifetime for the C^2B_2 state at 248 nm of 1-2 ps. In the present study, the angular distribution of the H-atom product from the UV photodissociation of allyl radical is isotropic (Figure 6.9), suggesting that the time scale of photodissociation of the allyl radical at 228 nm is longer than one rotational period of the allyl radical (> ps). The pump-probe experiment in this study (Figure 6.10) shows that the lower limit of dissociation rate of the allyl radical at 228 nm is at the magnitude of 10^8 s^{-1}. Both of these two facts indicate that the dissociation time scale of the allyl radical at 228 nm excitation is long (> ps), which is consistent with the previous lifetime and dissociation time investigations as mentioned above. This long dissociation from the excited E^2B_1 ($3p_x$) state allows the statistical excess energy distribution to each degree of freedom during the unimolecular dissociation of the allyl radical, which is consistent with the fraction of translation energy release $\langle f_T \rangle$ values (0.18 to 0.22 from photolysis wavelength 216 nm to 245.75 nm) in the present study.

6.5 Conclusion

The H-atom dissociation channel of allyl radical was investigated for the first time at the photolysis wavelength ranging from 216 nm to 238 nm using the HRTOF technique. The H-atom PFY spectra with both allyl chloride and 1,5-hexadiene precursors peaked at 228 nm, which does not match the previous absorption spectra which peaked at 222 nm, indicating another possible dissociation channel in this region (e.g. CH_3 elimination channel). The H-atom TOF spectra at different wavelengths with both precursors confirmed the H signals were coming from the allyl dissociation. The product translational energy release was modest, with the distribution $P(E_T)$ peaking at around 9 kcal/mol. The fraction of average translational energy in the total available energy $\langle f_T \rangle$ increased gradually from 0.18 to 0.22 from 216 nm to 245.75 nm. The $P(E_T)$ distribution supported the production of allene and propyne. The product angular distribution was isotropic, with anisotropy parameter $\beta \approx 0$. The dissociation rate from the H-atom time profile had the lower limit 1×10^8/s. The dissociation mechanism was consistent with the internal conversion of the allyl radical from excited electronic state E^2B_1 ($3p_x$) to the ground electronic state followed by unimolecular dissociation on the ground electronic state to the products (allene + H and propyne + H).

References

(1) Webster, A. *Monthly Notices of the Royal Astronomical Society* **1993**, *265*, 421.

(2) Miller, J. A.; Klippenstein, S. J.; Georgievskii, Y.; Harding, L. B.; Allen, W. D.; Simmonett, A. C. *Journal of Physical Chemistry A*, *114*, 4881.

(3) Zhang, H. R.; Eddings, E. G.; Sarofirn, A. F. *Energy & Fuels* **2008**, *22*, 945.

(4) Hansen, N.; Li, W.; Law, M. E.; Kasper, T.; Westmoreland, P. R.; Yang, B.; Cool, T. A.; Lucassen, A. *Physical Chemistry Chemical Physics*, *12*, 12112.

(5) Currie, C. L.; Ramsay, D. A. *Journal of Chemical Physics* **1966**, *45*, 488.

(6) Tonokura, K.; Koshi, M. *Journal of Physical Chemistry A* **2000**, *104*, 8456.

(7) Callear, A. B.; Lee, H. K. *Transactions of the Faraday Society* **1968**, *64*, 308.

(8) van den Bergh, H. E.; Callear, A. B. *Transactions of the Faraday Society* **1970**, *66*, 2681.

(9) Jenkin, M. E.; Murrells, T. P.; Shalliker, S. J.; Hayman, G. D. *Journal of the Chemical Society-Faraday Transactions* **1993**, *89*, 433.

(10) Bayrakceken, F.; Aktas, S.; Unlugedik, A.; Karaaslan, I. *Spectrochimica Acta Part a-Molecular and Biomolecular Spectroscopy* **2003**, *59*, 1663.

(11) Minsek, D. W.; Blush, J. A.; Chen, P. *Journal of Physical Chemistry* **1992**, *96*, 2025.

(12) Blush, J. A.; Minsek, D. W.; Chen, P. *Journal of Physical Chemistry* **1992**, *96*, 10150.

(13) Minsek, D. W.; Chen, P. *Journal of Physical Chemistry* **1993**, *97*, 13375.

(14) Gasser, M.; Frey, J. A.; Hostettler, J. M.; Bach, A.; Chen, P. *Journal of Physical Chemistry A* **2010**, *114*, 4704.

(15) Tae-Kyu, H.; Baumann, H.; Oth, J. F. M. *Journal of Chemical Physics* **1986**, *85*, 1438.

(16) Oliva, J. M.; Gerratt, J.; Cooper, D. L.; Karadakov, P. B.; Raimondi, M. *Journal of Chemical Physics* **1997**, *106*, 3663.

(17) Aquilante, F.; Jensen, K. P.; Roos, B. O. *Chemical Physics Letters* **2003**, *380*, 689.

(18) Matsika, S.; Yarkony, D. R. *Journal of the American Chemical Society* **2003**, *125*, 10672.

(19) Mach, T. J.; King, R. A.; Crawford, T. D. *Journal of Physical Chemistry A* **2010**, *114*, 8852.

(20) Deyerl, H. J.; Gilbert, T.; Fischer, I.; Chen, P. *Journal of Chemical Physics* **1997**, *107*, 3329.

(21) Deyerl, H. J.; Fischer, I.; Chen, P. *Journal of Chemical Physics* **1999**, *110*, 1450.

(22) Fischer, I.; Chen, P. *Journal of Physical Chemistry A* **2002**, *106*, 4291.

(23) Stranges, D.; Stemmler, M.; Yang, X. M.; Chesko, J. D.; Suits, A. G.; Lee, Y. T. *Journal of Chemical Physics* **1998**, *109*, 5372.

(24) Stranges, D.; O'Keeffe, P.; Scotti, G.; Di Santo, R.; Houston, P. L. *Journal of Chemical Physics* **2008**, *128*.

(25) Chen, C.; Braams, B.; Lee, D. Y.; Bowman, J. M.; Houston, P. L.; Stranges, D. *Journal of Physical Chemistry Letters* **2010**, *1*, 1875.

(26) Szpunar, D. E.; Morton, M. L.; Butler, L. J.; Regan, P. M. *Journal of Physical Chemistry B* **2002**, *106*, 8086.

(27) Szpunar, D. E.; Liu, Y.; McCullagh, M. J.; Butler, L. J.; Shu, J. *Journal of Chemical Physics* **2003**, *119*, 5078.

(28) Davis, S. G.; Law, C. K.; Wang, H. *Journal of Physical Chemistry A* **1999**, *103*, 5889.

(29) Schultz, T.; Fischer, I. *Journal of Chemical Physics* **1997**, *107*, 8197.

(30) Schultz, T.; Fischer, I. *Journal of Chemical Physics* **1998**, *109*, 5812.

(31) Olivella, S.; Sole, A.; Bofill, J. M. *Journal of the American Chemical Society* **1990**, *112*, 2160.

(32) Mann, D. J.; Hase, W. L. *Journal of the American Chemical Society* **2002**, *124*, 3208.

(33) Xu, K. S.; Amaral, G.; Zhang, J. S. *Journal of Chemical Physics* **1999**, *111*, 6271.

(34) Amaral, G.; Xu, K. S.; Zhang, J. S. *Journal of Chemical Physics* **2001**, *114*, 5164.

(35) Zhou, W. D.; Yuan, Y.; Chen, S. P.; Zhang, J. S. *Journal of Chemical Physics* **2005**, *123*, 054330.

(36) Zare, R. N. *Mol. Photochem.* **1972**, *4*, 1.

CHAPTER 7

Future work

The previous five chapters (2-6) have reported the studies of photodissociation dynamics of several important free radicals using the HRTOF technique, which has shown great energy resolution and high sensitivity of the H-product detection. This chapter will discuss several other radicals which are related to the previous ones in this dissertation, as well as their preliminary work.

7.1 Ultraviolet photodissociation dynamics of the phenyl radical

7.1.1 Brief introduction

Phenyl radical (C_6H_5) is the simplest aromatic radical and is predicted to be the primary intermediate in the formation of polycyclic aromatic hydrocarbons (PAHs) which are thought to lead to the eventual formation of soot. Therefore, many studies have been performed to characterize the spectroscopy and kinetic properties of this radical.

The absorption spectrum of the phenyl radical was first observed by Porter and Ward[1] in 1965. A series of sharp bands in the 530-440 nm region was found and attributed to the $^2B_1 \leftarrow {}^2A_1$ transition. The gas phase ultraviolet spectrum of phenyl is

essentially featureless, consisting of a broad band extending from 225 to 340 nm with the band maximum around 245-250 nm.[2-4] In 1999, Radziszewski[5] recorded a continuous absorption spectrum of phenyl radicals isolated in an argon matrix covering the entire visible and near UV region. Three band systems were recorded with the origins at 510.5 nm, 235.1 nm and 211.5 nm, which were assigned to the transitions from the ground state to the $^2B_1$, $^2A_1$ and $^2B_2$ excited electronic states, respectively. The band system at 211.5 nm was observed for the first time and had a series of sharp structures while the band at 235.1 nm was broad and unstructured.

Figure 7.1 shows the potential energy diagram and several electronic states of the phenyl radical. The energies of the various pathways are based on the previous calculation by Madden et al.[6], while the energies of the electronic states are based on the previous absorption spectrum of the phenyl radical[5]. There are three dissociation pathways for the phenyl radical at the ground electronic state, which are *o*-C_6H_4 + H, *l*-C_6H_4 + H and *n*-C_4H_3 + C_2H_2 as shown in the following equations:[6]

$$c\text{-}C_6H_5\ (X^2A_1) + h\nu \rightarrow o\text{-}C_6H_4 + H, \qquad \Delta H_{rxn,0} = 76.0 \text{ kcal/mol}$$

$$c\text{-}C_6H_5\ (X^2A_1) + h\nu \rightarrow l\text{-}C_6H_4 + H, \qquad \Delta H_{rxn,0} = 91.0 \text{ kcal/mol}$$

$$c\text{-}C_6H_5\ (X^2A_1) + h\nu \rightarrow n\text{-}C_4H_3 + C_2H_2, \qquad \Delta H_{rxn,0} = 98.2 \text{ kcal/mol}$$

According to the energies of different transition states, the direct dissociation from the phenyl radical (*c*-C_6H_5) to the *o*-C_6H_4 (ortho-benzyne) is the most energetic favorable H

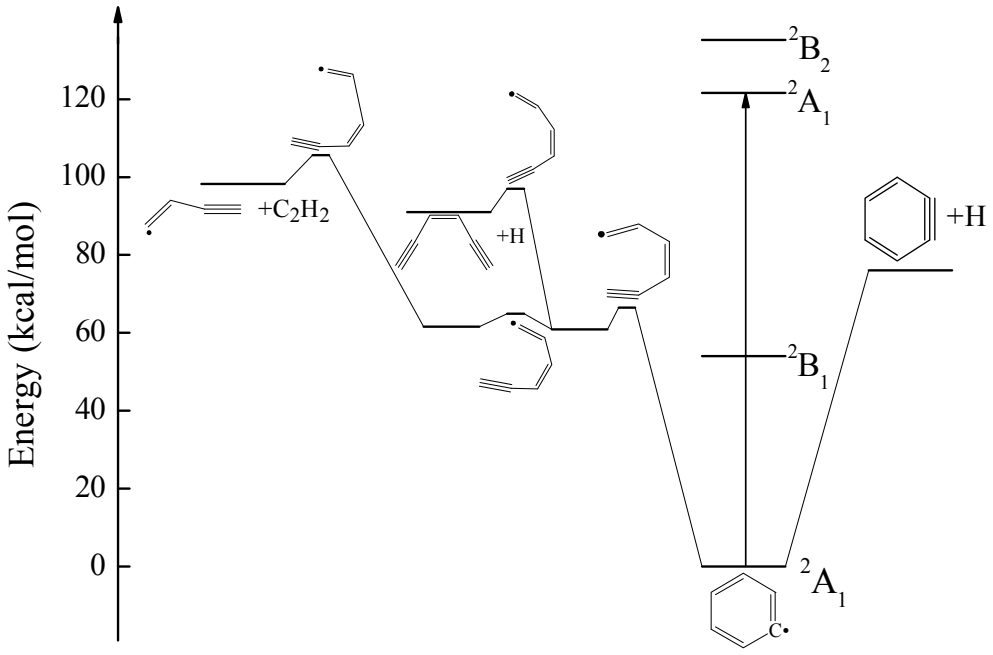

Figure 7.1 Potential energy diagram of the C_6H_5 system. Three possible dissociation channels *o*-C_6H_4 + H, *l*-C_6H_4 + H and *n*-C_4H_3 + C_2H_2 are shown in the figure. The energetics and pathways are based on the theoretical calculations in Ref 6 while the energies of the excited electronic states of the phenyl radical are based on Ref 5. The arrow indicates the photolysis wavelength region employed in the present study.

dissociation channel with an activation energy 76.0 kcal/mol. The other H dissociation channel leading to *l*-C_6H_4 (1,5-hexadiyn-3-ene) has a higher activation barrier 97.0 kcal/mol. The only non-hydrogen dissociation channel shown in Figure 7.1 is the *n*-C_4H_3 + C_2H_2 with a even higher barrier 105.6 kcal/mol.

Very recently, the Neumark's group[7] studied the photodissociation dynamics of the phenyl radical using the photofragment translational spectroscopy at 248 nm and 193 nm. They found the dissociation channel of the phenyl radical at 248 nm was *o*-C_6H_4 + H and the dissociation mechanism was the statistical decay on the ground electronic state of the phenyl radical. At 193 nm, the dissociation pathways were C_6H_4 + H (either *o*-C_6H_4 + H or *l*-C_6H_4 + H) and *n*-C_4H_3 + C_2H_2 with the latter one being the dominant channel. However, they did not obtain the branching ratio of these two channels at 193 nm.

7.1.2 Experimental

The HRTOF technique and experimental setup have been described in the previous chapters. Chlorobenzene and bromobenzene were selected to be the precursors to generate phenyl radical with the 193-nm radiation since these two precursors have been previously[8-10] confirmed to be an efficient compound to produce C_6H_5 radical. The C_6H_5 radical beam was dissociated by a slightly focused UV photolysis laser radiation (at 231-267 nm, 0.2-0.8 mJ/pulse, linewidth 0.3 cm^{-1}). The H atoms produced from the C_6H_5

photodissociation were tagged by two-color resonant excitation (121.6+366.3 nm), i.e., from 1^2S to 2^2P via the H-atom Lyman-α transition and then further to a high-n Rydberg state. A small fraction of the radiatively metastable Rydberg H atoms drifted with their nascent velocities toward a microchannel plate (MCP) detector that is positioned perpendicular to the molecular beam, and were field-ionized in front of the detector and detected. The nominal flight length was 37.02cm, which was calibrated by 236 nm photodissociation of HBr [with the spin-orbit splitting of Br($^2P_{3/2}$) and Br($^2P_{1/2}$)]. The ion signals were amplified by a fast preamplifier, and the H-atom TOF spectra were recorded and averaged by using a multichannel scaler.

The H-atom photofragment yield (PFY) spectra (i.e., action spectra) were measured using two methods. The first method involved integrating the net HRTOF spectra (after the background removal) as a function of photolysis wavelength. The second method was based on collecting the H-atom product REMPI signals as a function of photolysis wavelength. The H-atom REMPI experiment has been described in the previous chapters.

7.1.3 Preliminary results

The TOF spectra of the H-atom product for the photodissociation of C_6H_5 were measured in the photolysis wavelength region 231-267 nm (near the $^2A_1$ electronic excited state), with the photolysis laser polarization parallel and perpendicular to the

flight path, respectively. In order to identify the origins of the H-atom signals and to establish procedures for background subtraction, four types of TOF spectra were taken: (1) full spectrum, with both the 193-nm radiation on (for C_6H_5 radical production) and the UV photolysis radiation on, plus the Rydberg atom tagging probe-laser radiations (121.6+366.3 nm); (2) precursor background spectrum, with the 193-nm radiation off but the UV photolysis radiation on, plus the probe-laser radiations; (3) radical background spectrum, with both the 193-nm radiation on and probe radiations on, but the UV photolysis radiation off; and (4) probe-laser background spectrum, with both the 193-nm radiation off and the UV photolysis radiation off, but only the probe radiations on. The background spectra (3) and (4) were observed to be essentially identical, with a negligibly small background in the time range of interest. The precursor background spectrum (2) represents the main background, i.e., contributions from photolysis of chlorobenzene or bromobenzene precursor by the UV photolysis radiation. The net H-atom TOF spectrum of phenyl photodissociation is obtained by removing the background spectrum (2) (with the 193-nm radiation on but the UV photolysis radiation off) from the full spectrum (1) (with both the 193-nm radiation and UV photolysis radiation on). The net H-atom product TOF spectrum at 235 nm photolysis wavelength with 0.35-0.4 mJ/mm^2 UV radiation intensity is shown in Figure 7.2 in open circles (○). Lower photolysis power is used to minimize the two photon dissociation of C_6H_5 radical.

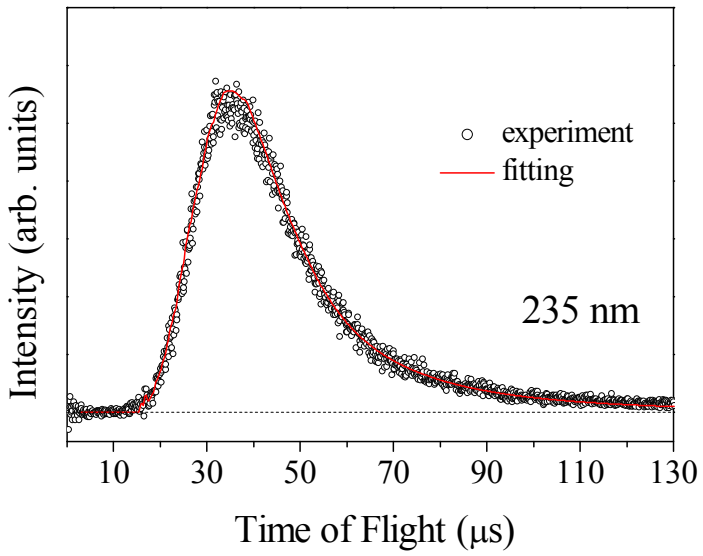

Figure 7.2 H-atom TOF spectra of jet-cooled phenyl radical at photolysis wavelength 235 nm, produced from 193-nm photolysis of chlorobenzene precursor. This is the net TOF spectra with the full spectrum minus the 193-off background. The photolysis radiation power intensity is 0.35-0.4 mJ/pulse. The solid line is the forward convolution fitting for the experimental TOF spectrum which is discussed later.

The solid line in Figure 7.2 is forward convolution fitting for the experimental TOF spectrum.

To confirm that the observed HRTOF spectrum is originated from photolysis of the phenyl radical, two types of action or PFY spectra, integral HRTOF intensity as a function of photolysis wavelength and H-atom PFY spectrum using H-atom (1+1') REMPI, were recorded. The resulting H-atom action spectra from 215-226 nm and 231-267 nm are plotted in Figure 7.3. The full circles and open circles represent the HRTOF action spectrum and H-atom REMPI action spectrum, respectively. For comparison, three previous UV absorption spectra[2,4,5] of phenyl radical are plotted as solid, dashed and short dotted lines in the same figure. All three absorption spectra reported a broad absorption peak for the phenyl radical at same wavelength region, but with different maximum positions. This may be due to the different detection techniques for the absorption of phenyl radical used in these three studies. The H-atom PFY spectra from our study, HRTOF and REMPI, agree well with each other. Both of them show a decreasing trend from photolysis wavelength 231 nm to 267 nm and from 226 nm to 215 nm. The H-atom PFY spectra are very broad, which agree well with the three absorption spectra, showing the H-atom product in the TOF spectrum (Figure 7.2) originates from the photodissociation of the phenyl radical.

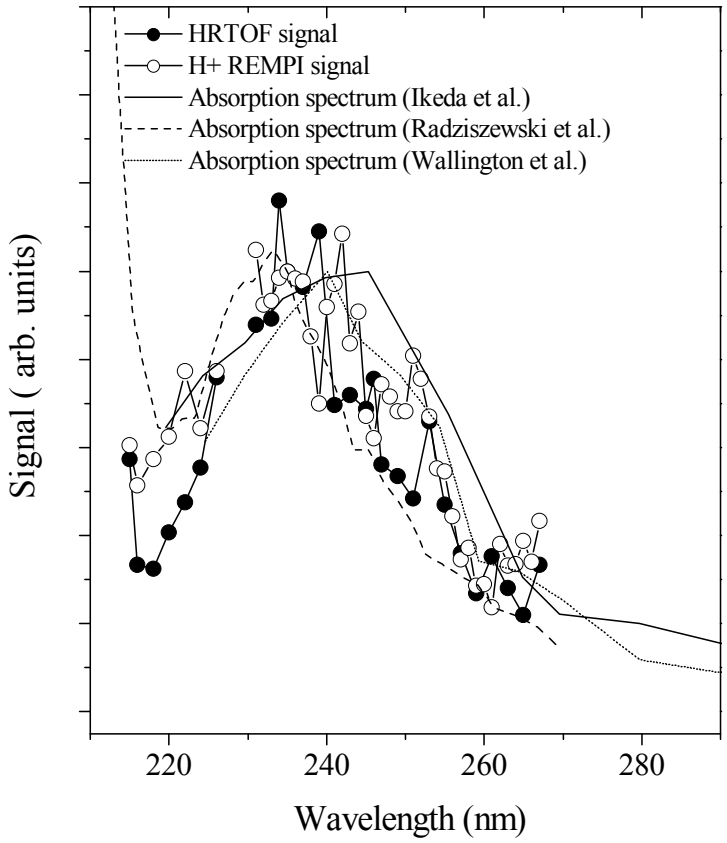

Figure 7.3 H-atom product yield (PFY) spectra as a function of photolysis excitation energy in the region of 215-267 nm. Full circles (●) represent the integrated HRTOF signals while the open circles (○) represent the H^+ REMPI signals using the chlorobenzene precursor. Solid, dashed and short dotted lines are the absorption spectra taken from Refs 2, 4, 5. The photolysis laser power is normalized for the PFY spectra.

Another method is also used to verify the origin of the H-atom product for the photodissociation of the phenyl radical. Except for the chlorobenzene precursor, bromobenzene was employed as the precursor to generate C_6H_5 radical. Figure 7.4 shows two net H-atom product TOF spectra at 235 nm photolysis wavelength with 0.3-0.4 mJ/mm^2 UV radiation intensity using these two different precursors. The signal-to-noise ratio for the TOF spectrum from bromobenzene precursor is smaller than the spectrum from chlorobenzene. This is due to the fact that the vapor pressure of bromobenzene is lower than the chlorobenzene at the same temperature. In order to get higher concentration of precursor molecules in the gas phase, higher temperature must be used which will increase the risk that the high-temperature precursor molecules get condensed near the pulsed valve thus blocking the flow of the molecular beam. However, the shape of the TOF spectrum for the bromobenzene is basically the same as the one for chlorobenzene, which confirms the origin of the H-atom product in the TOF spectrum.

The net H-atom TOF spectrum of the jet-cooled C_6H_5 photodissociation is transformed to total center-of-mass (CM) translational energy distributions, $P(E_T)$'s. The CM translational energy of products, E_T, is converted from the H-atom flight time t_H using the following equation:

$$E_T = \left(1+\frac{m_H}{m_{C_6H_4}}\right)E_H + \frac{m_H}{m_{C_6H_4}}E_{C_6H_5} = \frac{1}{2}m_H\left(1+\frac{m_H}{m_{C_6H_4}}\right)\left(\frac{L}{t_H}\right)^2 + \frac{m_H}{m_{C_6H_4}}E_{C_6H_5} \quad (1)$$

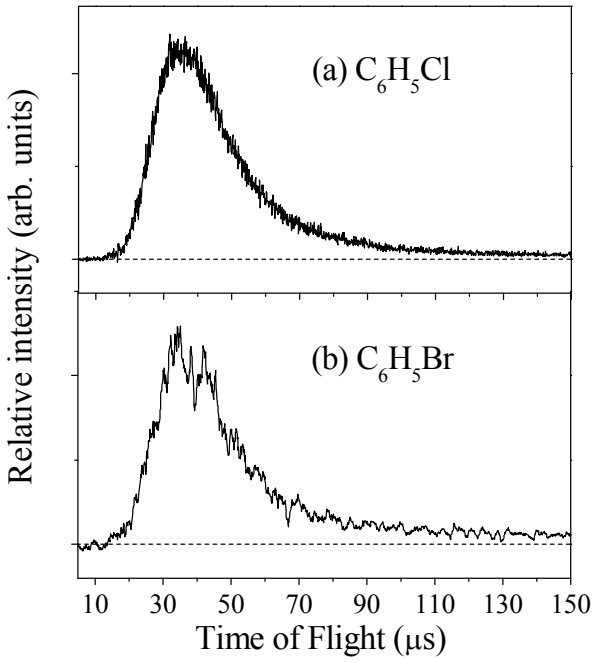

Figure 7.4 H-atom TOF spectra of jet-cooled phenyl radical at photolysis wavelength 235 nm, produced from 193-nm photolysis of (a) chlorobenzene and (b) bromobenzene precursor. These are the net TOF spectra with the full spectrum minus 193-off background. The photolysis radiation power intensity is 0.3-0.4 mJ/pulse.

where E_H and $E_{C_6H_5}$ are the laboratory translational energies of the H-atom photofragment and the parent C_6H_5 radical, respectively, and L is the flight length. The second term $\frac{m_H}{m_{C_6H_4}} E_{C_6H_5}$ is due to the parent C_6H_5 radical motion in the molecular beam that is orthogonal to the TOF path, but it is small compared with the first term (products' CM translation). In this experiment, the correction due to $\frac{m_H}{m_{C_6H_4}} E_{C_6H_5}$ is ~ 13 cm^{-1}, based on an estimated beam velocity of 551 m/s for the C_6H_5/Ar gas mixture at room temperature before supersonic expansion. The resulted $P(E_T)$ distribution of the 235 nm photodissociation of C_6H_5 using chlorobenzene as a precursor is shown in Figure 7.5. This $P(E_T)$ is a relative probability distribution. It has a broad feature that peaks at low energy around 7 kcal/mol and extends to large translational energy of ~50 kcal/mol. The maximum available energy for each dissociation channel is labeled on the figure based on the theoretical study of Lin's group.[6] While the $P(E_T)$ distribution presented here is obtained by direct conversion of the TOF spectrum, it can also be derived from modeling the TOF spectrum in a forward-convolution procedure. The solid line in Figure 7.5 shows the optimized $P(E_T)$ distribution which corresponds to the solid line fitting in Figure 7.2. It is derived from modeling the TOF spectrum in a forward-convolution procedure. In this procedure, the H-atom TOF spectrum is calculated by using a trial CM translational energy distribution $P(E_T)$ convoluted with the instrument and molecular beam functions.

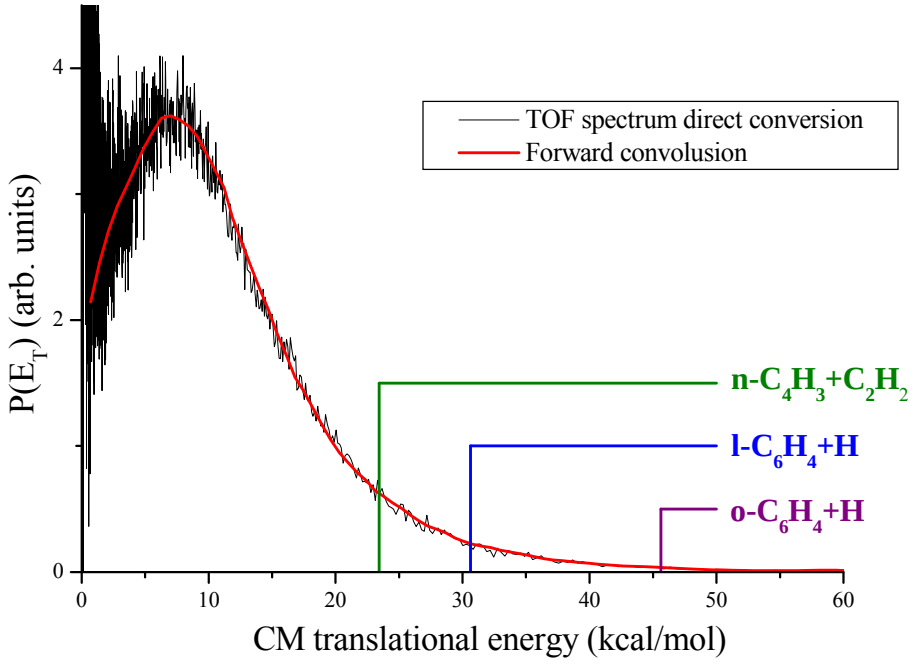

Figure 7.5 Center-of-mass product translational energy distributions, $P(E_T)$, of the H + C_6H_4 product channel from 235 nm photodissociation of C_6H_5 with chlorobenzene as precursor. The dotted $P(E_T)$ distribution is directly converted from the H-atom TOF spectra in Figure 7.2 while the solid line is derived from modeling the TOF spectrum in a forward-convolution procedure.

The calculated TOF spectrum is iteratively optimized by comparison with the experimental spectrum and readjustment of the trial $P(E_T)$ distribution until an optimized $P(E_T)$ distribution is reached. The forward-convolution approach is particularly helpful when the TOF spectrum is noisy, such as those at low photolysis power.

The H-atom product angular distributions in the UV photodissociation of the phenyl radical are examined using linearly polarized laser radiation. Figure 7.6 (upper two panels) illustrates the H-atom TOF spectra of C_6H_5 radical at 235 nm photolysis radiation, with the polarization direction perpendicular and parallel to the TOF axis. The two TOF spectra are identical, indicating an isotropic H atom product angular distribution. The linearly polarized light preferentially excites those radicals with their electronic transition dipole moment parallel to the electric $\boldsymbol{E}$ of the polarized laser radiation. The photofragment angular distribution is given by $I(\theta) = (1/4\pi)[1 + \beta\ P_2(\cos\theta)]$, where β is the anisotropy parameter ($-1 \leq \beta \leq 2$), θ is the angle between the electric vector of the polarized laser radiation $\boldsymbol{E}$ and the recoiling velocity vector of the H-atom product (the direction of detection or the TOF axis), and $P_2(\cos\theta)$ is the second Legendre polynomial. Using this equation and the H-atom TOF spectra at 235 nm, an anisotropy parameter $\beta \approx 0$ is derived for the H + C_6H_4 product channel in the C_6H_5 photodissociation (the lower panel in Figure 7.6). The isotropic product angular distributions indicate that the photodissociation time scale is longer than the rotational period (~ps) of C_6H_5 radical.

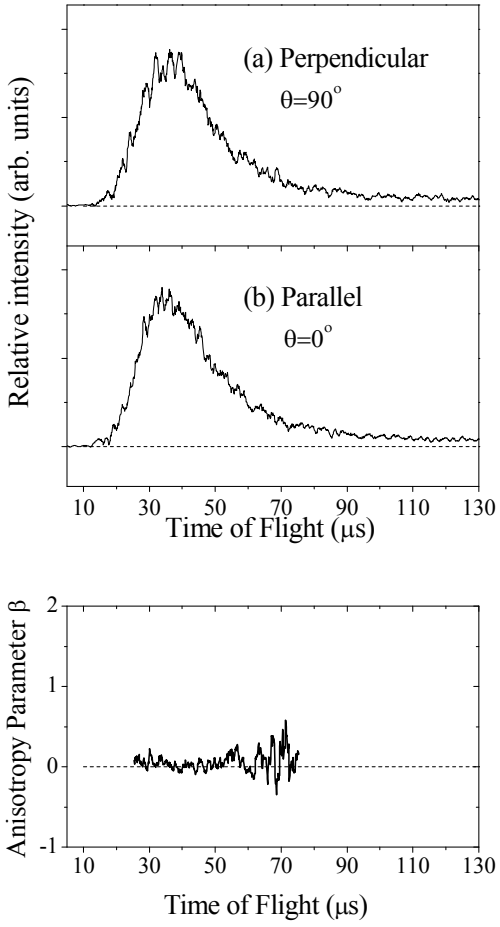

Figure 7.6 H-atom TOF spectra of 235 nm photodissociation of C_6H_5, with the polarization ***E*** vector of the photolysis radiation (a) perpendicular (θ = 90°) and (b) parallel (θ = 0°) to the TOF axis. The signals have been normalized to the same photolysis power and laser shots. Anisotropy parameter β is plotted as a function of H-atom time of flight. The β parameter stays close to the limit of an isotropic angular distribution.

7.2 Ultraviolet photodissociation dynamics of the 1-propenyl and 2-propenyl radical

7.2.1 Brief introduction

Both the 1-propenyl and 2-propenyl radicals are the isomers of the allyl radical with higher energy. Figure 6.1 in this dissertation shows that the most stable C_3H_5 isomer is the allyl radical, while the 1-propenyl radical ($CHCHCH_3$) and 2-propenyl radical (CH_2CCH_3) lie 23.0 and 19.4 kcal/mol above the allyl radical, respectively. It is important to investigate their energetics and dissociation pathways since the 1-propenyl and 2-propenyl radicals are important intermediates in combustion chemistry and are related to the formation of soot in flame. In addition, because the 1-propenyl and 2-propenyl radicals participate in the potential energy diagram of the C_3H_5 species, studying their dissociation pathways will better determine the branching ratio of the different dissociation channels of the allyl radical since the allyl radical isomerizes to both of the 1-propenyl and 2-propenyl radicals at high internal energy.

The unimolecular dissociations of the 1-propenyl and 2-propenyl radicals have been investigated previously by Butler's group.[11,12] In 2001, Mueller et al. [11] studied the primary and the secondary photodissociation of 2-chloropropene with 193 nm radiation using the photofragment translational spectroscopy. After the 2-chloropropene was

dissociated by the 193-nm photon, the 2-propenyl radical generated from the 2-chloropropene precursor still had enough internal energy to overpass the dissociation barrier to form the products allene + H or propyne + H (see Chapter 6). The branching ratio of these two H dissociation channels were investigated with the internal energy of the 2-propenyl radical 0-18 kcal/mol above the propyne + H channel, which indicates that the dissociation of the 2-propenyl radical was performed basically on the ground electronic state of the allyl radical (53-71 kcal/mol above the energy of the allyl radical). In their study, they found that the barrier to the allene + H channel was higher than that to the propyne + H channel, which indicates that the allene + H channel was more facile than the propyne + H channel at higher internal energy within the investigating range. This is also consistent with the theoretical work of Davis et al. as shown in Figure 6.1 of this dissertation. In 2002, Morton et al. [12] used the similar method to study the primary and the secondary decomposition of 1-bromopropene with 193 nm radiation. Three dissociation pathways were obtained for the unimolecular decomposition of 1-propenyl radical, which were propyne + H channel, $CH_3 + C_2H_2$ channel, and the isomerization to the allyl radical followed by the dissociation to the allene + H channel. Among all these three dissociation channels, the $CH_3 + C_2H_2$ channel was found to be dominant at lower internal energy while the other two H dissociation channels opened at higher internal energy. This is also consistent with Figure 6.1 of this dissertation although they pointed

out the isomerization barrier to form the allene + H was too high comparing to the propyne + H barrier.

7.2.2 Preliminary results

In the present study, 2-bromopropene and 2-chloropropene were used as precursors to generate the 2-propenyl radical while 1-bromopropene was used to generate 1-propenyl radical. In order to confirm the H-atom products were from the photodissociation of the 2-propenyl and 1-propenyl radical, the TOFMS spectra of all the precursors were taken to verify the production of the 2-propenyl and 1-propenyl radical in the molecular beam, as shown in Figure 7.7 and 7.8. The H-atom product yield (PFY) spectra for the 1-propenyl and 2-propenyl radicals were shown in Figure 7.9. The H-atom TOF spectra for the 2-propenyl and 1-propenyl radical were shown in Figure 7.10 and 7.11. CM translational energy distributions which were converted directly from the H-atom TOF spectra were shown in Figure 7.12 and 7.13 for the 2-propenyl and 1-propenyl radicals.

More work needs to be done in the future for these two C_3H_5 isomers, such as the H-atom action spectra and the pump-probe time delay study, in order to figure out the dissociation pathways and the energetics of these two radicals.

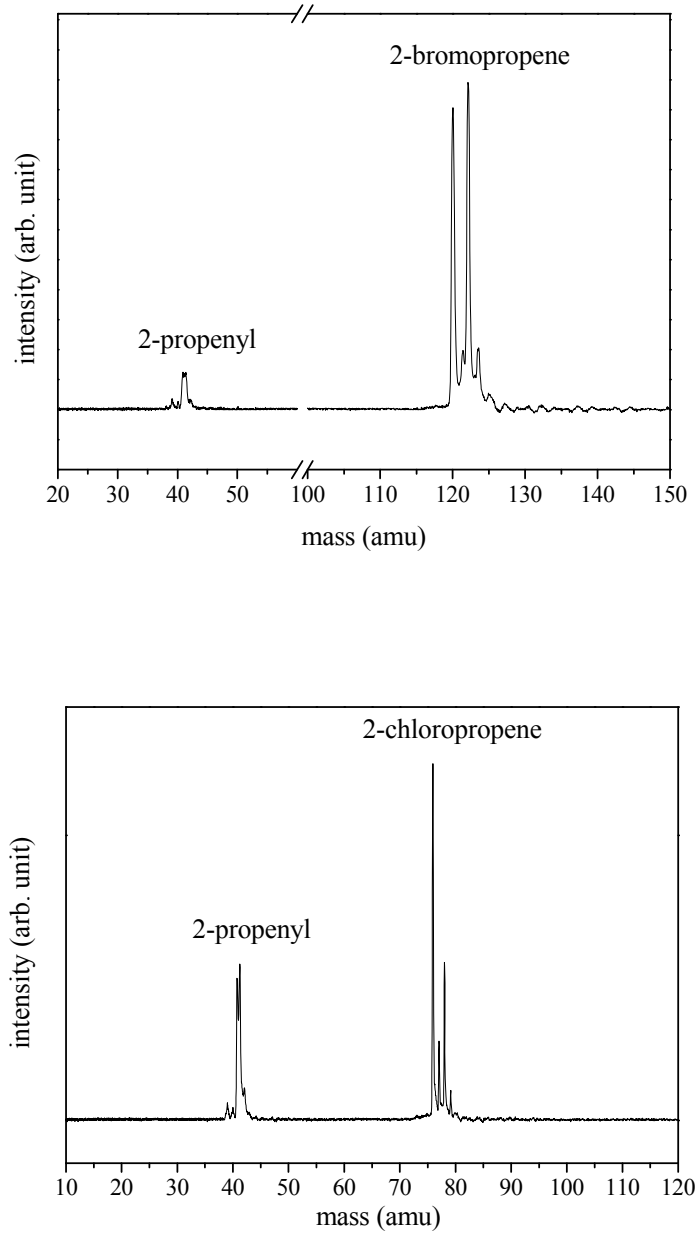

Figure 7.7 121.6 nm VUV photoionization mass spectrum of the 2-propenyl radical beam using the 2-bromopropene and 2-chloropropene precursors in Ar carrier gas. These are the net mass spectrum with the 193 nm photolysis laser on minus off. The main products in each figure are the 2-propenyl radical at m/z = 41 amu and the precursor peak.

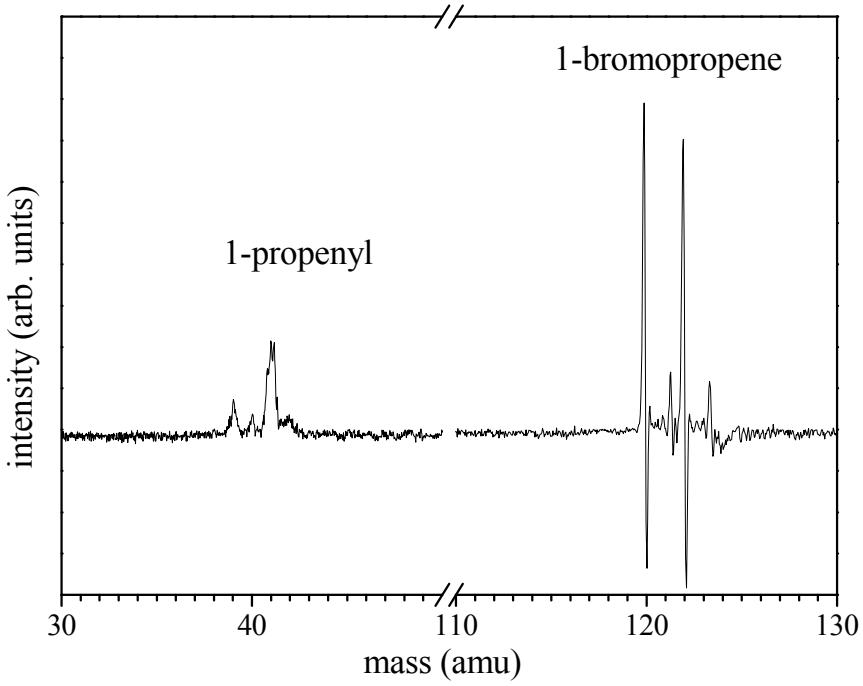

Figure 7.8 121.6 nm VUV photoionization mass spectrum of the 1-propenyl radical beam using the 1-bromopropene precursor in Ar carrier gas. This is the net mass spectrum with the 193 nm photolysis laser on minus off. The main products in the figure are the 1-propenyl radical at m/z = 41 amu and the precursor peak.

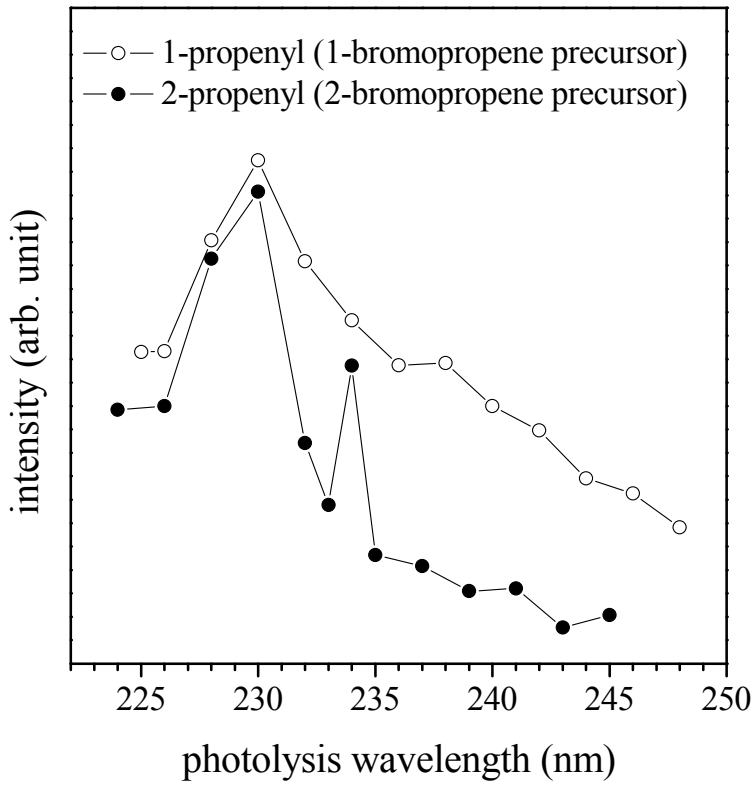

Figure 7.9 H-atom product yield (PFY) spectra of the 1-propenyl and 2-propenyl radicals as a function of photolysis excitation energy. Open circles（○) represent the integrated HRTOF signals of 1-propenyl radical using the 1-bromopropene precursor in the photolysis wavelength region 225-248 nm. Full circles (●) represent the integrated HRTOF signals of 2-propenyl radical using the 2-bromopropene precursor in the photolysis wavelength region 224-245 nm.

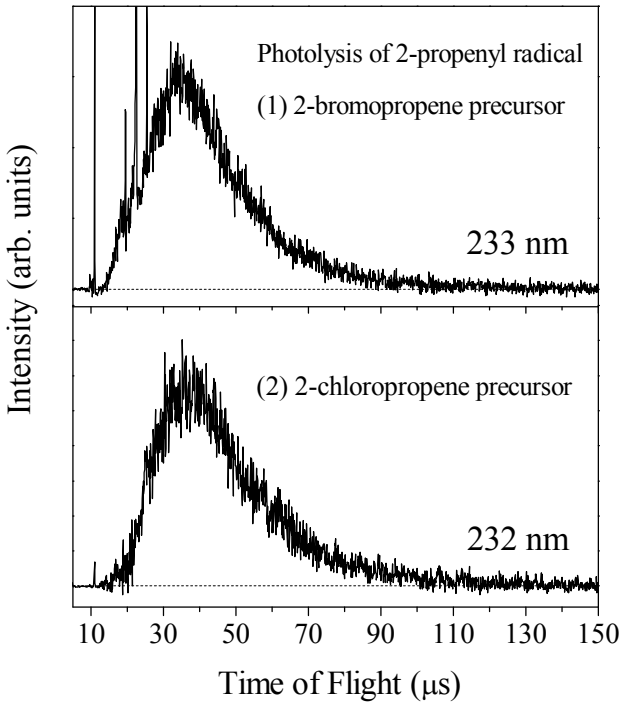

Figure 7.10 H-atom TOF spectra of jet-cooled 2-propenyl radical at photolysis wavelength (1) 233 nm and (2) 232 nm, produced from 193-nm photolysis of (1) 2-bromopropene precursor and (2) 2-chloropropene precursor. These are the net TOF spectra with the full spectrum minus the background. The polarization vector of the photolysis laser radiation is parallel ($\theta = 0°$) to the TOF axis.

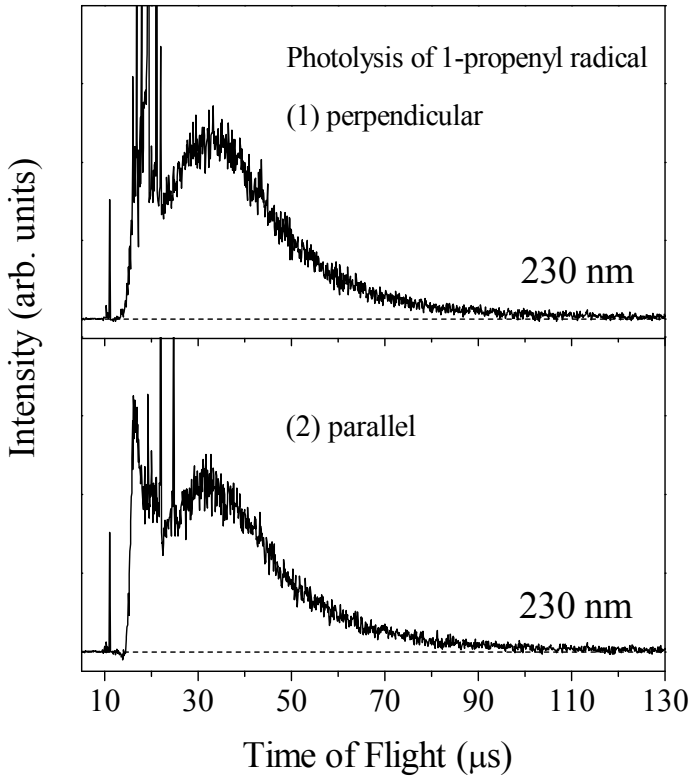

Figure 7.11 H-atom TOF spectra of jet-cooled 1-propenyl radical at photolysis wavelength 230 nm with polarization ***E*** vector of the photolysis radiation (1) perpendicular ($\theta = 90°$) and (2) parallel ($\theta = 0°$) to the TOF axis. The 1-propenyl radical was produced from 193-nm photolysis of 1-bromopropene precursor. These are the net TOF spectra with the full spectrum minus the background.

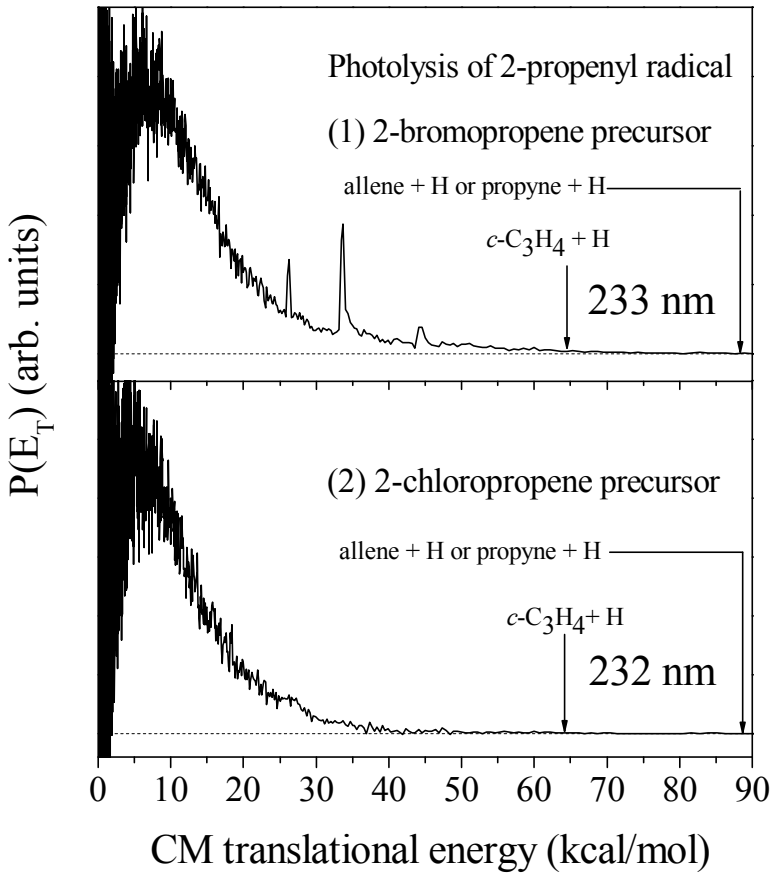

Figure 7.12 Center-of-mass product translational energy distributions, $P(E_T)$, of the H + C_3H_4 product channel from 233 nm and 232 nm photodissociation of 2-propenyl with (1) 2-bromopropene (2) 2-chloropropene as precursor. The $P(E_T)$ distributions are directly converted from the H-atom TOF spectra in Figure 7.10. The maximum translational energies for the three H dissociation channels of 2-propenyl are shown by the arrows in the figure.

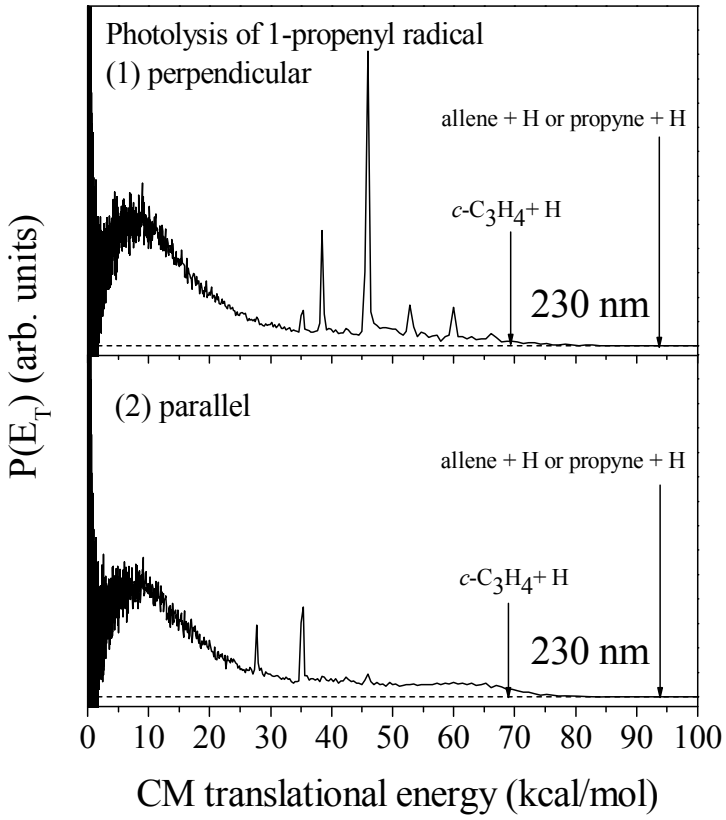

Figure 7.13 Center-of-mass product translational energy distributions, $P(E_T)$, of the H + C_3H_4 product channel from 230 nm photodissociation of 1-propenyl with 1-bromopropene as precursor. The polarization ***E*** vector of the photolysis radiation was (1) perpendicular (θ = 90°) and (2) parallel (θ = 0°) to the TOF axis. The $P(E_T)$ distributions are directly converted from the H-atom TOF spectra in Figure 7.11. The maximum translational energies for the three H dissociation channels of 1-propenyl are shown by the arrows in the figure.

References

(1) Porter, G.; Ward, B. *Proceedings of the Royal Society of London Series a-Mathematical and Physical Sciences* **1965**, *287*, 457.

(2) Ikeda, N.; Nakashima, N.; Yoshihara, K. *Journal of the American Chemical Society* **1985**, *107*, 3381.

(3) Engert, J. M.; Dick, B. *Applied Physics B-Lasers and Optics* **1996**, *63*, 531.

(4) Wallington, T. J.; Egsgaard, H.; Nielsen, O. J.; Platz, J.; Sehested, J.; Stein, T. *Chemical Physics Letters* **1998**, *290*, 363.

(5) Radziszewski, J. G. *Chemical Physics Letters* **1999**, *301*, 565.

(6) Madden, L. K.; Moskaleva, L. V.; Kristyan, S.; Lin, M. C. *Journal of Physical Chemistry A* **1997**, *101*, 6790.

(7) Negru, B.; Goncher, S. J.; Brunsvold, A. L.; Just, G. M. P.; Park, D.; Neumark, D. M. *Journal of Chemical Physics* **2010**, *133*, 074302.

(8) Kadi, M.; Davidsson, J.; Tarnovsky, A. N.; Rasmusson, M.; Akesson, E. *Chemical Physics Letters* **2001**, *350*, 93.

(9) Park, M. S.; Lee, K. W.; Jung, K. H. *Journal of Chemical Physics* **2001**, *114*, 10368.

(10) Ichimura, T.; Mori, Y. *Journal of Chemical Physics* **1973**, *58*, 288.

(11) Mueller, J. A.; Parsons, B. F.; Butler, L. J.; Qi, F.; Sorkhabi, O.; Suits, A. G. *Journal of Chemical Physics* **2001**, *114*, 4505.

(12) Morton, M. L.; Miller, J. L.; Butler, L. J.; Qi, F. *Journal of Physical Chemistry A* **2002**, *106*, 10831.